Universitat Autònoma de Barcelona

NEW OXYNITRIDE MATERIALS WITH LUMINESCENT, MAGNETIC AND CATALYTIC PROPERTIES

Ashley Phillip Black Serra

Universitat Autònoma de Barcelona

NEW OXYNITRIDE MATERIALS WITH LUMINESCENT, MAGNETIC AND CATALYTIC PROPERTIES

Ashley Phillip Black Serra

Tesis Doctoral

Programa de Doctorado en Ciencia de Materiales

Directora: **Amparo Fuertes Miquel**

Tutor: **Lluís Escriche Martínez**

Departamento de Química

Facultad de Ciencias

2017

Instituto de Ciencia de Materiales de Barcelona

Consejo Superior de Investigaciones Científicas

Campus de la UAB

08193 Bellaterra (Barcelona)

Universidad Autónoma de Barcelona

Departamento de Química 08193 Bellaterra (Barcelona)

Memoria presentada para aspirar al Grado de Doctor por

Ashley Phillip Black Serra

Visto bueno de

Amparo Fuertes Miquel

Bellaterra, 21 de abril de 2017

La Dra. **Amparo Fuertes Miquel**, Profesora de Investigación del CSIC en el instituto de Ciencia de Materiales de Barcelona.

CERTIFICA:

Que Ashley Phillip Black Serra, licenciado en Química, ha realizado bajo su dirección el trabajo que lleva por título "*New oxynitride materials with luminescent, magnetic and catalytic properties*", que se presenta en esta memoria para optar al grado de Doctor por la Universidad Autónoma de Barcelona.

Y para que así conste, firma el presente certificado en Bellaterra, 21 de abril de 2017.

Prof. Amparo Fuertes Miquel Dr. Lluís Escriche Martínez

A mi madre, María Aurora

"It's the possibility of having a dream come true that makes life interesting"

Pablo Coelho

Acknowledgements

En primer lugar quisiera agradecer especialmente a la Prof. Amparo Fuertes por su excelente trabajo de dirección, agradezco que me haya dado la oportunidad de trabajar con una gran variedad de materiales, así como las numerosas horas que ha dedicado a trasmitirme su pasión por la síntesis y la caracterización estructural. Valoro enormemente la actitud explorativa y el rigor científico con el que lleva a cabo su trabajo de investigación. Ha sido un verdadero lujo poder contar con una persona de tu calibre para guiarme a lo largo de este proceso de aprendizaje. Asimismo, ha sido un placer formar parte del Departamento de Química del Estado Sólido que han sido el caldo de cultivo en el que he podido madurar como científico pero sobretodo un entorno rico en valores en el que he podido rodearme de magnificas personas que me han ayudado a crecer.

En segundo lugar quisiera agradecer al Prof. Alejandro Goñi por su colaboración a la hora de caracterizar las propiedades luminiscentes de los materiales así como por su valiosa contribución a la discusión de resultados. También quisiera agradecer al Dr. Carlos Frontera por su ayuda con los afinamientos Rietvelt de las estructuras, por trasmitirme parte de su destreza con el manejo del Fullprof así como por su trato cercano y amigable que hicieron que las largas estancias en el sincrotrón hayan sido francamente memorables.

I would like to thank Prof. Ram Sheshadri for accepting me for a two month stay in his laboratory (*Materials Research Laboratory, University of California, Santa Barbara*, USA) as for supervising my research on the luminescent properties of the phosphors presented in this thesis as to Dr.

Kristin Denault for her collaboration in the characterization of luminescent properties of some samples. I would also like to thank Dr.Michael Gaultois to introduce me in to spark plasma sintering (SPS) methodologies. I would also like to thank all three for welcoming me into the MRL and for sharing with me a chip of their scientific knowledge, their good sense of humour and traditions as my first Thanksgiving day. I would also like to thank Amanda Strom, instrument scientist, for the wonderful instrument training and assistance that she gave me. I thank all the members of Ram's group and MRL folks that I met there, Clayton, Anna, Jason, Megan, Leo, Greg, Timo, Manuel, ...

I would like to thank Prof. Ryu Abe for the warm welcoming and generous hospitality with which he attended me during my two month stay in his laboratory (*Department of Energy and Hydrocarbon Chemistry, Graduate School of Engineering, Kyoto University, Kyoto, Japan*). During my stay I could develop my research on metal oxynitride semiconductors for photocatalytic splitting of water in a cutting edge scientific environment and at the same time feel like one more member of his group or should I say of the Abe Lab family. I would like to thank specially to assistant professor Higashi and Tomita san for their guidance during the lab procedures, and the excellent quality time spent out of the lab, so as to Hajime Suzuki (Ishiro) for his friendship and active collaboration in the photocatalytic characterization of the samples presented in this thesis. I would equally like to thanks all the members of Abe Sensei group for their generous welcoming, funny moments and great memories that we shared there: Eri, Ukita, Iwase, Yabuuchi, Kunioku, Takashi, Haitham, Sato, Yuta, Nitta, ...

I would also like to thank Prof. Paul Attfield from the University of Edinburgh for his collaboration on determination of the magnetic structure of chromium samples presented in this thesis, so as for his collaboration on the neutron diffraction study of anion order in $Sr_{1-x}Ba_xTaO_2N$ ($0 \leq x \leq 1$) (these results are not included in the present work). I also want to thank Hanna Johnston who performed the neutron diffraction Rietveld refinements of the $LnCrO_{3-x}N_x$ samples. I also want to thank the experimental team for the numerous hours spent on the data acquisition at GEM and HRPD lines at the ISIS and on D1B, D2B and D20 at the ILL: Lucy Clark and Alex Sinclair so as to the beamline scientists Aziz Daoud-Aladine and David Keen at ISIS and specially to Clemens Ritter at ILL for his professionality and implication during the data acquisition that insured us to get the best data quality possible.

I also want to thank Prof. A. Sundaresan and Dr. Nitesh Kumar from the Jawaharal Nehru Centre for Advance Scientific Research in Bangalore, India for the electrical measurements performed on the hafnium and zirconium perovskites presented in this work.

A continuación quisiera agradecer a todas las personas de la esfera UAB, los miembros del Departamento de Química del Estado Sólido y servicios científico técnicos del ICMAB sin las cuales este trabajo no habría sido posible.

Dr. Judith Oró la mano derecha (con mucha mano izquierda) del grupo de nitruros, gracias por ayudarme tantísimas veces con los hornos de amonolisis, realmente ha habido periodos en los que ha sido un mano a mano con la preparación de muestras antes de los temidos *deadlines* para los experimentos de neutrones y sincrotrón, sin ti trabajos como el Sr_2FeWO_5N no habrían sido posibles. Gracias Judith también por los

trabajos de microscopia electrónica de transmisión y difracción de electrones que has llevado a cabo sobre los oxinitrurosilicatos y perovskitas presentes en este trabajo así como por introducirme numerosos conceptos cristalográficos importantes, ha sido un gusto trabajar con una persona tan amigable como tú. También quisiera agradecer especialmente a Roberta Ceravola y Marixa Arnedillo por los análisis termogarvimetricos y el buen humor con el que he compartido el día a día en la zona experimental. Así mismo quisiera agradecer a los miembros del servicio de rayos X Anna Crespi, Joan Esquius y Xavi Campos, que hacen que el servicio funcione como un reloj suizo engrasado con buen ambiente, así como a Pablo Garcia del servicio de rayos X de ICN2 y a Dr. Bernat Bozzo por las medidas de susceptibilidad magnética y las fructíferas discusiones de resultados. Gracias a la Dra. Vega Lloveras por su entrenamiento en el servicio de espectroscopia, así como a Regina Roca de los servicios de análisis elemental de la UB por los incontables análisis de nitrógeno que ha realizado.

Je voudrais aussi remercier a tous les étudiants de l'université de Rennes qui sont venu réaliser leur stage de licence ou master avec nous, dans le groupe des nitrures : Delphine Amilien, William Bonin, Charles Beurel, Léna Le Pivaingt et Johnny Gautier, vous aves tous êtes des super étudients avec qui j'ais aussi beaucoup appris est passé des super moments dans et dehors du Lab. Mercie pour votre excellant travail expérimental!

También quisiera agradecer a todos los amigos que he conocido a lo largo de estos años que han hecho que el camino haya sido la mejor parte del viaje. Todos los compañeros del despacho *On fire*! : Alex (mi mentor), Nina, Laura, Stefania (el comité de sabias), Pedro y Manu (los desertores), Roberta, María y Tibo (me voy tranquilo sabiendo que dejo el despacho en

buenas manos). Mi pequeña familia en el campus, el grupo de Lunch time, A muerte y Climb-Arte: Alex, Diana, Gustau, Bernis[3], Fede, James, Kumy, Fabian, Mateo, Roque, Max, Laura, Blai, Juanlu, Roberto, Pablo, Roqueta, Pedro, Kevin,… con vosotros he compartido mis pasiones, inquietudes y la mayoría del tiempo libre, os debo los mejores momentos de estos años gracias a todos!

Ela, conocerte ha sido lo mejor que me ha pasado, contar contigo como compañera en la vida es una experiencia enriquecedora y super divertida, disfruto mucho de nuestros contrastes y cada día aprendo algo contigo, gracias por tu apoyo.

Finalmente, quisiera agradecer a mi preciosa familia, a mi hermana, Paloma, y a mi madre, María Aurora, por sus incontables esfuerzos y sacrificios. Tú has sido quien me ha enseñado a luchar por lo que uno quiere y a amar lo que uno tiene. A mis amigos de mi tierra que sois como hermanos para mi y todas las personas que han plantado una semilla o regado mi camino. A todos vosotros, muchas gracias!

Por último, quisiera agradecer al Ministerio de Economía, Industria y Competitividad que han financiado esta tesis mediante los proyectos MAT2011-24757, MAT2014- 43400-R y SEV-2015-0496, y una beca de formación de personal investigador (FPI) con referencia BES-2012-057404 asignada al primer proyecto.

Abstract

In recent years oxynitride materials have received increasing attention because of their emerging applications as photocatalysts, phosphors, pigments, dielectrics and magnetic materials.

This thesis reports the synthesis and characterization of two new oxynitride phosphors with potential application in warm white light LED technologies. The new compounds $LaSrSiO_3N$ and $LaBaSiO_3N$ activated with Eu^{2+} are orange-red light-emitting luminescent materials under excitation in the UV-blue range. We also report that the solid solution $Sr_{2-x}La_xSiO_{4-x}N_x$ ($0 \leq x \leq 1$), can be obtained by concomitant substitution of Sr^{2+} by La^{3+} and O^{2-} by N^{3-} in Sr_2SiO_4. By controlling the composition the emission colours can be tuned from yellow ($x = 0.2$) to orange-red ($x = 1$) for Eu^{2+} phosphors and from blue-green ($x = 0.2$) to orange-yellow ($x = 1$) in Ce^{3+} doped samples.

On the other hand, this thesis has been directed towards the synthesis and study of new oxynitride perovskites extending the range of this group of compounds to the transition metals Cr and Hf.

$LnCrO_{3-x}N_x$ perovskites with Ln = La, Pr and Nd and nitrogen contents up to $x = 0.59$ have been synthesised through ammonolysis of $LnCrO_4$ precursors. Nitride substitution induces oxidation of Cr^{3+} to Cr^{4+} as the mechanism of charge compensation and the consequences of this on magnetic ordering transitions have been studied. Hole-doping through O^{2-}/N^{3-} anion substitution suppresses magnetic order but far less drastically than Ln^{3+}/M^{2+} (M = Ca, Sr) cation substitutions.

Finally, we show the synthesis, structure, electrical and photocatalytic properties of new hafnium oxynitride perovskites $LnHfO_2N$ where Ln= La, Pr, Nd and Sm, and the previously reported analogous compound $LaZrO_2N$. They crystallize in the orthorhombic $GdFeO_3$-type superstructure and show band gaps between 3.4 and 2.8 eV. The time course of O_2 and H_2 evolution under Xenon lamp 300 W irradiation showed that the hafnium perovskites have the adequate oxidation and reduction potential to conduct the overall water splitting reaction in presence of a sacrificial agent. Dielectric and resistivity measurements showed that both Hf and Zr perovskite oxynitrides are electric insulators with dielectric constants between 16 and 30 at room temperature.

Resum

En les darreres dècades els oxinitrurs han rebut un interès creixent degut al vast rang d'aplicacions en els quals han mostrat una aplicabilitat potencial. Destaquen les seves propietats com fotocatalitzadors actius en el visible en processos de fotòlisi d'aigua, pigments inorgànics no tòxics, fòsfors per a LEDs (*light emitting diodes*) de llum blanca, materials amb magneto resistència colossal i materials dielèctrics o ferroelèctrics.

En aquesta tesi presentem la síntesi i caracterització de dos nous fòsfors amb potencial aplicació en tecnologia LED de llum blanca. Els oxinitrursilicats $LaSrSiO_3N$ i $LaBaSiO_3N$ quan són activats amb Eu^{2+} emeten llum de color vermell ataronjat sota excitació amb radiació blava o UV. La solució sòlida $Sr_{2-x}La_xSiO_{4-x}N_x$ ($0 \leq x \leq 1$) es pot obtenir per la substitució concomitant de Sr^{2+} per La^{3+} i O^{2-} per N^{3-} en l'òxid Sr_2SiO_4. Mitjançant el control de la composició, es pot modificar el color de l'emissió des del grog ($x = 0.2$) fins a vermell ataronjat ($x = 1$) quan es dopa amb Eu^{2+} i des del blau verdós ($x = 0.2$) fins taronja groguenc ($x = 1$) quan es dopa amb Ce^{3+}.

D'altra banda, aquesta tesi també ha tingut com a objectiu la síntesi i estudi de nous oxinitrurs amb estructura de perovskita extenent el rang d'aquest grup de compostos als metall de transició Cr i Hf.

Les perovskites $LnCrO_{3-x}N_x$ amb Ln = La, Pr, Nd i continguts de nitrogen fins $x = 0.59$ van ser sintetitzats per mitjà de la amonòlisis dels precursors $LnCrO_4$. La substitució d'oxigen per nitrogen indueix l'oxidació de Cr^{3+} a Cr^{4+} com a mecanisme de compensació de càrrega i les conseqüències que comporta sobre les propietats magnètiques han sigut investigades. El dopatge amb forats en les perovskites $LnCrO_3$ produït mitjançant la

substitució dels anions O^{2-} per N^{3-} suprimeix l'ordre magnètic però menys dràsticament que quan és induït per la substitució catiònica de Ln^{3+} per M^{2+} (M = Ca, Sr).

Finalment, presentem la síntesi, caracterització estructural i l'estudi de les propietats elèctriques i fotocatalítiques dels nous oxinitrurs amb estructura de perovskita de hafni $LnHfO_2N$ (Ln = La, Pr, Nd, Sm) i del compost anàleg $LaZrO_2N$. Aquests materials cristal·litzen en una estructura ròmbica de tipus $GdFeO_3$ i presenten *band gaps* entre 3.4 i 2.8 eV. L'evolució d'H_2 i O_2 produïda sota la il·luminació amb radiació d'un llum de Xenó de 300 W va demostrar que les perovsquites de hafni tenen els potencials de reducció i oxidació adequats per dur a terme dissociació de la molècula d'aigua en presència dels convenients agents de sacrifici. Les mesures de permitivitat dielèctrica i resistivitat elèctrica van mostrar que els compostos $LnHfO_2N$ (Ln = La, Pr, Nd, Sm) són aïllants elèctrics amb constants dielèctriques entre 16 i 30 a temperatura ambient.

Table of contents

Acknowledgements ..... **I**

Abstract ..... **VII**

Resum ..... **IX**

Table of contents ..... **XI**

Index of figures ..... **XVI**

Index of tables ..... **XXVII**

1 Introduction **1**

1.1 Nitride vs oxide: tuning properties through anion substitution 2

1.2 Properties of nitrides and oxynitrides 5

1.2.1 Nitrides 5

1.2.2 Oxynitrides 8

1.3 Objectives 11

1.4 Oxynitridosilicate phosphors for white LED 12

1.4.1 White LED technology, energy saving impact and strategies 12

1.4.2 Phosphors for solid state lighting 16

1.4.3 Silicon-based oxynitride phosphors 24

1.5 Perovskites: From Oxides to Oxynitrides 28

1.5.1 Anion order in perovskite oxynitrides 31

1.5.2 Electronic properties of oxynitride perovskites 33

1.5.3 Photocatalytic properties of perovskite oxynitrides 36

2 Methods 41

2.1 Synthesis of oxynitrides 42

2.1.1 Thermal Ammonolysis 42

2.1.2 High temperature solid state synthesis 46

2.2 Determination of the cationic and anionic stoichiometry 48

2.2.1 Combustion analysis 48

2.2.2 Thermal analysis 49

2.2.3 Energy dispersive X-ray spectroscopy 49

2.3 Structural characterization 50

2.3.1 Laboratory X-ray powder diffraction 50

2.3.2 Synchrotron X-ray powder diffraction 50

2.3.3 Neutron powder diffraction 51

2.3.4 Electron diffraction 52

2.4 Optical characterization 53

2.4.1 Diffuse reflectance 53

2.4.2 Photoluminescence measurements 55

2.4.3 Photoluminescence quantum yield 56

2.5 Electrical and magnetic properties characterization 56

2.5.1 Magnetic susceptibility 56

2.5.2 Electrical resistivity and dielectric measurements 57

2.6 Photocatalytic measurements 57

2.6.2 Photoelectrochemical measurements 58

2.6.3 Gas evolution measurement 59

3 Oxynitridosilicate Phosphors for Solid-State White Lighting: Synthesis and luminescent properties of $M_{2-x}La_xSiO_{4-x}N_x$: Eu^{2+} or Ce^{3+} (M= Sr, Ba ; 0≤x≤1) 63

3.1 Introduction 64

3.2 Objectives 66

3.3 Results and discussion 67

3.3.1 Synthesis of oxyninitridosilicates with β-K_2SO_4 structure 67

3.3.2 Chemical characterization 70

3.3.3 Structural Characterization 74

3.3.4 Photoluminescent properties 98

3.3.5 Ferromagnetism of $LaEuSiO_3N$ 119

3.4 Conclusions 120

4 Nitride tuning of lanthanide chromites 125

$LnCrO_{3-x}N_x$ (Ln = La, Pr, Nd, Sm; 0< x ≤0.59) 125

4.1 Introduction 126

4.2. Objectives 127

4.3. Results and discussion 128

4.3.1 Synthesis of $LnCrO_{3-x}N_x$ ($0 \le x \le 0.59$) Ln = La, Pr, Nd and Sm 128

4.3.1 Determination of nitrogen contents of $LnCrO_{3-x}N_x$ by combustion analysis 133

4.3.2 Structural Characterization 133

4.3.3 Magnetic properties 146

4.3.4 Effect of O^{2-}/N^{3-} anion substitution *vs* Ln^{3+}/M^{2+} (M= Ca, Sr) cation substitution on the magnetic properties of lanthanide chromites 150

4.4. Conclusions 153

5 Hafnium and zirconium oxynitride perovskites, synthesis, structure, electrical properties and photocatalytic activity 155

5.1 Introduction 156

5.2 Objectives 159

5.3 Results and discussion 159

5.3.1 Synthesis of $LnHfO_2N$ Ln = La, Nd, Sm, Pr. 159

5.3.2 Synthesis of $LaZrO_2N$ 161

5.3.3 Chemical characterization 162

5.3.4 Structural Characterization 165

5.3.5 Diffuse reflectance spectra 178

5.3.6 Photocatalytical activity 181

5.3.7 Electrical properties 195

5.4 Conclusions 200

6 Conclusions 202

7 Publications 209

8 Bibliography 213

Index of figures

Figure 1.1. Schematic band structures in semiconducting transition metal oxides and oxynitrides. 4

Figure 1.2. Curve of human eyes sensitivity to light according to its colour. 14

Figure 1. 3. Schematic of the three principal white lightening strategies. (a) A tree-LED strategy with (RGB) LED chips. (b) A three-phosphor strategy with UV LED and RGB phosphors. (c) A blue LED with a yellow downconverting phosphor and representative spectrum from such device. 15

Figure 1. 4. a) Energy level diagram of Ce^{3+}, Eu^{2+} and Eu^{3+} in oxide host lattices, b) Configurational-coordinate diagram of a luminescent centre. 18

Figure 1. 5. Schematic energy level diagram for Eu^{2+} showing the effect of the host. 19

Figure 1. 6. The 1931 CIE diagram. The Plankian locus is showed in black, and the colour coordinates of some common phosphors are plotted. 23

Figure 1. 7. The ideal ABX_3 perovskite structure showing the coordination of the B- and A-site cations. 29

Figure 1. 8. (a) N/O order in ABO_2N perovskite oxynitride. (b) π bonding of d orbitals with O/N lone pairs showing three and two interactions in the *cis*- and *trans*- configurations respectively. *Cis*-$(MN)_n$ chain formation arising from local anion order (c) Disorder of chains within planes. (d) 3D partial order configurations. 33

Figure 1. 9. Schematic diagram illustration of water splitting over semiconductor photocatalyst, (i) light absorption and photo-excitation of electron-hole pairs, (ii) charge separation and migration to the surface, and (iii) oxidation and reduction reactions at the surface. (a) indicates sacrificial oxidizing reagent, (b) indicates sacrificial reducing reagent and (c) indicates co-catalyst, typically Pt for reduction and CoO_x for oxidation. 37

Figure 2. 1. Equilibrium constant of dissociation of NH_3 as function of the temperature (b) % of decomposition of NH_3 as function of the flow rate at different temperatures..... 43

Figure 2. 2. Ammonolysis furnace. 44

Figure 2. 3. High temperature tubular furnace 46

Figure 2. 4. Molybdenum boat and zirconium foil 47

Figure 2. 5. Schematic representation of the rotation method used to reconstruct the reciprocal lattice by electron diffraction. c^* is the common axis for all patterns. 53

Figure 2. 6. Scheme and image of the photoelectrochemical setup..... 59

Figure 2. 7. Scheme and image of the closed gas-circulation system. 60

Figure 3. 1. TGA curves in O_2 for $Sr_{2-x}La_xSiO_{4-x}N_x$ samples. 71

Figure 3. 2. Energy dispersive X-ray spectra of $Sr_{2-x}La_xSiO_{4-x}N_x$ ($0.0 \leq x \leq 1.0$)..... 73

Figure 3. 3. Structural model of $LaMSiO_3N$ compounds showing zig-zag chains of sites M1 (grey polyhedra) and M2 (green polyhedra) running along a, and b) coordination polyhedra of cations. Anions are represented by red (oxygen) and light blue (mixed oxygen/nitrogen) spheres. 78

Figure 3. 4. Observed and calculated powder X-ray diffraction patterns for $LaSrSiO_3N$. 79
Figure 3. 5. Observed and calculated powder X-ray diffraction patterns for $LaBaSiO_3N$. 80
Figure 3. 6. Observed and calculated powder X-ray diffraction patterns for $LaEuSiO_3N$. 81
Figure 3. 7. Observed and calculated powder neutron diffraction patterns for $LaBaSiO_3N$ for data collected on the 90^o detector bank (a), and backscattering detector bank (b) of HRPD. 82
Figure 3. 8. Observed and calculated synchrotron X-ray powder diffraction patterns for $La_xSr_{2-x}SiO_{4-x}N_x$. 87
Figure 3. 9. Refined parameters from synchrotron X-ray powder diffraction data of $Sr_{2-x}La_xSiO_{4-x}N_x$ samples as a function of La/N content. The parameters of sample with x=0.8 were obtained from laboratory X-ray diffraction data. 89
Figure 3. 10. Bond valence sums, average bond distances and polyhedral volumes and distortions of sites M1 (blue points, dotted line) and M2 (red points, solid line) in $Sr_{2-x}La_xSiO_{4-x}N_x$. 90
Figure 3. 11. X-ray powder diffraction patterns of $LaSr_{1-x}Eu_xSiO_3N$ (top) and $La_{1-x}Ce_xSrSiO_3N$ (bottom) with (x=0.0, 0.01, 0.02, 0.05, 0.1). 92
Figure 3. 12. X-ray powder diffraction patterns of $LaBa_{1-x}Eu_xSiO_3N$ (top) with (x=0.0, 0.01, 0.02, 0.05, 0.1) and $LnMSiO_3N$ (bottom) with (M=Sr, Eu; Ln=La, Nd). 93
Figure 3. 13. X-ray powder diffraction patterns for $Sr_{1.98-x}Eu_{0.02}La_xSiO_{4-x}N_x$ ($0 \geq x \geq 1$) and enlarged areas of the intense reflections around Q=2 $Å^{-1}$ region. 94

Figure 3. 14. X-ray powder diffraction patterns for $Sr_{2-x}La_{x-0.02}Ce_{0.02}SiO_{4-x}N_x$ ($0 \geq x \geq 1$) and enlarged areas of the intense reflections around Q=2 $Å^{-1}$ region. 94
Figure 3. 15. Electron diffraction patterns, indexing and reconstruction of the reciprocal lattice along the [010]* zone axis of $LaSrSiO_3N$. Circles indicate multiple diffraction reflections. 96
Figure 3. 16. Electron diffraction micrographs along the zone axes [100]*, [010]* and [001]* for (a) Sr_2SiO_4, (b) $LaSrSiO_3N$, (c) $LaBaSiO_3N$ and (d) $LaEuSiO_3N$. The structural modulation along b* is indicated by arrows whereas circles indicate multiple diffraction reflections. 97
Figure 3. 17. Normalized excitation and emission spectra of $LaSr_{1-x}Eu_xSiO_3N$ (x=0.01, 0.02, 0.05, 0.1) 100
Figure 3. 18. Normalized excitation and emission spectra of $LaBa_{1-x}Eu_xSiO_3N$ (x=0.01, 0.02, 0.05) 100
Figure 3. 19. Normalized excitation and emission spectra of $La_{1-x}Ce_xSrSiO_3N$ (x=0.01, 0.02, 0.05, 0.1). 101
Figure 3. 20. Emission spectra of $LaSr_{1-x}Eu_xSiO_3N$ with different Eu^{2+} concentration (λ_{ex}=405 nm). 103
Figure 3. 21. Emission spectra of $La_{1-x}Ce_xSrSiO_3N$ with different Ce^{3+} concentration (λ_{ex}=405 nm). 103
Figure 3. 22. Normalized excitation (λ_{em}=550 nm, dotted line) and emission (λ_{ex}=405 nm, solid line) spectra of $LaSr_{0.95}Eu_{0.05}SiO_3N$ and $Sr_{1.95}Eu_{0.05}SiO_4$.[22] 104
Figure 3. 23. Normalized excitation (λ_{em}=550 nm, dotted line) and emission spectra with deconvolutions (λ_{ex}=405 nm, solid line) collected at room temperature for $La_xSr_{2-x}SiO_{4-x}N_x:Eu^{2+}$ samples. 105

Figure 3. 24. Normalized excitation (λ_{em}=550 nm, dotted line) and emission spectra with deconvolutions (λ_{ex}=405 nm, solid line) collected at room temperature for $La_xSr_{2-x}SiO_{4-x}N_x:Ce^{3+}$ samples.....107
Figure 3. 25. Diffuse reflectance spectra of (a) $LaSrSiO_3N$, $La_{0.95}Ce_{0.05}SrSiO_3N$, $LaSr_{0.95}Eu_{0.05}SiO_3N$, (b) $LaBaSiO_3N$, $LaBa_{0.95}Eu_{0.05}SiO_3N$, (c) $LaEuSiO_3N$, (d) $NdSrSiO_3N$, (e) $NdEuSiO_3N$, and Kubelka-Munk plot of (f) $LaSrSiO_3N$ (g) $LaBaSiO_3N$, (h) $LaEuSiO_3N$, (i) $NdSrSiO_3N$, (j) $NdEuSiO_3N$. 109
Figure 3. 26. Diffuse reflectance spectra of $Sr_{2-x}La_xSiO_{4-x}N_x$ (blue solid line) and $Sr_{2-x}La_xSiO_{4-x}N_x:Eu^{2+}$ (red dotted line) samples.....111
Figure 3. 27. Kubelka-Munk plots of $Sr_{2-x}La_xSiO_{4-x}N_x$ were (a) x=0.2, (b) x=0.3 and (c) x=0.5.....112
Figure 3. 28. CIE color coordinates of $LaSr_{1-x}Eu_xSiO_3N$ for $0.01\leq x\leq 0.1$.....115
Figure 3. 29. CIE color coordinates of $LaBa_{1-x}Eu_xSiO_3N$ for $0.01\leq x\leq 0.05$...115
Figure 3. 30. CIE color coordinates of $La_{1-x}Ce_xSrSiO_3N$ for $0.01\leq x\leq 0.1$.....116
Figure 3. 31. CIE diagram showing the change of emission colour in $Sr_{2-x}La_xSiO_{4-x}N_x$ activated with Eu^{2+} (from green to red, square markers) and with Ce^{3+} (from blue to yellow, cross markers). 117
Figure 3. 32. Pictures of commercial LED (405 nm) covered with silicon caps containing $Sr_{2-x}La_xSiO_{4-x}N_x:Eu^{2+}$ phosphors (a) x=0.2, (b) x=0.3, (c) x=0.5.....118
Figure 3. 33. Magnetic-field dependence of the magnetization of $LaEuSiO_3N$ at T = 2, 4, 6, 10, 20 and 50 K. Inset: FC-ZFC magnetic susceptibility. 119
Figure 4. 1. Flowchart of $LnCrO_4$ synthesis by the Pechini method. 130
Figure 4. 2. TGA and DSC curves in air of the Pechini dry resins obtained for the synthesis of $LnCrO_4$ compounds for the lanthanides (a) La, (b) Pr, (c) Nd and (d) Sm.....132
Figure 4. 3. X-ray powder diffraction patterns of $LnCrO_4$ where Ln=La, Pr, Nd and Sm. 134

Figure 4. 4. Observed and calculated synchrotron X-ray powder diffraction patterns at room temperature for (a) $LaCrO_{2.72}N_{0.28}$, (b) $PrCrO_{2.81}N_{0.19}$, (c) $NdCrO_{2.58}N_{0.42}$, (d) $SmCrO_{2.76}N_{0.24}$.....136
Figure 4. 5. Structural models for $LnCrO_{3-x}N_x$ compounds, where Ln = (a) La, (b) Pr, (c) Nd, (d) Sm.....139
Figure 4. 6. Cell parameters for Ln = Nd and volumes for Ln = La, Pr and Nd as a function of nitrogen content in $LnCrO_{3-x}N_x$ perovskites.....140
Figure 4. 7. Observed and calculated room temperature neutron powder diffraction patterns for $LaCrO_{2.72}N_{0.28}$ (λ= 1.594 Å).....141
Figure 4. 8. Observed and calculated neutron powder diffraction patterns at 10 K for $LaCrO_{2.72}N_{0.28}$ with magnetic diffraction peaks from Cr spins marked below the nuclear diffraction peaks (λ=2.524 Å).....141
Figure 4. 9. Observed and calculated room temperature neutron powder diffraction patterns for $PrCrO_{2.64}N_{0.36}$ (λ= 1.36 Å). 142
Figure 4. 10. Observed and calculated neutron powder diffraction patterns at 1.5 K for $PrCrO_{2.64}N_{0.36}$ with magnetic diffraction peaks from Cr and Pr spins marked below the nuclear diffraction peaks (λ=2.524 Å).....142
Figure 4.11. Observed and calculated neutron powder diffraction patterns at room temperature for $NdCrO_{2.58}N_{0.42}$ (λ=1.36 Å). 143
Figure 4.12. Observed and calculated neutron powder diffraction patterns at 1.5 K for $NdCrO_{2.58}N_{0.42}$, with magnetic diffraction peaks from Cr and Nd spins marked below the nuclear diffraction peaks (λ=2.524 Å). 143
Figure 4. 13. Magnetic susceptibility data for selected $LnCrO_{3-x}N_x$ samples with (a) Ln = La, (b) Ln = Pr, and (c) Ln = Nd, and nitrogen contents x as shown. Inset in (b) shows the enlarged region around T_N. 147

Figure 4. 14. Magnetic structure for (a) $LaCrO_{2.72}N_{0.28}$ at 10 K and (b) $NdCrO_{2.58}N_{0.42}$ at 1.5 K refined from neutron diffraction. The Cr ions are shown as green spheres. Ordered Cr moments along the b axis are shown as red arrows. Ordered Nd moments along the c axis are shown as blue arrows.....149
Figure 4. 15. Thermal variation of refined Cr magnetic moment for (a) $LaCrO_{2.72}N_{0.28}$, (b) $PrCrO_{2.64}N_{0.36}$ and (c) variations of the Nd and Cr moments in $NdCrO_{2.58}N_{0.42}$.....150
Figure 4. 16. Cr spin ordering temperatures for doped $LnCrO_3$ materials ($LnCrO_{3-x}N_x$ (Ln= La, Pr, Nd), $La_{1-x}Sr_xCrO_3$, and $La_{1-x}Ca_xCrO_3$) as a function of Cr^{4+} content x; (a) measured T_N's, and (b) T_N^0 values corrected for lattice effects as described in the text. The shaded regions show the different T_N^0 variations for nitride and cation doped samples.....152
Figure 5. 1. Observed and calculated X-ray powder diffraction patterns for Hf_2ON_2.....161
Figure 5. 2. TGA and DSC curves in O_2 for $LnHfO_2N$ with the lanthanides (a) La, (b) Pr, (c) Nd and (d) Sm.....163
Figure 5. 3. Laboratory X-ray diffraction patterns of (a) $LaZrO_2N$, (b) $LaHfO_2N$, (c) $PrHfO_2N$, (d) $NdHfO_2N$, (e) $SmHfO_2N$.....165
Figure 5. 4. Observed and calculated synchrotron X-ray powder diffraction patterns for $LaHfO_2N$. The inset shows a magnification of the high Q region. 167
Figure 5. 5. Observed and calculated synchrotron X-ray powder diffraction patterns for $PrHfO_2N$. Tick marks indicate allowed reflections for $PrHfO_2N$ (upper set) and TiO_2 from the cryostat (lower set). The inset shows a magnification of the high Q region.....167

Figure 5. 6. Observed and calculated synchrotron X-ray powder diffraction patterns for $NdHfO_2N$. The inset shows a magnification of the high Q region. 168
Figure 5. 7. Observed and calculated synchrotron X-ray powder diffraction patterns for $SmHfO_2N$. Tick marks indicate allowed reflections for $SmHfO_2N$ (upper set) and TiO_2 from the cryostat (lower set). The inset shows a magnification of the high Q region. 168
Figure 5. 8. Observed and calculated synchrotron X-ray powder diffraction patterns for $LaZrO_2N$. Tick marks indicate allowed reflections for $LaZrO_2N$ (upper set), $La_2Zr_2O_7$ impurity (middle set) and ZrN impurity (lower set). The inset shows a magnification of the high Q region. 169
Figure 5. 9. Cell parameters and volume against the Ln^{3+} ionic radius for Ln = La, Pr, Nd, and Sm(CN=8)[11].....172
Figure 5. 10. Structural model for $LnHfO_2N$, where Ln = (a) La, (b) Pr, (c) Nd, (d) Sm. $Hf(O/N)_6$ octahedrons are represented in light blue, La^{3+} in blue, Pr^{3+} in green, Nd^{3+} in orange and Sm^{3+} in purple. 172
Figure 5. 11. Rietveld fit to room temperature neutron powder diffraction patterns for $LaHfO_2N$. 176
Figure 5. 12. Rietveld fit to room temperature neutron powder diffraction patterns for $LaZrO_2N$. Tick marks indicate allowed reflections for $LaZrO_2N$ (upper set), V can (middle upper set), $La_2Zr_2O_7$ (middle lower set) and ZrN (lower set).....176
Figure 5. 13. Images of (a) $LaZrO_2N$ and $LnHfO_2N$ powders where Ln= (b) La, (c) Pr, (d) Nd, (e) Sm. 178
Figure 5. 14. Diffuse reflectance spectra of (a) $LaZrO_2N$, (c) $LaHfO_2N$, (e) $NdHfO_2N$, (h) $SmHfO_2N$ and Kubelka-Munk plot of (b) $LaZrO_2N$, (d) $LaHfO_2N$, (f) $NdHfO_2N$, (i) $SmHfO_2N$. 180

Figure 5. 15. Photoelectrodes prepared by deposition of, (a) $LaHfO_2N$, (b) $NdHfO_2N$ and (c) $SmHfO_2N$ particles on FTO glass. 181
Figure 5. 16. Current-voltage curves in aqueous 0.1 M Na_2SO_4 solution (pH ≈ 6) under intermittent visible (blue line) and full range (red line) light irradiation for $LnHfO_2N$ where Ln = (a) La, (b) Nd and (c) Sm electrodes. 183
Figure 5. 17. O_2 evolution (blue spots) from 50 mg of IrO_x(1wt%)-$LaHfO_2N$ in 250 ml of a 10 mM solution of $AgNO_3$ and H_2 evolution (red spots) from 50 mg of Pt(1wt%)-$LaHfO_2N$ in 250 ml of a 20 vol.% Methanol solution under 300 W Xe lamp (λ > 300 nm). 186
Figure 5. 18. O_2 evolution (blue spots) from 50 mg of $LaHfO_2N$ in 250 ml of a 10 mM solution of $AgNO_3$ under 300 W Xe lamp (λ > 300 nm). 187
Figure 5. 19. X-ray photoelectron spectra of, (a) IrO_x-$LaHfO_2N$, (b) Pt-$LaHfO_2N$ and (c) IrO_x-$LaHfO_2N$ after O_2 evolution. 188
Figure 5. 20. Wavelength dependency of, (a) O_2 evolution from 50 mg of IrO_x(1wt%)-$LaHfO_2N$ in 250 ml of a 10 mM solution of $AgNO_3$, and (b) H_2 evolution from 50 mg of Pt(1wt%)-$LaHfO_2N$ in 250 ml of a 20 vol.% methanol solution under 300 W Xe lamp with different cut-off filters (λ > 300, 350, 480 nm). 189
Figure 5. 21. O_2 evolution (blue spots) from 50 mg of $NdHfO_2N$ in 250 ml of a 10 mM solution of $AgNO_3$ and H_2 evolution (red spots) from 50 mg of Pt(0.3 wt%)-$NdHfO_2N$ in 250 ml of a 20 vol.% methanol solution under 300 W Xe lamp (λ > 300 nm). 190
Figure 5. 22. O_2 evolution (blue spots) from 50 mg of IrO_x(1wt%)-$LnHfO_2N$ where Ln = (a) Pr, (c) Sm, in 250 ml of a 10 mM solution of $AgNO_3$. H_2 evolution (red spots) from 50 mg of Pt(1wt%)-$LnHfO_2N$ where Ln = (b) Pr, (d) Sm, in 250 ml of a 20 vol.% methanol solution and N_2 coevolution (black spots) under 300 W Xe lamp (λ > 300 nm). 191

Figure 5. 23. X-ray photoelectron spectra of IrO_x-$LnHfO_2N$ where Ln = (a) Pr, (d) Sm, Pt-$LnHfO_2N$ where Ln = (b) Pr, (e) Sm and IrO_x-$LnHfO_2N$ were Ln = (c) Pr, (f) Sm after O_2 evolution. 193
Figure 5. 24. O_2 evolution (blue spots) from 50 mg of $LaZrO_2N$ in 250 ml of a 10 mM solution of $AgNO_3$ and N_2 coevolution (black spots) under visible light 300 W Xe lamp (λ > 400 nm) irradiation. 194
Figure 5. 25. Temperature dependence of resistivity of (a) $LaZrO_2N$ and (b) $NdHfO_2N$. 196
Figure 5. 26. Scanning electron microscopy image of $NdHfO_2N$ ceramic fired at 1500^0C for 3h. 197
Figure 5. 27. Temperature dependence of dielectric permittivities of (a) $LaHfO_2N$, (b) $NdHfO_2N$, (c) $SmHfO_2N$ and (d) $LaZrO_2N$ measured at 100 kHz. 199
Figure 5. 28. (a) Frequency dependence of dielectric permittivities of $LaHfO_2N$ and $SmHfO_2N$; and temperature dependence of dielectric loss of (b) $NdHfO_2N$ and (c) $LaZrO_2N$ measured at 5 and 1000 kHz. 199

Index of Tables

Table 1.1. Properties of nitrogen and oxygen..... 3
Table 1. 2. Selected SiAlON phosphors..... 27
Table 3. 1. Nitrogen content determined by combustion analysis for $(La,Sr)_2Si(O,N)_4$ samples 70
Table 3. 2. Nitrogen contents determined by TGA for $Sr_{2-x}La_xSiO_{4-x}N_x$ samples..... 72
Table 3. 3. Atomic coordinates, cation and anion occupancies for $LaSrSiO_3N$ from the refinement of X-ray powder diffraction data 79
Table 3. 4. Atomic coordinates, cation and anion occupancies of $LaBaSiO_3N$ from the refinement to X-ray powder diffraction data.....80
Table 3. 5 Atomic coordinates, cation and anion occupancies for $LaEuSiO_3N$ from the refinement of X-ray powder diffraction data..... 81
Table 3. 6 Atomic coordinates, cation and anion occupancies for $LaBaSiO_3N$ from the refinement of neutron diffraction data..... 82
Table 3. 7. Crystallographic and refinement data for $LaSrSiO_3N$, $LaEuSiO_3N$ and $LaBaSiO_3N$..... 83
Table 3. 8. Bond Valence Sums (BVS) for $LaMSiO_3N$ compounds..... 83
Table 3. 9. Bond distances and cell parameters for $LaSrSiO_3N$, $LaEuSiO_3N$, $LaBaSiO_3N$ (this work) and related silicates with β-K_2SO_4 structure..,..... 84
Table 3. 10. Atomic coordinates and occupancies for $La_{0.5}Sr_{1.5}SiO_{3.5}N_{0.5}$..... 88
Table 3. 11. Crystallographic and refinement data from synchrotron X-ray diffraction data (λ=0.458996 Å, T=298 K) for $La_xSr_{2-x}SiO_{4-x}N_x$ (x= 0.0, 0.2, 0.3, 0.5, 1.0) 88

Table 4.1. Synthesis conditions of several $LnCrO_{3-x}N_x$ samples (Ln=La, Pr, Nd, Sm) 129
Table 4. 2. Nitrogen content determined by combustion analyses. 133
Table 4. 3. Summary of the *Pbnm* model for $LaCrO_{2.72}N_{0.28}$ refined against room temperature synchrotron X-ray powder diffraction data. 137
Table 4. 4. Summary of the *Pbnm* model for $PrCrO_{2.81}N_{0.19}$ refined against room temperature synchrotron X-ray powder diffraction data. 137
Table 4. 5. Summary of the *Pbnm* model for $NdCrO_{2.58}N_{0.42}$ refined against room temperature synchrotron X-ray powder diffraction data. 138
Table 4. 6. Summary of the *Pbnm* model for $SmCrO_{2.76}N_{0.24}$ refined against room temperature synchrotron X-ray powder diffraction data. 138
Table 4. 7. Summary of the *Pbnm* model for $LaCrO_{2.72}N_{0.28}$ refined against room temperature neutron powder diffraction data. 144
Table 4. 8. Summary of the *Pbnm* model for $PrCrO_{2.64}N_{0.36}$ refined against room temperature neutron powder diffraction data. 145
Table 4. 9. Summary of the *Pbnm* model for $NdCrO_{2.58}N_{0.42}$ refined against room temperature neutron powder diffraction data. 145
Table 4. 10. Values of Néel temperatures and other magnetic parameters from Curie-Weiss fits to data above T_N for Ln = Pr and Nd samples.....148
Table 4. 11. Summary of the magnetic refinements for *Pbnm* models at low temperatures using D1B neutron diffraction data. Refined lattice parameters and ordered moments at Cr and Nd sites are shown. 149
Table 5. 1. Nitrogen content determined by combustion analysis for $LnMO_2N$ samples (M= Zr, Hf) 162
Table 5. 2. Nitrogen content determined by TGA.....164

Table 5. 3. Summary of the *Pnma* model for $LaHfO_2N$ refined against room temperature synchrotron X-ray powder diffraction data. 169
Table 5. 4. Summary of the *Pnma* model for $PrHfO_2N$ refined against room temperature synchrotron X-ray powder diffraction data. 170
Table 5. 5. Summary of the *Pnma* model for $NdHfO_2N$ refined against room temperature synchrotron X-ray powder diffraction data. 170
Table 5. 6. Summary of the *Pnma* model for $SmHfO_2N$ refined against room temperature synchrotron X-ray powder diffraction data. 171
Table 5. 7. Summary of the *Pnma* model for $LaZrO_2N$ refined against room temperature synchrotron X-ray powder diffraction data. 171
Table 5. 8. Goldschmidt tolerance factor and observed tolerance factor for selected perovskite oxynitrides. 174
Table 5. 9. Summary of the *Pnma* model for $LaHfO_2N$ refined against room temperature neutron powder diffraction data. 177
Table 5. 10. Summary of the *Pnma* model for $LaZrO_2N$ refined against room temperature neutron powder diffraction data. 177

Chapter I

Introduction

1.1 Nitride vs oxide: tuning properties through anion substitution

Oxygen has the ability to form stable compounds with the majority of metals in a great variety of compositions and structures. Some of multinary oxides such as $PbZr_xTi_{1-x}O_3$ ($0 \leq x \leq 1$)[1], $BaTiO_3$,[2] $La_{1-x}Ca_xMnO_3$,[3] $LiCoO_2$,[4] $LiFePO_4$,[5] $YBa_2Cu_3O_7$[6] and $Y_3Al_5O_{12}$:Ce^{3+} [7, 8] are of great technological relevance due to their properties and applications as piezoelectric, ferroelectric, colossal magnetoresistant, cathode materials for batteries, high T_c superconductors and phosphors for white solid state lighting. Oxygen and nitrogen show close chemical and structural features such as ionic radius and preferent coordination numbers that makes possible to substitute one by the other preserving the crystal structure. Nitrogen shows lower electronegativity and higher polarizability (**Table 1.1**) than oxygen and the nitride anion is more charged than oxide. These differences make possible to modulate the oxidation state of the cations and the covalent character of bonding by substituting oxygen by nitrogen. The introduction of nitrogen in an oxide modifies the energy of electronic levels as a consequence of the lower electronegativity of nitrogen which induces a decrease of the band gap and a higher covalent character of the bonds, and because the higher charge of nitride increases the crystal field splitting (**Figure 1.1**). The higher polarizability of nitrogen increases the nephelauxetic effect (expansion of the electron cloud) and decreases the interelectronic repulsion and the energy of d orbitals.

Table 1.1. Properties of nitrogen and oxygen.[9]

	N	O
Anion charge (z)	**-3**	**-2**
Electronegativity	**3.0**	**3.4**
Atomic polarizability/Å^3	**1.10**	**0.80**
Electronic affinity (A $\rightarrow$A^{z-}/kJ mol^{-1})	**1736**	**601**
Bond energy A-A (kJ mol^{-1})[10]	**941**	**499**
Ionic radii / Å (for CN=IV)[11]	**1.46**	**1.38**
Coordination number (CN)	**II-VIII**	**II-VIII**

For chemical reasons, only a limited number of elements other than nitrogen may substitute oxygen. Mixed anion systems can be formed by incorporation of hydrogen,[12] nitrogen, fluorine,[13] chlorine,[14] bromine,[15, 16] iodine,[17] sulphur,[18] selenium[19] or in limited cases by combination of two of these elements in the same compound.[20] Anion substitution has showed to modify the properties of oxides in different way as the more conventional cation doping, and drastic changes can be obtained even at a doping level mostly due to the changes of ionicity of the metal-anion bond. Within the two last decades oxynitrides have received increasing attention and have been identified as a fascinating class of new materials.[21-23] However, the formation of oxynitrides is thermodynamically unfavourable compared to the formation of oxides because of the high bond energy of the diatomic molecule of N_2 that is about twice that of O_2 (945 KJ/mol for N≡N vs. 498 KJ/mol for O=O) and, for more ionic compounds, also because of the large electronic affinity of nitrogen (1736 KJ/mol for N$\rightarrow$N^{3-} vs 601 KJ/mol for O$\rightarrow$O^{-2})[10].

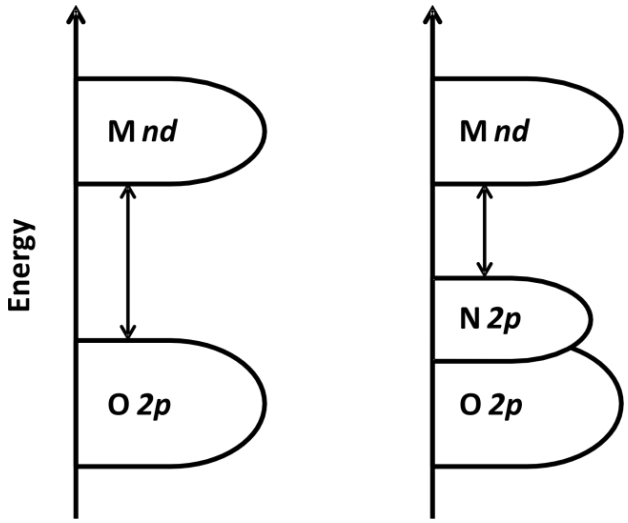

Figure 1.1. Schematic band structures in semiconducting transition metal oxides and oxynitrides.

Contrarily to oxygen, nitrogen is atmophile element,[24] ranking only thirty-first element in the earth's crust, where most nitrogen is present as ammonium ion, substituting to a small extent for alkali ions in minerals. Sinoite (Si_2N_2O) is the only naturally occurring oxynitride reported, which so far has only been found in two meteorites.[25]

Because of the lower stability of nitrides with respect to oxides the synthetic preparation of oxynitrides requires more challenging methods. High activation temperatures are often needed which in some cases are beyond the limits of stability of metal nitride bond. Substantial progress on nitrides has been done because of the development of new synthetic approaches that use alternative nitrogen sources to N_2 gas, such as NH_3, amide, diimides, azide, urea or routes that go through an intermediate hydride.[26-31]

1.2 Properties of nitrides and oxynitrides

1.2.1 Nitrides

The first pioneering studies on nitrides were performed during the '20s and '30s. Then they were extensively studied by Juza and co-workers in the immediate post-war decades.[26, 32] Generally, nitrides can be grouped into tree types: metallic, ionic and covalent. However it is not always trivial to establish which is the dominating character of a bond, especially in multinary compounds were more than one type of bond can exist. An alternative or complementary classification can be done referring exclusively to the number of elements found in its composition, being binary, ternary, etc… and/or by the stoichiometry of the compound. A full description of nitride compounds is out of the scope of this work and for it the lecturer is referred to the works: *Nitrides of metals of the first transition series* (1966) by R.Juza,[26] *Crystal chemistry of inorganic Nitrides* (1992) by Brese and O'Keeffe[28] and *Structural families in nitride chemistry* (1998) by D. H. Gregory.[33] Here, I will rather offer a selection of relevant compounds that may play an important industrial role, show a promising potential, or fascinating structure or property exemplifying the wide extend of properties and richness of their physicochemistry.

The transition metal binary nitrides (TiN, ZrN, HfN, VN, NbN, TaN, WN) are commonly referred to as refractory hard metals. They possess an unusual combination of properties. They show high melting points (up to 3000^0C), extremely high hardness (almost equal to that of diamond), good electrical and thermal conductivity, superconductivity at low temperature and good corrosion resistance. This unique combination of properties leads to applications in hard wear resistant coatings on cutting tools,[34] jet

propulsion, rocket technology, refractory vessels for metallurgy,[35] electrode materials in fused salt electrolysis,[26] diffusion barriers in microelectronics[36] and superconducting detectors used in high speed astronomy for detection of extra solar planets.[37] Hf_3N_4 and Zr_3N_4 have been reported as hard and semiconducting materials.[38] While moving toward less electropositive transition metals the applications of nitrides decrease fairly steadily. For instance, chromium nitrides surfaces are still fairly hard but for manganese nitrides hardness varies greatly with the type of phase and for iron nitrides no sintered specimens can be prepared.[26] Resistance to corrosion is also lower for these later transition metals. Nevertheless, they show interesting electronic properties since we move from paramagnetism in TiN to antiferromagnetism in CrN and ferrimagnetism in Mn_4N to ferromagnetism for Fe_4N and Fe_2N.

For ionic nitrides totally different characteristics are found, being their main feature their sensitivity to hydrolysis, as they quickly lose nitrogen in the form of ammonia when exposed to atmospheric moisture. This makes difficult their preparation, characterization and imposes very strict conditions for their practical use. The ionic character is found in Li_3N, which is the only stable alkali metal nitride, alkaline earth elements and in the lanthanides (LnN).

Covalent nitrides, specially the group III nitrides, (BN, AlN, GaN, InN) are of a great technological relevance. BN is isoelectronic with carbon and shows a layered structure similar to graphite. Also a high pressure zinc blend polymorph type equivalent to diamond structure of carbon is found for BN. Furthermore, white graphene, atomically thin hexagonal boron nitride (hBN)[39] and BN nanotubes[40] can also be prepared, giving a great potential to BN in nanotechnological applications. AlN is an electrical insulator with a high thermal conductivity and a similar thermal expansion coefficient

which is close to that of silicon. These physical characteristics make it a suitable material for microelectronics and optoelectronics. Epitaxially grown thin film crystalline aluminium nitride is used for surface acoustic wave sensors for microelectromechanical systems (MEMS).[41] Epitaxial GaN, InN semiconductors and AlGaN/GaInN multiple heterostructures are the active material used in high efficiency blue light emitting diodes (LED) that have revolutionized the lightening industry in the last decade.[42] Motivated by the remarkable successes of GaInN LED devices, efforts are being made to develop high quantum efficiency InGaN/GaN multiple quantum well solar cells for application in concentrator photovoltaics.[43]

Other relevant covalent nitrides are those from groups IV and V such as Si_3N_4 and P_3N_5. Sintered silicon nitride has hardness, thermal stability, and resistance to wear similar to the above mentioned transition metal nitrides.[44] It finds applications as abrasive material, cutting tools, in engine parts such as ceramic bearings for space shuttles and it was identified as one of the few materials capable of surviving the thermal gradients generated in hydrogen/oxygen rocket engines.[45] Whereas phosphorous nitride is not well known from a structural point of view, it is used to prepare phosphorous oxynitride (PON) which is isoelectronic with SiO_2 and leads to a large and intriguing family of compounds.[46, 47]

Ternary nitrides exist with stoichiometries AMN, AMN_2, A_2MN_3 and A_3MN_3 were A is an alkaline earth metal or a lanthanide and in some cases also transition metals, and M can be a transition metal or group III and IV metal. These compounds show mixed ionocovalent bonding and often present 2-D layered type structure for which some of them, such as LiNiN,[48] have received attention as battery material due to its intercalation properties. Other layered mixed anion nitrides such as β-MNX (M= Zr, Hf; X= Cl, Br) present superconductivity with critical temperatures up to 25 K.[49, 50]

1.2.2 Oxynitrides

The exploration of oxynitride materials was belated compared to that of nitrides. Some rare pioneering works done on materials used in incandescent bulbs filaments date from 1908[51], the first niobium oxynitrides were described by G. Brauer in 1960,[52] and systematic research of oxynitride chemistry was done by Roger Marchand in the decades of '80s and '90s.[27, 53] But it has been only in the recent years that oxynitride materials have been identified as a fascinating class of new materials and are receiving significant attention. Oxynitrides can be understood as a metal oxide in which oxygen has been partially substituted by nitrogen. As a result oxynitrides may present combined advantages of metal oxides and nitrides. They are usually prepared by heating metal oxides under nitrogen or ammonia gas or by solid state reaction between oxides and nitrides. A detailed explanation of the oxynitride synthesis is addressed in the methods chapter. A more detailed description of oxynitride compounds is shown in the reviews *Nitrides and Oxynitrides: Preparation, Crystal Chemistry and Properties* (1991)[27] as well as *Ternary and higher order rare-earth nitride materials: synthesis and characterization of ionic-covalent oxynitride powders* (2002)[54] both from R. Marchand's group. A systematic and detailed description of techniques and methods can be found in the review entitled *Perovskite-related oxynitrydes- Recent developments in synthesis characterization and investigations of physical properties* (2009)[23] by Anke Weidenkaff et al. A clear and objective overview of the state of the art in functional oxynitrides can be found in the reviews *Synthesis and properties of functional oxynitrides- from photocatalysis to CMR materials* (2010)[9], as well as in *Chemistry and applications of oxynitride perovskites* (2011)[21] and *Metal oxynitrides as emerging materials with photocatalytic*

and electronic properties (2015)[22] all from Amparo Fuertes. Oxynitride compounds can be found in a great variety of compositions and structures. Quaternary compounds show a wide number of structural types including scheelites,[55] baddeleyites,[56] fluorites,[57] apatites,[58] perovskites,[59] pyroclores[60] and spinels[56].

The field of application in which oxynitride materials are receiving the greatest attention is in heterogeneous photocatalytic water splitting as they happen to be active in the visible range of light. Being active in the visible region extends the theoretical maximum solar conversion from 2% for UV light active materials to 16% or 32% for semiconductors with absorption edges at 600 nm or 800 nm, respectively.[61] The actual record in quantum efficiency for a visible active heterogeneous photocatalyst in pure water is for Cr/Rh-modified GaN:ZnO solid solution with of QE=5.9%.[62] Other widely studied visible active oxynitride photocatalysts are TaON, $LaTiO_2N$, $CaNbO_2N$, $CaTaO_2N$, $SrTaO_2N$, $BaTaO_2N$ and $LaTaON_2$. Some of them do not have the appropriate band potentials to oxidize and reduce water but can be used in two-step water splitting (z-scheme) system.[61] Niobium and tantalum perovskite oxynitrides present a wide spectrum of bright colours ranking from yellow to dark red and the possibility to tune the band gap through the $CaTaO_2N$-$LaTaON_2$ solid solution gives place to a variety of nontoxic pigments that could replace cadmium-containing materials.[63] $SrTaO_2N$ and $BaTaO_2N$ present dielectric constants of 4900 and 2900, respectively, with a relaxor-type ferroelectric behaviour.[64] As both compounds crystallize in centrosymmetric space groups, local *cis* ordering of nitrides in the TaO_4N_2 octahedra together with polar cooperative disorder of N-M-N chains have been suggested to be at the origin of the dielectric properties.[65, 66] Also, ferroelectricity has been induced in compressively strained $SrTaO_2N$ epitaxial thin films,[67] and $(Ba,Sr)TiO_{3-x}N_y$

thin films have been explored as possible high temperature dielectrics for telecommunication devices.[68] Other oxynitrides such as $SrMoO_2N$ show notable electronic transport with a high Seebeck coefficient[69] and $EuNbO_2N$[70] and $EuWON_2$,[71] which show colossal magnetoresistance (CMR) at low temperatures, are of fundamental interest and potential practical importance for new memory and sensor technologies. A special attention should be given to the so called oxynitridoaluminosilicates or SiAlONs discovered in the early 1970 by Oyama and Jack.[72, 73] This family of ceramic materials is obtained by the partial substitution of Si^{4+} by Al^{3+} and N^{3-} by O^{2-} in Si_3N_4. This discovery has given place to a manifold world in which the oxysilicates, the nitridosilicates, oxonitridosilicates and the nitridoaluminosilicates are therefore subgroups of SiAlONs. Introducing nitrogen into oxysilicates leads to significant extent of structural possibilities as it extends the range of the degree of condensation κ, (κ = Si:(O,N)) from κ=1/2 for SiO_2 up to κ=3/4 for Si_3N_4, giving place to mono-, bi- or tri-dimensional silicate tetrahedral networks. A number of SiAlONs exhibit promising material properties, high chemical and thermal stability, transparency in the visible region, large band gap, and much higher hardness than fused silica glass. For instance, aluminium oxynitride (AlON) has almost the hardness of sapphire, making this material a leading candidate for lightweight high-performance transparent armour applications such as bulletproof and blast-resistant windows.[74] Transparent and colourless materials with non-centrosymmetric crystal structure, such as $M_2Si_5N_8$ with M = Ca, Sr, are receiving a growing interest as nonlinear optical materials (NLO) utilized as optical switches, optical data processing in computer and optical signal processing devices.[75] Among other applications a number of Eu^{2+} or Ce^{3+} doped nitridosilicates and oxonitridosilicates such as, $Y_4Si_2O_7N_2:Ce^{3+}$,[76] $Y_2Si_3O_3N_4:Ce^{3+}$,[76]

$M_2Si_5N_8:Eu^{2+}$,[77] and $MSi_2O_2N_2:Eu^{2+}$ (M=Ca, Sr, Ba),[78] have emerged as highly effective optical materials affording phosphor-converted light-emitting diodes (pc-LEDs).

As the research progresses in this field, the nature of nitrogen bonding to metals will continue to deliver surprising new compounds with promising new properties.

1.3 Objectives

Among all the variety of properties of oxynitride materials, the aim of this thesis has been directed towards two specific goals: first, the research of new oxynitride phosphors for white LED technology, based on orthosilicate β-K_2SO_4 structure. Second, the research of new oxynitrides with perovskite structure and the study of their electronic and photocatalytic properties. Accordingly, this thesis is structured in two sections. Section one collects the results obtained on the new family of oxynitridosilicates $LaSrSiO_3N$ and $LaBaSiO_3N$ activated with europium or cerium,[79] as well as the study on tuning the luminescent properties of the orthosilicate $Sr_2SiO_4:Eu^{2+}$ trough the coupled introduction of N^{3-}/La^{3+}.[80] Section two includes the work performed on new oxynitrides with perovskite structure. In turn, this section is divided in two chapters. First, it presents the work performed on the new oxynitride lanthanum chromites $LnCrO_{3-x}N_x$ with Ln= La, Pr, Nd and Sm and a study of the effect of nitrogen on their antiferromagnetic properties.[81] Second, it shows the new hafnium oxynitrides with perovskite structure $LnHfO_2N$ (Ln=La, Nd, Sm), their synthesis and electric and photocatalytic properties in water splitting. The thesis covers several

oxynitride synthesis methods, detailed structural characterization by electron, neutron and X-ray diffraction as well as optical, electrical, magnetic and photocatalytic properties characterization. The following section will introduce the fundaments and state of the art of oxynitridosilicate phosphors for solid state lighting and perovskite oxynitrides.

1.4 Oxynitridosilicate phosphors for white LED

1.4.1 White LED technology, energy saving impact and strategies

Lightening plays a major role in our quality of life. The development of light emitting diodes (LEDs) has made high efficient direct conversion of electricity to light possible. This has been possible thanks to the development by Nakamura, Amano and Akasaki of the candela-class, high-brightness, blue (In,Ga)N double-heterostructure device for which they received the Noble Prize in Physics 2014.[42, 82] The challenging development of a high energy blue LED enabled to generate white light by its combination with a wide band emitting phosphor that partially downconverts the blue emission to longer wavelengths covering the full range of visible light. This results in a simple LED device that produces white light efficiently. As a consequence the lightening industry has experienced a great revolution in the recent years and many governments worldwide have phased out the traditional incandescent bulb (which converts only between 1% and 5% of the electricity that they consume into usable light) in favour of the most efficient devices such as compact fluorescent lamps (CFL) and white LEDs. Solid state lighting devices offer

advantages over alternative devices such as CFLs including long lifetime, much higher efficiencies, instant start, spectral flexibility and absence of toxic elements such as mercury.

Regarding the energy saving impact of SSL the department of energy of US (DOE) has determined that by 2030, LED technology can potentially save 261 terawatt-hours (TWh) annually, a 40% reduction of the site electricity consumption forecasted for a "no-LED" scenario. This electricity savings correspond to about 4.5 quads of primary source energy (1 quad= five times the energy of the Tsar Bomba nuclear test). This would eliminate the need of 30 1000 MW power plants that would avoid the generation of 185 million tons of CO_2.[83] A similar fraction of total electrical production (about 20 %) is dedicated to lightening in Europe so a proportional equivalence energy saving would be expected for Europe. The International Energy Agency (IEA) has estimated that worldwide lighting is responsible for emissions of approximately 1900 Mt CO_2 per year, equivalent to 70 % of the emissions from the world's light passenger vehicles,[84] this is why it has been pointed out that switching towards SSL is the most cost effective way to reduce our energy consumption and could make a big contribution to controlling global CO_2 emissions and reduction of our carbon footprint.

Efficiency, lifetime, and cost are not the only factors that determine adoption of lighting sources. The perceived colour of light and the way in which illuminated coloured surfaces appear are also important. Indeed, for years, this was the main obstacle to the widespread adoption of compact fluorescents.[85] The curve in **Figure 1.2** displays the sensitivity of the human eye to light, which corresponds to the response of the cone cells (termed S, M, and L for short, medium, and long wavelength receptors, respectively).

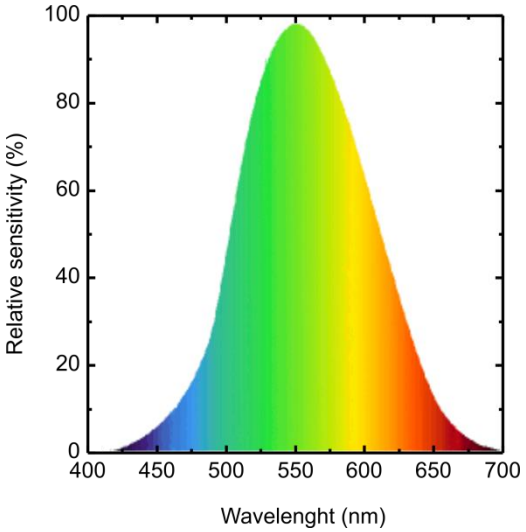

Figure 1.2. Curve of human eyes sensitivity to light according to its colour.

Maximum sensitivity occurs at 550 nm in the yellow-green. Note that the sensitivity drops drastically bellow 450 nm and extends above 650 nm. When designing a light source, an optimum colour rending will be obtained when the emission of the lightening source matches the human eye sensitivity curve and all illumination beyond the limits of perception will only contribute to energy losses.

There are three principal strategies for creating white light with a solid-state device (**Figure 1. 3**). The first strategy consists of a multiple LED chip emitting at different wavelengths in a single device. This device has the advantageof none energy loss due to the use of a downconverting phosphor but it has very poor colour rendering index due to the sharpness of LED emission spectra. Additionally, it requires a complex circuitry that increases the cost.

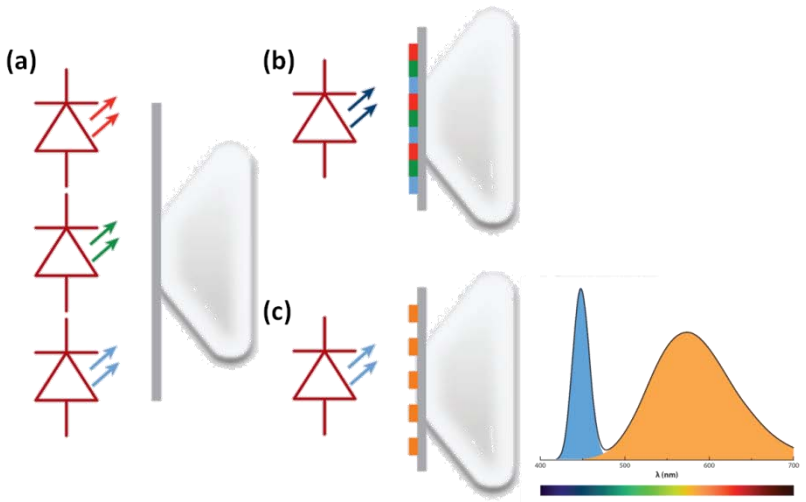

Figure 1. 3. Schematic of the three principal white lightening strategies. (a) A tree-LED strategy with (RGB) LED chips. (b) A three-phosphor strategy with UV LED and RGB phosphors. (c) A blue LED with a yellow downconverting phosphor and representative spectrum from such device. Reproduced from Ref.[86] with permission from Annual Reviews of Material Research.

The second strategy consists of the use of a UV LED chip and a combination of red, green and blue (RGB) downconverting phosphors. This device can cover a broad range of emission wavelengths, giving a good colour rendering index and it is the preferential choice if a warm light is desired. Nevertheless, the large Stoke shift inherent to the use of a UV LED and the possible reabsorption of the emissions of other phosphors in a multiple phosphor configuration add loss mechanisms and decrease their efficiency. The third SSL strategy is the use of a blue LED chip with one single broad band yellow phosphor that partially downconverts some of the blue radiation. This is the most common device produced today, due to the high efficiency of the blue (InGaN) LED and the yellow-emitting cerium doped yttrium aluminium garnet (YAG:Ce) and despite the relatively poor colour rending (CRI<80) that produces a cold white light due to his lack of emission in the red region of visible spectrum.[87]

1.4.2 Phosphors for solid state lighting

Phosphors consist of a host lattice doped with a small amount of an active ion, typically a few mole percent or less. The active ions have energy levels that can be populated by direct excitation or indirectly by energy transfer absorbing the high energy light and downconverting it to lower energies. Generally, two types of active ions can be distinguished. In the first type, the optical transitions take place between two $4f^n$ levels, this occurs typically for lanthanide ions Ln^{3+}, which are characterized for showing sharp line emission bands due to the weak interaction between the well shielded $4f^n$ orbital of the activator and the host lattice. The 4f energies of rare earth ions vary systematically with the number of electrons in the atom following the spin-pairing theory of Jorgensen[88], and the transition energy can be predicted using the Dieke diagram[89]. The second type of the optical transitions involves transitions between $4f^{n-1}5d^1$ and $4f^n5d^0$ levels. This occurs typically for Mn^{2+}, Eu^{2+} and Ce^{3+}, as well as for s^2 ions like Pb^{2+}. These activator ions strongly interact with the host lattice. They are characterized by showing broad excitation and emission bands due to the strong coupling of the electronic states with the vibration modes of the host lattice. Their half width FWHM is related to the Stokes shift (S) [equations (1a) and (1b)], that is the energy difference between the absorption and emission maxima. S_e, S_g are Huang-Rhys parameters for the excited and ground state, respectively[90] (See figure 2).

$$FWHM = \sqrt{8ln2}\sqrt{2kT}\sqrt{S}\ [eV] \quad (1a)$$

$$S = S_e\,\hbar\omega_e + S_g\hbar\omega_g \quad (1b)$$

For Eu^{2+} and Ce^{3+} the optical transition takes place between $4f^{n-1}5d^1$ and $4f^n$ levels (**Figure 1. 4a**) giving rise to a broad range of emission and excitation energies. The broadening can be explained by two phenomena: the Franck-Condon principle[91] and the breaking of the degeneracy of the 4f ground state. The first effect results in transitions with many different energies due to different vibrational states of the 4f and 5d levels. The second effect results from the spin-orbit coupling of the 4f ground state into multiple levels. For Ce^{3+} this results in the splitting in two ^2F states, $^2F_{5/2}$ and $^2F_{7/2}$, separated by 2000 cm^{-1}. The most illustrative way to understand the luminescent process is through the configurational-coordinate diagram (**Figure 1. 4b**), where the potential energy of the luminescent centre in the crystal lattice is plotted as a function of the configurational coordinate *r* for the ground state *g* and the first excited state. Here *r* represents the distance between the central cation and the surrounding anions. The vibrational states are represented schematically by horizontal lines in the parabola. The fact that the optical excitation and emission correspond to vertical lines is attributable to the rapid nature of electronic transitions as compared to vibrational movements, which involve the heavy nuclei. Once in an excited state, the system will relax towards the equilibrium state of the excited level due to the coupling of electrons with the phonons and will dissipate heat during the process. From this state or nearby levels the system returns to the ground state by emitting radiation. Since the luminescent centre can be in various vibrational states both at the ground level and at the excited level and since the emission shows a Stokes shift ($\Delta r \neq 0$), the transitions occur in a broad band of energies. Non-radiative return from the excited state to the ground state is possible via the intersection point *S* of the two curves.

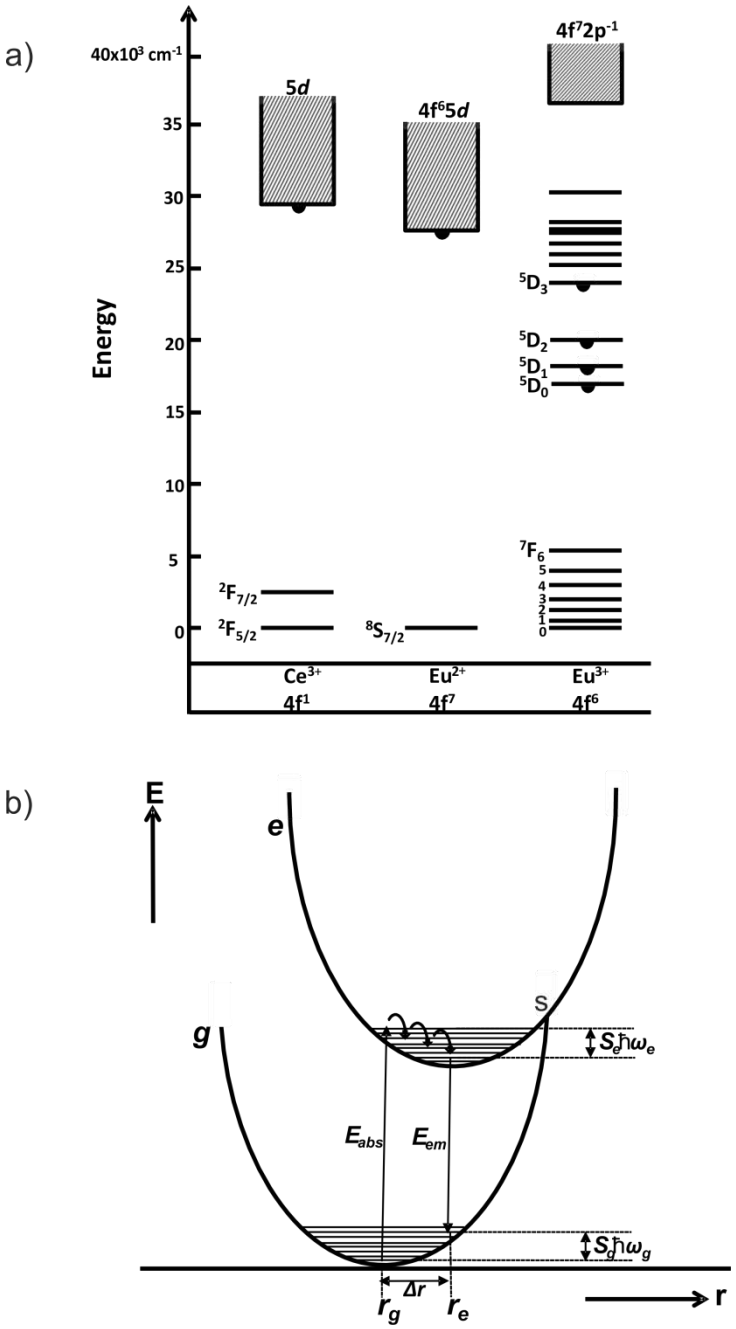

Figure 1. 4. a) Energy level diagram of Ce^{3+}, Eu^{2+} and Eu^{3+} in oxide host lattices, b) Configurational-coordinate diagram of a luminescent centre. Reproduced from ref's[90, 92] with permission from John Wiley and Sons.

From this intersection position it can be understood why the emission can be quenched at higher temperatures. This requires an activation energy, which can be supplied at higher temperatures (thermal quenching) or it may also, during the thermal relaxation from the highest vibrational state of the excited state, occupy a vibrational level situated at the point of intersection *S*. From this point the centre will return non-radiatively to the equilibrium configuration of the ground state, dissipating heat in the process. This also explains why phosphors having an emission with a large Stokes shift (↑Δr) usually exhibit a low quenching temperature.[92]

The optical properties of a phosphor with the activators Ce^{3+} and Eu^{2+} depend both on the activator ion and on the host crystal structure. The electronic energy levels of an activator ion in a crystal differ greatly from those of a free ion (**Figure 1. 5**).

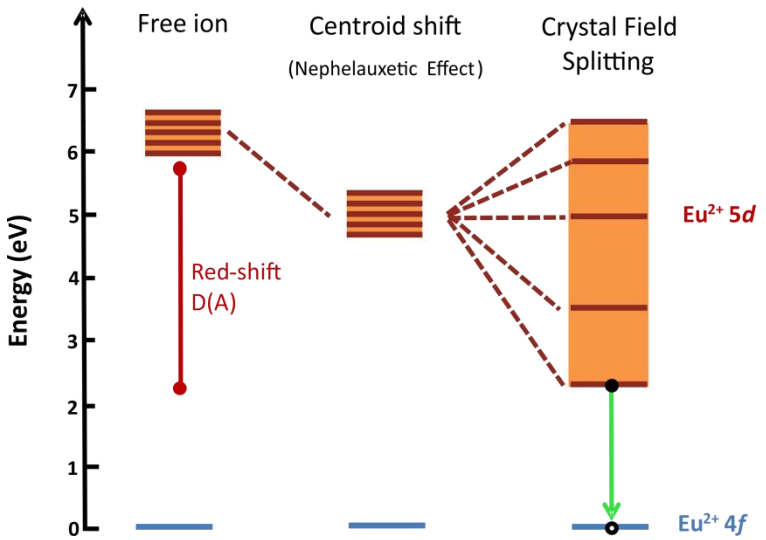

Figure 1. 5. Schematic energy level diagram for Eu^{2+} showing the effect of the host.

As a free ion, Ce^{3+} or Eu^{2+} has an energy gap between the 4f ground state and the 5d excited state of roughly 6 eV. When an activator ion is

imbedded in a host crystal, two major effects determine the photoluminescent properties: the centroid shift and the crystal field splitting. The first effect, the centroid shift, is the lowering in energy of the 5d levels of the activator ion due to a decrease in the interelectronic repulsion. This stabilization is related to the polarizability of the surrounding anion ligands and to the covalency of the crystal. As the degree of covalency increases, the interelectronic repulsion decreases, and the d orbitals get stabilized. This process is known as the nephelauxetic effect. The centroid shift increases with increasing anion polarizability and decreasing cation electronegativity. The second effect, the crystal field splitting, refers to the difference in energy between the highest and lowest 5d levels and it is an effect of the host crystal. The magnitude of the crystal field splitting depends on the bond lengths from the activator ion to the coordinating anions, the degree of covalency of the metal ligand bonding, the coordination environment and the symmetry of the activator site. By the point charge model an approximation to the crystal field splitting magnitude with bond length is given by the equation:[93]

$$D_q = \frac{Ze^2r^4}{6R^5} \quad (2)$$

Where Z is the charge or valence of the anion, e is the charge of an electron, r is the radius of the d wave function, and R is the bond length. As the bond length of the active ion decreases the crystal field increases. The coordination geometry also has a strong effect on the crystal field splitting of the 5d levels. Dorenbos determined that it tends to be larger for octahedral coordination, followed by cubic and dodecahedral coordination.[94] Furthermore, the distortion of an active site may have an important effect on the crystal field splitting; increasing distortion will

result in a larger crystal field splitting and a consequent increase in the maximum emission wavelength.

To summarize, the spectral position of the emission band depends on three factors:

- Covalency (the nephelauxetic effect) which reduces the energy difference between the $4f$ and $5d$ levels.
- Crystal field splitting of $5d$ levels: a large low-symmetry crystal field will decrease the lowest crystal-field component from which the emission originates.
- The Stokes shift.

Because one of the most important requirements for a luminescent material is a high light output, it is imperative that in such a material the radiative return from the excited state has a much higher probability than the non-radiative ones. To quantify the efficiency of the luminescence process in a phosphor the quantum efficiency (QE) is defined as the ratio of the number of emitted photons to the number of absorbed photons.

$$QE = \frac{n(emitted\ photons)}{n(absorbed\ photons)}\ [\%] \tag{3}$$

Some important photoluminescent materials show QE values close to 100 %, and values above 70 % are required for technical applications. There are several processes and conditions that favour a non-radiative relaxation to occur. As we already introduced all phosphors show a dependence of the QE with temperature. As the temperature increases the number and energy of vibrational modes increases as it does the probability to occupy a vibrational level situated at the point of intersection S of the coordinate diagram where the system can tunnel to a high vibrational level of the ground state g. This non-radiative process is known as thermal quenching.

Host materials with a rigid network structure will provide potentially less localized vibrational pathways for thermal quenching.[95] A second quenching mechanism common to all phosphors is the concentration quenching. The concentration quenching in rare earth active ions is usually caused by the energy transfer among active ions. The probability of the energy transfer between two active ions is inversely proportional to the n^{th} power of the distance between the active ions. With an increase of active ion concentration, the distance between ions decreases, and the probability of energy transfer increases. After excitation, during the thermal relaxation to the lower energy state of the excited 5d state, the probability of energy transfer to lower 5d levels in the same or different sites increases with the concentration of the active ion. This results in the decrease or absence of the emission due to the transition from the $4f^{n-1}5d^1$ to the $4f^n$ levels.[92, 96] Finally, another frequent type of radiation-less transition is the photoionization and electron transfer quenching. This process can take place when the relative position of the energies of the excited state of the active ion is close to the conduction band of the host material. This implies that in the excited state an electron can easily be ionized from the centre to the conduction band. It may recombine non-radiatively with a hole somewhere else, greatly diminishing the quantum efficiency, or it may attract to the hole in the ionized centre, forming an exciton, and recombine radiatively or non-radiatively from this impurity-bond exciton state.[97]

Besides the quantum yield, the quality of a phosphor material is further characterized by its colour point, the lumen equivalent, the reflection spectrum, and the emission lifetime under the given excitation conditions.

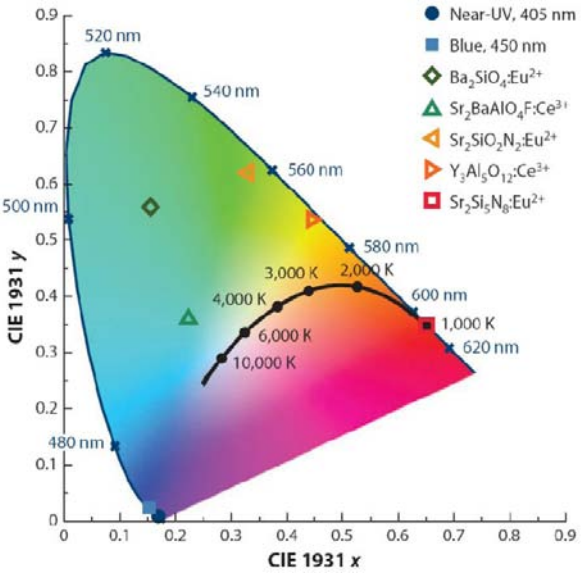

Figure 1. 6. The 1931 CIE diagram. The Plankian locus is showed in black, and the colour coordinates of some common phosphors are plotted. Reproduced from Ref.[86] with permission from Annual Reviews of Materials Research.

The colour point is derived from the spectral energy distribution of the emission and is defined according to the convention of the Commission International de l'Eclerage (CIE) by the 1931 CIE diagram shown in **Figure 1. 6.** Monochromatic wavelengths outline the coloured area in the figure, delimiting the limit of human eye sensibility, and any colour in the visible spectrum can be represented by x and y coordinates. Some common phosphors are indicated as examples. White light is in the center of the diagram, with coordinates (1/3, 1/3). The colour of a combination of two colour coordinates can be find by drawing a straight line between the two points, and the final colour point will depend on the relative intensity of the two sources. The emission colour of a blackbody radiator at different temperatures is shown in the middle of Figure 1.6. The quality of light is also determined by the colour rending index (CRI), which measures the ability of a light source to render the true colour of an object. This value is

calculated by comparing the reflection spectra of selected test colours obtained by irradiation under the investigated light source and with a blackbody with the same correlated colour temperature. By definition CRI can adopt values between 0 and 100.

1.4.3 Silicon-based oxynitride phosphors

A new family of inorganic compounds based on the SiX_4 (X = O, N) tetrahedra are increasingly gaining relevance as luminescent materials for solid state lighting devices. Due to the enormous structural variability that the SiX_4 tetrahedron gives as building block, a manifold variety of compounds with higher or lower crosslinked tetrahedra network can be built. The structural versatility of the so-called SiAlONs enables the preparation of phosphors with emission colours ranking from blue, green, yellow and up to red. Moreover they present excellent chromatic stability, high luminous efficacy and high colour rendering. **Table 1. 2** summarizes some of the most relevant SiAlONs phosphors.

α-Sialon type compounds are directly related to α-Si_3N_4. They are expressed trough the general formula $M_xSi_{12-m-n}Al_{m+n}O_nN_{16-n}$ where x is the solubility of the stabilizing cation M, m and n are the numbers of Al—N and Al—O bonds substituting for Si—N bonds in α-Si_3N_4. The crystal structure is a tridimensional network where all SiX_4 are interconnected by vertexes and the metal M partially occupies two interstitial sites compensating the charge difference caused by substitution. Activated calcium α-sialon ($CaSi_9Al_3ON_{15}$) shows blue, green or yellow emission when doped with Ce^{3+}, Yb^{2+} and Eu^{2+}, respectively.[98-100]

The La—Si—O—N system is a representative example of the relationship between the amount of N^{3-} incorporated into the SiX_4 groups and the degree of interconnection between these tetrahedra. When increasing the N:O ratio, the silicon tetrahedral network changes from isolated SiO_3N or SiO_4 tetrahedra in $La_5Si_3O_{12}N$, trimeric $Si_3O_6N_3$ rings in $LaSiO_2N$ and a three-dimensional $(Si_8O_4N_{11})n$ network for $La_3Si_8O_4N_{11}$. These three compounds emit blue colour with maximum emissions between 416 and 478 nm when doped with Ce^{3+}.[101]

$MSi_2O_2N_2$ with M = Ca, Sr and Ba represent a class of compounds containing layers of $(Si_2O_2N_2)^{2-}$. These consist of $SiON^{3-}$ tetrahedrons where the N atom bridges three Si atoms and the O atom bonds terminally to silicon. The three structures $CaSi_2O_2N_2$, $SrSi_2O_2N_2$ and $BaSi_2O_2N_2$ are closely related with different orientation and topology of the silicate layers and the metal coordination sites. When they are activated with Eu^{2+}, the changes in coordination environments are accompanied by changes in the emission colour, going from yellow to blue while increasing the size of the alkaline earth metal.[102]

Europium doped $M_2Si_5N_8$ with M = Ca, Sr and Ba are presently some of the commercially used red phosphors. The host compounds show a three-dimensional SiX_4 network composed by vertex-sharing SiN_4 tetrahedra in which half of the N atoms are bonded to two Si atoms and the other half N atoms bond to three Si atoms. The structural rigidity induced by the three-dimensional network contributes to the exceptional high quantum efficiency and high thermal stability of these materials despite of their large stock-shift of about 40.000 cm^{-1}.[77, 103]

Europium doped $CaAlSiN_3$ is also a commercial red phosphor with a three-dimensional network. The structure is built up by $(Si/Al)N_4$ tetrahedra

where 1/3 of the N atoms are linked to two Si/Al atoms and 2/3 of the remaining N atoms are bonded to three Si/Al neighbours forming $(Si/Al)_6N_{18}$ vertex-linked rings.[104]

Recently, several potential narrow-band red-emitting phosphors were developed by W. Schnick's group. $M[LiAl_3N_4]$,[105] $M[Mg_3SiN_4]$[106] and $M[Mg_2Al_2N_4]$[107] with (M = Ca, Sr) are isostructural to UCr_4C_4. $M[LiAl_3N_4]$ shows a highly condensed network of vertex and corner-sharing AlN_4 and LiN_4 tetrahedra, and the structure of $M[Mg_3SiN_4]$ is built up by SiN_4 tetrahedra connected by two edges and one corner to MgN_4 tetrahedra. The high degree of condensation and rigidity of these structures contributes to narrow the red emission band width.

By using the single particle diagnostic approach,[108] several new host materials have been discovered in the series of compounds in the Ba_3N_2—AlN—Si_3N_4 system. Some of the most relevant discoveries are blue-emitting $BaSi_4Al_3N_9:Eu^{2+}$,[101] and yellow-emitting $Ba_5Si_{11}Al_{17}N_{25}:Eu^{2+}$[109] and $La_3BaSi_5N_9O_2:Ce^{3+}$.[110]

In this thesis we report the synthesis and luminescent properties of novel host materials $LaMSiO_3N$ (M = Sr, Ba) and $Sr_{2-x}La_xSiO_{4-x}N_x$ when doped either by Eu^{2+} or Ce^{3+} as red-orange phosphors for white LED technology.

Table 1. 2. Selected SiAlON phosphors.

Host	Activator	λ_{ex} (nm)	λ_{em} (nm)	Emission colour	Ref.
$LaAl(Si_{6-z}Al_z)N_{10-z}O_z$	Ce^{3+}	360	475	Blue	111
$CaSi_9Al_3ON_{15}$	Ce^{3+}	380	495	Blue	99
$CaSi_9Al_3ON_{15}$	Yb^{2+}	445	550	Green	98
$CaSi_9Al_3ON_{15}$	Eu^{2+}	300-420	581	Yellow	100
$Y_{10}(Si_6O_{22}N_2)O_2$	Ce^{3+}	358	437-465	Blue	112
$Y_{10}(Si_6O_{22}N_2)O_2$	Mn^{2+}	266-419	614	Red	112
$Y_2Si_3O_4N_3$	Ce^{3+}	310-390	475	Blue	113
$LaSiO_2N$	Ce^{3+}	356	416	Blue	101
$La_3Si_8O_4N_{11}$	Ce^{3+}	365	424	Blue	101
$La_5Si_3O_{12}N$	Ce^{3+}	361	478	Blue	101
$Si_{6-z}Al_zO_zN_{8-z}$	Eu^{2+}	303-400	538	Green	114
$CaSi_2O_2N_2$	Eu^{2+}	355	560	Yellow	102
$SrSi_2O_2N_2$	Eu^{2+}	360	537	Green	102
$BaSi_2O_2N_2$	Eu^{2+}	380	494	Blue	102
$SrYSi_4N_7$	Eu^{2+}	340	548-570	Green	115
$BaYSi_4N_7$	Eu^{2+}	348	503-527	Green	115
$Ca_2Si_5N_8$	Eu^{2+}	390	623	Red	103
$Sr_2Si_5N_8$	Eu^{2+}	400	640	Red	103
$Ba_2Si_5N_8$	Eu^{2+}	400	650	Red	77
$CaAlSiN_3$	Eu^{2+}	450	650	Red	104
$CaSiN_2$	Eu^{2+}	400	605	Red	116
$CaSiN_2$	Ce^{3+}	535	625	Red	116
$M[LiAl_3N_4]$ (M=Ca,Sr)	Eu^{2+}	470,440	668,654	Red	105
$M[Mg_3SiN_4]$ (M=Ca,Sr)	Ce^{3+}/ Eu^{2+}	480,440	585,615	Red	106
$M[Mg_2Al_2N_4]$ (M=Ca,Sr)	Eu^{2+}	440,440	607,612	Red	107
$Ba_5Si_{11}Al_{17}N_{25}$	Eu^{2+}	405	568	Yellow	109
$BaSi_4Al_3N_9$	Eu^{2+}	365	500	Blue	101
$Ba_2LiSi_7AlN_{12}$	Eu^{2+}	400	515	Blue	117
$Sr_3Si_{5.5}Al_{2.5}O_{9.5}N_{5.5}$	Eu^{2+}	355	469	Blue	108
$La_3BaSi_5N_9O_2$	Ce^{3+}	440	578	Yellow	110

1.5 Perovskites: From Oxides to Oxynitrides

Discovered in 1838 by Gustave Rose and named in honour of the Russian mineralogist Lev Perovski, Perovskite is the mineral name of calcium titanate.[118] Nowadays, perovskite materials constitute a manifold family of compounds with an exceptional spectrum of applications. From multiferroic rare-earth manganites and ferrites $BiMnO_3$[119] and $BiFeO_3$,[120] colossal magnetoresistant $La_{1-x}Sr_xMnO_3$[121] and ordered double perovskite Sr_2FeMoO_6,[122] piezoelectrics $PbZr_xTi_{1-x}O_3$,[1] and layered superconducting cuprates $YBa_2Cu_3O_7$[6] to the organo halide perovskite solar cell material $CH_3NH_3PbBr_3$[123], the number of functional compounds with a perovskite related structure continues to increase.

The ideal perovskite has the general formula ABX_3, where A and B are metal cations of different sizes and X is an anion like = O^{2-}, N^{3-}, S^{2-} or the halides. The A-site cation is typically larger than B-site cation and similar in size to the X-site anions. **Figure 1. 7** shows the structure of an ideal cubic perovskite with space group *Pm-3m*. In such structure, the A cations are surrounded by 12 anions in cubo-octahedral coordination and the B cations are surrounded by six anions in octahedral coordination. The X anions are coordinated by 2 B-site cations and 4 A-site cations.

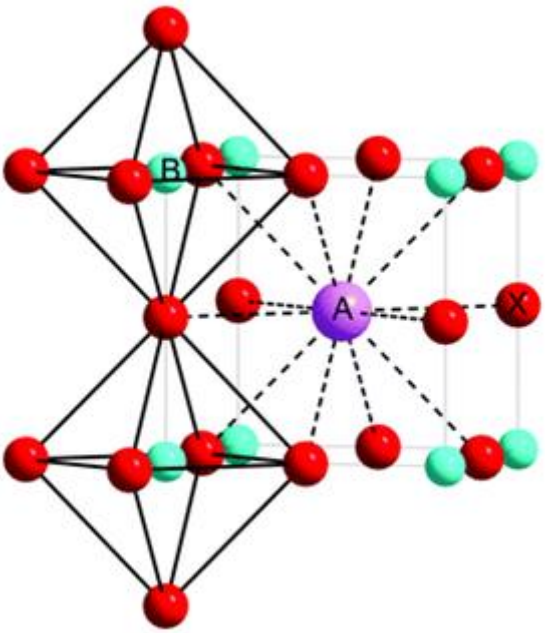

Figure 1. 7. The ideal ABX_3 perovskite structure showing the coordination of the B- and A-site cations.

Goldschmidt[124] established the relation between the size of different cations and anions that are able to accommodate in a more or less distorted perovskite structure. The parameter known as the tolerance factor *(t)* is defined as:

$$t = \frac{(R_A + R_x)}{[\sqrt{2}(R_B + R_x)]} \tag{4}$$

Were R_A, R_B and R_x are the ionic radii of A, B and X ions, respectively. The perovskite phase may form if t is close to 1. As t decreases, the A-site ion becomes too small for the cuboctahedral site. In these cases, the structure distorts through rotating of the octahedra known as "tilting" reducing the volume of the interstice and improving the structure stability. Tilting of the octahedral necessarily reduces the symmetry of the aristotype space group *Pm-3m* and generates derivative sub-groups of lower symmetry. Glazer

associated particular tilt systems with space groups.[125] From the 23 Glazer tilt systems describing octahedral tilting in perovskites, there are two crystal symmetries that are more commonly observed when there is a single ion in the A site. These are the orthorhombic $GdFeO_3$ structures with tilt system ($a^+ b^- b^-$) and space group *Pnma* and the rombohedral ($a^- a^- a^-$) tilt system with space group *R-3c*. The first is predominant for structures where tolerance factor is smaller than 0.975 and the second is favoured when *t* is in the range of (0.975-1.02). These tilt systems minimize the Madelung energy of the crystal lattice by maximizing the covalent bonding and minimizing the electrostatic repulsion. The first and second order Jahn-Teller effects induce further distortions from the ideal structure in some ABX_3 perovskites.

Perovskites show a large variety of interesting properties like colossal magnetoresistance, ferroelectricity, dielectricity, catalytic activity and optical properties. The reason for this broad range of properties comes from the large flexibility of the atomic arrangement, which provides the opportunity to incorporate a vast range of ions with different size. Structural distortions have a strong effect on the electronic and magnetic properties.

A direct way of modifying the properties of perovskites consists in anionic substitution at the X-site. In perovskite oxynitrides the incorporation of trivalent nitrogen into the divalent oxygen anion sublattice induces the oxidation of the cations as a charge compensation mechanism.

A limited number of cations can fit into the $AB(O,N)_3$ composition with perovskite structure. Depending on the O/N ratio the sum of cationic charges can vary between +6 (for a perovskite oxide) and +9. For the composition ABN_3 the only reported compound is $ThTaN_3$ with (q_A,

q_B)=(4,5) .[126] For the cationic charge sum of +8 the combination (3, 5) is reported for $LaNbON_2$[127] and $LaTaON_2$[63] with the composition $ABON_2$, and the (2, 5-6) combination is shown by the mixed oxidation state compound $EuWO_{1.58}N_{1.42}$[128] . The most extense group of perovskite oxynitrides has the composition ABO_2N. These compounds are known for cation oxidation states (2, 5) and (3, 4) so that the A site is occupied by alkaline earth metals such as (Ca, Sr, Ba) or Eu^{2+} or a lanthanide, and the B site is occupied by the transition metals V, Nb, Ta, Ti or Zr.[64, 129, 130] Layered Ruddlesden-Popper oxynitrides are known for the series $(SrO)(SrNbO_2N)_n$ (n=1,2),[131] A_2TaO_3N (A=Sr, Ba)[132] and the rare earth aluminates Ln_2AlO_3N (Ln=La→Eu).[133] The tolerance factor for existing perovskite oxynitrides ranges from 0.878 to 1.038 as calculated from ionic radii.

1.5.1 Anion order in perovskite oxynitrides

Many perovskite oxynitrides present partial or total ordering of nitrogen and oxygen in the different anion sites. Anion ordering or rotations and tilts of the MO_4N_2 (or MO_2N_4) octahedron lead to structural phase transitions and symmetry lowering.[134] Neutron diffraction is sensitive to small anion displacements as the scattering lengths of light and heavy atoms are comparable, and it also offers high O/N scattering contrast (b(O) = 0.581 fm; b(N) = 0.936 fm). Electron diffraction is able to reveal small symmetry distortions that are not evidenced from neutron experiments.[59] Anion ordering in crystal systems presenting independent anion sites can be predicted by Pauling's second crystal rule (PSCR).[135] This states that the electrical charge of an anion (q) in a site should compensate the sum of the bond strengths (b) of the cations to which it is coordinated:[136]

$$b = \sum_i \frac{z_i}{v_i} \quad (5)$$

Where z_i is the electrical charge of each cation bonded to a given anionic position and ν_i its coordination number. In accordance to PSCR, nitride with higher charge than oxide, will occupy the sites showing larger bond strength sums. In $SrNbO_2N$, $SrTaO_2N$ and more recently in RVO_2N (R = La, Pr, Nd),[130] a local *cis* arrangement has been suggested from electron diffraction and high resolution neutron diffraction studies. Refinements of $SrMO_2N$ (M= Nb, Ta) converged to an ordered model with oxide anions ordered on one axis of the pseudocubic cell with 50/50 O/N mixture present on the other two. Additionally, a symmetry lowering from I4/mcm to Fmmm observed by electron diffraction was compatible with *cis*-ordering.[59, 137] The preferred *cis* arrangement may be explained in terms of maximum overlap of vacant d orbitals in π bonding with the anion lone pairs. In the *cis* configuration the four anion p type lone pairs can interact with three vacant d orbitals of the transition metal whereas in the *trans* geometry they interact with two d orbitals (**Figure 1. 8b**). The combination of the *cis*-coordination of each M cation by two nitrides and the linear coordination of each nitride by two M cations results in the formation of YigYag —M—N— chains. As there are two choices for the 90º turn at each M atom, the zigzag chains can distort and form rings within the planes or at higher temperatures they can partially occupy the out-of-plane anion sites giving place to three dimensional partially ordered configurations.

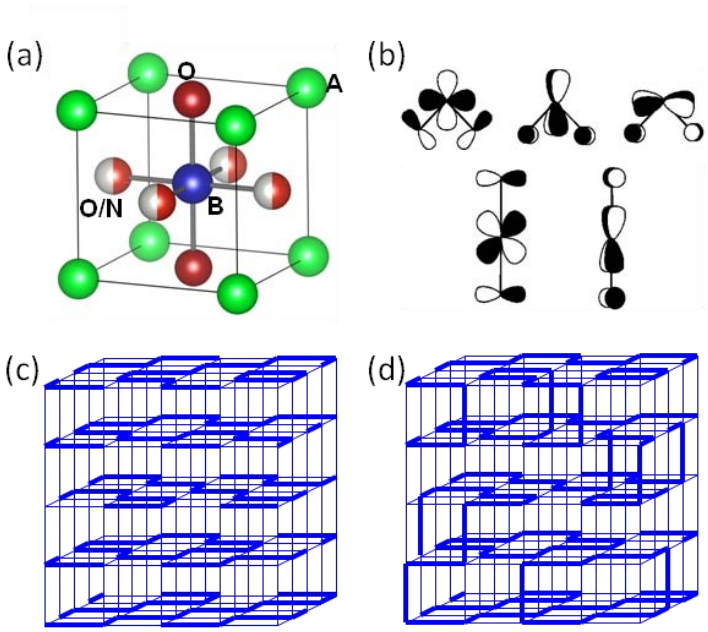

Figure 1. 8. (a) N/O order in ABO_2N perovskite oxynitride. (b) π bonding of d orbitals with O/N lone pairs showing three and two interactions in the *cis*- and *trans*- configurations respectively. *Cis*-$(MN)_n$ chain formation arising from local anion order (c) Disorder of chains within planes. (d) 3D partial order configurations. Adapted from Ref. [22] with permission from the Royal Society of Chemistry.

1.5.2 Electronic properties of oxynitride perovskites

Since the early discovery of piezoelectricity by J. and P. Curie in 1880 and the first pyroelectric materials such as the La Rochel salts in the early 20', to the first switchable ferroelectric materials such as $BaTiO_3$,[138] and later on the hegemonic lead zirconate titanate in the middle 50' and more recent research for lead-free piezoelectrics,[139] the applications of such materials have led to a random variety of inventions such as sonar, microbalance,

capacitors, scanning probe microscopes (STM, AFM), non-volatile random access memories, quartz watches and cigarette lighters.

The first pioneering studies on the thermal dependence of magnetic properties of materials were also done by P. Curie at the end of 19th century. Upon the hundreds of applications that magnetic materials receive in our modern life I will just highlight a few: power conversion, electrical motors, signal transfer LH/HF, loudspeaker, sensors, data recording and data storage. Basically, the zettabytes of information that humankind stores worldwide are scripted into a magnetic material. Despite the technological relevance of magnetite, it was not until 2011 that its magnetic structure was finally resolved.[140] Intense research is presently focused on the development of giant magnetoresistant materials for spintronics application and the development of multiferroic materials. The challenge of developing multiferroic materials resides in two self-excluding conditions that must be found simultaneously in the same material: the magnetic properties arising from unpaired d^n or f^n electrons of transition metals or lanthanides, respectively, must couple with a dipole generated by a significant displacement of d^0 cation such as Ti^{4+} in a switchable ferroelectric.[141] Materials with high dielectric constants and low dielectric losses, ferroelectrics, ferromagnetic and those with magnetic properties coupled to the electrical properties such as multiferroics, magnetocapacitors and magnetoresistant materials are of fundamental interest and elemental to our technological progress.

The substitution of oxygen by nitrogen in oxidic perovskites induces structural and electronic changes. $BaTaO_2N$ and $SrTaO_2N$ exhibit high dielectric permittivities, of 4900 and 2900, respectively at room temperature, although both show nonpolar point group symmetries.[64] This can be understood by considering the local arrangement of O/N in the

TaO_4N_2 octahedra. Computational studies showed that in a perfectly anion ordered compound, either *cis*- or *trans*- isomers will form polar octahedral units leading to ferroelectric or antiferroelectric properties.[142] $BaTaO_2N$ presents a disordered anion arrangement where the long range order of Ta displacements is lost showing a relaxor-type behaviour.[64] Classical ferroelectricity has been observed for the compressively strained $SrTaO_2N$ epitaxial thin films.[143] Dielectric constants of $SrNbO_2N$ and $LaTiO_yN_x$ films have been reported to be 5000 and 1000 at 300K, respectively.[23, 144] Nitrogen doping of $Ba_xSr_{1-x}TiO_3$ films proved to improve the dielectric constants by 1.44 with respect to the undoped material.

Recently, $MnTaO_2N$ with polar $LiNbO_3$-type structure was reported by H. Kageyama group. This material exhibits a helical spin order at room temperature with a propagation vector of [0,0,0.3] that is interpreted as a consequence of strong frustration induced by three inequivalent J_2 and J_2' couplings generated by the mixed anionic environment. Moreover, due to the lack of weak ferromagnetic component, that could have been generated by Dzyaloshinskii-Moriya interactions in the G-type structure no multiferroic behaviour was observed in $MnTaO_2N$.[145]

$EuMO_2N$ with M= Nb, Ta[70] and W[128] are insulating paramagnets at room temperature with effective moments close to the ideal value of 7.94 μ_B expected for S=7/2 of Eu^{2+}. They order ferromagnetically at Curie temperatures of 5 K for Nb and Ta and 12 K for W. However, the magnetoresponse of the Ta compound is very different from that of Nb and W compounds. $EuTaO_2N$ is highly insulating with resistivity $>10^{+9}$ Ω·cm below T_c. While for $Eu^{2+}(Nb^{5+}_{1-y}Nb^{4+}_y)O_{2+y}N_{1-y}$ and $EuWO_{1+x}N_{2-x}$ colossal negative magnetoresistance is observed below the ferromagnetic ordering transition temperature. The magnetotransport properties arise from the electron doping induced by anion nonstoichiometry in Nb compound were

the d-band carrier spins couple with the localized S=7/2 spins of Eu^{2+}. For W compounds p doping allows an additional hole magnetotransport resulting from double exchange between Eu^{2+} and Eu^{3+} that lead to polarization of the Eu^{3+} spin and orbital angular moment. In $EuTaO_2N$ the oxidation state of tantalum is +5 which is consistent with the strong insulating behaviour. [70, 71]

Molybdenum perovskite oxynitrides, $AMoO_{3-x}N_x$ (A = alkaline earth) have been reported as thermoelectric materials. They show low electrical conductivities and Seebeck coefficients from 15 to 30 μV/K.[146]

Vanadium perovskite oxynitrides $RVO_{3-x}N_x$ (R = La, Pr, Nd; $0 \leq x \leq 1$) show antiferromagnetic order that is gradually suppressed with nitridation as the concentration of V^{3+} decreases. A frequency dependent spin glass transition is observed at 29K for La compounds and a similar anomaly is observed at 134 K for Pr and at 136 K for Nd compounds.[130]

In this thesis we report the effect of nitride on the antiferromagnetic ordering for new $LnCrO_{3-x}N_x$ perovskites (Ln = La, Pr, Nd, Sm) that show Neel temperatures between 200-300 K. We also report the first hafnium oxynitride perovskites $LnHfO_2N$ (Ln = La, Pr, Nd, Sm) and investigate their dielectric properties.

1.5.3 Photocatalytic properties of perovskite oxynitrides

Solar energy incident on earth in 1h (4.3×10^{20} J) by far exceeds the energy currently consumed on the planet in 1 yr (3.9×10^{20} J in 2013).[147] Simultaneous solar energy conversion and storage by photochemical splitting of water into H_2 and O_2, the fuels of a hydrogen based energy economy, can be achieved by heterogeneous catalysis. Today, over 130

materials are known to catalyze the overall splitting of water according to equation:

$$H_2O + h\nu \rightarrow H_2 + \frac{1}{2}\,O_2 \qquad \Delta G^0 = 238\ kJ\ mol^{-1} \qquad (5)$$

However, no material has been capable to exceed the threshold of 10% efficiency under visible light needed to make this technology commercially feasible.[148] So far, the efficiency record holder is for Cr/Rh-modified GaN/ZnO with a QE=5.9 % in pure water and under visible light.

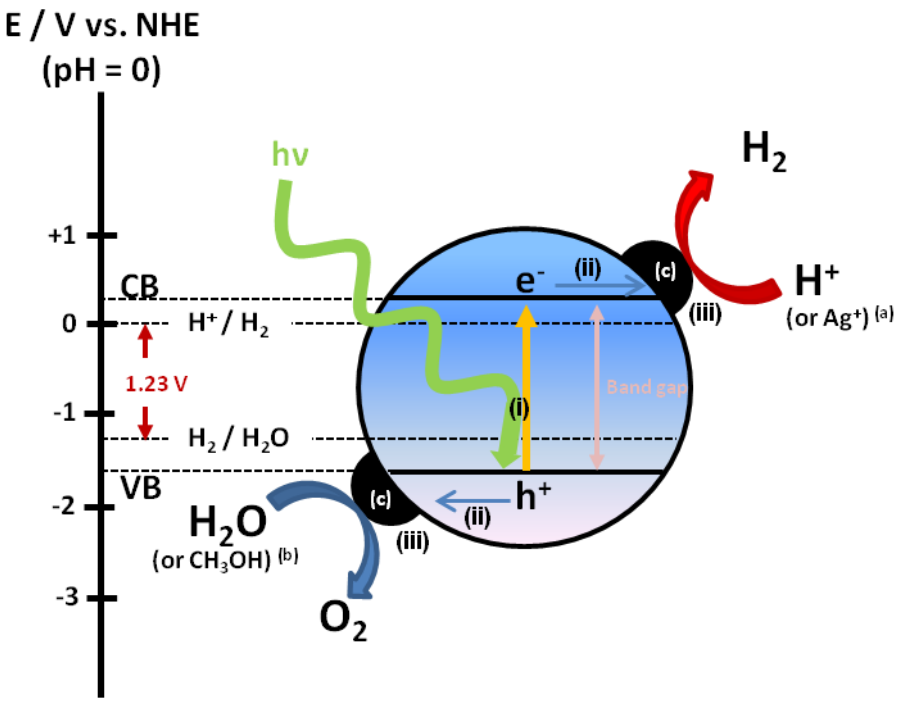

Figure 1. 9. Schematic diagram illustration of water splitting over semiconductor photocatalyst, (i) light absorption and photo-excitation of electron-hole pairs, (ii) charge separation and migration to the surface, and (iii) oxidation and reduction reactions at the surface. (a) indicates sacrificial oxidizing reagent, (b) indicates sacrificial reducing reagent and (c) indicates co-catalyst, typically Pt for reduction and CoO_x for oxidation.

Figure 1. 9. shows a schematic diagram of water splitting reaction over a heterogeneous semiconductor photocatalyst. This process involves tree main steps: (i) absorption of photons with higher energy than the semiconductor bandgap, leading to the generation of electron (e^-) – hole (h^+) pairs in the semiconductor particle; (ii) charge separation followed by migration of these photogenerated charge carriers to the surface of the particles; (iii) surface chemical reactions between the carriers and adsorbed molecules (e.g. H_2O). Several conditions must be satisfied by the inorganic semiconductor catalyst in order that the simultaneous water reduction and oxidation reaction occurs. The flat band potential of the semiconductor must be more negative than the reduction potential of water (0.0 V vs NHE) to produce H_2, and the valence band edge must be more positive than the oxidation potential of water (+1.23 V vs NHE) to produce O_2. Furthermore, the photocatalyst must be stable against photocorrosion. A sufficiently narrow bandgap to absorb visible light is also a requirement for highly efficient solar conversion photocatalysts. The overall water splitting reaction is a multielectron process where sites for 4-electron oxidation of water are required to produce O_2 which makes the reaction extremely challenging. Co-catalysts such as Pt, NiO and RuO_2 are usually loaded to improve charge carrier separation and induce active sites for multielectron oxidation and reduction reactions. Sacrificial reagents such as methanol for H_2 evolution and Ag^+ for O_2 evolution are often employed to evaluate the photocatalytic activity for water splitting. The sacrificial reagent acts as an electron donor or hole scavenger when it is irreversibly oxidized at the valence band of the semiconductor or it acts as an electron acceptor or electron scavenger when it is reduced at the conduction band. These half reactions of water splitting are employed to

evaluate if a photocatalyst satisfies the thermodynamic and kinetic potentials required for H_2 and O_2 evolution.

The main advantage of oxynitride photocatalysts over oxides is that as the 2p orbitals of nitrogen are at a higher energy level than those of oxygen so the valence band of oxynitride photocatalyst will be located at a less positive potential than for an oxide. This enables oxynitride semiconductors to have both a sufficient negative conduction band for H_2 production and a sufficiently narrow band gap (< 3.0 eV) for visible light absorption. These conditions have proven to be intrinsically difficult to find in an oxide semiconductor. The reported oxynitrides are not active for water splitting into H_2 and O_2 without sacrificial reagent,[149] they can be unstable and readily become deactivated though photocorrosion or self-oxidation. Nevertheless, the co-evolution of N_2 as a self oxidation product of oxynitride photocatalysts can be suppressed by doping or addition of cocatalysts such as IrO_2 or CoO_x.

Perovskite oxynitrides of d^0 cations Ti^{4+}, Nb^{5+} and Ta^{5+} with band gaps between 1.9 and 2.5 eV have shown to be active for H_2 or O_2 evolution under light of maximum wavelength of 500-600 nm. Theoretical calculations have shown that numerous perovskite oxynitrides have the appropriate band potentials for both water oxidation and reduction under visible light. So far, only $LaMg_xTa_{1-x}O_{1+3x}N_{2-3x}$ ($x \geq 1/3$),[150] $LaTiO_2N$[151] when loaded with IrO_2 and $CaNbO_2N$[152] have been reported to carry on the overall water splitting reaction. Tantalum perovskites $MTaO_2N$ (M = Ca, Sr, Ba) have shown to be active for H_2 evolution but not for water oxidation. $SrNbO_2N$ is active only for O_2 evolution and other niobium perovskite oxynitrides such as $BaNbO_2N$ and $LaNbO_2N$ are not active or showed poor activity.[153, 154] In order to overcome the stringent requirements of a one step water splitting reaction a single material must present the appropriate

thermodynamic and kinetic potential to evolve simultaneously H_2 and O_2. Domen and co-workers developed a two step photoexcitation mechanism between two different photocatalysts. This process is known as the Z-scheme and it enables to combine numerous visible light active materials that are either only active for water oxidation or water reduction employing the appropriate redox mediator, often (I^-/IO_3^-) or (Fe^{3+}/Fe^{2+}), that transports the charge from one particle to the other.[155-157] This system also presents the ability to produce separately H_2 and O_2. A significant disadvantage of the Z-scheme is that it requires the double amount of photons to achieve the same production as a one step system.

In this thesis we describe the photocatalytic activity in water splitting under visible light or UV light of $LnMO_2N$ (M= Zr, Hf) perovskites in presence of a sacrificial reagent, employing Pt, IrO_2 or CoO_x as cocatalysts.

Chapter II

Methods

This chapter is focused in the general description of the synthesis conditions and characterization techniques used in this thesis. A detailed description and fundaments of the techniques are beyond the scope of this work. However, in some cases, a brief description of the fundaments might be given to ensure a good understanding of this manuscript.

2.1 Synthesis of oxynitrides

2.1.1 Thermal Ammonolysis

Ammonolysis reactions were carried out in sintered alumina boats containing the oxide precursor powders. The samples were placed inside a quartz tube under ammonia gas at flow rates between 180 and 1000 ml/min and treated at temperatures between 700 ^{0}C and 1100 ^{0}C. As a rule of thumb it can be considered that the ammonia flow rate depends on the reaction temperature in such a way that as higher is the temperature, higher the flow rate must be, in order to minimize the dissociation of NH_3 into N_2 and H_2 before reaching the sample:

$$NH_3\,(g) \rightarrow \frac{1}{2}\,N_2\,(g) + \frac{3}{2}\,H_2\,(g)$$

The kinetics of the dissociation is slow and its extent can be controlled by the flow rate. For instance, at 700 ^{0}C the % of decomposition varies from 10% for flow rate of 150 ml/min to 45% for 50 ml/min (**Figure 2. 1b**).[22, 158]

It has been suggested that the active nitriding species are adsorbed partial decomposition products of ammonia, NH_2 (ads), NH (ads) and N(ads).[159] During nitridation the oxygen anions at the surface exchange with the absorbed nitrogen to give nitride anions, and the oxygen is removed into the gas by reaction with the high concentration of surface hydrogen to form water vapour.

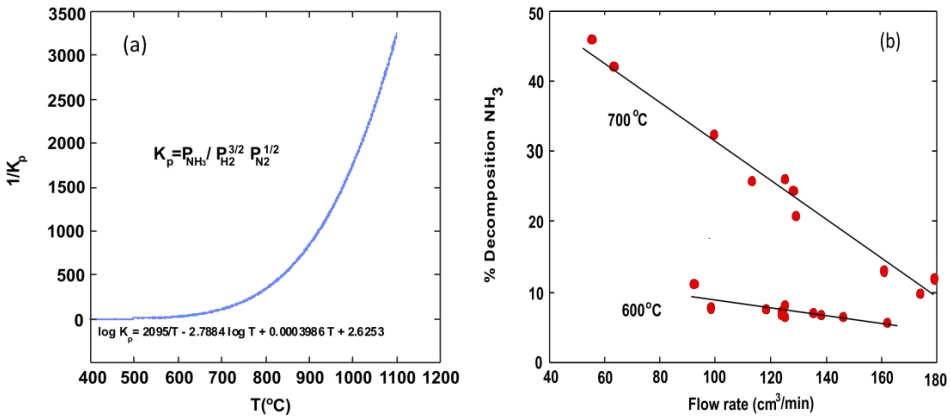

Figure 2. 1. Equilibrium constant of dissociation of NH_3 as function of the temperature (b) % of decomposition of NH_3 as function of the flow rate at different temperatures. Reproduced from Ref. [22] with permission from The Royal Society of Chemistry.

$$oxide + NH_3\,(g) \rightarrow\ oxynitride +\ H_2O\ \uparrow\ (g)$$

The formation of the thermodynamically stable water molecule is the main driving force of the ammonolysis reaction. A high flow rate also removes the H_2O from the sample surface preventing backward equilibrium reaction.

Because of the presence of H_2 the ammonolysis reaction may produce reduced compounds. Such is the case of ionocovalent oxynitrides of more electronegative late transition metals for which the reducing behaviour of NH_3 together with the presence of H_2 favour the formation of interstitial nitrides with the cations in low oxidation estates.[26, 33]

Figure 2. 2. Ammonolysis furnace.

As ammonia is a dangerous toxic gas and flammable in air at moderate temperatures (auto-ignition point 651^{0}C at air content between 16-27 %)[160] numerous precautions are taken during handling and reaction to work safely. The furnace is located in a fume hood equipped with an uninterruptible power supply system (UPS) and a sensor controlled electrovalve that will cut the ammonia flow and stop the furnace controller if an ammonia concentration over 3 ppm is detected in the furnace room (**Figure 2. 2**). Additionally, the existence of ammonia leaking is controlled with pH indicator before and during the reaction. At the outlet of the ammonia flow two bubblers loaded with diluted acetic acid (0.1 M) are placed to neutralize all the excess of ammonia, increasing safety and minimizing the environmental impact.

The ammonolysis reaction was used to prepare the oxynitride lanthanide chromites $LnCrO_{3-x}N_x$ (Ln = La, Pr, Nd, Sm). The synthesis conditions are detailed in section 4.2.

2.1.1.1 Soft-chemistry reactions: the Pechini method

In a conventional solid state reaction the reactants are manually mixed together in an agate mortar and pestle and the subsequent reaction rate depends to a large degree on the particle size, degree of homogenization and contact between the grains. In order to improve the limitations of homogeneity and reactivity of the conventional solid state methods, the preparation of complex multinary compounds can be carried out through the previous preparation of an oxide precursor containing the designed composition by a *Chimie douce*-type process. The most commonly used methods are the amorphous citrate process, pioneered by Pechini in 1967,[161] decomposition of coprecipitation precursors,[162] citrate sol-gel route or the self propagating glycine-nitrate process.[163] In the Pechini method, metal ions are complexed in an aqueous solution with α-hydroycarboxilic acids such as citric acid. These chelates can undergo polyesterification when heated with a polihydroxy alcohol such as ethylene glycol which prevents selective precipitation as water is evaporated. On the removal of the excess of solvent, a solid resin containing the metals is formed. The resin is then decomposed by heating to remove the organic constituents, leaving the desired composition as a residue. The ammonolysis of precursors prepared by the Pechini method generally produces high-surface-area, compositionally homogeneous fine powders, usually with low levels of residual carbon.

Detailed synthetic conditions for the synthesis of $LnCrO_4$ compounds by the Pechini method are detailed in section 4.3.

2.1.2 High temperature solid state synthesis

The main difficulty in preparing oxynitrides by this method lies in the precautions needed to avoid traces of moisture and oxygen around the sample. At the given temperature, the affinity of a metal towards oxygen is always greater than for nitrogen. Thus, under nitriding conditions, a very low oxygen partial pressure is enough to irreversibly cause the formation of an oxygenated product.

Figure 2. 3. High temperature tubular furnace

High temperature solid state synthesis of oxynitrides under N_2 flow was carried out in a tubular furnace at temperatures between 1300 and 1500^{0}C (**Figure 2. 3.**), starting from the stoichiometric mixture of the metal oxides or carbonates and one or more metal nitrides or oxynitrides, so that the nitrogen is incorporated to the product from one of the reactants. The stoichiometric mixture of reactants is vigorously mixed in an agate mortar and pestle and pressed in to a pellet to insure a good homogeneity, increase the particle contact and hence the reaction rates. Lanthanide oxides must

be dried thoroughly prior to weighing by overnight heating at temperatures from 600 to 1000 ^{0}C. The pellet is placed in a molybdenum boat and covered with a zirconium foil that acts as a sacrificial agent protecting the sample from traces of moisture and oxygen that might be adventitiously present in the reaction media.

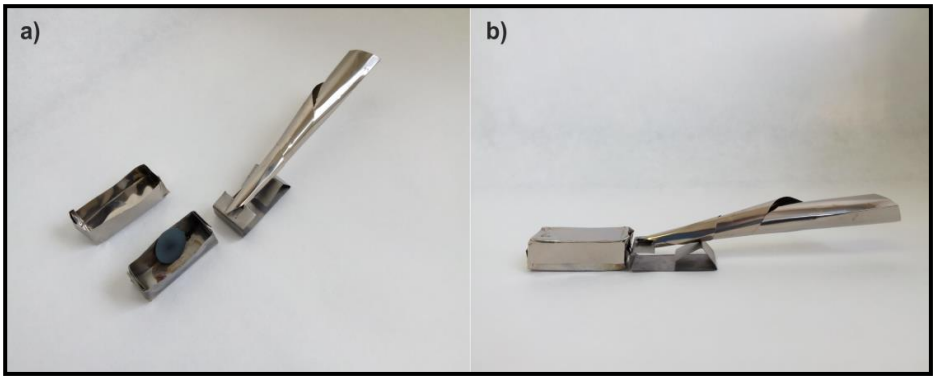

Figure 2. 4. Molybdenum boat and zirconium foil

Before the crucible an additional sacrificial zirconium foil shaped in a conical form is placed. Both elements are placed in the center of the high density impervious sintered alumina tube as shown in **Figure 2. 4**. The tubular furnace is connected to a vacuum pump. A dynamic vacuum of 0.1 mbar is first performed to eliminate the adsorbed moisture followed by several cycles of pump/fill with N_2 (99.9999%, Air liquid) or N_2/H_2 (95%/5% V/V, Air liquide, 99.999%)(traces of H_2O and O_2 below 0.5 ppm and 0.1 ppm respectively).

The synthesis starting with hygroscopic reactants such as alkaline earth metal oxides were performed under controlled atmosphere using a Schlenk tube and a Labconco glove box operating in Ar (99.995 %, Carburos Metálicos) for handling the samples. All material used for the sample

preparation in the glove box were dried overnight at 70^0C in a vacuum oven.

The high temperature synthesis approach was used to prepare the oxynitride orthosilicates $LnMSiO_{4-x}N_x$ (Ln= La, Nd, Ce and M = Sr, Ba, Eu) and $Sr_{2-x}La_xSiO_{4-x}N_x$ ($0 \leq x \leq 1$), and the zirconium and hafnium oxynitride perovskites $LnHfO_2N$ (Ln= La, Pr, Nd, Sm). The synthetic conditions are described in sections 3.3 and 5.3, respectively.

2.2 Determination of the cationic and anionic stoichiometry

The precise determination of the cationic and anionic composition is of high importance in the characterization of oxynitrides since the physical properties can be strongly dependent even on slight modifications in the stoichiometry. Two common analytical techniques used for the determination of nitrogen contents in oxynitrides are combustion analysis and thermogravimetric analysis (TGA). The cationic stoichiometry was determined by energy dispersive X-ray spectroscopy (EDX).

2.2.1 Combustion analysis

Typically three replicates weighing between 1000 and 2000 μg were burned under oxygen at 1060^0C using mixtures of MgO, WO_3 and Sn powder as additives and atropine as a reference standard. The elemental analyzer was a Thermo Fisher Scientific EA CE 1108.

In this technique the product from combustion N_2 (g) is carried by Helium gas and quantified using a thermal conductivity detector.

2.2.2 Thermal analysis

Thermogravimetric analyses (TGA) were performed in a NETZSCH -STA 449 F1 Jupiter instrument for the determination of the nitrogen content of the oxynitrides from oxidation experiments in oxygen gas. Simultaneous thermogravimetric/differential calorimetry experiments (TGA/DSC) was used to study the thermal stability in different gases of the oxynitrides, the thermal behaviour of solid state reactant mixtures and the thermal combustion of resins prepared by the Pechini method. The measurements were performed between 25 and 1500 ^{0}C with heating rates of 2-10 ^{0}C min^{-1} under O_2, air or N_2, using a gas flow rate of 50-70 ml/min and alumina crucibles.

2.2.3 Energy dispersive X-ray spectroscopy

The energy dispersive X-ray spectroscopy (EDX) is used to qualitatively or semi-quantitatively analyze the chemical composition of the samples. This characterization technique relies on the fundamental principle that each element has a unique atomic structure allowing unique set of peaks on its X-ray emission spectrum. The quantitative analysis is performed by integration of the area below the selected peak of the energy spectra. EDX has been very useful for the study of the phase composition of the samples and the optimization of the synthesis conditions as it can provide the

chemical composition of individual crystals. The analyses were performed in a FEI Quanta 200 FEG scanning electron microscope equipped with an EDAX detector with an energy resolution of 132 eV. With this detector we were able to determine the cationic ratio of the crystals whereas the precise determination of oxygen and nitrogen was not possible.

2.3 Structural characterization

2.3.1 Laboratory X-ray powder diffraction

X-ray diffraction has been used as a fundamental technique for routinely determination of samples purity and phase identification. Data acquisition was performed with a Rigaku RU-200B diffractometer equipped with a rotating anode and a Siemens D5000 diffractometer, using the copper Kα radiation (λ= 1.5418 Å). Data were typically collected for 2θ between 5^0 and 70^o/ 100^0 with step of 0.02^0 and scan speed of 1 to 5^0/min. For air sensible samples as the reactants SrO or BaO, the samples were prepared in the glovebox using a Kapton® film to protect them from air during data acquisition.

2.3.2 Synchrotron X-ray powder diffraction

Synchrotron X-ray powder diffraction data were taken on pure samples to obtain accurate unit cell parameters and atom coordinates. It has been particularly useful for studying the effects of composition on cell parameters and determining accurate bond distances.

The data for samples with compositions $Sr_{2-x}La_xSiO_{4-x}N_x$ (x = 0, 0.2, 0.3, 0.5, 0.8, 1) were collected at room temperature using capillary sample holders (0.5 mm diameter) on the 11-BM instrument at the Advanced Photon Source (APS), Argonne National Laboratory (USA) using λ= 0.458996 Å.

Data for samples with compositions $LnCrO_{3-x}N_x$ and $LnHfO_2N$ with (Ln = La, Pr, Nd, Sm) were collected at room temperature using capillary sample holders (0.3-0.5 mm diameter) in the angular range $1.038^0 \leq 2\theta \leq 61.09^0$ at the MSPD beamline of the ALBA Synchrotron (Cerdanyola del Valles, Spain). Using a double Si (111) crystal monochromator, a wavelengths between 0.4127 Å and 0.6263 Å was selected and calibrated with Si NIST.

2.3.3 Neutron powder diffraction

Neutron powder diffraction is a powerful and very useful tool for the determination of the crystal structure of oxynitrides as it is sensitive to small anion displacements because the scattering lengths of the light and heavy atoms are comparable. It also provides high scattering contrast between oxygen and nitrogen. Furthermore, neutrons posses a magnetic dipole moment that interact with unpaired electrons, giving rise to magnetic scattering allowing the study of the magnetic structure of materials.

Time of flight neutron powder diffraction data from a 0.5 g $LaBaSiO_3N$ sample and a 0.5 g $LaMO_2N$ (M = Zr, Hf) sample were collected at room temperature on the high-resolution diffractometer HRPD at the ISIS spallation source, Rutherford Appleton Laboratory, U.K.

Room temperature neutron powder diffraction data for $LaCrO_{2.72}N_{0.28}$ were collected on the D2B diffractometer at the Institut Laue-Langevin (ILL), Grenoble using 450 mg of sample placed in a 5 mm diameter vanadium can. The neutron wavelength was 1.594 Å. Room temperature data were collected for $NdCrO_{2.58}N_{0.42}$ and $PrCrO_{2.64}N_{0.36}$ on the D20 diffractometer also at the Institut Laue-Langevin. The neutron wavelength was 1.36 Å using a take-off angle of 118^0. Low temperature neutron powder diffraction was carried out on all the samples on the D1B diffractometer at the ILL. The neutron wavelength was 2.524 Å. For the Ln= La and Nd samples a series of scans were taken at intervals of approximately 6.5 K between 10 K – 315 K for Ln= La and approximately 3.5 K between 1.5 K- 215 K for R= Nd. For Ln= Pr, data was collected in 50 K intervals between 1.5 K and 250 K.

2.3.4 Electron diffraction

Electron diffraction has been used to determine the unit cell parameters and space group of the samples. It has also been used to study the homogeneity of the samples and for the identification of amorphous particles.

The electron diffraction study was performed in a 120 KV JEOL 1210, transmission electron microscope (TEM), with a resolution of 3.2 Å and equipped with a analytical sample holder GATAN with tilting angles $\pm 60^0$ in *X* and $\pm 30^0$ in *Y.*

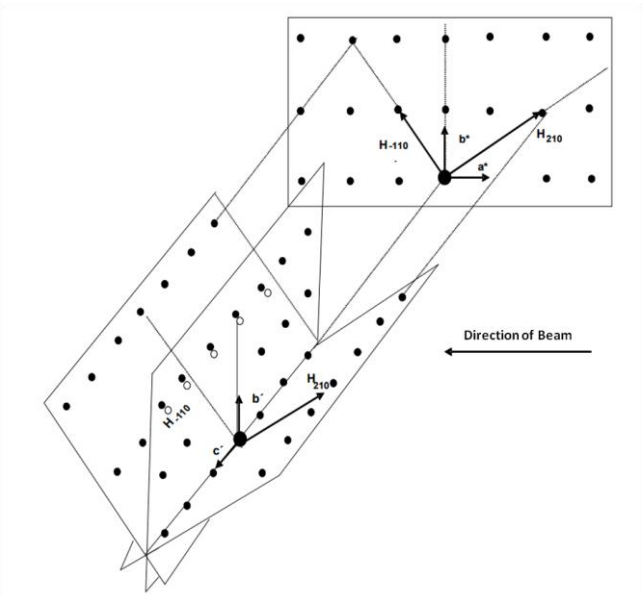

Figure 2. 5. Schematic representation of the rotation method used to reconstruct the reciprocal lattice by electron diffraction. c^* is the common axis for all patterns.

The space group and cell parameters were determined by the rotation method, consisting in the reconstruction of the reciprocal cell from a set of planes that have one common crystallographic axis, as shown in **Figure 2. 5.**

2.4 Optical characterization

2.4.1 Diffuse reflectance

Diffuse reflectance is an excellent technique to determine the band gap of semiconducting powders. The absorption of semiconductor is proportional to the band gap energy as shown by the equation:

$$\alpha \propto \frac{(h\nu - E_0)^{\eta}}{h\nu} \quad (1)$$

Were hν is the incident photon energy, E_0 is the band gap energy and η is ½ for direct allowed transitions and 1 for indirect allowed transitions. When light is scattered in a perfect diffuse manner and all specular reflection is avoided, then α becomes K/2, were K is the Kubelka-Munk absorption coefficient. Assuming that the sample has an infinite thickness (sample experimental thickness of 3 mm) so no light is transmitted, a Kubelka-Munk function can be applied to a diffuse reflectance spectrum:

$$F(R_\infty) = \frac{(1 - R_\infty)^2}{2R_\infty} = \frac{K}{S} \quad (2)$$

Taking eq.1 and eq.2 and considering α=K/2 and η=1/2 eq.3 can be obtained:

$$[F(R_\infty)h\nu]^{2} = A\left(h\nu - E_g\right) \quad (3)$$

Were A is a constant.

Experimentally, absolute reflectance R_∞ is substituted by relative reflection R using the reflectance of PTFE as a reference (R_{PTFE}). Eq.4

$$R_\infty = \frac{R_{sample}}{R_{PTFE}} \quad (4)$$

By drawing a Tauc plot where the $[F(R_\infty)h\nu]^2$ is plotted against hν ,the value of band gap is obtained as the hν value at the point of intersection of the tangent line to the point of inflection of the absorption edge with the abscissa axis.

The diffuse reflectance spectra of samples $Sr_{2-x}La_xSiO_{4-x}N_x$ (x = 0, 0.2, 0.3, 0.5, 0.8, 1), $Sr_{1.98-x}Eu_{0.02}La_xSiO_{4-x}N_x$ (x = 0, 0.2, 0.3, 0.5, 1), $Sr_{2-x}La_{x-0.02}Ce_{0.02}SiO_{4-x}N_x$ (x = 0.2, 0.3, 1), $LaEuSiO_3N$, $LaBaSiO_3N$, $NdEuSiO_3N$,

$LnHfO_2N$ (Ln=La, Pr, Nd, Sm) and $LaZrO_2N$ were obtained at room temperature on a UV-Vis-NIR Varian Cary 5000 spectrophotometer, with operational range of 190-3300 nm. The band gaps were determined by using the Tauc plot and the Kubelka-Munk method as explained above.[164, 165]

2.4.2 Photoluminescence measurements

The excitation and emission photoluminescent spectra of $LaM_{1-x}Eu_xSiO_3N$, $La_{1-x}Ce_xMSiO_3N$ *(x=0, 0.01, 0.02, 0.05, 0.1) (M=Sr, Ba),* $Sr_{1.98-x}Eu_{0.02}La_xSiO_{4-x}N_x$ (x = 0, 0.2, 0.3, 0.5, 1) and $Sr_{2-x}La_{x-0.02}Ce_{0.02}SiO_{4-x}N_x$ (x = 0.2, 0.3, 1) were measured on two different equipments.

The excitation spectra were measured on a Horiba Jobin Yvon FluoroMax-4 spectrofluorometer equipped with an integrating sphere, a xenon source, a photomultiplier detector (range 200 nm to 850 nm) and a photodiode reference detector. The wavelength range is 200 nm to 950 nm.

The Photoluminescence (PL) spectra were measured at room temperature using the 405 nm line of a solid-state laser for excitation and collected using a LabRam HR800 spectrometer equipped with a charge-coupled device detector. PL spectra were corrected for the spectral response of the spectrometer by normalizing each spectrum employing the detector and grating characteristics. The incident light power density was about 1 W/cm^2.

2.4.3 Photoluminescence quantum yield

The photoluminescent quantum yield (PLQY) of $LaM_{1-x}Eu_xSiO_3N$, $La_{1-x}Ce_xMSiO_3N$ *(x=0, 0.01, 0.02, 0.05, 0.1) (M=Sr, Ba),* $Sr_{1.98-x}Eu_{0.02}La_xSiO_{4-x}N_x$ (x = 0, 0.2, 0.3, 0.5, 1) and $Sr_{2-x}La_{x-0.02}Ce_{0.02}SiO_{4-x}N_x$ (x = 0.2, 0.3, 1) were measured using a Horiba Quanta-f, 6 in. diameter, spectralon coated integrating sphere. The phosphor powders were encapsulated in silicone resin (GE Silicones, RTV-615) and deposited on transparent quartz substrates (Chemglass). A neutral density filter and a long pass filter (LPF430) were used to prevent saturation of the detector on the excitation acquisition and to cut off the second harmonic at the emission measurement, respectively. A correction factor was introduced in the PLQY calculus to take into account the wavelength dependent attenuation introduced by the integrating sphere and the filters.

2.5 Electrical and magnetic properties characterization

2.5.1 Magnetic susceptibility

Magnetic susceptibility measurements were performed using a Quantum Design SQUID magnetometer. The magnetization of $LaEuSiO_3N$ was measured between 2 and 300 K in fields of 0.0025 and 0.5 T. M(H) curves were measured up to 7 T for temperatures between 2 K and 50 K. The magnetic measurements of $LnCrO_{3-x}N_x$ (Ln = La, Pr, Nd, Sm) were performed at H=2000 G between 10 K and 400 K. Silicone capsules were used as sample holder and the amount of sample used was between 20 mg and 200 mg.

2.5.2 Electrical resistivity and dielectric measurements

Electrical resistivities measurements were carried out for $LaZrO_2N$ and $NdHfO_2N$ samples between 100 and 300 K. The dielectric permittivities were measured for $LaZrO_2N$ and $LnHfO_2N$ (Ln = La, Nd, Sm) as a function of the temperature (between 2 and 350 K) and the frequency. All the electrical measurements were performed in Physical Property Measurement System (PPMS, Quantum Design, USA) using a custom made multifunctional probe. DC resistivity was measured using a Keithley Electrometer/High resistance meter (model 6517A). Dielectric properties were measured using the Agilent (E4980A) Precision LCR meter. Electrical contacts to the sample were made using silver paste and copper wire. The data were recorded while warming the sample.

2.6 Photocatalytic measurements

2.6.1 Preparation of Photoelectrodes by the squeezing method

Typically, 20 mg of $LnHfO_2N$ (Ln= La, Pr, Nd, Sm) powder was suspended in 20 µl of water. After 2 minutes of sonication, the optimum density of the slurry was determined by visual inspection. Later, few drops of the slurry were deposited on the surface of the fluorine-doped tin oxide (FTO) glass and rapidly extended by mean of a glass wand. The as deposited electrodes were subjected to a postnecking treatment to promote interparticle electron transfer, by five drop wise additions of 50 µl of a 10 mM solution

of $Cl_2HfO{\cdot}8H_2O$ in MeOH in intervals of 15 min., followed by heating under ammonia flow of 20 ml/min at 450 ^{0}C for 0.5 h.

2.6.2 Photoelectrochemical measurements

Photocurrent measurements were performed on $LnHfO_2N$ (Ln = La, Nd, Hf) coated on conductive substrate (FTO) using Pt as counter electrode, Ag/AgCl as a reference electrode and a Na_2SO_4 solution (0.1 M, pH 6) as electrolyte. The potential of the working electrode was controlled using a potentiostat. The solution was purged with Ar gas for over 5 min prior to the measurement to exclude any dissolved air. The electrodes were irradiated by a 300-W Xe lamp (LX-300F, Cermax). For the visible light measurements a cutoff filter (L-42, Hoya) was used to block the light in the ultraviolet region (k\400 nm). The irradiated area was 4.5 cm^2 (1.5 ×3 cm^2). The range of potential measured was from -1 to 1 V vs Ag/AgCl and the illumination was chopped in 1 s intervals. The photocurrent was evaluated under full range Xe lamp and under visible light conditions by performing two consecutive current–potential scan on the same photoelectrode. A scheme and image of the equipment is displayed in **Figure 2. 6.**

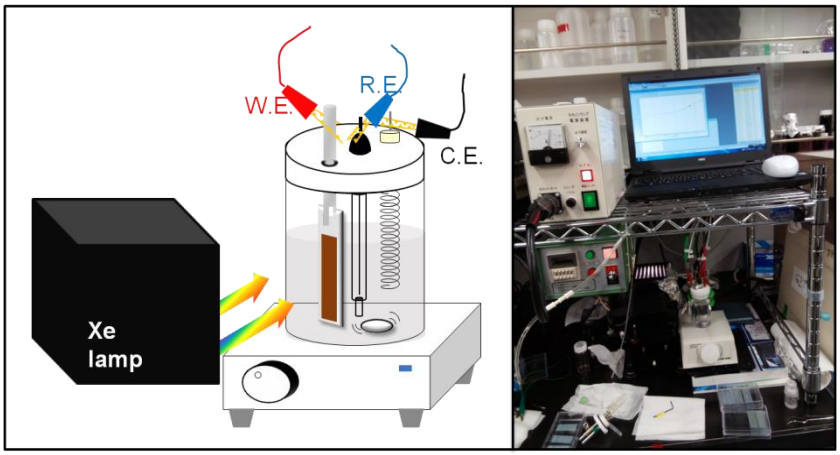

Figure 2. 6. Scheme and image of the photoelectrochemical setup.

2.6.3 Gas evolution measurement

Photocatalytic reactions were carried out using a Pyrex glass reactor connected to a closed gas-circulation system. For the photocatalytic water oxidation (O_2 evolution), the catalyst powder (50 mg) was suspended in 250 mL of an $AgNO_3$ 10 mM aqueous solution. For the photocatalytic water reduction (H_2 evolution), the catalyst powder (50 mg) was suspended in 250 mL of a 20 vol.% methanol solution. Prior to reaction the slurries were sonicated for 10 min. By mean of a set of magnetic stirrer and bar, vigorous stirring was kept during the reaction time. The reaction vessel was immersed in a thermostatic bath and the closed gas-circulation system was evacuated by several pump/ fill cycles until complete removal of air. The suspensions were irradiated using a 300 W Xe lamp. For the visible light measurements a cutoff filter (L-42, Hoya) was used to block the light in the ultraviolet region (k\400 nm). The evolved gases were analyzed by on-line gas chromatography (detector; TCD, column packing; molecular sieve 5 A,

Ar carrier). A scheme and image of the equipment is displayed in **Figure 2. 7.**

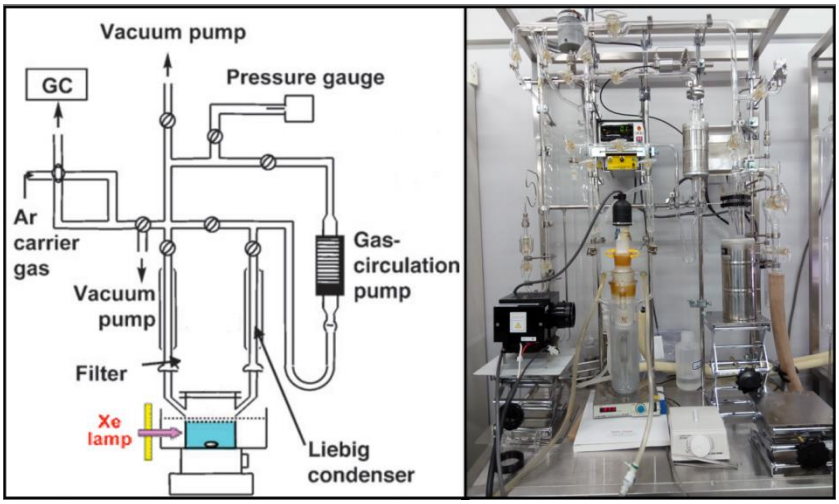

Figure 2. 7. Scheme and image of the closed gas-circulation system.

Section I

Oxynitridosilicates

Chapter III

Oxynitridosilicate Phosphors for Solid-State White Lighting: Synthesis and luminescent properties of $M_{2-x}La_xSiO_{4-x}N_x$: Eu^{2+} or Ce^{3+} (M= Sr, Ba ; $0 \leq x \leq 1$)

3.1 Introduction

The development of high-brightness blue (In,Ga)N double-heterostructure LEDs by Suhuji Nakamura and co-workers in 1995[42, 82] made possible the efficient generation of white light by its combination with a wide band emitting yellow phosphor. Since then, numerous efforts have been directed towards the design of an efficient blue to orange/red phosphor converter.[104, 166-169] Currently, the most common commercial white LED device uses $Y_{3-x}Ce_xAl_5O_{12}$ ($YAG:Ce^{3+}$) phosphor as down-converter, despite it has a relatively poor color rendering index due to its lack of emission in the red region of visible spectrum.[170] As the perceived color of light and the way in which illuminated coloured surfaces appear is a determinant factor for the adoption of lighting devices, it is necessary to improve and expand the number of wide band emitting phosphors with high color rendering.[171]

Silicon-based nitride phosphors such as $MSi_2O_2N_2:Eu^{2+}$,[172-174] $M_2Si_5N_8:Eu^{2+}$ (M = Ca, Sr, Ba),[77] $CaAlSiN_3:Eu^{2+}$ [175] and $CaSiN_2:Ce^{3+}$ [116] show excellent efficient blue to orange/red conversion. Among oxynitridosilicates, only few examples of orthosilicates with isolated silicon tetrahedra have been reported. For Li_8SiN_4, an example of nitridosilicate with isolated $[SiN_4]$ tetrahedra, no precise structural data has been reported.[176] Few oxynitrido apatites are known, which are poorly nitrided and contain some nitrogen either in the channel anion sites or in the silicate groups.[177, 178] Schnick et al. reported $Gd_3(SiON_3)O$ as an example of an orthosilicate-type (oxy)nitridosilicate containing $[SiON_3]^{7-}$ ions,[179, 180] and Marchand et al. reported the rare earth oxynitridosilicates $LnEuSiO_3N$ (Ln = La, Nd, Sm) with a β-K_2SO_4 structure containing $[SiO_3N]^{5-}$ groups.[181]

The orthosilicate phosphors $M_2SiO_4:Eu^{2+}$ (M = Ca, Sr, Ba) are important, highly efficient luminescent materials with emission wavelengths from ca. 500 nm to 600 nm under excitation with UV light from ca. 300 to 450 nm and internal quantum efficiencies ranging from 30 % to 90 % depending on the composition and synthesis conditions.[94, 182-188] The host compounds adopt different structures with relative stability depending on the alkaline earth cation with increasing polymorphism as the cation size decreases. The stable polymorph of Sr_2SiO_4 below 85 °C is the monoclinic β-phase with space group $P2_1/n$. Above this temperature it transforms into the orthorhombic α'-phase, β-K_2SO_4 type with *Pmnb* space group. This polymorph can be stabilized at room temperature by doping with a larger cation as Ba^{2+} or with Eu^{2+} and is the only one reported for Ba_2SiO_4.[189, 190] All of them show two crystalografically independent sites for cations with coordination numbers (CN) 10 and 9. Crystal site engineering offers the possibility to tune the luminescent color of a phosphor by changing the coordination environment of the activator.[191] Wide band, red luminescent emissions can be generated with Eu^{2+} or Ce^{3+} doping in sites with a strong crystal field splitting and large covalency of bonding.

By the concomitant substitution of O^{2-} by N^{3-} and M^{2+} by La^{3+} in M_2SiO_4, a new family of orthosilicate-type oxynitridosilicate with formula $LaMSiO_3N$ (M=Sr, Ba) has been prepared. $LnEuSiO_3N$ (Ln = La, Nd, Sm) compounds were previously reported by Marchand et al. Due to the chemical similarity in terms of oxidation state, ionic radius and coordination number of Eu^{2+} and Sr^{2+} the existence of the analogous strontium compound $LaSrSiO_3N$ was anticipated. When the new oxynitridosilicates are doped with Eu^{2+} or Ce^{3+}, the highly covalent environment created by nitrogen decreases the energy of 5*d* levels of the active ions. The high effective charge of N^{3-} coordinating the active ion induces large crystal field splitting. The overall

effect of introducing N in the host crystal results in long-wavelength emission from the $4f^{n-1}5d^1$ to $4f^n$ transition of the Eu^{2+} or Ce^{3+} ions in the oxynitride phosphor. $LnMSiO_3N$ compounds are adequate hosts for Eu^{2+} doping by substitution the alkaline earth cation or for Ce^{3+} doping by substitution of La^{3+}.

3.2 Objectives

The detailed objectives can be summarized as follows:

- Synthesis of $LaSrSiO_3N$ and $LaBaSiO_3N$ host materials and their corresponding europium and cerium activated luminescent materials with compositions $LaM_{1-x}Eu_xSiO_3N$ and $La_{1-x}Ce_xMSiO_3N$ (x=0, 0.01, 0.02, 0.05, 0.1) (M=Sr, Ba).
- Study and optimization of luminescent properties of Eu^{2+} and Ce^{3+} - activated $LaSrSiO_3N$ and $LaBaSiO_3N$.
- Study of the influence of the coupled La/N introduction in Sr_2SiO_4: Synthesis of the solid solution $Sr_{2-x}La_xSiO_{4-x}N_x$ (x = 0, 0.2, 0.3, 0.5, 0.8, 1) and the corresponding active materials $Sr_{1.98-x}Eu_{0.02}La_xSiO_{4-x}N_x$ (x = 0, 0.2, 0.3, 0.5, 1) and $Sr_{2-x}La_{x-0.02}Ce_{0.02}SiO_{4-x}N_x$ (x = 0.2, 0.3, 1).
- Study of the variation of luminescent properties with the gradual introduction of La/N in Sr_2SiO_4 activated with europium or cerium.
- Determination of the photoluminescence quantum yield (PLQY) and CIE (Commission Internationale de l'Eclairage) 1931 color coordinates of all samples.
- Evaluation of the warmness of the white light produced by $Sr_{2-x}La_xSiO_{4-x}N_x:Eu^{2+}$ phosphors in a LED test device.

3.3 Results and discussion

3.3.1 Synthesis of oxyninitridosilicates with β-K_2SO_4 structure

3.3.1.1 Synthesis of $LaMSiO_3N:Eu^{2+}$ or Ce^{3+} (M=Sr, Ba)

The oxynitride orthosilicates $LaM_{1-x}Eu_xSiO_3N$ (x=0, 0.01, 0.02, 0.05, 0.1) (M=Sr, Ba) and $La_{1-x}Ce_xSrSiO_3N$ (x=0, 0.01, 0.02, 0.05, 0.1) were prepared by the solid state reactions:

$$3\,La_2O_3 + 6(1-x)MO + 3x\,Eu_2O_3 + \left(\frac{3}{2}+\frac{1}{3}x\right)Si_3N_4 + \left(\frac{3}{2}-\frac{3}{2}x\right)SiO_2 \rightarrow 6\,LaM_{1-x}Eu_xSiO_3N + \frac{2}{3}x\,N_2$$

and

$$3(1-x)\,La_2O_3 + 6x\,CeO_2 + 6\,SrO + \left(\frac{3}{2}+\frac{1}{3}x\right)Si_3N_4 + \left(\frac{3}{2}-\frac{3}{2}x\right)SiO_2 \rightarrow 6\,La_{1-x}Ce_xSrSiO_3N + \frac{2}{3}x\,N_2$$

The alkaline earth metal oxides MO (M=Sr, Ba) were prepared by overnight decomposition of the corresponding carbonate $SrCO_3$ (Alfa Aesar, 99.994%), $BaCO_3$ (Aldrich, 99.99 %) at 1000°C under a dynamic vacuum of $5x10^{-2}$ mbar. La_2O_3 (Aldrich, 99.99 %), Eu_2O_3 (Aldrich, 99.99 %) and SiO_2 (Aldrich, 99.995 %) were previously dried at 950 °C for 4 h to eliminate presence of water and hydroxide groups. CeO_2 (Aldrich, 99.995 %) was dried at 300 °C for 4 h. Heating above this temperature may result in partial reduction of Ce^{4+} to Ce^{3+} and consequent to unknown stoichiometry $CeO_{2-\delta}$. All air sensitive oxides and Si_3N_4 (α-phase, Alfa Aesar, 99.9%) were transferred to the glove box in a schlenk tube. Powders were weighed and thoroughly mixed in an agate mortar for 30 min, loaded into an evacuable pellet die and sealed in two zipper plastic bags. Once the pellet was pressed at 10 bar, it was removed from the zipper bags, loaded into a molybdenum boat, covered with zirconium foil that acts as oxygen and moisture scavenger and then loaded into the sintered alumina furnace tube.

Immediately, the tube was connected to the sealed fittings system and left under dynamic vacuum until the start of the reaction. Two cycles of pump/fill were performed to purge air and moisture from the reaction media. The reactions were carried out under N_2/H_2 (95 %: 5 %, Air liquide, 99.999%) flow of 100 ml/min. The reducing atmosphere helps to stabilize the divalent oxidation state of Eu although the reduction of Eu^{3+} to Eu^{2+} takes place with N^{3-} arising from Si_3N_4 through the following reaction:

$$3Eu^{3+} + N^{3-} \rightarrow 3Eu^{2+} + \frac{1}{2} N_2\,(g) \uparrow$$

The thermal treatments were optimized for each system in order to avoid the presence of secondary phases. The strontium and europium compounds were fired at 1350 ^{0}C for 3h and the barium compounds were prepared at 1500 ^{0}C for 6.5 h. Heating and cooling rates were kept constant as represented in the following scheme:

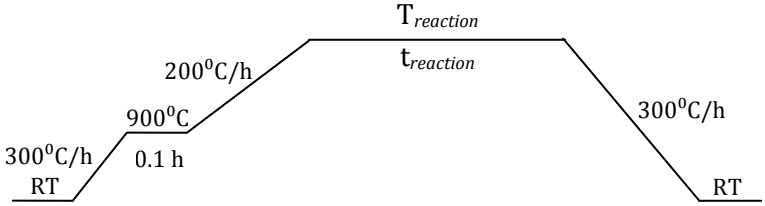

The oxygen content in the reactants mixture was empirically optimized to take into account all adventitious sources of oxygen that were present in the reaction media. The optimum ratio of oxygen in the product vs oxygen in the reactants was found to be 1.055.

3.3.1.2 Synthesis of $LnEuSiO_3N$ (Ln=La, Nd)

The oxynitridosilicates $LaEuSiO_3N$ and $NdEuSiO_3N$ were prepared by the following reaction:

$$3\,Ln_2O_3 + 3\,Eu_2O_3 + 2\,Si_3N_4 \rightarrow 6\,LnEuSiO_3N + N_2$$

Lanthanide and europium oxides were previously dried at 950 °C for 4 h. Graphitic carbon (Aldrich) powder was added in 1.4 % (w/w) as oxygen scavenger so as adventitious oxygen was eliminated from the reaction media by the following reactions:

$$C\,(s) + \frac{1}{2}O_2 \rightarrow CO\,(g)\uparrow \; and \; CO(g) + \frac{1}{2}O_2 \rightarrow CO_2(g)\uparrow$$

Sample preparation was carried out in the glove box following the same procedure above described for $LaMSiO_3N$ compounds. The reactions were carried out under a N_2/H_2 (95 %: 5 %) flow of 100 ml/min at 1350^0C for 3h.

3.3.1.3 Synthesis of the solid solution $La_xSr_{2-x}SiO_{4-x}N_x$: Eu^{2+} or Ce^{3+} ($0 \leq x \leq 1$)

Samples with compositions $Sr_{2-x}La_xSiO_{4-x}N_x$ (x = 0, 0.2, 0.3, 0.5, 0.8, 1), $Sr_{1.98-x}Eu_{0.02}La_xSiO_{4-x}N_x$ (x = 0, 0.2, 0.3, 0.5, 1) and $Sr_{2-x}La_{x-0.02}Ce_{0.02}SiO_{4-x}N_x$ (x = 0.2, 0.3, 1) were prepared in a similar manner as $LaMSiO_3N$ compounds but in this case the O/N ratio was controlled by adjusting the silicon nitride to silicon oxide ratio and introducing the corresponding stoichiometric amount of lanthanum. The general reaction for the undoped compounds is:

$$\frac{x}{2}\,La_2O_3 + (2-x)SrO + \frac{x}{4}Si_3N_4 + \frac{(4-3x)}{4}SiO_2 \rightarrow Sr_{1-x}La_xSiO_{4-x}N_x$$

Total oxygen in the reactants was adjusted using the empirical ratio previously found for the synthesis of $LaMSiO_3N$: $O_{products}/O_{reactans}$= 1.055. Reactants were prepared and handled in the same way as previously described for $LaMSiO_3N$ samples. The reactions were carried out under an N_2/H_2 (95 %: 5 %) flow of 100 ml/min at 1500^0C for 3h.

3.3.2 Chemical characterization

3.3.2.1 Determination of nitrogen content by combustion analysis

The nitrogen contents determined by combustion analyses are summarized in **Table 3. 1.**

Table 3. 1. Nitrogen content determined by combustion analysis for $(La,Sr)_2Si(O,N)_4$ samples

Sample	1st assay	2nd assay	Avg.	N content
$LaSrSiO_3N$	4.41	4.62	4.52	1.02(3)
$LaSr_{0.99}SiO_3N:Eu_{0.01}$	4.47	4.57	4.52	1.02(2)
$LaSr_{0.98}SiO_3N:Eu_{0.02}$	4.59	4.37	4.48	1.02(3)
$LaSr_{0.95}SiO_3N:Eu_{0.05}$	4.24	4.29	4.27	0.97(1)
$LaSr_{0.90}SiO_3N:Eu_{0.1}$	4.40	4.24	4.32	1.00(3)
$La_{0.99}SrSiO_3N:Ce_{0.01}$	4.45	4.51	4.48	1.01(1)
$La_{0.98}SrSiO_3N:Ce_{0.02}$	4.36	4.49	4.43	1.00(2)
$La_{0.95}SrSiO_3N:Ce_{0.05}$	4.45	4.46	4.46	1.01(1)
$La_{0.90}SrSiO_3N:Ce_{0.1}$	4.54	4.51	4.53	1.02(1)
$LaBaSiO_3N$	4.25	4.24	4.25	1.11(1)
$LaBa_{0.99}SiO_3N:Eu_{0.01}$	4.57	4.58	4.58	1.20(1)
$LaBa_{0.98}SiO_3N:Eu_{0.02}$	4.47	4.38	4.43	1.16(1)
$LaBa_{0.95}SiO_3N:Eu_{0.05}$	4.45	4.54	4.50	1,18(1)
$LaEuSiO_3N$	4.21	4.19	4.20	1.14(1)
$Sr_{1.8}La_{0.2}SiO_{3.8}N_{0.2}$	0.95	1.00	0.98	0.19(1)
$Sr_{1.7}La_{0.3}SiO_{3.7}N_{0.3}$	1.36	1.38	1.37	0.28(1)
$Sr_{1.5}La_{0.5}SiO_{3.5}N_{0.5}$	2.40	2.41	2.41	0.50(2)

The values of nitrogen per formula correspond to the nominal stoichiometry within the standard deviation of the measurement for all strontium compounds either doped with europium or cerium. However, the nitrogen contents per formula for the barium compounds are slightly above those expected for their nominal composition. The results obtained for the members of the solid solution show that the substitutions in Sr_2SiO_4 of Sr by La and of O by N occur as a charge compensation mechanism.

3.3.2.2 Thermogravimetric analysis

The TGA curves in oxygen for the members of the solid solution $Sr_{2-x}La_xSiO_{4-x}N_x$ (x = 0.2, 0.3, 0.5, 1.0) are shown in **Figure 3. 1**.

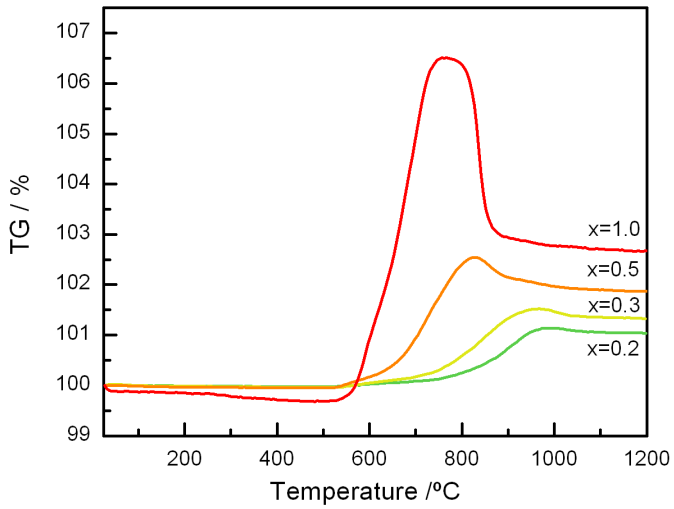

Figure 3. 1. TGA curves in O_2 for $Sr_{2-x}La_xSiO_{4-x}N_x$ samples.

The oxynitridosilicates react with oxygen according to:

$$A_aB_bSiO_{4-x}N_{x\,(s)} + \frac{3x}{4}O_{2\,(g)} \rightarrow A_aB_bSiO_{4+\frac{x}{2}\,(s)} + \frac{x}{2}N_{2\,(g)}$$

The oxidation process generally leads to the corresponding oxide for each composition. The amount of evolved nitrogen can be determined from the weight gain (Δm) and can be used to quantify the nitrogen content (x):

$$x = \frac{\Delta m}{(\frac{3}{2}M(O_2) - M(N_2))} \times \frac{M\,(A_aB_bSiO_{4+\frac{x}{2}})}{m\,(A_aB_bSiO_{4+\frac{x}{2}})}$$

Where $M(N_2)$ and $M(O_2)$ are the molar masses of molecular nitrogen and oxygen. $M(A_aB_bSiO_{4+x/2})$ and $m(A_aB_bSiO_{4+x/2})$ are the molar mass of the formed oxide and its weight, respectively.

The nitrogen contents determined by TGA are summarized in **Table 3. 2.**

Table 3. 2. Nitrogen contents determined by TGA for $Sr_{2-x}La_xSiO_{4-x}N_x$ samples.

Sample	T_{onset}	Δm (%)	N content
$Sr_{1.8}La_{0.2}SiO_{3.8}N_{0.2}$	780	1.07	0.29
$Sr_{1.7}La_{0.3}SiO_{3.7}N_{0.3}$	764	1.38	0.39
$Sr_{1.5}La_{0.5}SiO_{3.5}N_{0.5}$	665	1.92	0.57
$LaSrSiO_3N$	590	2.99	0.97

As expected the TGA curves show a gradual increase in mass gain with the increase of La/N substitution in Sr_2SiO_4. Nitrogen contents determined by TGA in oxygen were consistent with results of chemical analyses. The decomposition of the samples to the oxides started at temperatures between 550 °C (for x=1) and 750 °C (for x=0.2). For the samples with larger nitrogen contents the weight increased to a maximum and then decreased at higher temperatures. This behaviour is typical of oxynitrides

and it has been interpreted through the formation of intermediate phases with weakly bonded N_2 molecules.[33] The observed *vs* calculated weight increases at 1000 °C were for x=0.2: 1.1 %/0.7 %; x=0.3: 1.4 %/1.1 %; x=0.5: 1.9 %/ 1.7 %; x=1: 3.0 %/3.2 %.

3.3.2.3 Energy dispersive X-ray spectroscopy

The energy dispersive X-ray spectra of the members of the solid solution $Sr_{2-x}La_xSiO_{4-x}N_x$ (x = 0.2, 0.3, 0.5, 1.0) are shown in **Figure 3. 2.**

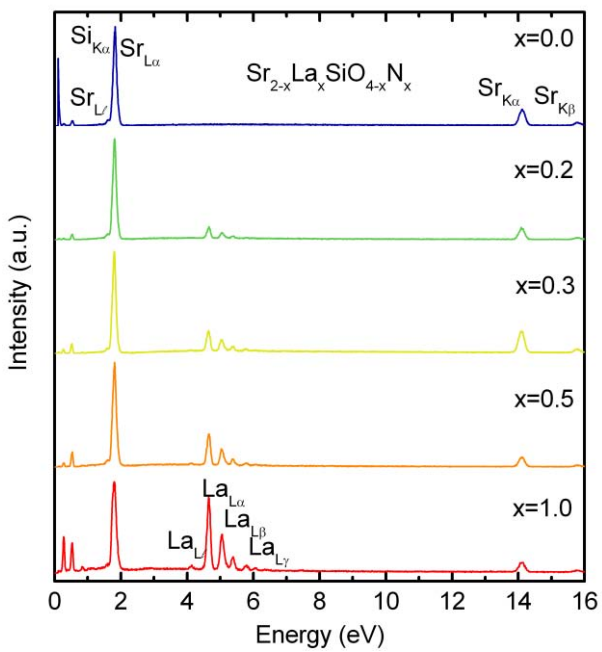

Figure 3. 2. Energy dispersive X-ray spectra of $Sr_{2-x}La_xSiO_{4-x}N_x$ ($0.0 \leq x \leq 1.0$)

Quantitative EDS analyses of individual particles of each sample confirmed the nominal cationic La: Sr: Si ratios and indicated that the samples were compositionally homogeneous.

The cation ratios were calculated following the method described by Cheetham[192] using Sr_2SiO_4 and $LaSrSiO_3N$ as standards. The constants $k_{La/Sr}$ and $k_{Sr/Si}$ were determined from 15 crystals of the standard compounds from the following equation:

$$k_{A/B} = \frac{I_B}{I_A} \times \frac{C_A}{C_B} \tag{3.1}$$

The obtained values were $k_{La/Sr}$=0.79(10) and $k_{Sr/Si}$=1.33(7).

The selected integrated intensities I_{La}, I_{Sr} and I_{Si} correspond to the $La_{L\alpha}$, $Sr_{K\alpha}$ and Si_{Ka} X-ray maximum emissions, respectively.

The average La : Sr : Si ratios obtained from ca. 10 individual particles for each sample were 0.2 : 1.8 : 1.1 (x = 0.2), 0.3 : 1.7 : 1.0 (x = 0.3), 0.6 : 1.5 : 1.0 (x = 0.5) and 0.9 : 1.0 : 1.2 (x = 1) which agree well with the nominal compositions within the standard deviations.

3.3.3 Structural Characterization

3.3.3.1 Crystal structure determination of $LaMSiO_3N$ (M=Sr, Ba, Eu) from X-ray and neutron powder diffraction data

The X-ray diffraction patterns of the oxynitridosilicates $LaMSiO_3N$ (M=Sr, Ba, Eu) and the neutron powder diffraction patterns of $LaBaSiO_3N$ were fitted by Rietveld refinement. Laboratory X-ray data were collected on a Rigaku RU-200B difractometer equipped with a rotating anode. The X-ray

wavelengths was that of the copper Kα radiation (λ= 1.5418 Å). Time of flight powder neutron diffraction data were recorded at room temperature on the high-resolution diffractometer HRPD at the ISIS spallation source, Rutherford Appleton Laboratory, U.K. The observed diffraction peaks of $LaMSiO_3N$ (M=Sr, Ba, Eu) compounds were indexed in the orthorhombic cell of the β-K_2SO_4 structure shown by the α' polymorph of Eu_2SiO_4 or alkaline earth silicates M_2SiO_4. Refinements were performed with Fullprof software.[193] The profile functions used was a Thompson-Cox-Hastings pseudo-Voigt convoluted with axial divergence asymmetry function for the X-ray data and a T.O.F. Convolution pseudo-Voigt with back-to-back exponential functions for the neutron data. Background was fitted with a polynomial function for the X-ray data and from a interpolated data file for the neutron data. The X-ray refinement results are presented in **Figure 3. 4** to **Figure 3. 6** and **Table 3. 3** to **Table 3. 5** . Refined cell parameters and general refinement agreement factors are given in **Table 3. 7**. Refined atomic coordinates, cation and anion occupancies are given in **Table 3. 3** to **Table 3. 5.** and bond distances are given in **Table 3. 9**. Neutron diffraction data collected on the 90° detector bank and on the backscattering detector bank were simultaneously refined. The results are presented in **Figure 3. 7** and **Table 3. 6**. A representation of the crystal structure is given in **Figure 3. 3.**

Starting lattice parameters and atomic coordinates were obtained from the orthorhombic polymorph of Eu_2SiO_4 using the Pmnb space group instead of the standard setting Pnma.[194] Refinements of cation occupancies in sites 1 and 2 were performed from powder X-ray diffraction data for $LaSrSiO_3N$ and from powder neutron diffraction data for $LaBaSiO_3N$, that provide enough contrast between the scattering factors of La-Sr and La-Ba respectively. In both cases these results showed a strong preference of the

larger alkaline earth cations or divalent Eu for the site M1 showing higher coordination number. The refined occupancies obtained by fixing the ratio of La:Ba and La:Sr to 1:1 were 0.804(8) for Ba and 0.196(8) for La at site 1 in $LaBaSiO_3N$ and 0.758(3) for Sr and 0.242(3) for La at the same site in $LaSrSiO_3N$. Refinement of cation site occupancies from X-ray diffraction data in $LaEuSiO_3N$ was possible despite the smaller difference between the scattering factors of La and Eu and led to similar values: 0.812(18) for Eu and 0.188(18) for La at site 1. The M1 and M2 sites form zig-zag chains running along the b axis and alternating along a. (**Figure 3.3**). Nitrogen/oxygen occupancies in $LaBaSiO_3N$ were refined from neutron diffraction data by constraining the total nitrogen content to the stoichiometric value. This lead to O/N occupancies of 1/0 in site X1, 0.542(14)/ 0.458 for site X2 and 0.729/0.271 for site X3. The anions in site X1 are coordinated to 3 M2, 1 M1 and 1 Si, whereas sites X2 and X3 are coordinated to 3 M1, 2 M2 and 1 Si (**Figure 3. 3b**). This results in larger bond strength sums for sites X2 and X3, which in accordance with Pauling's second crystal rule, agrees with the preferential occupancy of nitrogen for these sites. In agreement with Pauling's rule, the O/N occupancies in the X-ray diffraction data refinements of $LaSrSiO_3N$ and $LaEuSiO_3N$ were considered to be similar to those refined in $LaBaSiO_3N$ and were fixed to 1/0, 0.5/0.5 and 0.75/0.25 for sites X1, X2 and X3, respectively. Bond valence calculations were consistent with anion ordering and the observed N/O occupancies in the three compounds (see Table 3.8.). The average bond distance in $LaBaSiO_3N$ for M1 site is 2.928 Å, significantly smaller than that observed for isostructural Ba_2SiO_4 (2.983 Å) as a consequence of the substitution of c.a. 20 % Ba^{2+} for La^{3+}. This effect is more important than the expansion caused by the substitution of one O^{2-} by N^{3-} (rO^{2-} = 1.38 Å (CN IV); rN^{3-} = 1.46 Å (CN IV))[11], which should be significant in this site

with a large number of bonds to the nitrided anion positions X2 and X3 (9 bonds to X2, X3 *vs* 1 bond to X1). For the M2 site the contraction in the average bond distance with respect to Ba_2SiO_4 is more important (2.718 Å in $LaBaSiO_3N$ *vs.* 2.824 Å in Ba_2SiO_4) because of the substitution of 80 % of Ba^{2+} by La^{3+} as well as the lower coordination to N atoms than M1 (3 bonds to X1 vs 6 bonds to X2, X3). The Si-X2 (1.682(18) Å) and Si-X3 (1.677(10) Å) bond distances in $LaBaSiO_3N$ are significantly longer than for Ba_2SiO_4 (Si-X1= 1.614(7) Å; Si-X2= 1.652(7) Å) because of the larger radius of nitride vs. oxide (see table 3.9). However, the bond distances to X1, occupied by oxygen in $LaBaSiO_3N$, are similar in both compounds within the experimental error. The observed average bond distances for the strontium and europium compounds are similar, according with the nearly identical ionic radii of Sr^{2+} and Eu^{2+} M1-X = 2.868 Å, M2-X= 2.687 Å for $LaSrSiO_3N$ and M1-X = 2.869 Å, M2-X= 2.685 Å for $LaEuSiO_3N$.

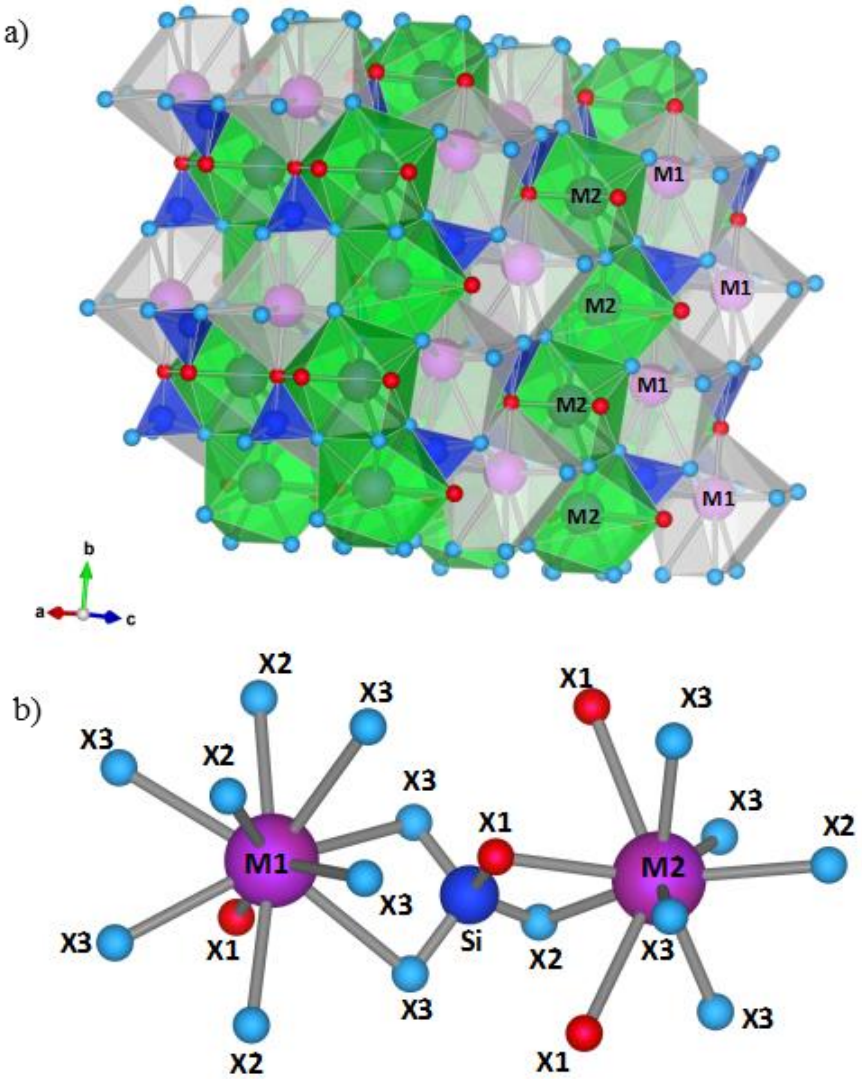

Figure 3. 3. Structural model of $LaMSiO_3N$ compounds showing zig-zag chains of sites M1 (grey polyhedra) and M2 (green polyhedra) running along a, and b) coordination polyhedra of cations. Anions are represented by red (oxygen) and light blue (mixed oxygen/nitrogen) spheres. Reproduced from reference [79] with permission of the Royal Society of Chemistry.

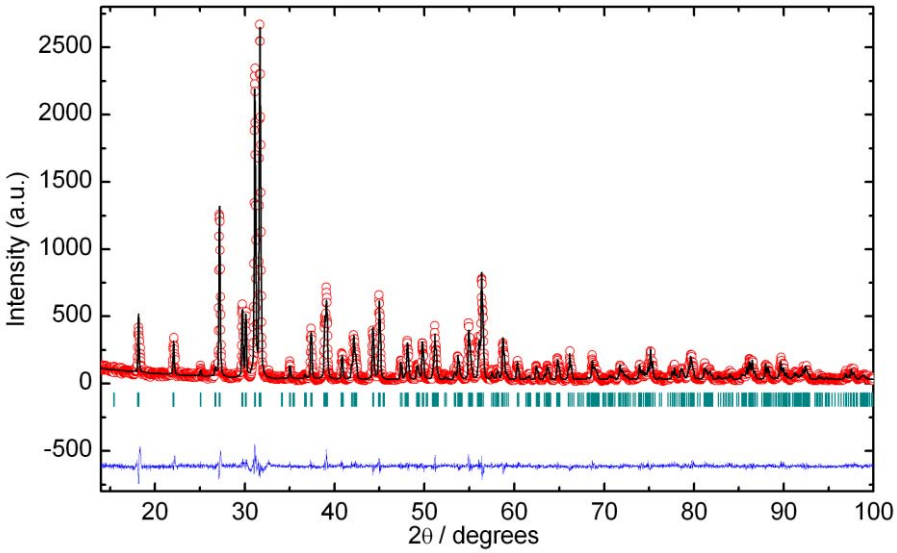

Figure 3. 4. Observed and calculated powder X-ray diffraction patterns for $LaSrSiO_3N$.

Table 3. 3. Atomic coordinates, cation and anion occupancies for $LaSrSiO_3N$ from the refinement of X-ray powder diffraction data .[(a)]

Site	Wyckoff position	x	y	z	Occupation factor
La1/ Sr1	4c	0.25	0.6552(3)	0.5782(3)	0.242(3)/0.758
La2/ Sr2	4c	0.25	0.0078(3)	0.30391(19)	0.758/ 0.242
Si	4c	0.25	0.2192(11)	0.5828(12)	1
O1/N1	4c	0.25	0.992(2)	0.5663(17)	1/0
O2/N2	4c	0.25	0.316(3)	0.436(2)	0.5/0.5
O3/N3	8d	0.014(2)	0.2874(17)	0.6652(19)	0.75/0.25

(a) Estimated standard deviations in parentheses are shown once for each independent variable. O/N occupation factors were considered fixed to those obtained in $LaBaSiO_3N$ from neutron diffraction. Refined isotropic B-factors were 1.01(7) $Å^2$ for La/Sr atoms, 1.32(18) $Å^2$ for silicon and 2.1(2) $Å^2$ for anions.

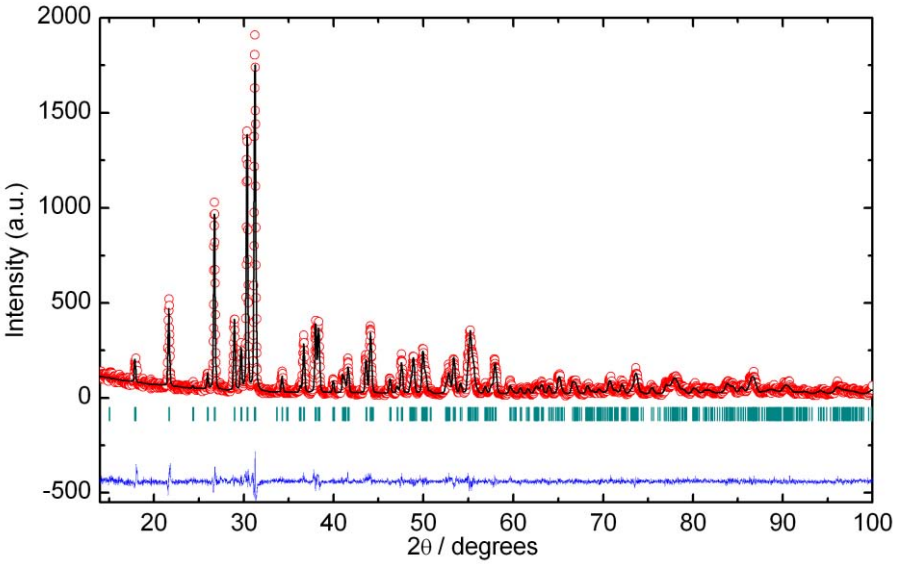

Figure 3. 5. Observed and calculated powder X-ray diffraction patterns for $LaBaSiO_3N$.

Table 3. 4. Atomic coordinates, cation and anion occupancies of $LaBaSiO_3N$ from the refinement to X-ray powder diffraction data .[(a)]

Site	Wyckoff position	x	y	z	Occupation factor
La1/ Ba1	4c	0.25	0.6593(3)	0.5782(3)	0.196(3)/0.804
La2/ Ba2	4c	0.25	0.0043(4)	0.30391(19)	0.804/ 0.196
Si	4c	0.25	0.2194(14)	0.5828(12)	1
O1/N1	4c	0.25	0.996(3)	0.5663(17)	1/0
O2/N2	4c	0.25	0.319(4)	0.436(2)	0.55/0.45
O3/N3	8d	0.019(3)	0.289(2)	0.6652(19)	0.73/0.27

(a) Estimated standard deviations in parentheses are shown once for each independent variable. La/Ba and O/N occupation factors were refined subject to the ideal stoichiometry. Refined isotropic B-factors were 0.61(9) $Å^2$ for La/Ba atoms, 0.32(14) $Å^2$ for silicon and 1.54(7) $Å^2$ for anions.

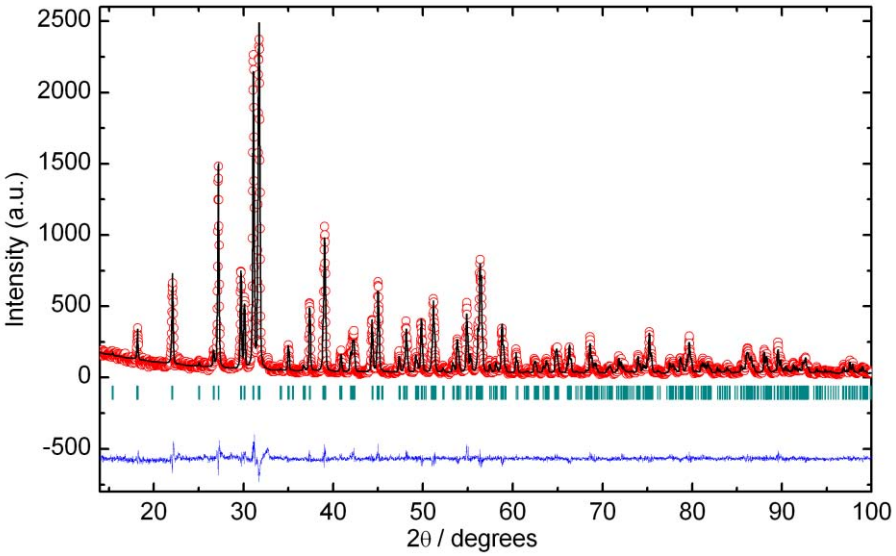

Figure 3. 6. Observed and calculated powder X-ray diffraction patterns for $LaEuSiO_3N$.

Table 3. 5 Atomic coordinates, cation and anion occupancies for $LaEuSiO_3N$ from the refinement of X-ray powder diffraction data.[(a)]

Site	Wyckoff position	x	y	z	Occupation factor
La1/ Eu1	4c	0.25	0.6547(3)	0.5780(2)	0.188(18)/0.812
La2/ Eu2	4c	0.25	0.0067(3)	0.30338(19)	0.812/ 0.188
Si	4c	0.25	0.2203(13)	0.5826(14)	1
O1/N1	4c	0.25	0.994(3)	0.569(2)	1/0
O2/N2	4c	0.25	0.312(4)	0.430(3)	0.5/0.5
O3/N3	8d	0.015(3)	0.283(2)	0.659(2)	0.75/0.25

(a) Estimated standard deviations in parentheses are shown once for each independent variable. La/Eu occupation factors were refined subject to the ideal stoichiometry. Refined isotropic B-factors were 1.03(7) $Å^2$ for La/Eu atoms, 1.06(7) $Å^2$ for silicon and 2.6(3) $Å^2$ for anions.

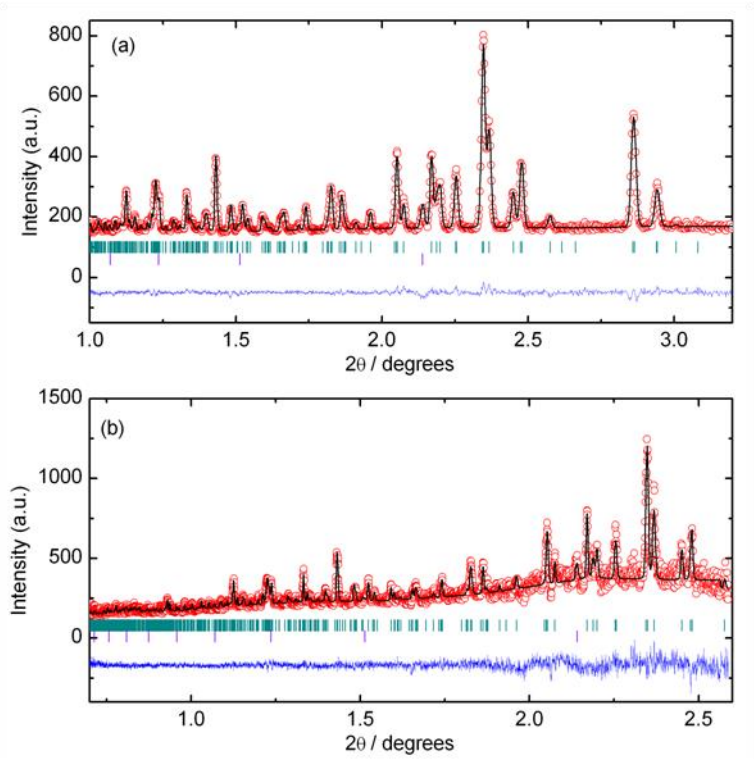

Figure 3. 7. Observed and calculated powder neutron diffraction patterns for $LaBaSiO_3N$ for data collected on the 90° detector bank (a), and backscattering detector bank (b) of HRPD.

Table 3. 6 Atomic coordinates, cation and anion occupancies for $LaBaSiO_3N$ from the refinement of neutron diffraction data. [(a)]

Site	Wyckoff position	x	y	z	Occ. Factor
La1/ Ba1	4c	0.25	0.6616(8)	0.5730(12)	0.188(7)/0.812
La2/ Ba2	4c	0.25	0.0040(8)	0.3044(5)	0.812/ 0.188
Si	4c	0.25	0.2236(11)	0.5812(16)	1
O1/N1	4c	0.25	0.0029 (9)	0.5659(9)	1/0
O2/N2	4c	0.25	0.3202(11)	0.4269(10)	0.542(14)/ 0.458
O3/N3	8d	0.0094(12)	0.2895(5)	0.6643(5)	0.729/0.271

(a) Estimated standard deviations in parentheses are shown once for each independent variable. La/Ba and O/N occupation factors were refined subject to the ideal stoichiometry. Refined isotropic B-factors were 0.61(9) $Å^2$ for La/Ba atoms, 0.32(14) $Å^2$ for silicon and 1.54(7) $Å^2$ for anions.

Table 3. 7. Crystallographic and refinement data for $LaSrSiO_3N$, $LaEuSiO_3N$ and $LaBaSiO_3N$

	$LaSrSiO_3N$	**$LaEuSiO_3N$**	**$LaBaSiO_3N$**	**$LaBaSiO_3N$**
Radiation	X-Ray Cu k_α	X-Ray Cu k_α	Neutron	X-Ray Cu k_α
T(K)	298	298	298	298
Space group	Pmnb	Pmnb	Pmnb	Pmnb
a(Å)	5.64362(14)	5.63246(14)	5.733(4)	5.73243 (15)
b(Å)	7.10719(17)	7.11675(18)	7.316(5)	7.31526 (17)
c(Å)	9.8062(2)	9.7998(2)	9.902(7)	9.9001 (2)
V(Å^3)	393.329(16)	392.825(17)	415.3(5)	415.154(18)
N_p, N_{irefl}[(a)]	4751, 264	4751, 240	1911, 281	4267, 263
P_p, P_i, P_g[(b)]	9, 17, 8	9, 15, 8	14, 18, 11	8, 17, 8
R_{Bragg}, R_f, χ^2	5.37, 4.52, 1.67	6.24, 4.62, 1.70	5.30, 4.4, 1.71	6.04, 4.06, 1.49
R_p, R_{wp}, R_{ex}[(c)]	9.65, 13.2, 14.9	9.19, 12.2, 9.36	2.43, 2.69, 2.06	10.7, 14.3, 11.7

(a) N_p, N_{irefl} refer to the number of experimental points and independent reflections.
(b) P_p, P_i, P_g, refer to the number of profile, intensity-affecting and global refined parameters, respectively.
(c) Conventional Rietveld R-factors (R_p, R_{wp} , R_{exp}) in %.

Table 3. 8. Bond Valence Sums (BVS) for $LaMSiO_3N$ compounds

Site	**$LaSrSiO_3N$**	**$LaBaSiO_3N$**	**$LaEuSiO_3N$**
La1/ M1	2.05(3)/1.69(2)	1.71(1)/2.35(2)[a]	2.02(4)/1.88(3)
La2/ M2	2.98(5)/2.44(3)	2.74(2)/3.78(3)[a]	2.96(5)/1.97(7)
Si	4.36(8)	3.86(5)	4.5(1)
O1	1.98(5)	2.04(3)	1.97(7)
O2/N2	2.13(7)/2.96(9)	2.03(4)/3.02(6)	2.10(9)/3.1(1)
O3/N3	2.03(4)/2.85(6)	1.99(3)/2.95(4)	2.14(6)/3.15(8)

(a) Deviations of BVS with respect to the formal charges of the cations for these sites are larger because of the mixed occupation and the differences between the ionic radii of Ba^{2+} and La^{3+}.

Table 3. 9. Bond distances and cell parameters for $LaSrSiO_3N$, $LaEuSiO_3N$, $LaBaSiO_3N$ (this work) and related silicates with β-K_2SO_4 structure.[(a)]

	$LaSrSiO_3N$	**Sr_2SiO_4**	**$LaEuSiO_3N$**	**Eu_2SiO_4**	**$LaBaSiO_3N$**	**Ba_2SiO_4**
M1-X1	2.397(14)	2.380(9)	2.42(2)	2.416(19)	2.500(9)	2.640(7)
M1-X2	2.79(2)	2.775(7)	2.84(3)	2.83(2)	2.920(12)	3.083(7)
M1-X2 (x2)	2.8326(18)	2.846(6)	2.827(3)	2.838(1)	2.870(2)	2.915(7)
M1-X3 (x2)	3.055(13)	3.019(7)	3.063(15)	3.013(11)	3.166(8)	3.174(7)
M1-X3 (x2)	2.998(17)	2.985(7)	3.038(19)	2.997(12)	3.036(12)	3.060(7)
M1-X3 (x2)	2.843(17)	2.849(6)	2.796(19)	2.821(12)	2.857(12)	2.904(7)
Average	**2.868**	**2.855**	**2.869(16)**	**2.858**	**2.928**	**2.983**
M2-X1	2.575(17)	2.602(9)	2.61(2)	2.607(17)	2.589(10)	2.846(7)
M2-X1 (x2)	3.096(7)	3.111(3)	3.081(8)	3.095	3.141(5)	3.114(7)
M2-X2	2.54(2)	2.623(7)	2.50(3)	2.57(2)	2.610(10)	2.699(7)
M2-X2	2.72(2)	2.622(8)	2.67(3)	2.646(19)	2.657(11)	2.759(7)
M2-X3 (x2)	2.591(12)	2.617(7)	2.572(15)	2.609(11)	2.630(7)	2.755(7)
M2-X3 (x2)	2.488(14)	2.507(6)	2.544(17)	2.503(12)	2.533(7)	2.686(7)
Average	**2.687**	**2.702**	**2.685(14)**	**2.693**	**2.718**	**2.824**
Si-X1	1.623(16)	1.612(9)	1.62(2)	1.578(19)	1.622(11)	1.614(7)
Si-X2	1.60(2)	1.635(8)	1.63(3)	1.60(2)	1.682 (18)	1.652(7)
Si-X3 (x2)	1.632(15)	1.616(6)	1.585(19)	1.615(13)	1.677(10)	1.632(7)
a (Å)	5.6436(14)	5.682(1)	5.63246	5.665(2)	5.733(4)	5.805(1)
b(Å)	7.10719(17)	7.090(1)	7.11675	7.137(3)	7.316(5)	7.499(1)
c(Å)	9.8062(2)	9.773(2)	9.7998	9.767(3)	9.902(7)	10.200(3)
V ($Å^3$)	393.329(16)	393.7	392.825	396	415.3(5)	444.02

(a) From powder X-ray diffraction data for $LaSrSiO_3N$ and $LaEuSiO_3N$, powder neutron diffraction data for $LaBaSiO_3N$ and single crystal X-ray diffraction for Sr_2SiO_4 (Catti, M.; Gazzoni, G.; Ivaldi, G.; Zanini, G. *Acta Cryst.* **1983**, *B39*, 674-679), Eu_2SiO_4 (Marchand, R.; l'Haridoon, P.; Laurent, Y. *J. Solid State Chem.* , **1978**, 24, 71-76) and Ba_2SiO_4 (Grosse, H-P; Tillmanns, E. *Cryst. Struct. Comm.* **1974**, *3*, 599-602.).

3.3.3.2 Crystal structure determination of members of the solid solution $Sr_{2-x}La_xSiO_{4-x}N_x$ (0≥x≥1) from synchrotron X-ray powder diffraction

Room temperature synchrotron X-ray diffraction data of $Sr_{2-x}La_xSiO_{4-x}N_x$ (x = 0, 0.2, 0.3, 0.5, 1.0) were refined in the *Pmnb* space group. Synchrotron data were recorded on the 11-BM instrument at the Advanced Photon Source (APS), Argonne National Laboratory using λ= 0.458996 Å. Rietveld refinements were performed using Fullprof program. The profile function used was a neutron time of flight convolution pseudo-Voigt with back-to-back exponential functions with an additional anisotropic strain broadening model (Laue class: *mmm*). The refinement results are shown in **Figure 3. 8**, **Table 3. 10** and **Table 3. 11**. Atomic coordinates, cation and anion occupancies for $La_{0.5}Sr_{1.5}SiO_{3.5}N_{0.5}$ are given in **Table 3. 10.** Refined cell parameters and general refinement agreement factors of all members of the solid solution are given in **Table 3. 11.** Refinement of La occupancies for samples with x=0.2, 0.3 led to negative values for site M1, and the relative La content in each cation site was fixed to that refined in the sample with x=0.5. For x=0.5 the refined occupancies obtained by fixing the ratio of La:Sr to the nominal stoichiometries were 0.054(9) and 0.446 for La at sites 1 and 2 respectively. In agreement with laboratory X-ray diffraction results this cation distribution shows a preferential occupation of La^{3+} with smaller ionic radius than Sr^{2+} of the CN=9 site. Anion occupancies for sites X1, X2 and X3 were fixed according to those found for $LaBaSiO_3N$ from neutron diffraction. Considering the coordination of M1 (3 X2, 6 X3, 1 X1) and M2 (2 X2, 4 X3, 3 X1) the anion distributions found in the two polyhedra of the barium compound were [M1 $O_{6.7}$ $N_{3.3}$] and [M2 $O_{6.8}$ $N_{2.2}$] which corresponds to an average N/O ratio larger for M1 than for M2

(N/O= 0.49 and 0.32 respectively).[79] In the solid solution $Sr_{2-x}La_xSiO_{4-x}N_x$ ($0 \leq x \leq 1$) the transition from the monoclinic *P2₁/n* symmetry of β-Sr_2SiO_4 polymorph to the orthorhombic *Pmnb* α', β-K_2SO_4 phase is observed for x =0.2. It has been reported that this polymorph can be stabilized by doping with a large cation as Ba^{2+} or with Eu^{2+}.[189, 190] Here we show that the concomitant introduction of La/N also stabilizes the low temperature polymorph. This is a consequence of the increase of bond valence sums of the cations induced by nitriding. The bond valence sums [32, 33,80] for Sr at this site are 1.78 for β-Sr_2SiO_4 and 1.58 for α'-Sr_2SiO_4[79, 80] whereas in the solid solution $Sr_{2-x}La_xSiO_{4-x}N_x$ it increases up to 1.69 (for $LaSrSiO_3N$). In the β form of Sr_2SiO_4 the Sr(1) atoms are shifted with respect to the α' phase where they are placed at a mirror plane and are largely underbonded to the oxygen atoms (Bond valence sums (BVS) = 1.58 in α' form *vs* 1.78 in β form). [189, 190] The α' form shows an incommensurate superstructure related to the tilting of SiO_4 tetrahedra that improves the bond valence of Sr(1) atoms.[195]

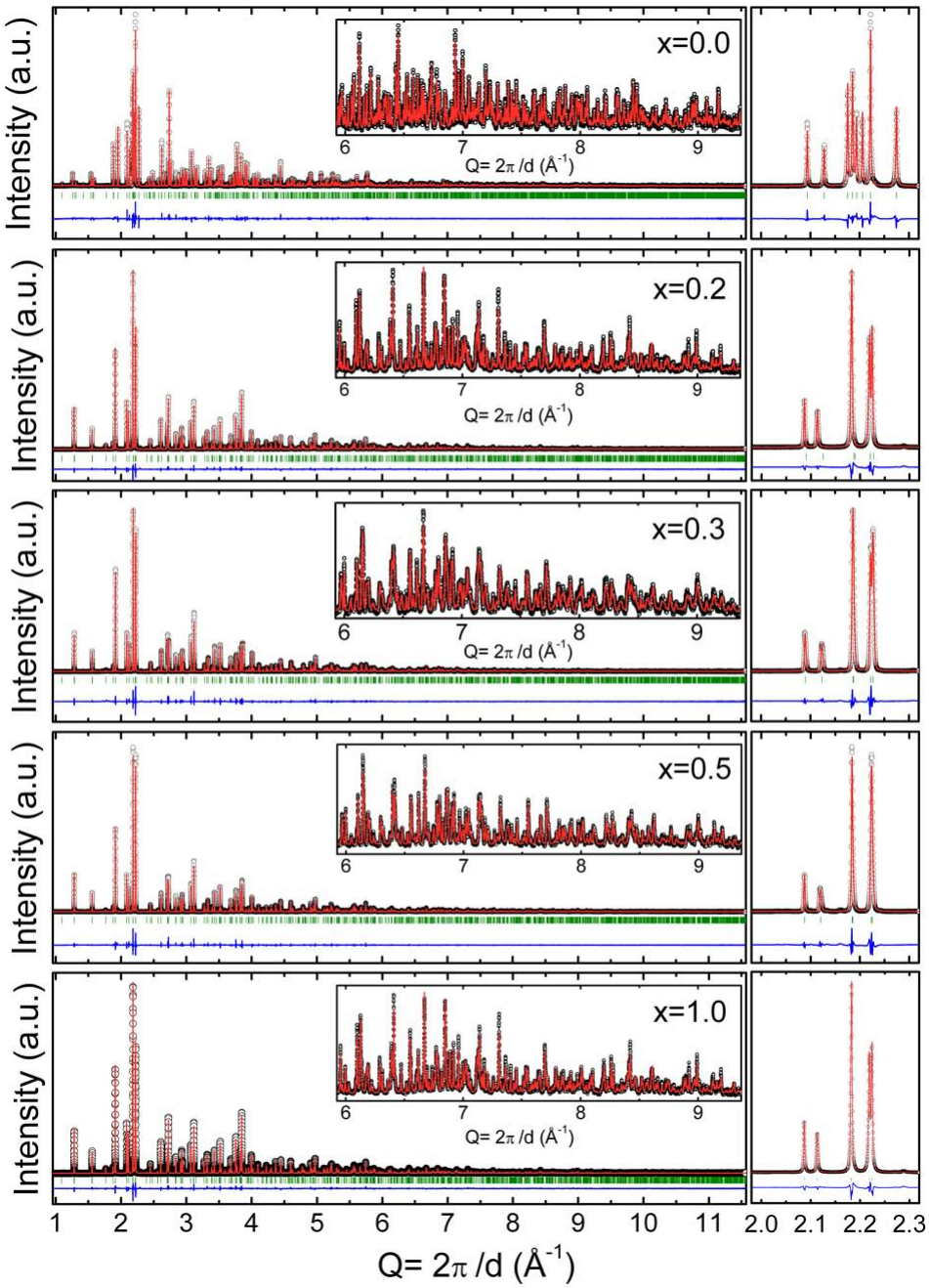

Figure 3. 8. Observed and calculated synchrotron X-ray powder diffraction patterns for $La_xSr_{2-x}SiO_{4-x}N_x$.

Table 3. 10. Atomic coordinates and occupancies for $La_{0.5}Sr_{1.5}SiO_{3.5}N_{0.5}$[a, b]

Site	Wyckoff position	x	y	z	Occupation factor
La1/Sr1	4c	0.25	0.65753(7)	0.4175(3)	0.054(9)/0.946
La2/Sr2	4c	0.25	0.00547(7)	0.42182(6)	0.446/0.554
Si	4c	0.25	0.2214(2)	0.69664(5)	1
O1/N1	4c	0.25	0.9950(5)	0.4343(4)	1/0
O2/N2	4c	0.25	0.3309(8)	0.5695(5)	0.5/0.5
O3/N3	8c	0.0124(5)	0.2864(4)	0.3380(4)	0.75/0.25

(a) La/Sr occupation factors were refined subject to the ideal stoichiometry.

(b) Refined isotropic B-factors were 0.83(3) Å^2 for Silicon, 2.06(9) Å^2 for O2/N2 and 1.74(7) Å^2 for O3/N3. Temperature factors were refined anisotropically for La/Sr and O1/N1. Resulting equivalent B-factors were 1.29 Å^2, 0.99 Å^2 and 2.95 Å^2 for La1/Sr1, La2/Sr2, Si and O/N, respectively.

Table 3. 11. Crystallographic and refinement data from synchrotron X-ray diffraction data (λ=0.458996 Å, T=298 K) for $La_xSr_{2-x}SiO_{4-x}N_x$ (x= 0.0, 0.2, 0.3, 0.5, 1.0) .

	β-Sr_2SiO_4	**$La_{0.2}Sr_{1.8}SiO_{3.8}N_0$**	**$La_{0.3}Sr_{1.7}SiO_{3.7}N_{0.3}$**
Space group	$P2_1/n$	Pmnb	Pmnb
a(Å)	7.08084(1)	7.09415(1)	7.10138(1)
b(Å)	5.66127(1)	5.65855(1)	5.65447(1)
c(Å)	9.75581(1)	9.75909(2)	9.76414(2)
β(°)	92.65152(8)		
V(Å^3)	390.658(1)	391.756(1)	392.075(1)
N_p, N_{irefl}[a]	34500, 2617	34500, 1394	34500, 1403
P_p, P_i, P_g[b]	17, 63, 7	13, 24, 39	15, 24, 6
R_{Bragg}, R_f, χ^2	5.0, 3.0, 1.43	4.16, 5.06, 1.38	4.88, 4.81, 2.01
R_p, R_{wp}, R_{ex}	9.20, 13.6, 11.34	9.51, 13.0, 11.13	8.98, 13.3, 9.45

	$La_{0.5}Sr_{1.5}SiO_{3.5}N_{0.5}$	**$LaSrSiO_3N$**
Space group	Pmnb	Pmnb
a(Å)	7.11001(1)	7.115473(5)
b(Å)	5.65225(1)	5.649858(5)
c(Å)	9.77777(2)	9.81723(1)
V(Å^3)	392.945(1)	394.666(1)
N_p, N_{irefl}[a]	34500, 1400	34500, 1435
P_p, P_i, P_g[b]	15, 29, 7	13, 26, 7
R_{Bragg}, R_f, χ^2	4.15, 3.6, 2.70	3.43, 3.88, 1.37
R_p, R_{wp}, R_{ex}	9.79, 14.4, 8.73	5.98, 9.38, 8.02

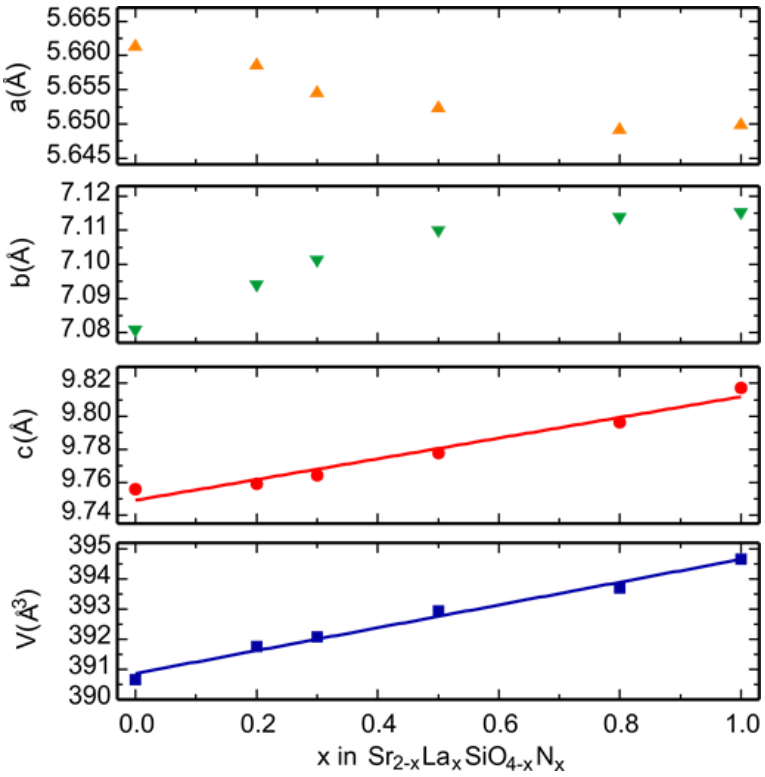

Figure 3. 9. Refined parameters from synchrotron X-ray powder diffraction data of $Sr_{2-x}La_xSiO_{4-x}N_x$ samples as a function of La/N content. The parameters of sample with x=0.8 were obtained from laboratory X-ray diffraction data.

Figure 3. 9 shows the variation of the refined cell parameters and unit cell volumes with La/N contents. The effect of the substitution of Sr and O by La and N respectively is stronger on the b and c axes. Both parameters as well as the cell volume increase with x showing that the increase of N^{3-} with larger ionic radius than O^{2-} (rO^{2-} = 1.38 Å (CN IV); rN^{3-} = 1.46 Å (CN IV))[11] outweighs the introduction of La^{3+} which is smaller than Sr^{2+}.

Figure 3. 10 shows the variation on x of the bond valence sums (BVS) and other structural parameters for sites M1 and M2.

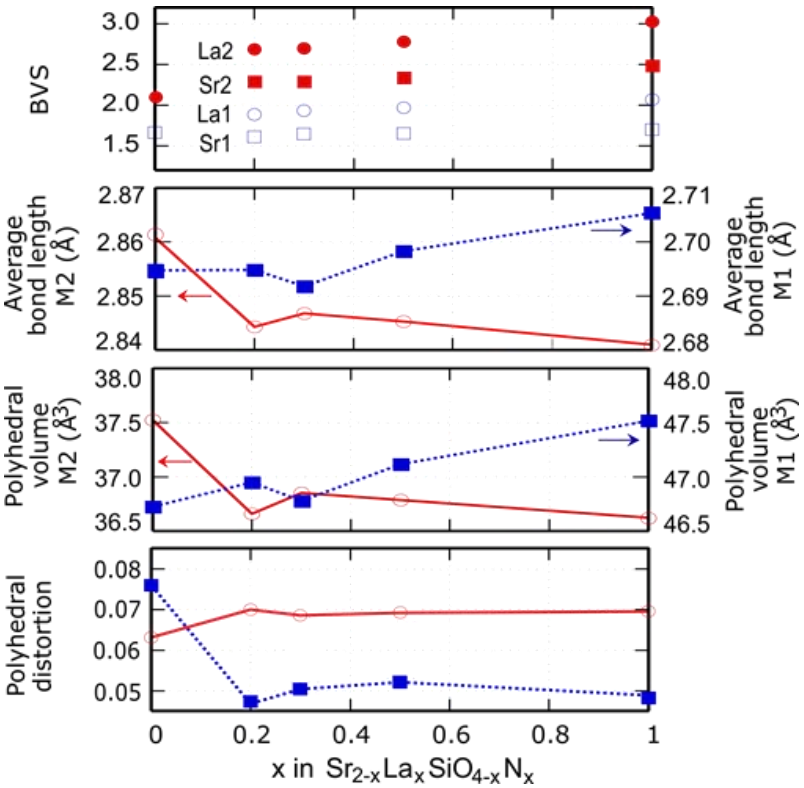

Figure 3. 10. Bond valence sums, average bond distances and polyhedral volumes and distortions of sites M1 (blue points, dotted line) and M2 (red points, solid line) in $Sr_{2-x}La_xSiO_{4-x}N_x$.

The major changes observed between x=0 and x=0.2 in bond lengths of M2 site, polyhedral distortion and polyhedral volume are a consequence of the change in symmetry from monoclinic (β' phase) to orthorhombic (α' phase). The average bond length and the polyhedral volume in site M1 increase with x as a consequence of the effect of nitriding that overcompensates the contraction induced by the substitution of Sr^{2+} by the smaller La^{3+}. In M2 site the reduction in the polyhedral volume with

increasing x is caused by the large proportion of La^{3+} (75 % for x=1) which is more important than the expansion caused by the introduction of N^{3-}.

3.3.3.3 X-ray diffraction patterns of Eu^{2+} or Ce^{3+} doped $LaMSiO_3N$ (M=Sr, Ba), $Sr_{2-x}La_xSiO_{4-x}N_x$ (0≥x≥1) and $NdMSiO_3N$ (M=Sr, Eu)

The host materials $LaMSiO_3N$ (M=Sr, Ba) and $Sr_{2-x}La_xSiO_{4-x}N_x$ (0≥x≥1) were doped with Eu^{2+} or Ce^{3+} active ions. **Figure 3. 11** and **Figure 3. 12** show the X-ray diffraction patterns of the samples with compositions $LaM_{1-x}Eu_xSiO_3N$ (x=0, 0.01, 0.02, 0.05, 0.1) (M=Sr, Ba), $La_{1-x}Ce_xSrSiO_3N$ (x=0, 0.01, 0.02, 0.05, 0.1), $LaEuSiO_3N$, $NdEuSiO_3N$ and $NdSrSiO_3N$. **Figure 3. 13** and **Figure 3. 14** show the X-ray diffraction patterns of Eu^{2+} or Ce^{3+} doped samples: $Sr_{1.98-x}Eu_{0.02}La_xSiO_{4-x}N_x$ (x = 0, 0.2, 0.3, 0.5, 1) and $Sr_{2-x}La_{x-0.02}Ce_{0.02}SiO_{4-x}N_x$ (x = 0.2, 0.3, 1). Except for the pattern of the compound $NdSrSiO_3N$ which showed one small unindexed peak at 2θ c.a 32.5 ° all samples were single phase and crystallized in the α' polymorph.

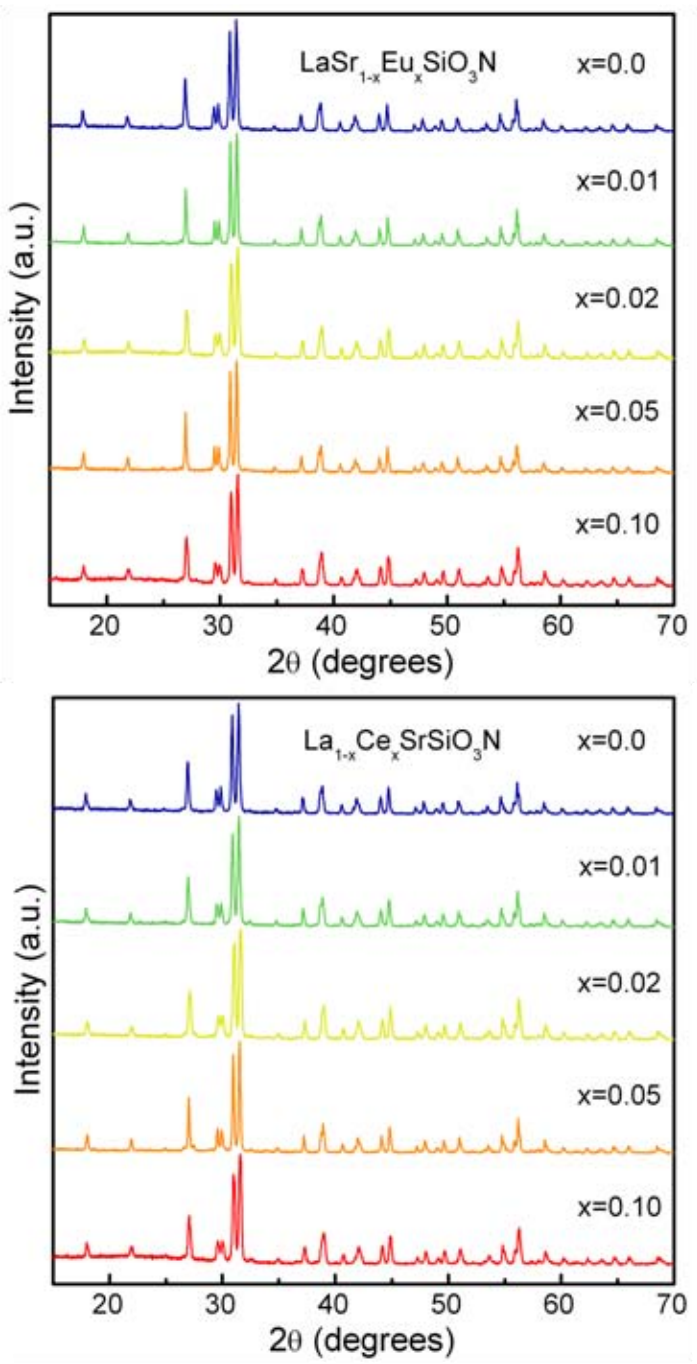

Figure 3. 11. X-ray powder diffraction patterns of $LaSr_{1-x}Eu_xSiO_3N$ (top) and $La_{1-x}Ce_xSrSiO_3N$ (bottom) with (x=0.0, 0.01, 0.02, 0.05, 0.1).

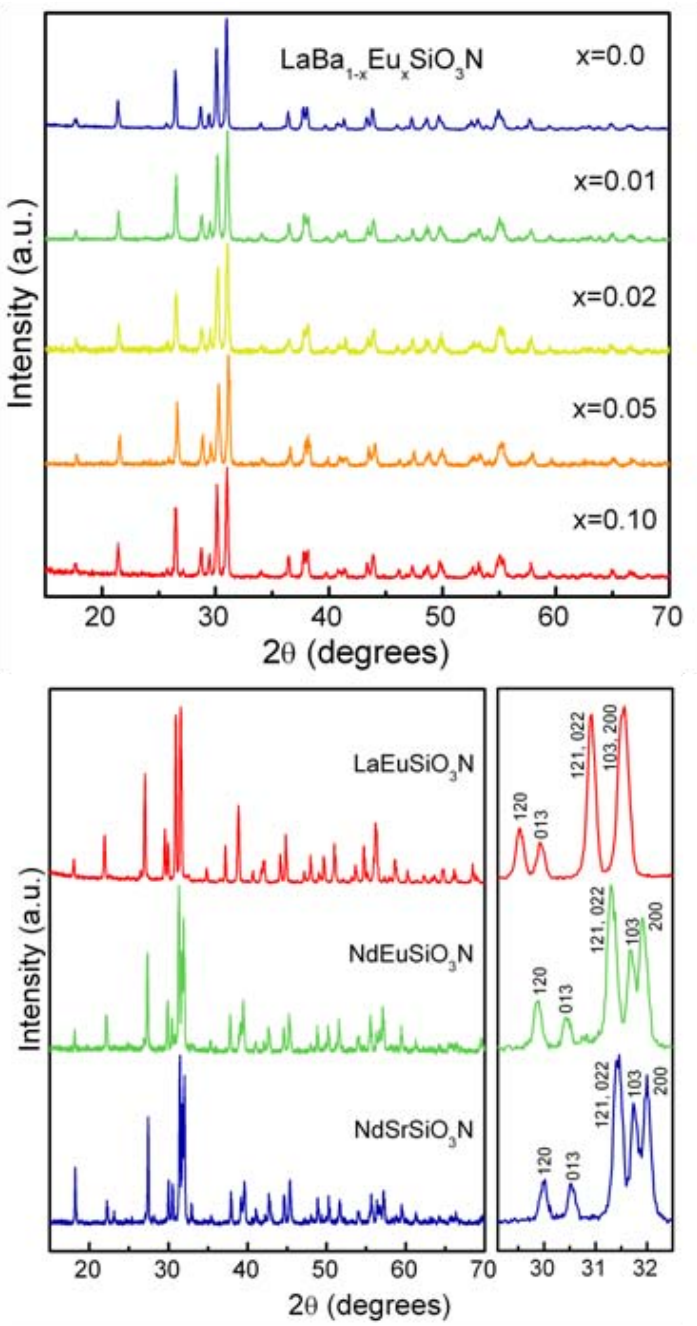

Figure 3. 12. X-ray powder diffraction patterns of $LaBa_{1-x}Eu_xSiO_3N$ (top) with (x=0.0, 0.01, 0.02, 0.05, 0.1) and $LnMSiO_3N$ (bottom) with (M=Sr, Eu; Ln=La, Nd).

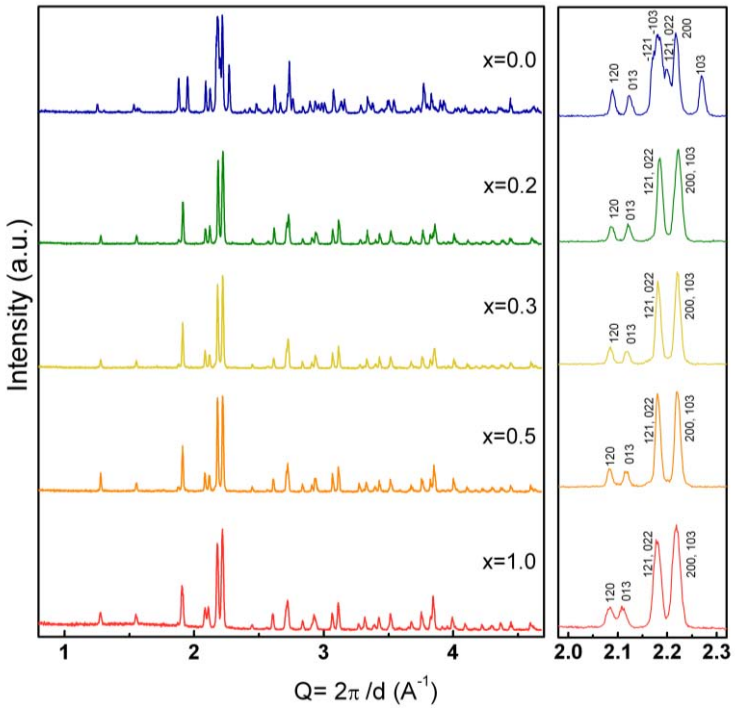

Figure 3. 13. X-ray powder diffraction patterns for $Sr_{1.98-x}Eu_{0.02}La_xSiO_{4-x}N_x$ (0≥x≥1) and enlarged areas of the intense reflections around Q=2 $Å^{-1}$ region.

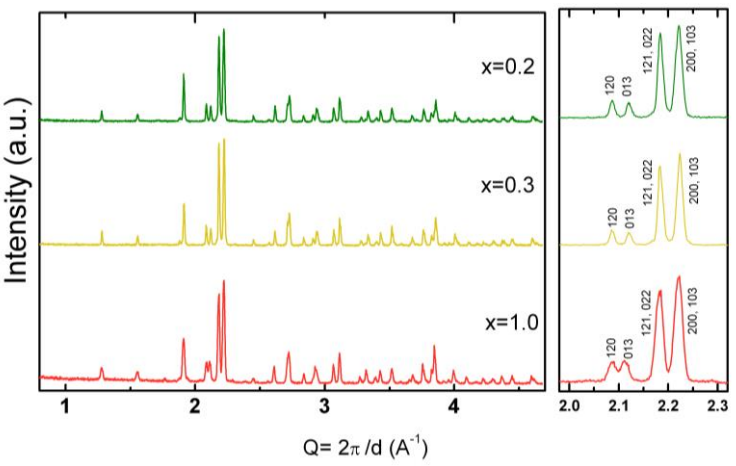

Figure 3. 14. X-ray powder diffraction patterns for $Sr_{2-x}La_{x-0.02}Ce_{0.02}SiO_{4-x}N_x$ (0≥x≥1) and enlarged areas of the intense reflections around Q=2 $Å^{-1}$ region.

3.3.3.4 Electron diffraction study of Sr_2SiO_4 and $LaMSiO_3N$ (M=Sr, Ba, Eu)

Figure 3. 15 shows electron diffraction micrographs obtained by rotating a crystal of $LaSrSiO_3N$ around the b* axis, together with the reconstruction of the reciprocal lattice and indexing of crystallographic planes. The obtained cell parameters are a= 5.56, b= 7.12 and c= 9.7 Å with extinction conditions h0l, h+l=2n+1; hk0, k=2n+1; h00, h=2n+1; 0k0, k=2n+1 and 00l, l=2n+1. These are compatible with the space groups $P2_1nb$ ($n^0$33) and *Pmnb* ($n^0$62), which corresponds to the structural model used in the Rietveld refinements.

Figure 3. 16 shows the observed electron diffraction patterns along the zone axes [001]*, [010]* and [001]* for individual crystals of Sr_2SiO_4, $LaSrSiO_3N$, $LaBaSiO_3N$ and $LaEuSiO_3N$. The reconstruction of the reciprocal lattices lead to the following parameters: Sr_2SiO_4 a=5.73 Å, b= 7.17 Å, c= 9.79 Å and $\beta \simeq 92^o$; $LaBaSiO_3N$ a=5.75 Å, b=7.45Å and c=9.93 Å, and $LaEuSiO_3N$ a=5.62 Å, b=7.08 Å and c=9.93 Å.

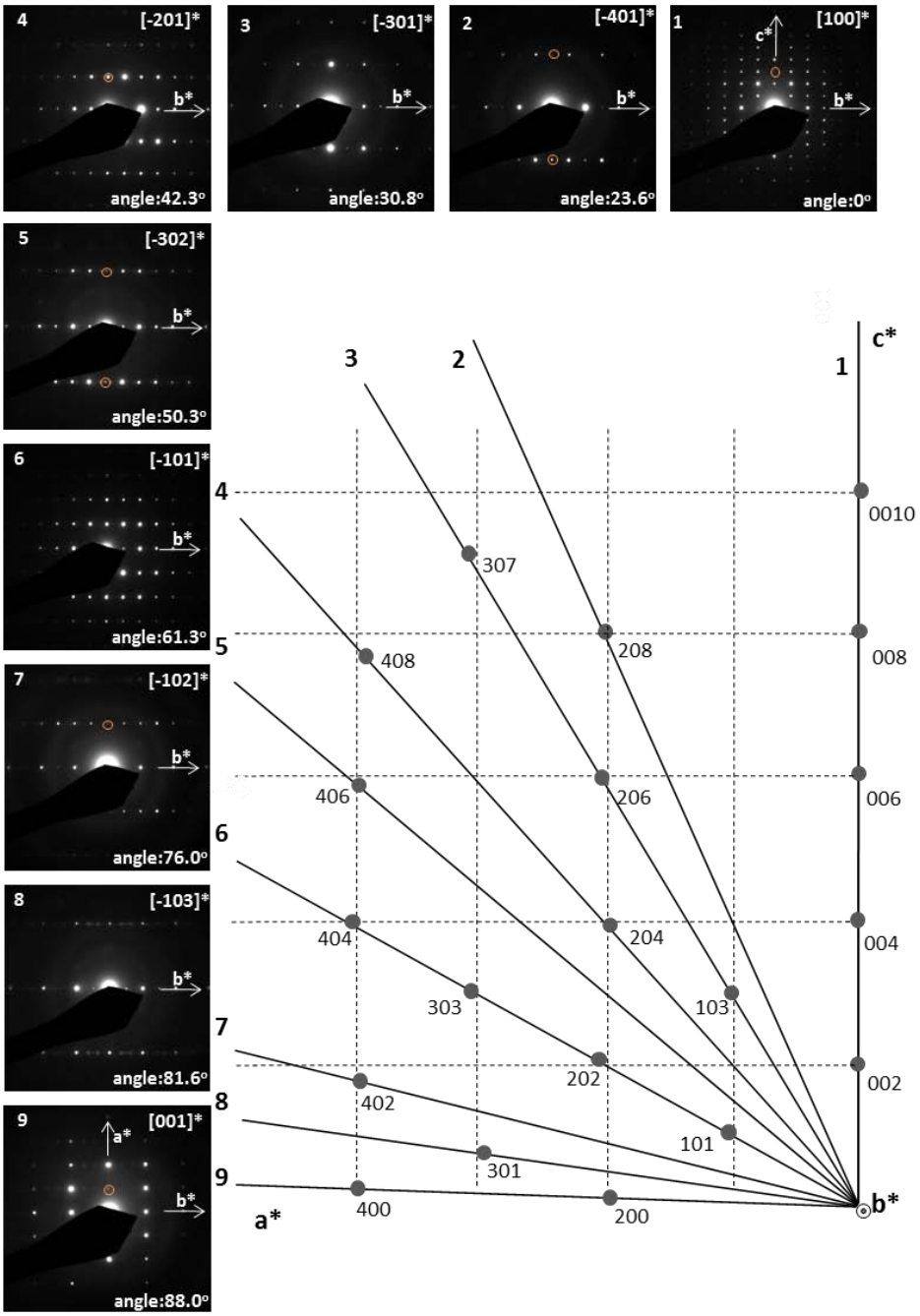

Figure 3. 15. Electron diffraction patterns, indexing and reconstruction of the reciprocal lattice along the [010]* zone axis of $LaSrSiO_3N$. Circles indicate multiple diffraction reflections.

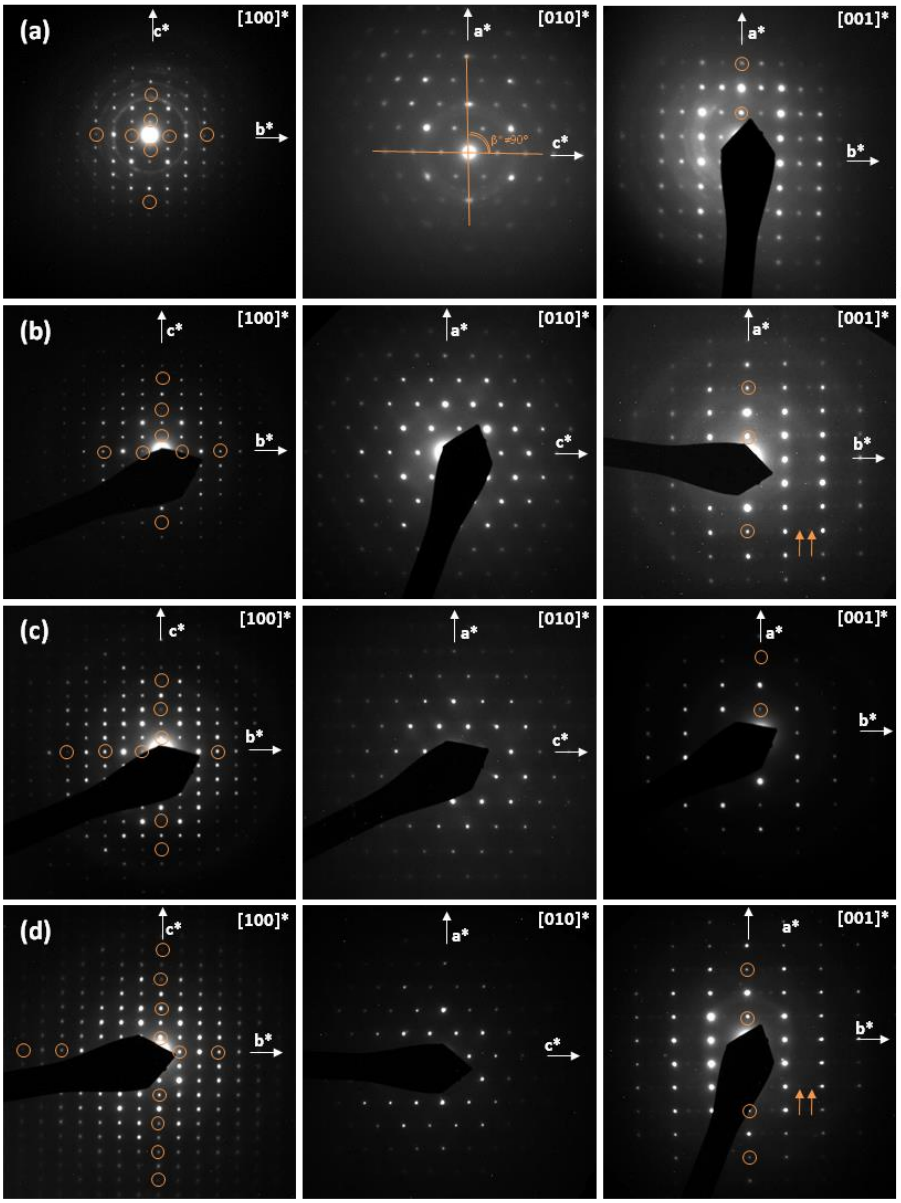

Figure 3. 16. Electron diffraction micrographs along the zone axes [100]*, [010]* and [001]* for (a) Sr_2SiO_4, (b) $LaSrSiO_3N$, (c) $LaBaSiO_3N$ and (d) $LaEuSiO_3N$. The structural modulation along b* is indicated by arrows whereas circles indicate multiple diffraction reflections.

The electron diffraction patterns of $LaSrSiO_3N$ and $LaEuSiO_3N$ showed an incommensurate superstructure along the b* axis with wave vectors q1= 0.30 b* for $LaSrSiO_3N$ and q1= 0.26 b* for $LaEuSiO_3N$. The satellite reflections are not visible in the powder X-ray diffraction patterns. Structure modulations have been also reported for the isostructural compound α'-Sr_2SiO_4, $Ba_{2-x}Ca_xSiO_4$ and Ca_2SiO_4, as well as for other compounds with β-K_2SO_4 related structures. [195, 196] In α'-Sr_2SiO_4 they have been interpreted as being a consequence of a gradual variation of the Sr(1)-O(2) lengths, thus the tilt of SiO_4 tetrahedra along a direction parallel to the modulation axis (b in the *Pmnb* space group) varies gradually and periodically.[195] The β polymorphs of Sr_2SiO_4 and Eu_2SiO_4[197] with monoclinic symmetry $P2_1/n$ show a similar but ordered tilting of the tetrahedra. In $LaEuSiO_3N$ and $LaSrSiO_3N$ the tilting axis coincides with the anion-ordering axis found in $LaBaSiO_3N$, passing through O1 and the silicon atoms. The satellite reflections are not observed in the compound $LaBaSiO_3N$ in analogy with Ba_2SiO_4 for which only the orthorhombic polymorph is known and no modulated structure has been reported.[196]

3.3.4 Photoluminescent properties

3.3.4.1 Luminescence excitation and emission spectra

3.3.4.1.1 Luminescent properties of $LaMSiO_3N$:Eu or Ce (M=Sr, Ba)

Figure 3. 17 and **Figure 3. 18** show the normalized excitation and emission spectra of $LaSr_{1-x}Eu_xSiO_3N$ and $LaBa_{1-x}Eu_xSiO_3N$ with (x=0.01, 0.02, 0.05, 0.1) and (x=0.01, 0.02, 0.05), respectively. The excitation spectra of barium and strontium compounds are similar for a given europium

content and consist of a band centred between 340 nm and 390 nm. Important band broadening extending the band up to 450 nm is observed with increasing europium concentration. The emission spectra of $LaSr_{1-x}Eu_xSiO_3N$ samples upon excitation at 405 nm consist of a broad band centred between 640 (for x = 0.01) and 675 nm (for x = 0.1), with two main components with intensities depending on the europium concentration, and wavelengths of 705 and 590 nm. The emission spectra of $LaBa_{1-x}Eu_xSiO_3N$ samples (x = 0.01, 0.02, 0.05) are similar to those of strontium compounds with no significant differences between the observed emission wavelengths for compounds with the same europium doping in the two hosts. In addition to these two bands, a shoulder is observed at ca. 520 nm in both the Sr and Ba samples. The intensity of the 705 nm band increases with increase in the europium concentration. Similar to the luminescence properties of $Sr_2SiO_4:Eu^{2+}$ and $Ba_2SiO_4:Eu^{2+}$,[182] the two components at wavelengths of 705 and 590 nm can be assigned to partially allowed electric dipole $4f^7 - 4f^6\ 5d^1$ transitions of Eu^{+2} occupying M1 and M2 crystallographic sites. Under excitation at 405 nm, the emission wavelengths for maximum intensity in Eu-doped $LaSrSiO_3N$ and $LaBaSiO_3N$ are remarkably long compared with those reported for (oxy)nitridosilicate phosphors but similar to those observed for $M_2Si_5N_8:Eu^{2+}$ (M = Ca, Sr, Ba) (λ_{em} = 623–650 nm) and $CaAlSiN_3:Eu^{2+}$ (λ_{max} = 650 nm).[77, 94, 198, 175] Compared with the europium-doped orthosilicates with β-K_2SO_4 structure Sr_2SiO_4 and Ba_2SiO_4, the emission wavelengths of the europium doped $LaMSiO_3N$ materials are red shifted from 490–570 nm to 640–675 nm (centroid).[186] This change is most likely a result of the increase in covalency induced by the substitution of one oxide by nitride in the SiX_4 tetrahedron and the increase in crystal field splitting induced by the substitution of one divalent cation by La^{3+} and one O^{2-} by N^{3-}.

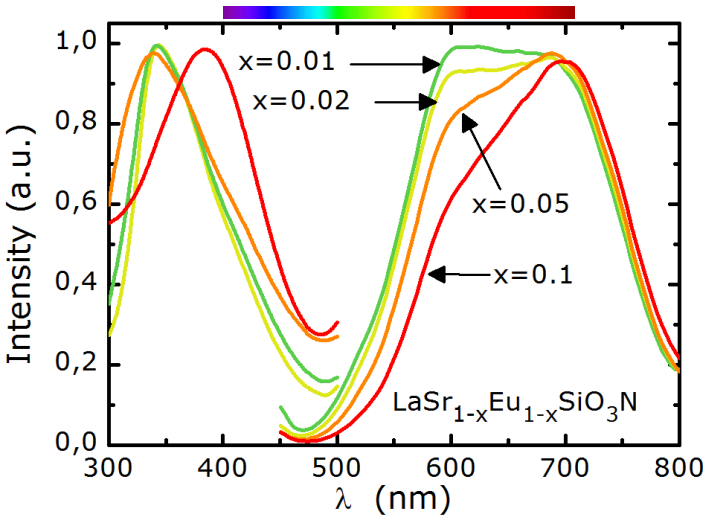

Figure 3. 17. Normalized excitation and emission spectra of $LaSr_{1-x}Eu_xSiO_3N$ (x=0.01, 0.02, 0.05, 0.1)

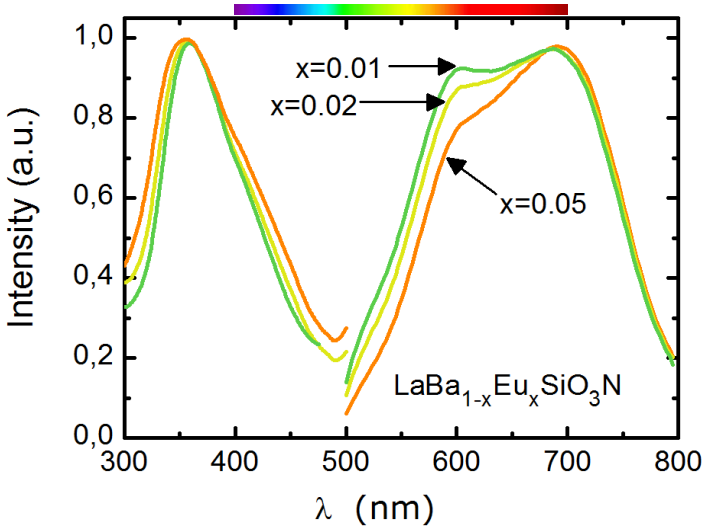

Figure 3. 18. Normalized excitation and emission spectra of $LaBa_{1-x}Eu_xSiO_3N$ (x=0.01, 0.02, 0.05)

Figure 3. 19 shows the normalized excitation and emission spectra of $La_{1-x}Ce_xSrSiO_3N$ (x = 0.01, 0.02, 0.05 and 0.1) samples. The excitation spectra

consist of broad band extending from 310 nm up to 450 nm with maximum intensity at 380 nm. The emission band shows three main components centred at 690, 580 and 520 nm, similar to the Eu^{2+}-activated samples that can be assigned to partially allowed electric dipole $4f^1 - 4f^0\ 5d^1$ transitions of Ce^{+3} occupying M1 and M2 sites. The band centred at 580 nm is more intense than the band at 690 nm, according with the preferential occupation of Ce^{3+} for one M1 site. The emission of the Ce samples is blue-shifted with respect to Eu^{2+}, in agreement with the empirical correlation reported by Dorenbos for Eu and Ce doped inorganic compounds.[199]

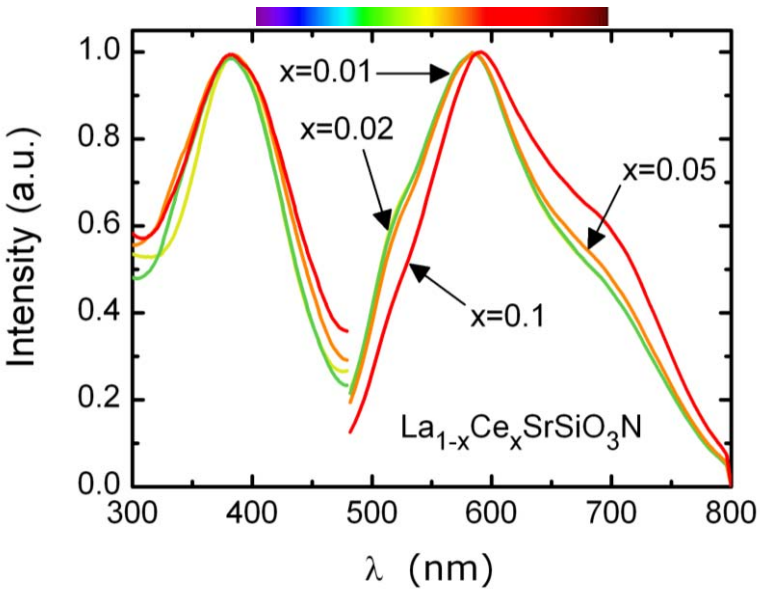

Figure 3. 19. Normalized excitation and emission spectra of $La_{1-x}Ce_xSrSiO_3N$ (x=0.01, 0.02, 0.05, 0.1).

Figure 3. 20 and **Figure 3. 21** show the photoluminescent spectra of $LaSr_{1-x}Eu_xSiO_3N$ and $La_{1-x}Ce_xSrSiO_3N$ with different Eu^{2+} and Ce^{3+} contents

(x=0.01 – 0.1), respectively. The photoluminescence intensity increases up to x=0.02, decreasing for higher doping because of concentration quenching. If we consider energy transfer between two identical centers S, the critical distance (R_c) is defined as the distance for which the transfer probability equals the emission probability of S. can be calculated It can be derived [96] with equation 3.2.

$$R_c \simeq 2\left(\frac{3V}{4\pi x_c n}\right)^{\frac{1}{3}} \tag{3.2}$$

where x_c is the critical concentration, n the number of lattice sites in the unit cell that can be occupied by activators and V is the volume of the unit cell. By taking the experimental and analytic values of V, n and x_c (394.6 $Å^3$, 8, 0.02, respectively), the critical transfer distance of Eu^{2+} and Ce^{3+} in $LaSrSiO_3N$ phosphor is 16.8 Å. This critical distance is similar to those determined for $Ba_2SiO_4:Eu^{2+}$ with R_c of 19 Å,[200] and for the standard phosphor YAG:Ce^{3+} with 18 Å.[201]

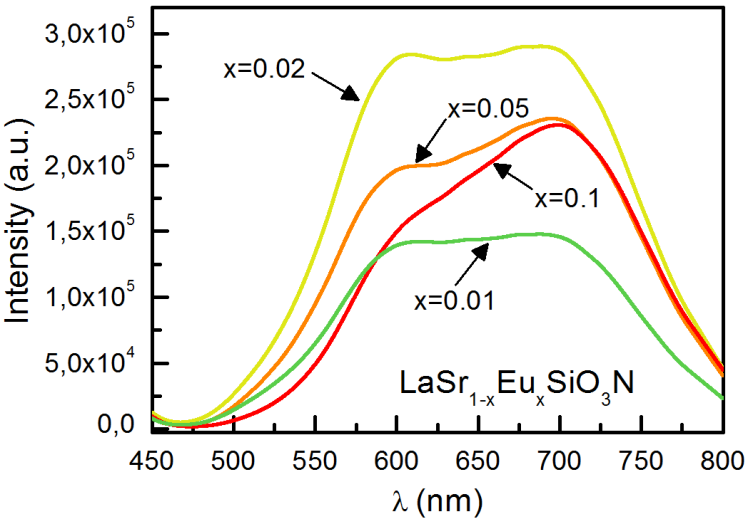

Figure 3. 20. Emission spectra of $LaSr_{1-x}Eu_xSiO_3N$ with different Eu^{2+} concentration (λ_{ex}=405 nm).

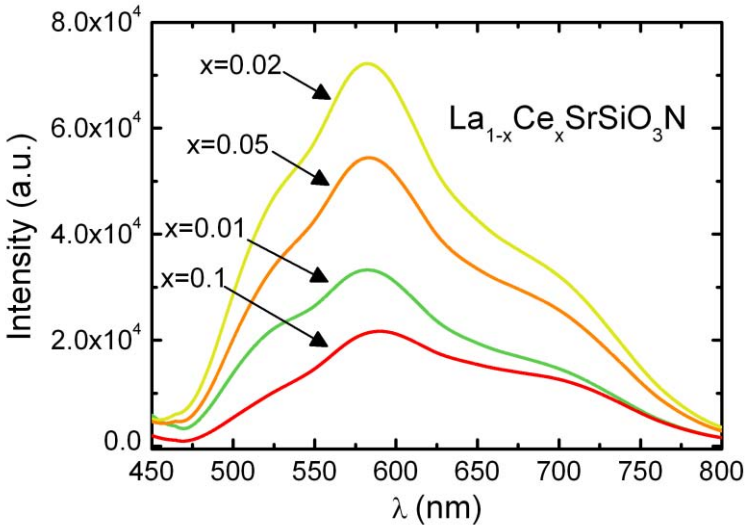

Figure 3. 21. Emission spectra of $La_{1-x}Ce_xSrSiO_3N$ with different Ce^{3+} concentration (λ_{ex}=405 nm).

3.3.4.1.2 Effect of coupled N/La introduction on the luminescent properties of $Sr_2SiO_4:Ln^{n+}$

A comparison of the excitation and emission photoluminescence spectra of the orthosilicate $Sr_2SiO_4:Eu^{2+}$ and the oxynitridosilicate $LaSrSiO_3N:Eu^{2+}$ is shown in **Figure 3. 22** The photoluminescent features of Eu^{2+} on shape and peak position remarkably change as a consequence of the coupled N/La introduction in Sr_2SiO_4.

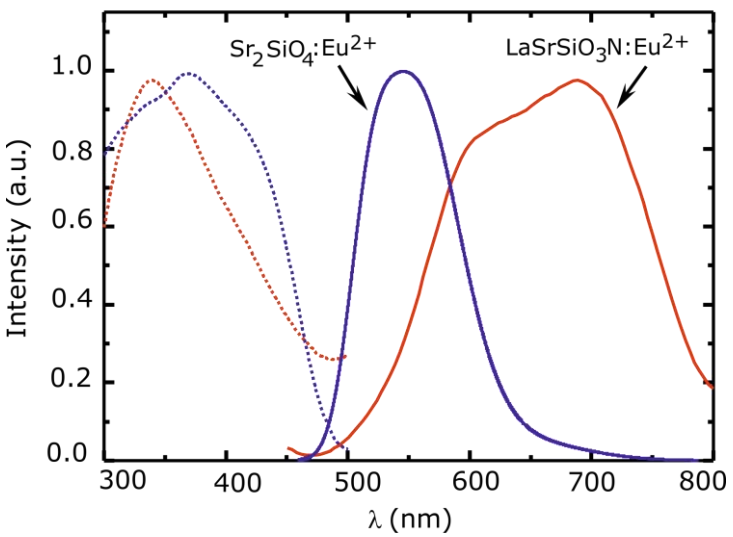

Figure 3. 22. Normalized excitation (λ_{em}=550 nm, dotted line) and emission (λ_{ex}=405 nm, solid line) spectra of $LaSr_{0.95}Eu_{0.05}SiO_3N$ and $Sr_{1.95}Eu_{0.05}SiO_4$.[22]

Under excitation with UV-blue light the emission wavelengths in $LaSr_{0.95}Eu_{0.05}SiO_3N$ are red shifted with respect to the oxide phosphor $Sr_2SiO_4:Eu^{2+}$ from ca. 550 nm to 650–700 nm.

The excitation and emission spectra of $Sr_{2-x}La_xSiO_{4-x}N_x$: Eu^{2+} samples (x=0.0, 0.2, 0.3, 0.5 and 1.0) are shown in **Figure 3. 23**. In all samples europium

content was kept constant at the photoluminescence optimum concentration (0.02 mol) as previously found in $LaSr_{1-x}Eu_xSiO_3N$. The excitation spectra collected at 550 nm consist of a broad band centred between 350 nm (for x=1) and 375 nm (for x=0).

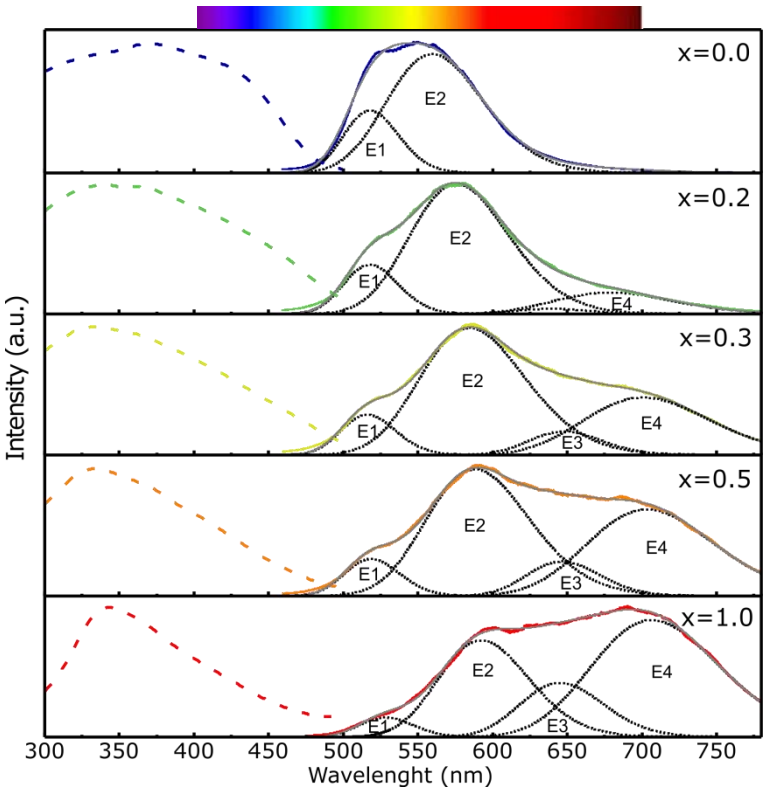

Figure 3. 23. Normalized excitation (λ_{em}=550 nm, dotted line) and emission spectra with deconvolutions (λ_{ex}=405 nm, solid line) collected at room temperature for $La_xSr_{2-x}SiO_{4-x}N_x:Eu^{2+}$ samples.

With increasing N/La content the excitation band narrows and shifts gradually towards shorter wavelengths. The observed emission upon excitation at 405 nm consists of a broad band centred between 550 nm (for x=0) and 650 nm (for x=1) with maximum intensity at c.a. 700 nm for x=1. This band can be assigned to the parity allowed $4f^65d^1 \rightarrow 4f^7$ transition of Eu^{2+} and it can be deconvoluted into two main components corresponding

to M1 and M2 sites, with longer and shorter wavelengths respectively, as in previously reported $Ba_2SiO_4:Eu^{2+}$, $Sr_2SiO_4:Eu^{2+}$ and $LaMSiO_3N:Eu$ (M=Sr, Ba). The best fits of the spectra of samples with $x \geq 0.3$ are obtained with two additional components which can be ascribed to different environments around Eu^{2+} resulting from the mixed occupation of Sr^{2+} and La^{3+} in the two crystallographic sites. The concomitant substitution of one Sr by La and one O by N in Sr_2SiO_4 produces, in addition to the red shift of the centroid of the band of ca. 100 nm, an important broadening, from fwhm = 100 nm for x = 0 to fwhm= 200 nm for x = 1. For x = 0 the band at higher energy is assigned to the M2 site and has lower intensity than the M1 band. The respective wavelengths of these bands are 518 and 560 nm. For x >0 a new component with λ between 679 and 706 nm is observed, with increasing intensity as La content increases. In our study of $LaMSiO_3N:Eu^{2+}$ (M = Sr, Ba) samples we tentatively assigned this band to M1 site, red shifted by the introduction of nitride. However the dependence of the intensity of this band with La content suggests that it is most likely due to the M2 sites occupied by the small and charged La^{3+} (75% of M2 sites in $LaSrSiO_3N$) that generates a stronger crystal field splitting than Sr^{2+}. The additional effects of covalency and large crystal field splitting caused by the introduction of nitride would induce the observed red shift of ca. 190 nm in this band with respect to $Sr_2SiO_4:Eu^{2+}$. The increase in intensity of this band is concomitant with the decrease in intensity of the band with highest energy centred between 518 nm (for x = 0) and 528 nm (for x = 1) which is assigned to the ca. 25% of M2 sites occupied by Sr^{2+}. According to this the central band at 560–590 nm would be assigned to the M1 sites occupied by Sr^{2+} (80% of M1 sites in $LaSrSiO_3N$), and a weak small component at ca. 640 nm would be due to the M1 sites occupied by La^{3+}(20% of M1 sites in $LaSrSiO_3N$). The energies of all components shift to

the red with increasing N/La substitution, as a result of the increase in covalency and the crystal field splitting. The large band broadening is most likely caused by the different N/O proportion in the M1 and M2 sites and crystal field splitting that would lead to different red-shift of the corresponding Eu^{2+} emissions. As a result of the red shift of the emission band and the blue shift of the excitation band the Stokes shift increases 175 nm from x = 0 to x = 1. All samples can be excited at near UV light (405 nm) and samples with x ≤ 0.3 can also be excited with blue (450 nm) light.

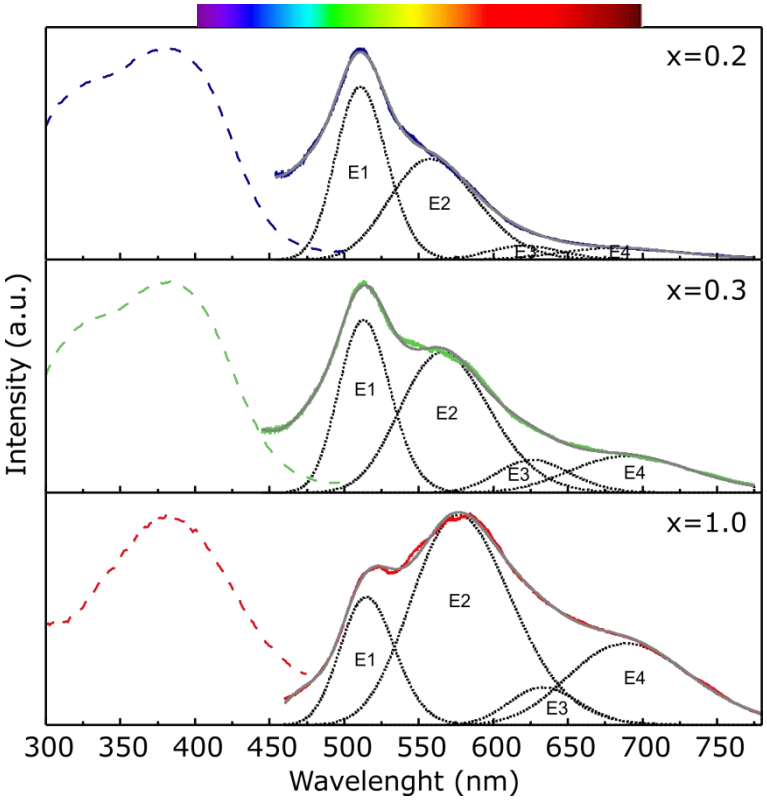

Figure 3. 24. Normalized excitation (λ_{em}=550 nm, dotted line) and emission spectra with deconvolutions (λ_{ex}=405 nm, solid line) collected at room temperature for $La_xSr_{2-x}SiO_{4-x}N_x:Ce^{3+}$ samples.

As for the Eu^{2+} activated compounds the deconvolution of emission spectra of $Sr_{2-x}La_xSiO_{4-x}N_x:Ce^{3+}$ samples (x = 0.2, 0.3, 1) (**Figure 3. 24**) show two

main components ascribed to the crystallographic sites M1 and M2 and two additional bands resulting from the mixed occupation of these sites by La^{3+} and Sr^{2+}. The range of wavelengths observed for the four components in this case are 680–690 nm, 620–633 nm, 558–577 nm and 511–515 nm with red shifting as La^{3+} content increases. Orange-red luminescence in (oxy)nitride Ce^{3+} activated compounds has been reported for $CaSiN_2$,[116] $La_3Si_6N_{11}$,[202] or $La_{10}Ge_6N_{2.46}O_{23.31}$.[58] In $Sr_{2-x}La_xSiO_{4-x}N_x:Ce^{3+}$ the observed long emission wavelengths are a consequence of the strong effect of the covalence of Ce–N bonds and crystal field splitting induced by N^{3-} enhanced by the introduction of La^{3+}. As for the samples $LaSrSiO_3N$: Ce^{3+} or Eu^{2+} the transition energies observed for both activators in a given member of the solid solution are related in agreement with the empirical correlation reported by Dorenbos for Eu^{2+} and Ce^{3+} in inorganic compounds.[199]

3.3.4.2 Diffuse reflectance spectra

3.3.4.2.1 Diffuse reflectance spectra of $LnMSiO_3N:Eu^{2+}$ or Ce^{3+} (M =Sr, Ba and Ln=La, Nd)

The body colours of $LaBaSiO_3N$ and $LaSrSiO_3N$ are white, whereas $LaEuSiO_3N$ is dark yellow. Eu or Ce doping of the alkaline earth compounds yielded pale yellow body colour samples. Diffuse reflectance spectra of the undoped $LaBaSiO_3N$ and $LaSrSiO_3N$ samples showed a drop in reflection in the UV region around 390 nm and 365 nm, respectively, whereas the onset of strong absorption for $LaEuSiO_3N$ sample is around 600 nm. (**Figure 3. 25**).

The band gaps as determined using the Kubelka–Munk function are 3.63, 3.83 and 2.35 eV for the barium, strontium and europium compounds, respectively. In addition to the host lattice absorption, diffuse reflection of

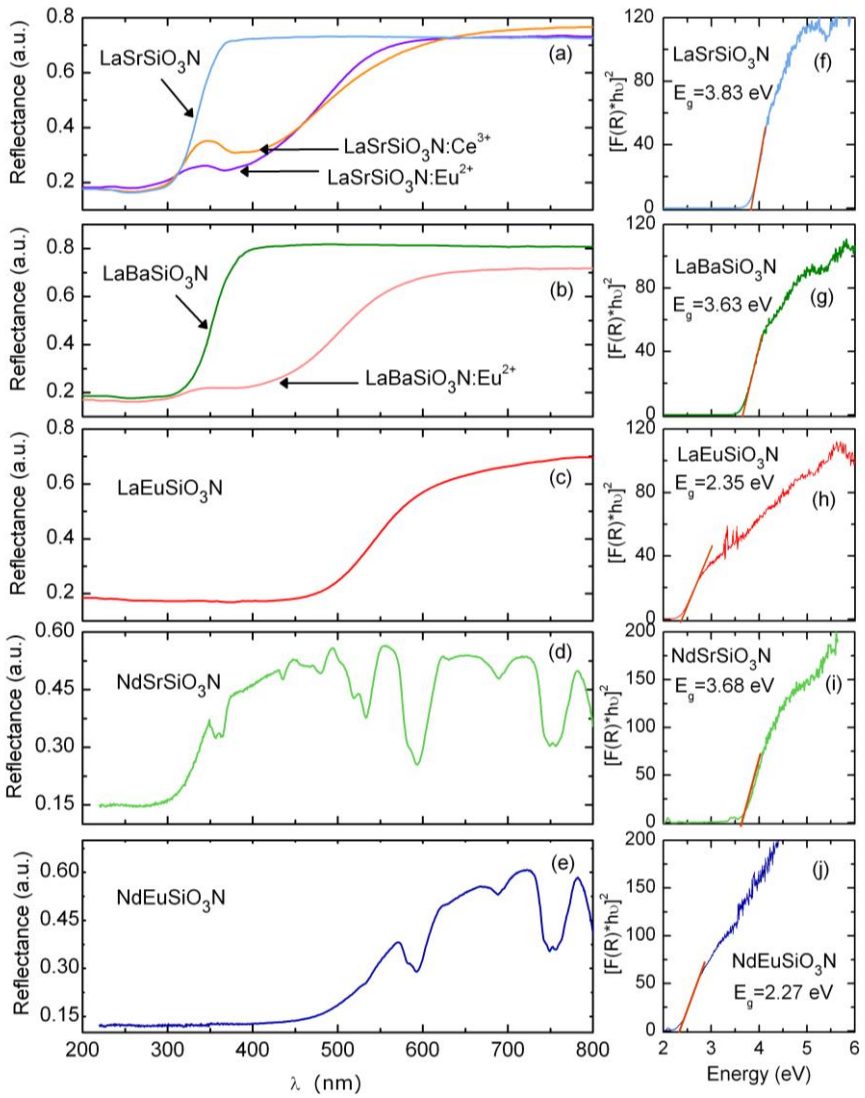

Figure 3. 25. Diffuse reflectance spectra of (a) $LaSrSiO_3N$, $La_{0.95}Ce_{0.05}SrSiO_3N$, $LaSr_{0.95}Eu_{0.05}SiO_3N$, (b) $LaBaSiO_3N$, $LaBa_{0.95}Eu_{0.05}SiO_3N$, (c) $LaEuSiO_3N$, (d) $NdSrSiO_3N$, (e) $NdEuSiO_3N$, and Kubelka-Munk plot of (f) $LaSrSiO_3N$ (g) $LaBaSiO_3N$, (h) $LaEuSiO_3N$, (i) $NdSrSiO_3N$, (j) $NdEuSiO_3N$.

$LaSr_{0.99}Eu_{0.01}SiO_3N$ shows an important absorption band in the region from 530 to 345 nm, corresponding to the $4f^7 \rightarrow 4f^6 5d^1$ transition of Eu^{2+}. $LaBa_{0.99}Eu_{0.01}SiO_3N$ shows a similar absorption band between 550 and 350 nm and $La_{0.99}Ce_{0.01}SrSiO_3N$ shows an absorption band between 580 and 350 nm, which can be assigned to the $4f^1 \rightarrow 4f^0 5d^1$ transition of Ce^{3+}. These results are consistent with the excitation spectra of the doped materials (Fig. 3.20 and 3.21). The neodymium compounds $NdSrSiO_3N$ and $NdEuSiO_3N$ showed absorption edges around 360 and 550 nm, respectively. These values are similar to those obtained for the lanthanum strontium and lanthanum europium oxynitridosilicates. Additionally, $NdSrSiO_3N$ and $NdEuSiO_3N$ exhibit several strong 4f electron transitions peaks located in the range between 350 and 800 nm. These bands are attributed to transitions between the ground-state $^4I_{9/2}$ and the excited states within the Nd^{3+} 4f shell. In particular, the most intense bands located at 530, 586 and 755 nm are ascribed to transitions from the ground state $^4I_{9/2}$ of the neodymium ion to $^2K_{18/2}$, $^4G_{7/2}$, $^4G_{9/2}$ for the peak at 530 nm, to $^4G_{5/2}$, $^2G_{7/2}$ for the peak at 586 nm and to $^4S_{8/2}$, $^4F_{7/2}$ for the peak at 755 nm.[203, 204] The E_g values estimated by means of the Kubelka-Munk method are 3.68 and 2.27 eV for the strontium and europium compounds, respectively.

3.3.4.2.2 Diffuse reflectance of the solid solution $Sr_{2-x}La_xSiO_{4-x}N_x:Eu^{2+}$ ($0 \leq x \leq 1$)

The diffuse reflection spectra of the europium doped samples in the solid solution $Sr_{2-x}La_xSiO_{4-x}N_x$ show the absorption of the host and a wide band in

the region from 300 to 500 nm corresponding to the $4f^7 \rightarrow 4f^65d^1$ transition of Eu^{2+} (**Figure 3. 26**).

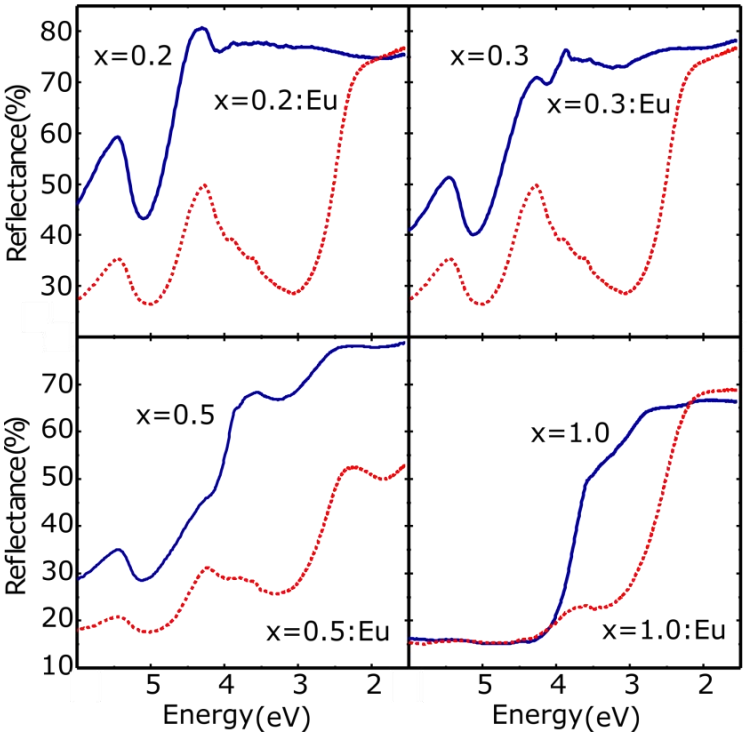

Figure 3. 26. Diffuse reflectance spectra of $Sr_{2-x}La_xSiO_{4-x}N_x$ (blue solid line) and $Sr_{2-x}La_xSiO_{4-x}N_x:Eu^{2+}$ (red dotted line) samples.

In agreement with the excitation spectra the absorption edge of the host is shifted towards lower energies with increasing x which leads to a progressive increase of the overlap between this band and the $4f^7 \rightarrow 4f^65d^1$ band.

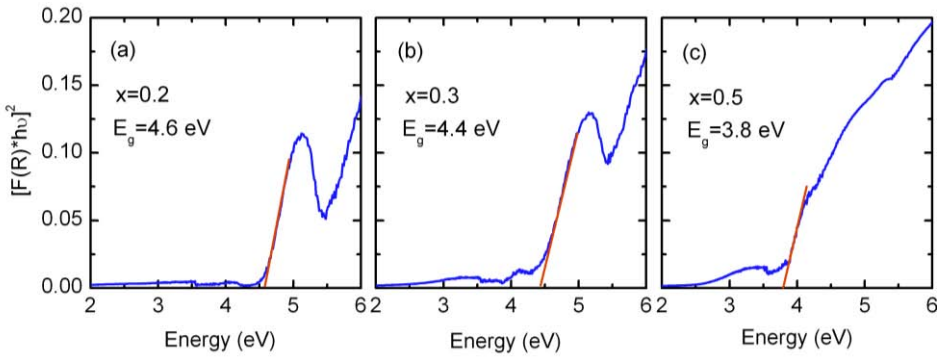

Figure 3. 27. Kubelka-Munk plots of $Sr_{2-x}La_xSiO_{4-x}N_x$ were (a) x=0.2, (b) x=0.3 and (c) x=0.5.

The band gap of the host materials was estimated, by means of the Kubelka-Munk method (**Figure 3. 27**) to be 4.6, 4.4 and 3.8 eV for x= 0.2, 0.3 and 0.5, respectively.

3.3.4.3 Photoluminescence quantum yield

The photoluminescence quantum yield (PLQY) of $Sr_{2-x}La_xSiO_{4-x}N_x:Eu^{2+}$, *$LaM_{1-x}Eu_xSiO_3N$ and $La_{1-x}Ce_xMSiO_3N$ (x=0, 0.01, 0.02, 0.05, 0.1; M = Sr, Ba)* phosphors was calculated using the method by Palsson et al.[205] with the equation 3.3:

$$\phi_f = \frac{(E_C - E_A)}{(L_A - L_C)} \tag{3.3}$$

where E_C is the integrated luminescence of the sample, E_A is integrated luminescence of the empty integrating sphere, L_A is the integrated excitation profile of the empty integrating sphere and L_C is the integrated excitation profile of the sample.[206] In case of $Sr_{2-x}La_xSiO_{4-x}N_x:Eu^{2+}$ (Eu^{2+}=0.02%) solid solution, a decrease of PLQY is observed as La/N

content increases through the solid solution, with 72% shown for x = 0; 33% for x = 0.2; 26% for x = 0.3; 20% for x = 0.5 and 4% for x = 1. In the Ce^{3+} samples the observed quantum yields are 16% for x = 0.2, 12% for x = 0.3 and 1% for x = 1. For the samples $LaSr_{1-x}Eu_xSiO_3N$ *and* $La_{1-x}Ce_xSrSiO_3N$ the PLQYs were 5.57% and 1.36% for x=0.01, 4.16% and 1.02% for x=0.02, 2.66% and 0.91% for x=0.05, 1.68% and 0.47% for 0.1 and 0.08% for the $LaEuSiO_3N$ sample. Finally, $LaBa_{1-x}Eu_xSiO_3N$ samples gave PLQYs of 3.8% for x=0.01, 4.1% for x=0.02 and 3.07% for x=0.05.

The large Stokes shift observed in these phosphors indicates a strong coupling of the 5d electrons with phonons. Thermal quenching seems to be the most plausible mechanism for the non-radiative relaxation of the excited state of the rare earth. The substitution of Sr^{2+} by La^{3+} contributes to lower the conduction band of the host reducing the energy difference between the lowest 5d state of the activator and the bottom of the conduction band, increasing the probability of a thermal promotion of the 5d electrons to the conduction band. This photoionization process has been described as one of the primary mechanisms for nonradiative transitions and consequent decrease of quantum efficiency.[97, 207] An additional factor that contributes to a low quantum efficacy is the inherent lack of rigidity of the orthosilicate structure, were their isolated, "floppy" SiO_4 tetrahedra, potentially provide localized vibration pathways for thermal quenching.[95, 185]

It is known that substitutions of trivalent active ions such as Ce^{3+} in divalent cation site increase the probability of non-radiative relaxation.[208, 209] This increase in the radiationless process arises from the greater expansion that the Ce^{3+} experiments in the excited state while it is located in a larger polyhedral volume site.[201] In accordance with bond distances,

and site volume, Ce^{3+} compounds are in a favourable condition to present lower PLQY due to partial substitution of Ce^{3+} in a divalent cation site. $Sr_{2-x}La_xSiO_{4-x}N_x$ hosts shows mixed cation occupancies and partial anion order, inducing multiple cation sites and increasing disorder in the host lattice which favours the non-radiative relaxation pathways and leads to a low quantum efficiency.

3.3.4.4 CIE1931 chromaticity diagram

3.3.4.4.1 CIE1931 chromaticity diagram of $LaMSiO_3N:Eu^{2+}$ or Ce^{3+} (M=Sr, Ba)

From the 298 K emission spectra, the CIE (Commission Internationale de l'Eclairage) chromaticity coordinates, illustrated in **Figure 3. 28** and **Figure 3. 29** are (0.520, 0.432) for x = 0.01, (0.527, 0.425) for x = 0.02, (0.529, 0.423) for x = 0.05 and (0.549, 0.415) for x = 0.1 in $LaSr_{1-x}Eu_xSiO_3N$. The values found for $LaBa_{1-x}Eu_xSiO_3N$ were very similar, (0.51, 0.424) for x = 0.01, (0.523, 0.428) for x = 0.02 and (0.540, 0.414) for x = 0.05 corresponding to orange-red emissions.

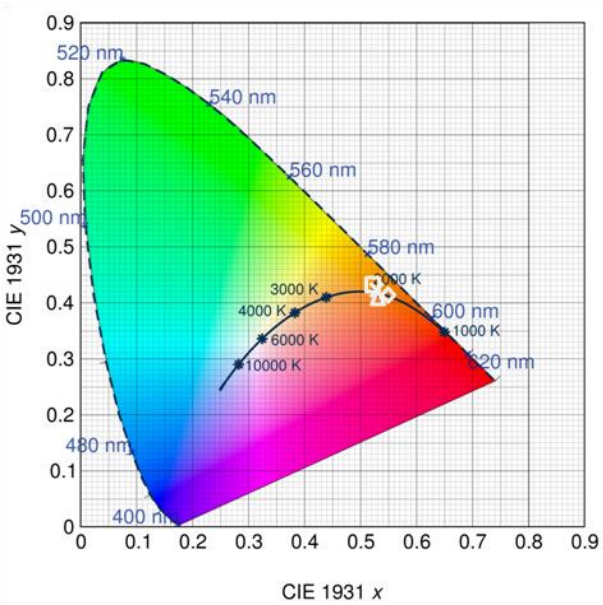

Figure 3. 28. CIE color coordinates of $LaSr_{1-x}Eu_xSiO_3N$ for $0.01 \leq x \leq 0.1$

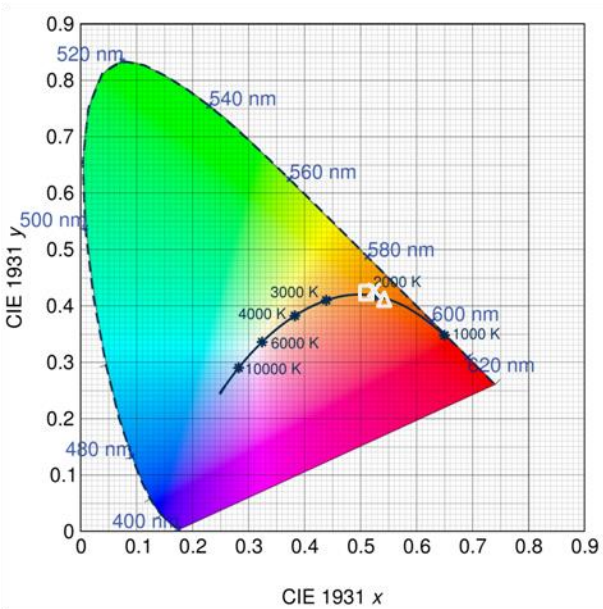

Figure 3. 29. CIE color coordinates of $LaBa_{1-x}Eu_xSiO_3N$ for $0.01 \leq x \leq 0.05$

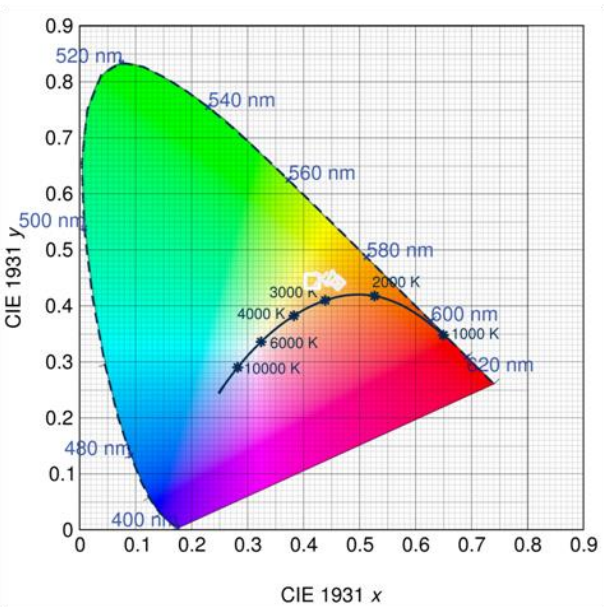

Figure 3. 30. CIE color coordinates of $La_{1-x}Ce_xSrSiO_3N$ for 0.01≤x≤0.1.

The CIE chromaticity coordinates found for $La_{1-x}Ce_xSrSiO_3N$ were (0.414, 0.445) for x = 0.01, (0.432, 0.449) for x = 0.02, (0.451, 0.451) for x = 0.05 and (0.463, 0.442) for x = 0.1 corresponding to yellow-orange emissions (**Figure 3. 30**).

3.3.4.4.2 CIE1931 chromaticity diagram of $La_xSr_{2-x}SiO_{4-x}N_x:Eu^{2+}$ or Ce^{3+} (0≤x≤1)

The CIE 1931 chromaticity diagram of $Sr_{2-x}La_xSiO_{4-x}N_x:Eu^{2+}$ (x = 0, 0.2, 0.3, 0.5 and 1) and $Sr_{2-x}La_xSiO_{4-x}N_x:Ce^{3+}$ (x = 0.2, 0.3 and 1) phosphors (**Figure 3. 31**) illustrates the wide range of colours that can be obtained by changing the La and N content in this host. The emission color shifts in $Sr_{2-x}La_xSiO_{4-x}N_x:Eu^{2+}$ from green-yellow for x = 0 (chromaticity coordinates x =

0.366, y = 0.572) to orange-red (chromaticity coordinates x = 0.528, y = 0.4232) for x = 1. The largest change in the chromaticity coordinates is appreciated for the sample with x = 0.2. For $Sr_{2-x}La_xSiO_{4-x}N_x:Ce^{3+}$ the emission color changes from blue-green for x = 0.2 (chromaticity coordinates x = 0.260, y = 0.398) to orange-yellow for x = 1 (x = 0.432, y = 0.449). As the CIE colour rendering index is based on human eye physiological perception of color all spectral emission above 700 nm do not contribute to the chromaticity coordinates. Consequently, the large increase in intensity of the red emission of Eu^{2+} phosphors with x ≥ 0.2 leads to a slight contribution to the shift into the red region of the CIE diagram.

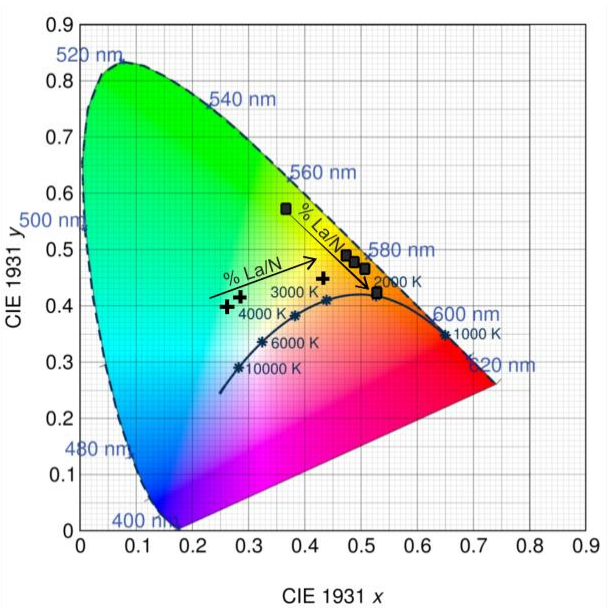

Figure 3. 31. CIE diagram showing the change of emission colour in $Sr_{2-x}La_xSiO_{4-x}N_x$ activated with Eu^{2+} (from green to red, square markers) and with Ce^{3+} (from blue to yellow, cross markers).

3.3.4.5 White LED test devices

In order to evaluate the warmness of the white light produced by $Sr_{2-x}La_xSiO_{4-x}N_x:Eu^{2+}$ phosphors LED tests were performed using commercially available LED (405 nm) as an excitation source for the yellow-red emitting phosphors. The phosphors were dispersed and melded using a silicone resin into a cap that attached to the commercial 405 nm LED.

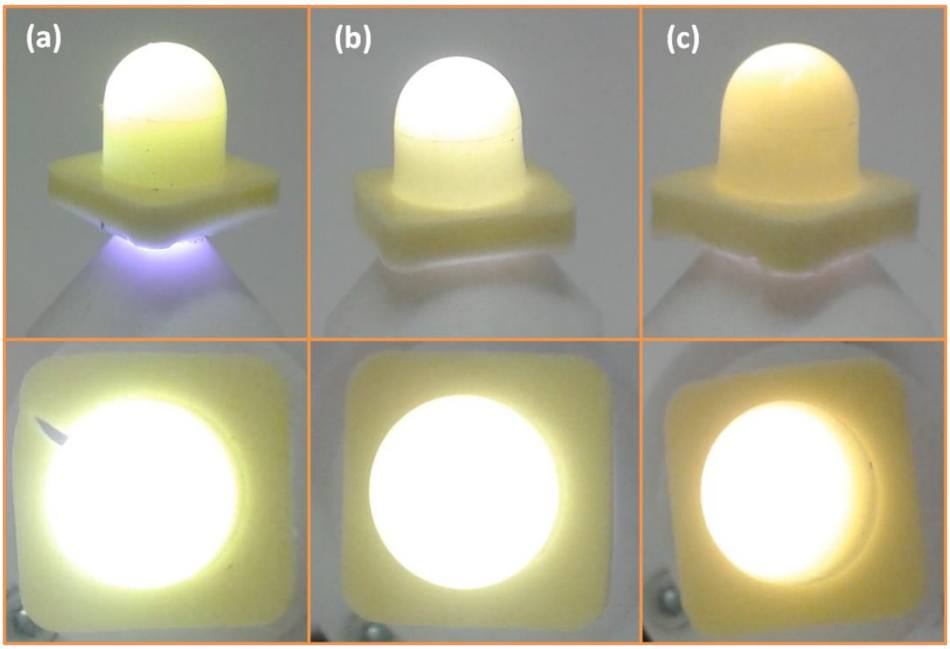

Figure 3. 32. Pictures of commercial LED (405 nm) covered with silicon caps containing $Sr_{2-x}La_xSiO_{4-x}N_x:Eu^{2+}$ phosphors (a) x=0.2, (b) x=0.3, (c) x=0.5.

From **Figure 3. 32** a gradual increase of light warmness is observed as La/N content increases in $Sr_{2-x}La_xSiO_{4-x}N_x:Eu^{2+}$.

3.3.5 Ferromagnetism of $LaEuSiO_3N$

$LaEuSiO_3N$ also shows a ferromagnetic transition at T_c = 3.0 K, below which field and zero-field-cooled susceptibilities diverge (**Figure 3. 33**).

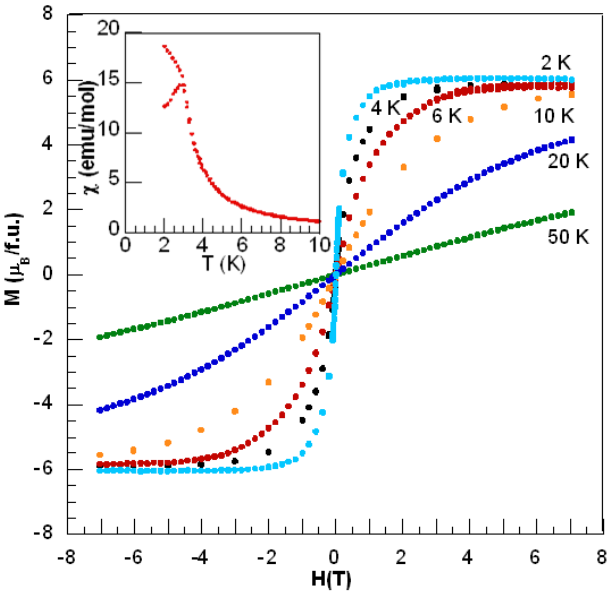

Figure 3. 33. Magnetic-field dependence of the magnetization of $LaEuSiO_3N$ at T = 2, 4, 6, 10, 20 and 50 K. Inset: FC-ZFC magnetic susceptibility.

The high temperature susceptibilities follow a Curie–Weiss behaviour, and the fit to 100–300 K gives an effective moment of 7.69 μ_B, which is close to the ideal value of 7.94 μ_B of Eu^{2+}, and a Weiss temperature of 4.8 K. Magnetization field loops show a typical behaviour for soft ferromagnets at low temperatures, and the saturated magnetization at 2 K is 6.1 μ_B. The similar compound Eu_2SiO_4 with monoclinic structure (β phase) is also ferromagnetic and shows a higher T_c of 7 K.[210] The Curie temperature of

$LaEuSiO_3N$ is similar to that shown by the layered oxynitridosilicate $EuSi_2O_2N_2$, which is ferromagnetic below 4.5 K.[211]

3.4 Conclusions

In summary, these results demonstrate the potential of the new family of lanthanum alkaline earth oxynitridosilicates $LaMSiO_3N$ (M=Sr, Ba) and the solid solution $Sr_{2-x}La_xSiO_{4-x}N_x$ ($0 \leq x < 1$) as hosts for luminescent materials analogous to the efficient phosphors $M_2SiO_4:Eu^{2+}$ but with longer emission wavelenghts originated by the introduction of nitride and a trivalent cation. Sr_2SiO_4 and $LaSrSiO_3N$ are end members of the solid solution $Sr_{2-x}La_xSiO_{4-x}N_x$ that is formed by charge balanced substitution of Sr^{2+} by La^{3+} and O^{2-} by N^{3-} in the strontium oxysilicate. The introduction of lanthanum and nitrogen induces a phase transition from the monoclinic β phase, which is the stable polymorph of Sr_2SiO_4 at room temperature to α', isostructural to β-K_2SO_4 for x = 0.2 These oxynitrides show partial order of La and the alkaline earth cations in the two sites M1 and M2, with preferred occupancy of La^{3+} (c.a. 75 % for $LaSrSiO_3N$ and 80 % for $LaBaSiO_3N$) at the nine-coordinated M2 sites as well as partial nitrogen order in sites X2 and X3 of the β-K_2SO_4 structure. The $\beta \rightarrow \alpha'$ transition is most likely induced by the increase in bond valence of the underbonded cations at M1 sites which is caused by nitriding. The introduction of La^{3+} allows the doping with Ce^{3+} cations in the Sr_2SiO_4 structure in addition to Eu^{2+}. Photoluminescence measurements of doped compounds with 0.02 Eu^{2+} or 0.02 Ce^{3+} per formula revealed that the La/N introduction in Sr_2SiO_4 produces an important red-shift of the emission, peaking at 580–700 nm for Eu^{2+}

samples and at 580 nm for Ce^{3+} samples under excitation at 405 nm. The emission colour is tuned by the La/N stoichiometry from green-yellow (x = 0) to orange-red (x = 1) for Eu^{2+} phosphors and from blue-green (x = 0.2) to orange-yellow (x = 1) in Ce^{3+} samples providing a new family of luminescent orthosilicate oxynitride materials with a wide range of emission wavelengths.

Section II

Oxynitride perovskites

Chapter IV

Nitride tuning of lanthanide chromites

$LnCrO_{3-x}N_x$ (Ln = La, Pr, Nd, Sm; $0 < x \leq 0.59$)

4.1 Introduction

Lanthanide chromites $LnCrO_3$ show an orthorhombic $GdFeO_3$ perovskite structure at room temperature. $LaCrO_3$ is an important ceramic material with applications as a mixed (electronic and ionic) conductor in fuel cells and heating elements,[212] and as an oxidation catalyst for CO or CH_4 combustion, with excellent chemical stability in both oxidizing and reducing atmospheres.[213] Magnetism in $LnCrO_3$ perovskites (Ln = La-Lu, Y) is also of fundamental interest. Cr^{3+} ions have three electrons in the 3d shell, which leads to total spin S=3/2. The antiferromagnetic order is G-type, were a Cr^{3+} ions couple with the six magnetic neighbours. The Néel temperature varies with the size and $4f^n$ moments of the Ln^{3+} cations.[214] Neutron diffraction studies of the $LnCrO_3$ family have shown that not only the Cr-O-Cr superexchange angle is governing the antiferromagnetic interactions but also there is a effect of *t-e* hybridization that is contributing to the dramatic changes observed on T_N.[215] In addition to the antiferromagnetism, $LnCrO_3$ perovskites present a weak ferromagnetism that arises from a very small canting of the antiferromagnetic moments due to an antisymmetric exchange between neighbouring magnetic spins. For $NdCrO_3$ in addition to the Cr-Cr interaction, a spin reorientation transition is observed around 34 K, as well as a hyperfine contribution from Nd at temperatures below 1K. $La_{1-x}Pr_xCrO_3$ solid solution within the compositional rage of $0.2 \leq x \leq 0.8$ exhibits a negative magnetization below the compensation temperature. This phenomenon has been understood as weakening of the anisotropy around Pr^{3+}, that arises from the substitution of nonmagnetic La^{3+} ($4f^0$). Chemical tuning through substitutions of A = Ca, Sr in $Ln_{1-x}A_xCrO_3$ perovskites enhances the magnitude of the magnetization

(M) below the magnetic transition and has a strong effect on the temperature dependence of M in the antiferromagnetic state.[216, 217] Sr and Ca doping depresses severely the magnetic transition temperature mostly as result from the doped-hole concentration which increases with substitution of La^{3+} by A^{2+}.

Nitride introduction in $LnCrO_3$ had not been reported before this work, and chromium oxynitrides had been reported only for three structure types: NaCl type $Cr_{1-x}(O,N)$,[218] antifluorite $Li_{10}CrN_4O_2$,[219] or $Li_{14}CrN_2O_8$[220] and apatite $Sm_8Cr_2Si_6N_2O_{24}$.[221] As stated in chapter 1, $AB(O,N)_3$ oxynitride perovskites for early transition metals B = Ti, V; Zr, Nb, Mo; and Ta, W have been studied extensively. Here we show that ammonolysis of $LnCrO_4$ precursors produces new $LnCrO_{3-x}N_x$ perovskites for Ln = La, Pr and Nd, with nitrogen contents up to x = 0.59. Nitride substitution induces oxidation of Cr^{3+} to Cr^{4+} as the mechanism of charge compensation and the consequences of this on magnetic ordering transitions have also been determined.

4.2. Objectives

The objectives of the present work performed on the new lanthanum chromites oxynitride perovskites can be summarized as follows:

- To extend the range of $AB(O,N)_3$ oxynitride perovskites to later 3d transition metal Cr for which oxynitride perovskites have not previously been reported.
- To study the effect of anion substitution on the crystal structure and magnetic properties of lanthanide chromium perovskites.

4.3. Results and discussion

4.3.1 Synthesis of $LnCrO_{3-x}N_x$ ($0 \leq x \leq 0.59$) Ln = La, Pr, Nd and Sm

$LnCrO_{3-x}N_x$ perovskites with Ln = La, Pr, Nd and Sm were synthesised by heating the corresponding $LnCrO_4$ precursors under flowing NH_3 (g) (*Carburos Metalicos, 99.9%*) for several 6 to 24 hour cycles at 700 - 800 ^oC with intermediate regrinding. The ammonolysis reaction was as follows:

$$LnCrO_4\,(s) + (2+x)NH_3\,(g) \rightarrow LnCrO_{3-x}N_x + (1+x)H_2O + N_2 + (2+\frac{x}{2})H_2$$

Ammonia flow was kept at 600 cc/min. Typically batches of 250 mg where placed in a 10 cm long sintered alumina boats ALSINT (*99.97% Al_2O_3*). The powders were in the alumina boat to maximize the solid-gas contact surface. Detailed synthesis conditions for each sample are summarized in **Table 4.1**. The samples were heated at 300 $^oC/h$ up to the reaction temperature and were cooled down in the furnace after each cycle. The reaction in NH_3 proceeds through the initial reduction of $LnCrO_4$ to give poorly nitrided $LnCrO_{3-x}N_x$ perovskites with chromium mainly in the Cr^{3+} state. Nitrogen content x increases with concomitant oxidation of Cr^{3+} to Cr^{4+} during subsequent ammonia treatments. The kinetics of nitriding were found to be slow; using low ammonia flow rates (below 600 cm^3/min), large samples, temperatures below 700 ^oC or short treatment times gave low nitrogen contents, while treatments above 800 ^oC led to partial decomposition of the perovskite and formation of Ln_2O_3. The reactivity in NH_3 showed to depend also from the particle size of the $LnCrO_4$ precursor. Prolonged reactions in NH_3 of small samples with high surface areas at 700-800 ^oC gave the most nitrided products.

Table 4.1. Synthesis conditions of several $LnCrO_{3-x}N_x$ samples (Ln=La, Pr, Nd, Sm)

Sample	T (^{0}C)	time/cycle (h)	n^0 cycles	Total time (h)	Mass (mg)
$LaCrO_{2.89}N_{0.11}$	700	6	9	54	300
$LaCrO_{2.75}N_{0.25}$	700	6	4	24	200
$LaCrO_{2.72}N_{0.28}$	700	10	3	30	300
$NdCrO_{2.85}N_{0.15}$	700	4.5	1	4.5	112
$NdCrO_{2.73}N_{0.27}$	700	16	10	160	250
$NdCrO_{2.68}N_{0.32}$	700	20	3	220	100
$NdCrO_{2.60}N_{0.40}$	700	7	2	15	100
$NdCrO_{2.57}N_{0.43}$	700	10	3	30	250
$NdCrO_{2.54}N_{0.46}$	700	10	3	30	250
$NdCrO_{2.41}N_{0.59}$	700	10	3	40	250
$PrCrO_{2.81}N_{0.19}$	550, 700	5,10	2	30	100
$PrCrO_{2.65}N_{0.35}$	700	10	3	30	250
$PrCrO_{2.35}N_{0.37}$	700	10	3	30	250
$SmCrO_{2.76}N_{0.24}$	850	4.5	1	4.5	250

The maximum analysed nitrogen contents were x = 0.28, 0.36, 0.59 and 0.24 for Ln = La, Pr, Nd and Sm respectively.

4.3.1.1. Synthesis of $LnCrO_4$ (Ln=La, Pr, Nd and Sm) precursors by the Pechini method

La_2O_3 (Aldrich, 99.9 %), Sm_2O_3 (Alfa Aesar, 99.998 %) or Nd_2O_3 (Aldrich, 99.9 %) were first fired at 900^{0}C during 12 hours and dissolved in HNO_3 0.1 M. Pr_6O_{11} (Aldrich, 99.9 %) was first fired at 600ºC during 4h and dissolved in HNO_3 0.1 M. Then $Cr(NO_3)_3{\cdot}9H_2O$ (Aldrich 99.99 %), $C_6H_8O_7$ (citric acid, Aldrich 99.5 %) and $C_2H_6O_2$ (ethyleneglycol), were subsequently added to the solution in molar ratios

Ln:Cr:$C_6H_8O_7$:$C_2H_6O_2$=1:1:1:1, with continuous stirring and heating at 55-80 ^{0}C. The solutions were evaporated for 12 h to form the precursor resins that were subsequently treated in synthetic air at 540^{0}C for 15 hours.

The synthesis of the lanthanide chromate precursors is summarized in the following flowchart (**Figure 4. 1**).

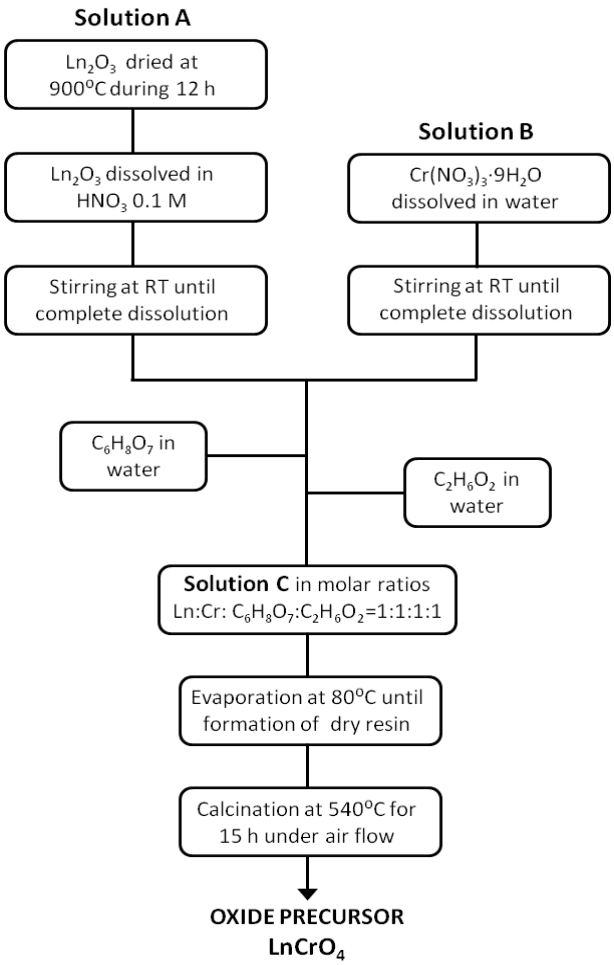

Figure 4. 1. Flowchart of $LnCrO_4$ synthesis by the Pechini method.

The citrate complexes were decomposed in air at appropriate temperatures to obtain the corresponding rare earth chromates. The calcination of the dry resin was carried out in a stepwise manner, as in the

scheme shown below because of the high exothermal character of the combustion reaction.

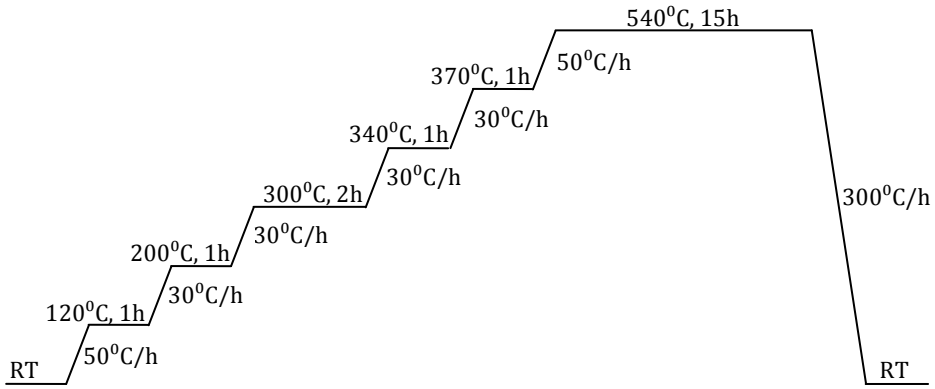

The heating treatment was performed using the data of the termogravimetric analysis and the differential scanning calorimetry (DSC) of the dry resin shown in **Figure 4. 2**. Thermal decomposition in air of the lanthanide chromate complex proceeds through various steps. In the TG curves at least four steps could be identified. The involved reactions are:[222] (i) dehydration together with the decomposition of the nitrates and (ii) decomposition of the citrate complex to produce an oxycarbonate; (iii) decomposition of the oxycarbonate to lanthanide chromate(V); and (iv) decomposition of chromate(V) to lanthanide chromite(III). The dehydration process and NO_3^- loss extends up to c.a. 250 ^{0}C and it is accompanied by a mass loss between 10 and 35 % depending on the initial amount of water contained in the resin. Decomposition of the anhydrous citrate complex starts around 350^{0}C, it is a strong exothermic process accompanied by the evolution of CO_2 and H_2O and a mass loss of 20-30%. At the end of this step, a stable oxycarbonate $LnCrO_{3-x}(CO_3)_x$, is formed. The oxycarbonate starts to decompose between 500 and 580^{0}C depending on the rare earth metal.

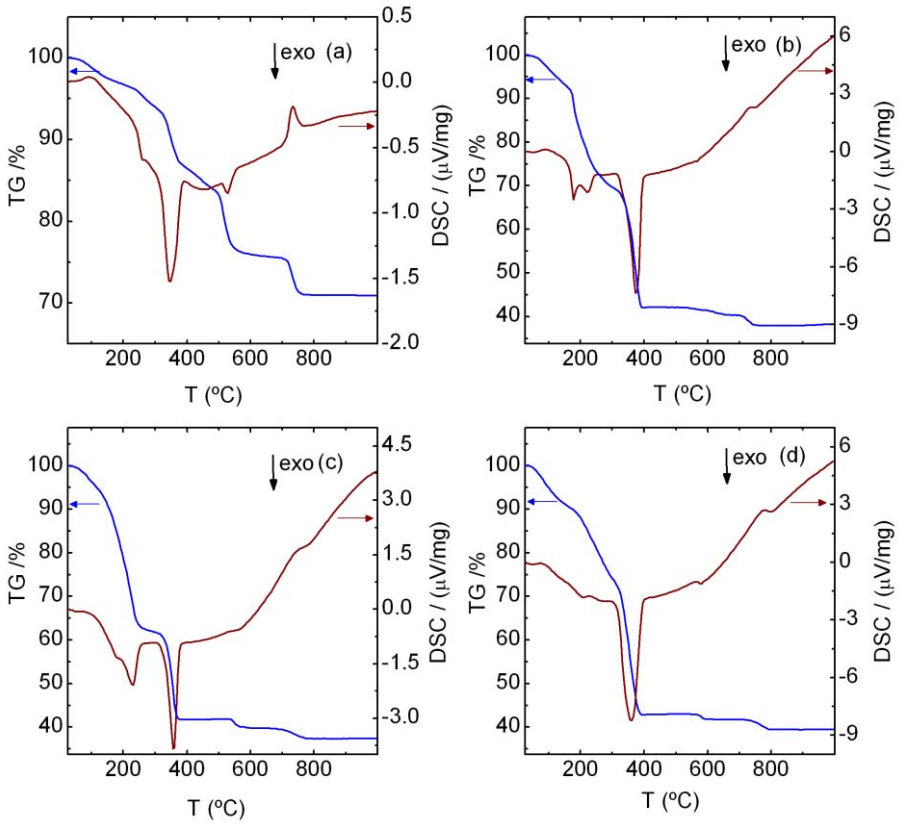

Figure 4. 2. TGA and DSC curves in air of the Pechini dry resins obtained for the synthesis of $LnCrO_4$ compounds for the lanthanides (a) La, (b) Pr, (c) Nd and (d) Sm.

The observed weight loss is between 4 and 12 % depending on the stoichiometry of the stable $LnCrO_{3-x}(CO_3)_x$ oxycarbonate.[222] The lanthanide chromate(V) was found to be stable in air up to temperatures between 700 and 780 ^{0}C. Above this temperature the final stage of decomposition was the reduction of $LaCrO_4$, to produce $LaCrO_3$. The color of the powder by the thermal treatment detailed above was dark green.

4.3.1 Determination of nitrogen contents of $LnCrO_{3-x}N_x$ by combustion analysis

The nitrogen contents determined by combustion analyses are summarized in the **Table 4. 2.**

Table 4. 2. Nitrogen content determined by combustion analyses.

Sample	1 st assay N (wt%)	2 nd assay N (wt%)	Avg. N (wt%)	N content
$LaCrO_{2.89}N_{0.11}$	0.69	0.68	0.69	0.11(2)
$LaCrO_{2.75}N_{0.25}$	1.50	1.48	1.49	0.25(2)
$LaCrO_{2.72}N_{0.28}$	1.68	1.64	1.66	0.28(2)
$NdCrO_{2.85}N_{0.15}$	0.88	0.86	0.87	0.15(2)
$NdCrO_{2.73}N_{0.27}$	1.56	1.55	1.56	0.27(2)
$NdCrO_{2.68}N_{0.32}$	1.91	1.79	1.85	0.32(2)
$NdCrO_{2.60}N_{0.40}$	2.25	2.31	2.28	0.40(2)
$NdCrO_{2.57}N_{0.43}$	2.44	2.45	2.45	0.43(2)
$NdCrO_{2.54}N_{0.46}$	2.59	2.64	2.62	0.46(2)
$NdCrO_{2.41}N_{0.59}$	3.38	3.37	3.38	0.59(2)
$PrCrO_{2.81}N_{0.19}$	1.11	1.14	1.13	0.19(2)
$PrCrO_{2.65}N_{0.35}$	2.08	2.07	2.11	0.35(2)
$PrCrO_{2.35}N_{0.37}$	2.19	2.18	2.19	0.37(2)
$SmCrO_{2.76}N_{0.24}$	1.33	1.38	1.36	0.23(2)

4.3.2 Structural Characterization

4.3.3.1 X-ray diffraction

The laboratory X-ray diffraction patterns of the lanthanide chromates $LnCrO_4$ (Ln=La, Pr, Nd, Sm) were satisfactory fitted by Rietveld refinement. $LaCrO_4$ crystallize in the monoclinic $P2_1/n$ space group (n^0 14). The refined cell parameters were a= 7.0349(2), b= 7.2346(2), c= 6.6916(2) Å and β=

104.915(1)^0. The patterns of praseodymium, neodymium and samarium were fitted in the tetragonal $I4_1/amd$ space group (n^0 141). The refined cell parameters were a= 7.2514(2), c= 6.3526(2) for $PrCrO_4$, a= 7.3108(4) , c= 6.4000(3) for $NdCrO_4$ and a= 7.2456(3), c= 6.3478(3) Å for $SmCrO_4$.

Figure 4. 3 shows the X-ray diffraction patterns of the lanthanide chromates $LnCrO_4$, where Ln=La, Pr, Nd, Sm.

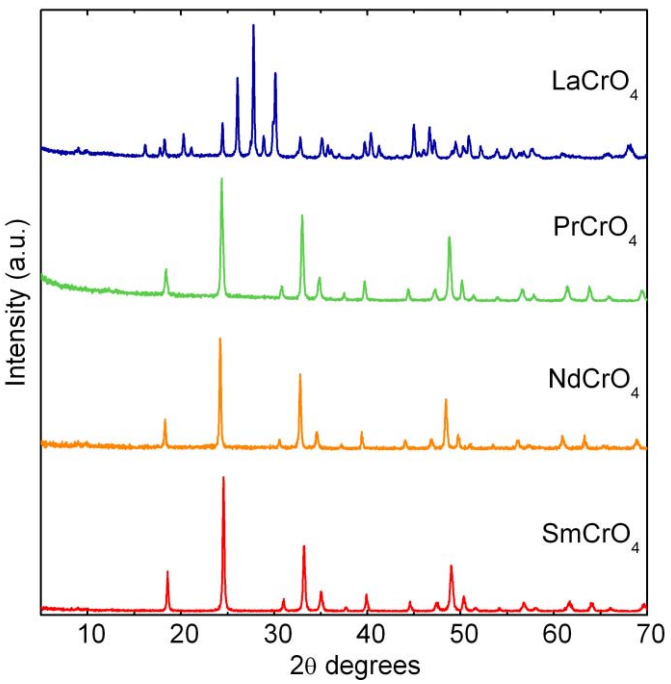

Figure 4. 3. X-ray powder diffraction patterns of $LnCrO_4$ where Ln=La, Pr, Nd and Sm.

Figure 4. 4 shows the Rietveld refinement of the synchrotron X-ray diffraction patters for $LnCrO_{3-x}N_x$ samples for Ln = La, Pr, Nd and Sm, and nitrogen contents of x = 0.28, 0.19, 0.42 and 0.24 respectively. Synchrotron data were collected from capillary (0.3 mm diameter) samples in the

angular range $1.038^{o} \leq 2\theta \leq 61.09^{o}$ at the MSPD beamline of the ALBA Synchrotron (Cerdanyola del Valles, Spain). Using a double Si (111) crystal monochromator, a short wavelength was selected and calibrated with Si NIST. The X-ray wavelengths were 0.619714 A for $LnCrO_{3-x}N_x$ with Ln = La, Pr, Nd and 0.412700 A for Ln = Sm. The detectors used were the high resolution MAD26 (for the Sm compound) and Mythen (for the La, Nd and Pr compounds). The secondary phase observed in the pattern on **Figure 4. 4c** is TiO_2 (rutile) that comes from the cryostat. All of the $LnCrO_{3-x}N_x$ products were found to adopt the orthorhombic $GdFeO_3$-type perovskite superstructure which was refined in the space group *Pbnm* ($n^{0}62$). The refinements were performed with Fullprof software.[193] Background refinement was performed by linear interpolation and the data were corrected for absorption. The initial cell parameters and atomic coordinates were taken from the analogous oxidic compounds $LnCrO_3$ with Ln = La, Pr, Nd and Sm. Nitrogen was constrained to the experimental value determined by combustion analysis and equally distributed in the equatorial and axial anionic sites. Cation occupancies were fixed to their nominal value. Refined cell parameters, atomic positions, bond distances, bond angles and general refinement agreement factors are summarized in **Table 4. 3** to **Table 4. 6.** A progressive decrease of cell volume and increase of tilting is observed as Ln^{3+} size decreases.

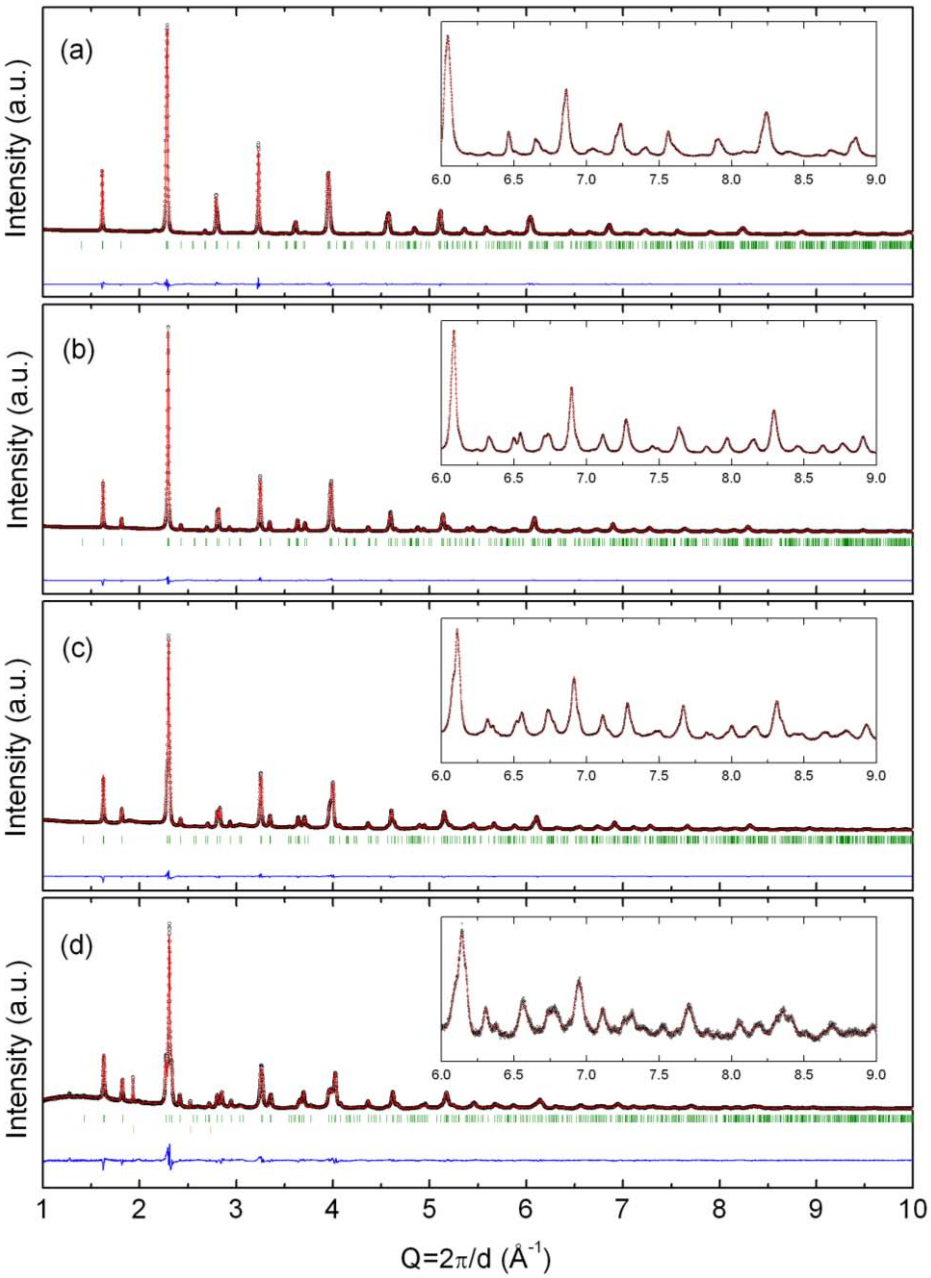

Figure 4. 4. Observed and calculated synchrotron X-ray powder diffraction patterns at room temperature for (a) $LaCrO_{2.72}N_{0.28}$, (b) $PrCrO_{2.81}N_{0.19}$, (c) $NdCrO_{2.58}N_{0.42}$, (d) $SmCrO_{2.76}N_{0.24}$.

Table 4. 3. Summary of the *Pbnm* model for $LaCrO_{2.72}N_{0.28}$ refined against room temperature synchrotron X-ray powder diffraction data.

Cell parameters (Å)				Agreement factors	
a = 5.52201(4)				R_{Bragg} = 1.75	
b = 5.48192(5)				R_{wp} = 4.33	
c = 7.6573(7)				χ^2 = 8.21	
Atom	Site	x	y	z	B_{iso} (Å^2)
La	4c	0.9978(2)	0.01274(9)	¼	0.715(6)
Cr	4b	½	0.0	0.0	0.344(8)
X1	4b	0.070(1)	0.493(1)	¼	0.31(4)
X2	8d	0.727(1)	0.268(1)	0.0353(5)	0.31(4)
		La-X1	La-X2	Cr-X1	Cr-X2
Bond length / Å		2.391(6)	2.474(5)×2	1.980(1)×2	1.953(6)×2
		2.660(6)	2.640(6)×2		1.989(6)×2
		2.879(6)	2.821(5)×2		
		3.136(6)	3.096(5)×2		
		Cr-X1-Cr		Cr-X2-Cr	
Bond Angle / °		157.45(5)		161.5(3)	

Table 4. 4. Summary of the *Pbnm* model for $PrCrO_{2.81}N_{0.19}$ refined against room temperature synchrotron X-ray powder diffraction data.

Cell parameters (Å)				Agreement factors	
a = 5.45535(4)				R_{Bragg} = 2.04	
b = 5.49076(3)				R_{wp} = 3.24	
c = 7.72751(5)				χ^2 = 3.93	
Atom	Site	x	y	z	B_{iso} (Å^2)
Pr	4c	0.9932(1)	0.03577(4)	¼	0.610(4)
Cr	4b	½	0.0	0.0	0.158(8)
X1	4b	0.0736(9)	0.4815(5)	¼	0.25(6)
X2	8d	0.7147(7)	0.2939(6)	0.0388(5)	0.25(6)
		Pr-X1	Pr-X2	Cr-X1	Cr-X2
Bond length / Å		2.382(5)	2.390(4)×2	1.976(1)×2	1.948(4)×2
		2.486(3)	2.6402(4)×2		2.016(3)×2
		3.075(3)	2.705(4)×2		
		3.107(5)	3.286(4)×2		
		Cr-X1-Cr		Cr-X2-Cr	
Bond Angle / °		155.80(4)		155.0(2)	

Table 4. 5. Summary of the *Pbnm* model for $NdCrO_{2.58}N_{0.42}$ refined against room temperature synchrotron X-ray powder diffraction data.

Cell parameters (Å)				Agreement factors	
a = 5.42787(3)				R_{Bragg} = 2.04	
b = 5.50102(3)				R_{wp} = 2.36	
c = 7.70936(4)				χ^2 = 7.72	
Atom	Site	x	y	z	B_{iso} (Å^2)
Nd	4c	0.9919(1)	0.04131(5)	¼	0.787(7)
Cr	4b	½	0.0	0.0	0.17(1)
X1	4b	0.0851(9)	0.484(7)	¼	0.53(4)
X2	8d	0.7190(7)	0.2935(7)	0.0410(5)	0.43(4)
		Nd-X1	Nd-X2	Cr-X1	Cr-X2
Bond length / Å		2.318(5)	2.401(4)×2	1.984(1)×2	1.928(4)×2
		2.487(3)	2.591(4)×2		2.030(4)×2
		3.108(3)	2.716(4)×2		
		3.148(5)	3.300(4)×2		
		Cr-X1-Cr		Cr-X2-Cr	
Bond Angle / °		152.57(4)		155.0(2)	

Table 4. 6. Summary of the *Pbnm* model for $SmCrO_{2.76}N_{0.24}$ refined against room temperature synchrotron X-ray powder diffraction data.

Cell parameters (Å)				Agreement factors	
a = 5.38586(7)				R_{Bragg} = 4.92	
b = 5.51951(6)				R_{wp} = 8.07	
c = 7.6784(1)				χ^2 = 3.70	
Atom	Site	x	y	z	B_{iso} (Å^2)
Sm	4c	0.9906(2)	0.0488(1)	¼	0.76(1)
Cr	4b	½	0.0	0.0	0.12(2)
X1	4b	0.089(1)	0.462(1)	¼	1.2(2)
X2	8d	0.721(1)	0.315(1)	0.0479(9)	0.87(2)
		Sm-X1	Sm-X2	Cr-X1	Cr-X2
Bond length / Å		2.344(7)	2.316(7)×2	1.990(2)×2	1.854(7)×2
		2.312(9)	2.586(7)×2		2.140(6)×2
		3.159(9)	2.707(7)×2		
		3.280(7)	3.419(7)×2		
		Cr-X1-Cr		Cr-X2-Cr	
Bond Angle / °		149.47(9)		149.8(3)	

Figure 4. 5 shows the structural model obtained from the Rietveld refinement of the synchrotron data for $LnCrO_{3-x}N_x$, where Ln = La, Pr, Nd and Sm.

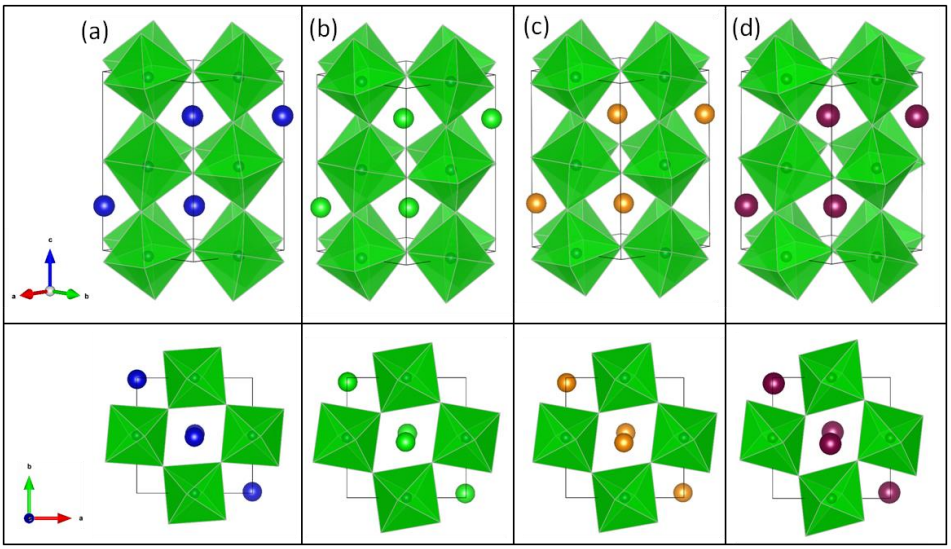

Figure 4. 5. Structural models for $LnCrO_{3-x}N_x$ compounds, where Ln = (a) La, (b) Pr, (c) Nd, (d) Sm.

The $Cr(O/N)_6$ octahedrons are represented in light green, (O/N) in red, La^{3+} in blue, Pr^{3+} in green, Nd^{3+} in orange and Sm^{3+} in purple. Projection along the pseudocubic subcell direction $[001]_p$ show the $Cr(O/N)_6$ octahedra tilts corresponding to ($a^- b^+ a^-$) tilt system in Glazer's notation.[125] With respect to the ideal cubic *Pm-3m* perovskite structure the orthorhombically distorted perovskite *Pbnm* structure is obtained by an anti-phase tilt of the adjacent $Cr(O/N)_6$ octahedra. As expected the magnitude of the distortion increases as Ln^{3+} size decreases.

Figure 4. 6 shows the variation of lattice parameters with N-content based on the refinements of laboratory X-ray diffraction data.

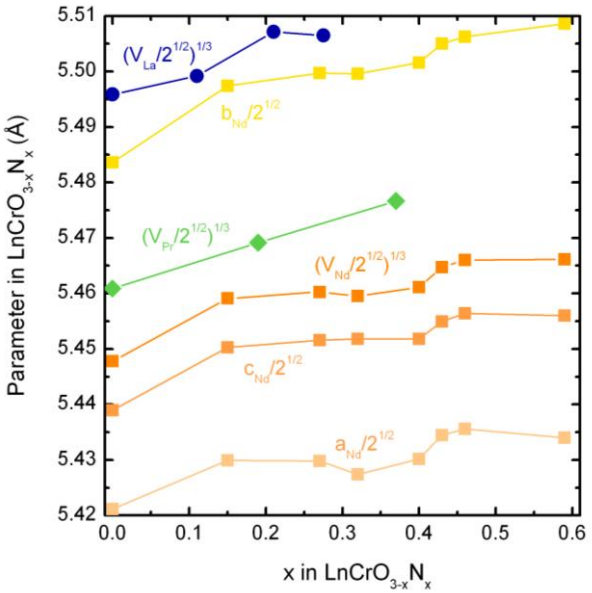

Figure 4. 6. Cell parameters for Ln = Nd and volumes for Ln = La, Pr and Nd as a function of nitrogen content in $LnCrO_{3-x}N_x$ perovskites.

The unit cell expands with x showing that the larger ionic radius of nitride with respect to oxide (1.48 vs. 1.40 Å) outweighs the increasing proportion of Cr^{4+} which is smaller than Cr^{3+} (0.55 Å for Cr^{4+} vs. 0.62 Å for Cr^{3+}).[11]

4.3.3.2 Neutron powder diffraction

Figure 4. 7 to **Figure 4.12** show the Rietveld fits to room temperature and 1.5 or 10 K neutron powder diffraction patterns for $LaCrO_{2.72}N_{0.28}$, $PrCrO_{2.64}N_{0.36}$ and $NdCrO_{2.58}N_{0.42}$.

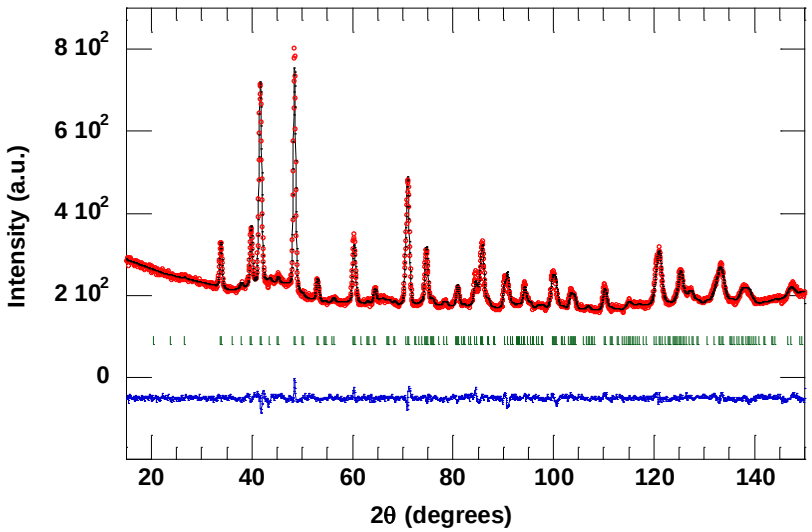

Figure 4. 7. Observed and calculated room temperature neutron powder diffraction patterns for $LaCrO_{2.72}N_{0.28}$ (λ= 1.594 Å).

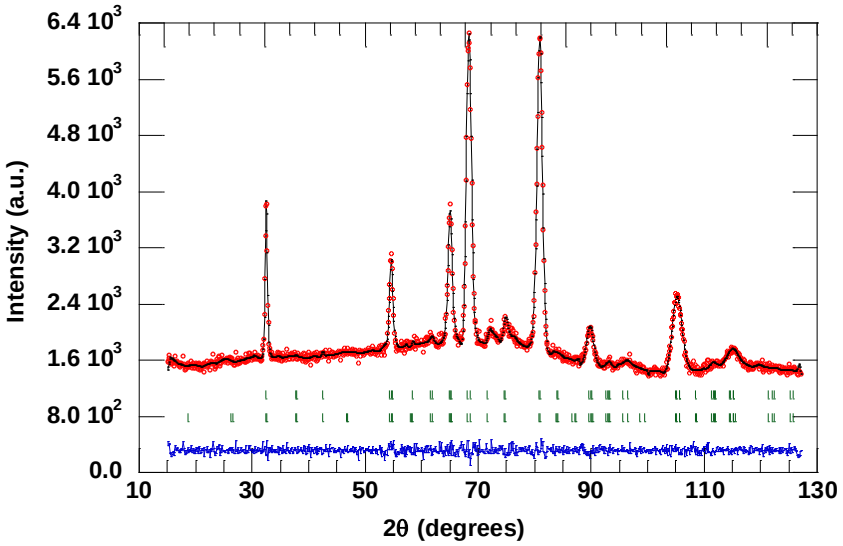

Figure 4. 8. Observed and calculated neutron powder diffraction patterns at 10 K for $LaCrO_{2.72}N_{0.28}$ with magnetic diffraction peaks from Cr spins marked below the nuclear diffraction peaks (λ=2.524 Å).

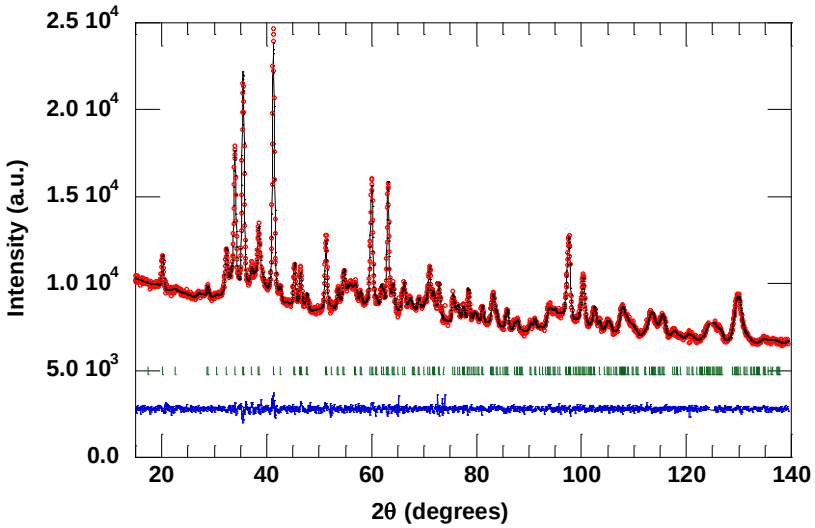

Figure 4. 9. Observed and calculated room temperature neutron powder diffraction patterns for $PrCrO_{2.64}N_{0.36}$ (λ= 1.36 Å).

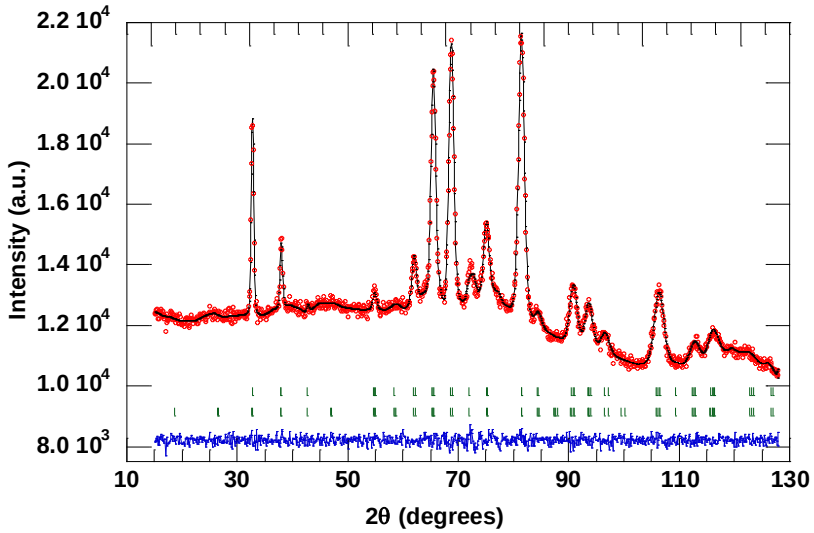

Figure 4. 10. Observed and calculated neutron powder diffraction patterns at 1.5 K for $PrCrO_{2.64}N_{0.36}$ with magnetic diffraction peaks from Cr and Pr spins marked below the nuclear diffraction peaks (λ=2.524 Å).

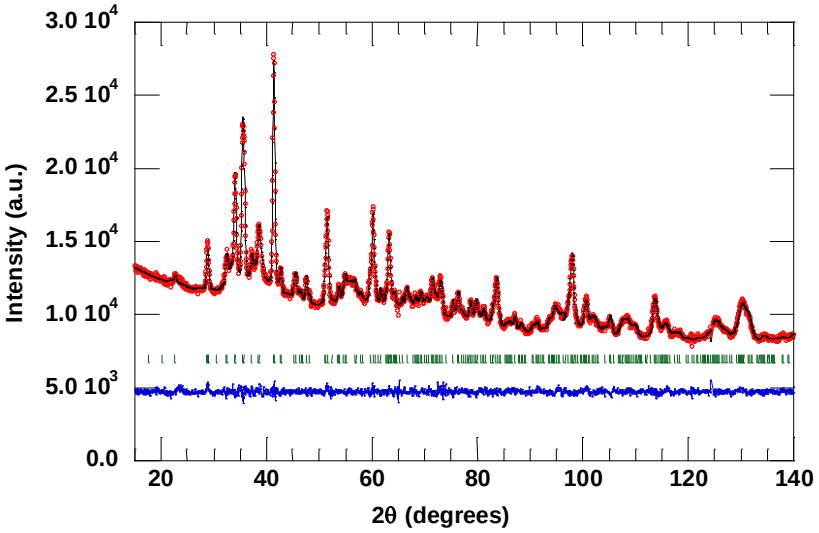

Figure 4.11. Observed and calculated neutron powder diffraction patterns at room temperature for $NdCrO_{2.58}N_{0.42}$ (λ=1.36 Å).

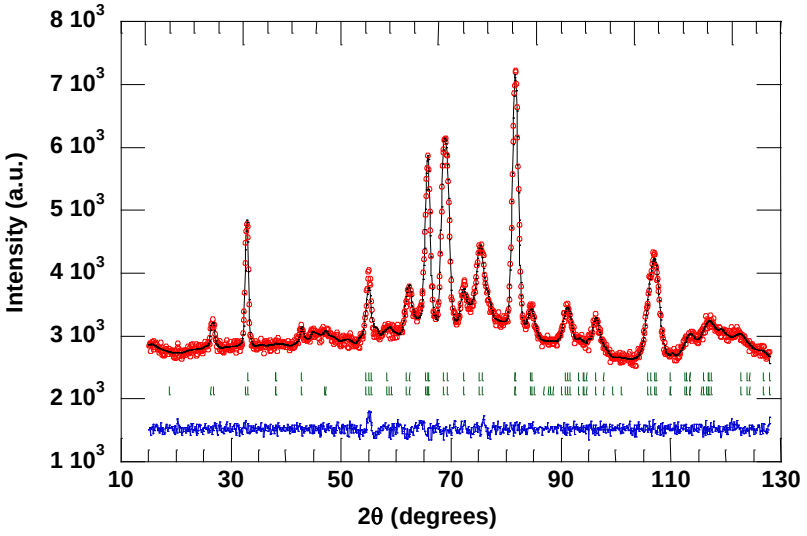

Figure 4.12. Observed and calculated neutron powder diffraction patterns at 1.5 K for $NdCrO_{2.58}N_{0.42}$, with magnetic diffraction peaks from Cr and Nd spins marked below the nuclear diffraction peaks (λ=2.524 Å).

The structures were refined in *Pbmn* space group. The refined cell parameters obtained from X-ray diffraction data were used as starting

parameters. Nitrogen was constrained to the experimental values determined by combustion analysis and initially equally distributed in the two anion sites. After refinement of (O/N) occupancies, no O/N order was detected, in keeping with their relatively small nitrogen contents (x < 0.42). Cation occupancies were fixed to their nominal value. Refined cell parameters, atomic positions, bond distances, bond angles and agreement factors are summarized in **Table 4. 7** to **Table 4. 9**.

Table 4. 7. Summary of the *Pbnm* model for $LaCrO_{2.72}N_{0.28}$ refined against room temperature neutron powder diffraction data.

Cell parameters (Å)				Agreement factors	
a = 5.5237(2)				R_{Bragg} = 4.53	
b = 5.4787(2)				R_{wp} = 2.45	
c = 7.7684(2)				χ^2 = 1.89	
Atom	Site	x	y	z	B_{iso} (Å^2)
La	4c	0.0037(8)	0.0152(7)	¼	0.038(4)
Cr	4b	½	0.0	0.0	0.036(5)
X1	4b	0.0671(7)	0.487(1)	¼	0.732(4)
X2	8d	0.7325(7)	0.2705(7)	0.0362(3)	0.732(4)
		La-X1	La-X2	Cr-X1	Cr-X2
Bond length / Å		2.376(6)	2.502(4)×2	1.978(8)×2	1.961(4)×2
		2.613(8)	2.638(5) ×2		1.981(4)×2
		2.911(8)	2.814(4) ×2		
		3.156(6)	3.085(4)×2		
		Cr-X1-Cr		Cr-X2-Cr	
Bond Angle / °		158.05(3)		161.5(2)	

Table 4. 8. Summary of the *Pbnm* model for $PrCrO_{2.64}N_{0.36}$ refined against room temperature neutron powder diffraction data.

Cell parameters (Å)				Agreement factors	
a = 5.3976(2)				R_{Bragg} = 2.16	
b = 5.4336(2)				R_{wp} = 1.40	
c = 7.6461(3)				χ^2 = 1.82	
Atom	Site	x	y	z	B_{iso} (Å^2)
Pr	4c	0.9959(2)	0.0302(8)	¼	0.341(7)
Cr	4b	½	0.0	0.0	0.599(4)
X1	4b	0.0756(9)	0.4843(7)	¼	0.599(4)
X2	8d	0.7106(5)	0.2904(5)	0.0403(4)	0.599(4)
		Pr-X1	Pr-X2	Cr-X1	Cr-X2
Bond length / Å		2.326(1)	2.348(6) ×2	1.956(1) ×2	1.958(3) ×2
		2.504(6)	2.635(7)×2		1.969(3) ×2
		2.997(6)	2.687(5) ×2		
		3.095(1)	3.236(6) ×2		
		Cr-X1-Cr		Cr-X2-Cr	
Bond Angle / °		155.4(4)		154.5(1)	

Table 4. 9. Summary of the *Pbnm* model for $NdCrO_{2.58}N_{0.42}$ refined against room temperature neutron powder diffraction data.

Cell parameters (Å)				Agreement factors	
a = 5.3715(2)				R_{Bragg} = 2.80	
b = 5.4459(2)				R_{wp} = 1.36	
c = 7.6316(2)				χ^2 = 2.07	
Atom	Site	x	y	z	B_{iso} (Å^2)
Nd	4c	0.9930(9)	0.0388(5)	¼	0.787(7)
Cr	4b	½	0.0	0.0	0.17(1)
X1	4b	0.0796(8)	0.4800(7)	¼	0.53(4)
X2	8d	0.7097(5)	0.2944(5)	0.0421(4)	0.43(4)
		Nd-X1	Nd-X2	Cr-X1	Cr-X2
Bond length / Å		2.319(6)	2.340(4)×2	1.958(1)×2	1.946(3)×2
		2.447(5)	2.602(4)×2		1.985(3)×2
		3.078(5)	2.674(4)×2		
		3.092(6)	3.288(4)×2		
		Cr-X1-Cr		Cr-X2-Cr	
Bond Angle / °		153.99(4)		153.16(1)	

4.3.3 Magnetic properties

$LnCrO_3$ perovskites are magnetic insulators with ordering transitions at 200-300 K due to antiferromagnetic coupling of localised S = 3/2 Cr^{3+} spins, although canting of moments leads to weak ferromagnetism. No further transitions are observed down to 4 K for $PrCrO_3$,[223] but $NdCrO_3$ has a complex low temperature behaviour, with Nd-Cr interactions driving a Cr spin reorientation transition at T_{SRT} = 34 K and Nd^{3+} spin ordering below 11 K.[224]

Susceptibility measurements for $LnCrO_{3-x}N_x$ perovskites (**Figure 4. 13**) show the magnetic ordering temperature T_N is reduced as x increases, for example from 293 to 285 to 281 K for $LaCrO_{3-x}N_x$ samples with x = 0, 0.11 and 0.28 respectively in Figure 4.14 (a). There is also a decrease in the weak ferromagnetic component below T_N, as evidenced by the decline in low temperature susceptibility with x. All samples have substantial localised Cr paramagnetic moments of 3-4 μ_B and negative Weiss temperatures showing that antiferromagnetic interactions between localised Cr^{3+}/Cr^{4+} moments are dominant. The Weiss temperature and effective moment per Cr ion both fall in magnitude with increasing x as Cr^{3+} is oxidised to Cr^{4+}, as observed in the $La_{1-x}Sr_xCrO_3$ system.[216] However, the spin reorientation transition temperature in $NdCrO_{3-x}N_x$, shown by the inflection in the data in **Figure 4. 13c**, increases going from x = 0 to x = 0.35, although the transition is no longer evident for the highly nitrided x = 0.59 sample.

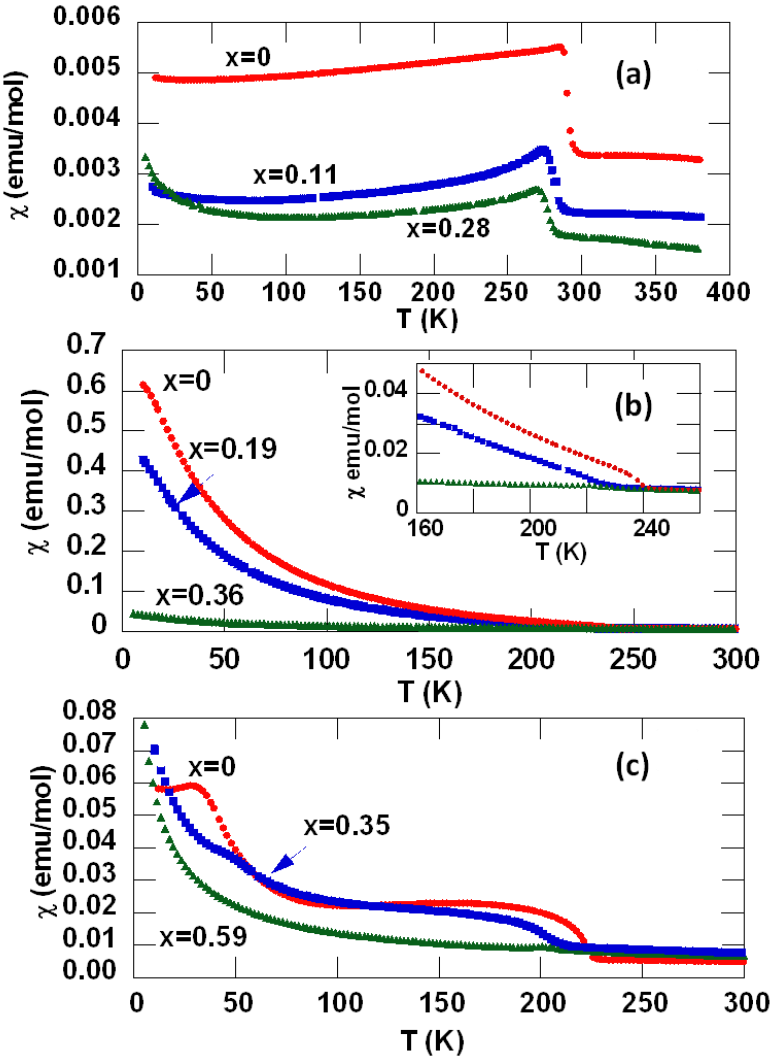

Figure 4. 13. Magnetic susceptibility data for selected $LnCrO_{3-x}N_x$ samples with (a) Ln = La, (b) Ln = Pr, and (c) Ln = Nd, and nitrogen contents x as shown. Inset in (b) shows the enlarged region around T_N.

Values of Néel temperatures and other magnetic parameters from Curie-Weiss fits to data above T_N are shown in **Table 4. 10**.

Table 4. 10. Values of Néel temperatures and other magnetic parameters from Curie-Weiss fits to data above T_N for Ln = Pr and Nd samples.

Ln, x	T_N/K	T_{SR}/K	θ/K	μ_{eff}/μ_B	$\mu_{eff}(Cr)/\mu_B$
La, 0	293				
La, 0.11	285				
La, 0.17	283				
La, 0.21	283				
La, 0.25	280				
La, 0.28	281				
Pr, 0	240	-	-217	5.50	4.17
Pr, 0.19	229	-	-156	5.17	3.73
Pr, 0.36	232	-	-43	4.30	2.38
Nd, 0	226	28	-251	4.72	3.03
Nd, 0.35	210	44	-138	5.21	3.75
Nd, 0.59	214	-	-91	4.60	2.84

Curie-Weiss fittings were not possible for Ln = La due to the high T_N. Effective Cr paramagnetic moments were estimated by subtracting the ideal Ln^{3+} contribution from the total as shown in following equation:

$$\mu_{eff}\ (Cr) = \sqrt{{\mu_{eff}}^2 - \mu_{eff}(Ln^{3+})^2}$$

Where $\mu_{eff}(Pr^{3+}) = 3.58$ and $\mu_{eff}(Nd^{3+}) = 3.62\ \mu_B$.

Magnetic order was characterised by variable temperature powder neutron diffraction. G-type antiferromagnetic order, in which each Cr moment is antiparallel to nearest neighbours in x, y and z directions, was observed below the T_N's in all cases. In **Figure 4. 8**, **Figure 4. 10** and **Figure 4.12**, the main magnetic peaks are around $2\theta = 32^0$, where the contribution of the crystal structure reflection is almost zero. Refinements were performed in both G_y- and G_z-type antiferromagnetic spin configuration of Cr^{3+} ions that have been reported for rare-earth orthochromites.[225, 226] A slightly smaller goodness of fit indicators was obtained for the G_y than for G_z. Antiferromagnetic Nd^{3+} spin order is also

observed for $NdCrO_{2.58}N_{0.42}$ at low temperatures. The magnetic structures are shown in **Figure 4. 14**. The praseodymium orthochromite, not shown in this figure, presents equivalent structure as lanthanum sample (**Figure 4. 14a**). Summary of the magnetic refinements including magnetic moments at low temperatures using D1B neutron diffraction data are shown in **Table 4. 11.**

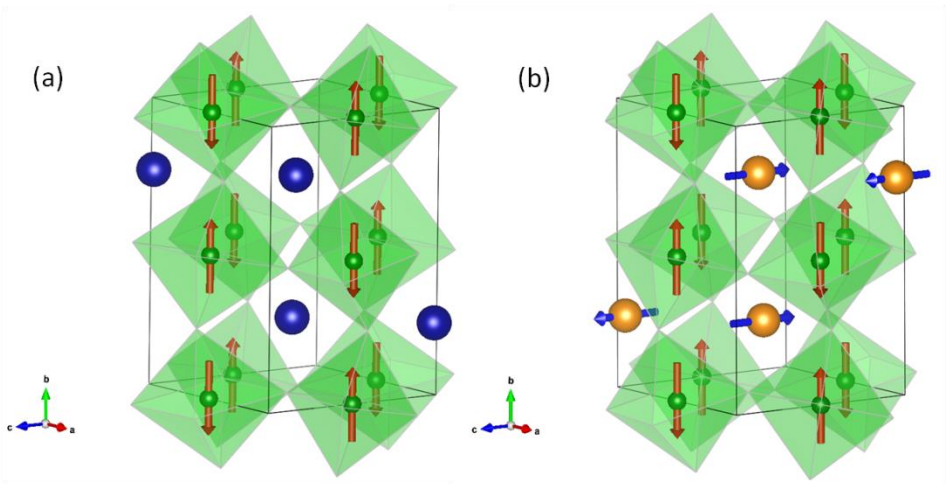

Figure 4. 14. Magnetic structure for (a) $LaCrO_{2.72}N_{0.28}$ at 10 K and (b) $NdCrO_{2.58}N_{0.42}$ at 1.5 K refined from neutron diffraction. The Cr ions are shown as green spheres. Ordered Cr moments along the b axis are shown as red arrows. Ordered Nd moments along the c axis are shown as blue arrows.

Table 4. 11. Summary of the magnetic refinements for *Pbnm* models at low temperatures using D1B neutron diffraction data. Refined lattice parameters and ordered moments at Cr and Nd sites are shown.

Sample	T/K	a/Å	b/Å	c/Å	μ_y(Cr)/μ_B	μ_z(Ln)/μ_B
$LaCrO_{2.72}N_{0.28}$	10	5.4508(9)	5.4086(6)	7.666(2)	2.73(5)	
$PrCrO_{2.64}N_{0.36}$	1.5	5.3258(7)	5.4039(7)	7.575(1)	2.60(8)	
$NdCrO_{2.58}N_{0.42}$	1.5	5.3569(7)	5.3922(6)	7.598(1)	2.59(5)	1.4(1)

Figure 4. 15 shows the thermal variation of refined Cr magnetic moment in $LnCrO_{3-x}N_x$ (Ln = La, Pr, Nd).

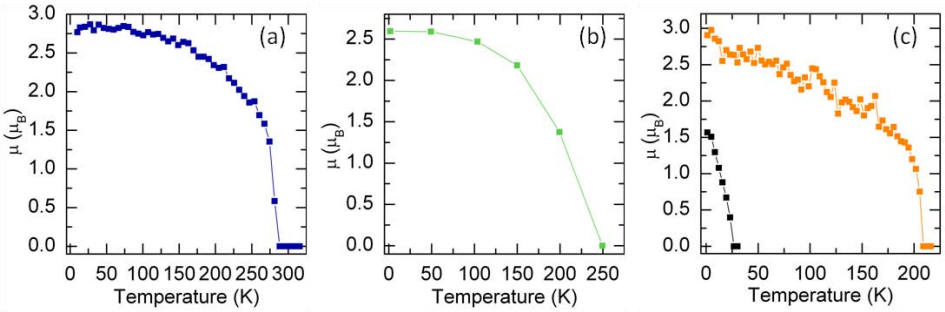

Figure 4. 15. Thermal variation of refined Cr magnetic moment for (a) $LaCrO_{2.72}N_{0.28}$, (b) $PrCrO_{2.64}N_{0.36}$ and (c) variations of the Nd and Cr moments in $NdCrO_{2.58}N_{0.42}$.

The saturated Cr moment values of 2.6-2.7 μ_B are in agreement with theoretical values for these mixed Cr^{3+}(S = 3/2)/Cr^{4+}(S = 1) phases, but the saturated Nd^{3+} moment in $NdCrO_{2.58}N_{0.42}$ is only 1.3 μ_B, showing that these moments are not fully ordered. It is notable that the Nd ordering temperature of 25 K is substantially higher than the 11 K transition reported for $NdCrO_3$. This shows that Nd-Cr spin-spin interactions are enhanced in the insulating $NdCrO_{3-x}N_x$ samples most likely through the presence of more covalent Nd-N-Cr connections.

4.3.4 Effect of O^{2-}/N^{3-} anion substitution *vs* Ln^{3+}/M^{2+} (M= Ca, Sr) cation substitution on the magnetic properties of lanthanide chromites

The variations of T_N with Cr^{4+} content x in our $LnCrO_{3-x}N_x$ samples and literature values for $La_{1-x}Sr_xCrO_3$[216] and $La_{1-x}Ca_xCrO_3$[227] systems are shown in **Figure 4. 16a**. In the pure $LnCrO_3$ perovskites, T_N falls from 293 K for Ln

= La to 226 K for Nd, as smaller Ln^{3+} cations lead to greater bending of Cr-O-Cr bridges and hence weakening of the magnetic superexchange interactions. The different T_N variations with x in the doped series are also in part because of lattice effects reflecting the different influences of N^{3-}, Sr^{2+} and Ca^{2+} as dopants. Previous studies of T_N variations in cation-doped $LnMnO_3$ and other perovskites showed that A-site cation size (equivalent to tolerance factor t) and disorder (variance σ^2) are important, and an approximate single-parameter correction for these effects was proposed.[228, 229] This can be extended to include anion-disorder in AMX_3 perovskites through the equation 4.1.

$$T_N{}^0 = T_N + A < (1 - \frac{d_{Ax}}{d_{Ax}{}^0})^2 > \quad (4.1)$$

where A is a constant, <> denotes an average, and d_{AX} is A-cation to anion distance. An ideal perovskite (with t = 1 and no disorder) at a given doping level x has transition temperature $T_N{}^0$ and $d_{AX}{}^0 = \sqrt{2}<d_{MX}>$ is calculated from the average M-X distance, here using standard 6-coordinate ionic radii for Cr^{3+}/Cr^{4+} cations and O^{2-}/N^{3-} anions.[11]

Systematic studies of multiple doped $LaCrO_3$ systems would be needed to extract an accurate value of the constant A. Here A = 3.0 x 10^4 K is estimated as this gives fair agreement between $T_N{}^0$ values for the three $LnCrO_3$ materials as shown in **Figure 4. 16b**. In this analysis, the Curie transition for an ideal $LnCrO_3$ perovskite with t = 1 is $T_N{}^0 \approx 320$ K. $T_N{}^0$ falls rapidly with x for Sr or Ca doping, however, the decrease with nitride doping is much less steep. This demonstrates that nitride doping has

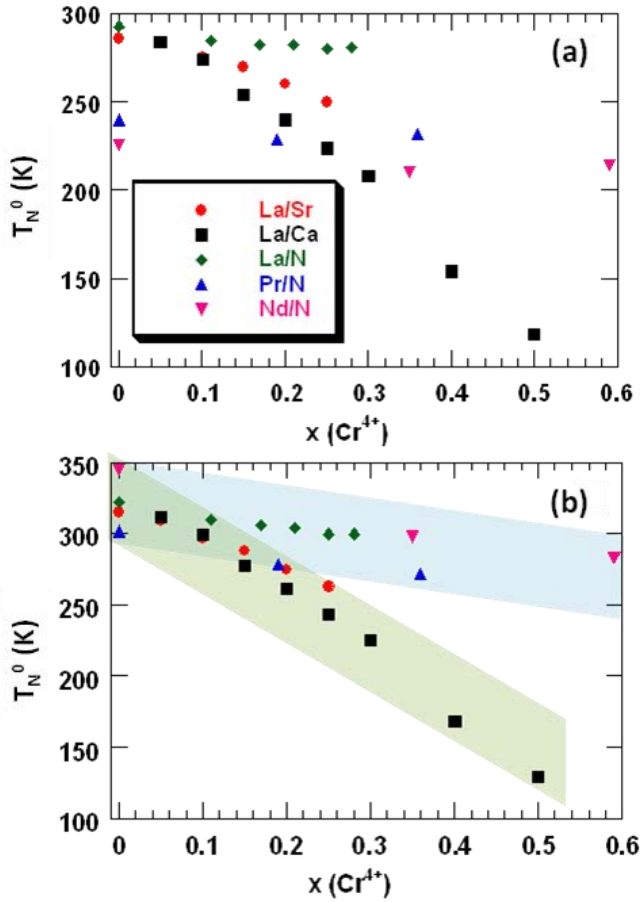

Figure 4. 16. Cr spin ordering temperatures for doped $LnCrO_3$ materials ($LnCrO_{3-x}N_x$ (Ln= La, Pr, Nd), $La_{1-x}Sr_xCrO_3$, and $La_{1-x}Ca_xCrO_3$) as a function of Cr^{4+} content x; (a) measured T_N's, and (b) T_N^0 values corrected for lattice effects as described in the text. The shaded regions show the different T_N^0 variations for nitride and cation doped samples.

another important electronic influence (which lies outside the above analysis of lattice effects); Cr-N-Cr superexchange interactions are evidently stronger than Cr-O-Cr interactions due to greater covalency and these partly offset the suppression of magnetic order T_N^0 due to doping so that T_N^0 remains relatively high even in the most highly nitrided $NdCrO_{2.41}N_{0.59}$ sample. The stronger covalent character of metal-nitride

bonds is a consequence of the lower electronegativity of nitrogen compared to oxygen and has been demonstrated by first principles calculations for several metal oxynitrides including perovskites.[142, 230] In $LnCrO_3$ perovskites the influence of the Cr-O-Cr angle on Néel temperatures for different lanthanides has been widely established. However in the present study it is difficult to determine the effect of nitride on Cr-(O,N)-Cr angles because neutron diffraction data are available only for one O/N ratio for each rare earth cation.

4.4. Conclusions

$AB(O,N)_3$ oxynitride perovskites for early transition metals B = Ti, V; Zr, Nb, Mo; Ta, W have been studied extensively. This study shows that careful ammonolysis of suitable precursors can extend the range to later 3d transition metals such as Cr for which oxynitride perovskites have not previously been reported. The present reactions have led to $LnCrO_{3-x}N_x$ compositions with x up to 0.59 for Ln = Nd. This is in keeping with a previous study of $LnVO_{3-x}N_x$ samples where higher nitrogen contents up to x = 1 were obtained for the smallest (Nd^{3+}) cation used.[231] Stabilisation of Cr^{4+} perovskite oxides such as $SrCrO_3$ requires high pressure, so it may be possible to obtain stoichiometric $LnCrO_2N$ perovskites by using smaller Ln cations under strongly nitriding conditions.

This study also demonstrates that hole-doping of $LnCrO_3$ perovskites through O^{2-}/N^{3-} anion substitution suppresses magnetic order far less drastically than Ln^{3+}/M^{2+} (M = Ca, Sr) cation substitutions do, and Nd spin-order is enhanced up to at least x = 0.4. The greater covalency of metal-nitride bonds compared to metal-oxide enhances magnetic interaction strengths, almost completely compensating for the intrinsic reduction in T_N

due to hole-doping. Hence, nitride-doping may be viewed as a more benign method for doping holes into metal oxides without suppressing electronic transition temperatures than traditional cation-substitution approaches. An insulator to metal transition is reported in $La_{1-x}Sr_xCrO_3$ materials at high Sr contents, and it will be useful to discover whether the same change can be driven by nitridation. Doped-$LaCrO_3$ is also important as a mixed conductor in fuel cells and as an oxidation catalyst for gas combustion and the effects of nitride substitution on these properties will also be of interest.

Chapter V

Hafnium and zirconium oxynitride perovskites, synthesis, structure, electrical properties and photocatalytic activity

$LnMO_2N$ (Ln = La, Pr, Nd, Sm; M= Hf, Zr)

5.1 Introduction

As stated in section 1.5 transition metal oxynitride perovskites $AMO_{3-x}N_x$ (A = alkaline earth metal or rare earth) show a wide variety of functionalities. Among other properties, oxynitride perovskites have been receiving great attention as heterogeneous photocatalysts. Since the discovery of the visible light activity of $LaTiO_2N$ in water splitting,[151] intense efforts have been directed towards the development of new oxynitride photocatalysts. Oxynitride perovskites of Ti^{4+}, Nb^{5+} and Ta^{5+} with d^0 configuration have shown to be active for H_2 or O_2 evolution. Only $LaMg_xTa_{1-x}O_{1+3x}N_{2-3x}$ ($x \geq 1/3$), [150]$LaTiO_2N$ and $CaNbO_2N$ have been reported to carry on the overall water splitting reaction.[152] Tantalum perovskites $MTaO_2N$ (M = Ca, Sr, Ba) have shown to be active for H_2 evolution but not for water oxidation. $SrNbO_2N$ is active only for O_2 evolution and other niobium perovskite oxynitride such as $BaNbO_2N$ and $LaNbO_2N$ are not active or showed poor activity.[153, 154]

Zirconium oxynitride perovskites $LnZrO_2N$ have been prepared for the rare earth elements La, Pr, Nd and Sm. S. J. Clarke et al. reported the synthesis of this compound by thermal ammonolysis of amorphous $La_2Zr_2O_7$ precursor.[129] The direct solid state synthesis of $LnZrO_2N$ (Ln = Pr, Nd, Sm) by high pressure was reported by M. Yang et al.[232] However, the electronic properties and photocatalytic activity of $LnZrO_2N$ have not been previously reported. Although, hafnium and zirconium show similar chemical properties, hafnium chemistry still remains much less explored. Several hafnium based oxides (ex: HfO_2, $HfSi_xO_y$, $HfAl_xO_y$) and especially hafnium oxynitride Hf_2ON_2 are important high *k* gate dielectric materials used to replace SiO_2 in field-effect transistors.[233] Alkaline earth hafnium

perovskites $AHfO_3$ (A = Ca, Sr, Ba) have been investigated as potential microwave resonators for wireless communications as their present low dielectric losses, high quality factors and medium permittivities.[234] At room temperature $BaHfO_3$ presents a cubic $Pm\bar{3}m$ space group while $SrHfO_3$ and $CaHfO_3$ adopt the $GdFeO_3$ orthorhombic crystal structure in the space group *Pnma*. $SrHfO_3$ undergoes several phase transitions until it adopts the $Pm\bar{3}m$ structure at temperatures higher than 1360 K.[235] Alkali earth hafnium and zirconium perovskites show band gaps between 5.7 and 4.8 eV.[236] These values limit absorption to photons with wavelengths below 250 nm suppressing all interest on their possible photocatalytic properties from the viewpoint of solar energy storage.

Here we show the synthesis, structure, electrical and photocatalytical properties of hafnium and zirconium oxynitride perovskites $LnMO_2N$ (Ln = La, Pr, Nd, Sm; M= Hf, Zr). These oxynitrides are isostructural to $SrHfO_3$, crystallizing at room temperature in the $GdFeO_3$-type structure with cell parameters $\sqrt{2}a_p \times \sqrt{2}a_p \times 2a_p$ where a_p is the cubic perovskite subcell parameter. The concomitant substitution of oxygen by nitrogen and the alkaline earth metal by a lanthanide in $AHfO_3$ (A=alkaline earth) leads to the first hafnium oxynitride perovskites.

Because of the lower electronegativity of nitrogen the top of the valence band in oxynitrides is higher in energy than in oxides leading to the reduction of the band gap. The extent of the band gap reduction is variable and depends on the nature of the cations and the amount of nitrogen introduced, and it may also be affected by symmetry changes occurring as a consequence of nitriding. From theoretical calculations the expected range of band gap reduction in d^0 transition metal oxide perovskites may be up to 4 eV.[237]

$LnMO_2N$ (Ln = La, Pr, Nd, Sm; M= Hf, Zr) are prepared by a high temperature synthesis method using HfO_2N_2 or ZrN as nitrogen source reactants and rare earth oxides, treated at 1500 ^{0}C in a N_2 atmosphere. Similar high temperature methods have been used for the synthesis of $ATaO_2N$ (A=Sr, Ba), Sr_2TaO_3N[132,238] or for $LnZrO_2N$ (Ln= Pr, Nd, Sm) in combination with high pressure.[232] In addition to the new $LnHfO_2N$ perovskites, $LaZrO_2N$ is prepared for the first time at high temperatures at ambient pressure. The body colours of the hafnium and zirconium oxynitrides are blue and green yellow respectively showing band gaps between 2.8 and 3.4 eV. These represent a significative reduction when compared to the analogous alkaline earth oxidic perovskites with the following reported band gaps: $SrHfO_3$, 5.7 eV; $BaHfO_3$ 4.8 eV[236], $SrZrO_3$, 5.6 eV.[239] Several oxynitride hafnium and zirconium perovskites show the appropriate band gap and redox potentials to carry on both water reduction and oxidation processes in presence of the adequate sacrificial agent. However, $LaHfO_2N$ shows the best performance in terms of production and stability towards photocorrosion. IrO_x showed to significantly enhance the O_2 evolution rate for $LaHfO_2N$, and $LaZrO_2N$ presents photocatalytic activity for O_2 evolution under visible light irradiation. The as synthesized pellets showed adequate degree of sinterization and electrical resistivity and dielectric measurements showed that nitridation does not induce a large change in the dielectric permittivities which are similar to those shown by the analogous alkaline earth oxidic compounds.

5.2 Objectives

The objectives can be summarized as follows:

- Synthesis of new lanthanide hafnium oxynitride perovskites by high temperature solid state reaction and crystal structure determination including the anion order study.
- Characterization as catalysts for photochemical splitting of water under UV and visible light and photoelectrochemical study.
- Characterization of their electrical properties: electrical resistivity and dielectrical measurements.

5.3 Results and discussion

5.3.1 Synthesis of $LnHfO_2N$ Ln = La, Nd, Sm, Pr.

$LnHfO_2N$ with Ln = La, Pr, Nd and Sm were prepared by the solid state reaction at 1500 ^{0}C under N_2 (Air Liquide, 99.9999 %) flow:

$$Hf_2ON_2\ (s) + \ Ln_2O_3\ (s) \rightarrow 2\ LnHfO_2N\ (s)$$

La_2O_3 (Aldrich, 99.99 %), Nd_2O_3 (Aldrich, 99.9 %) and Sm_2O_3 (Alfa Aesar, 99.998 %) were previously overnight dried under Ar flow at 900 ^{0}C. Pr_2O_3 was prepared from Pr_6O_{11} (Aldrich, 99.9 %) by thermal reduction at 1100 ^{0}C under N_2/H_2 (95%/5% v/v, Air Liquide, 99.999%) flow for 24h. 0.7 % (w/w) of graphitic C (Aldrich) was added to act as oxygen scavenger The powders were thoroughly mixed in an agate mortar for 30 min in the glove box, pressed into a pellet, placed in a molybdenum crucible and covered

with a zirconium foil. The mixtures were fired at 1500°C during 3 hours with heating and cooling rates of 300 °C/h for the lanthanum, neodymium and samarium samples. The praseodymium samples were treated during 15 h at 1500^0C using heating and cooling rates of 300 °C/h. Heating and cooling rates were kept constant as represented in the following scheme:

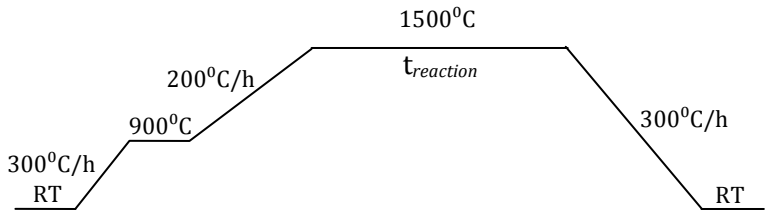

The hafnium oxynitride was synthesized by heating hafnium oxide under flowing ammonia gas for 3 cycles of 18 h at 1000 ^{0}C with intermediate regrinding. The ammonolysis reaction was as follows:

$$2\,HfO_2\,(s) + \,2\,NH_3(g)\, \rightarrow Hf_2ON_2\,(s) + \,3\,H_2O\,(g)$$

Ammonia flow was kept at 600 cc/min. Heating and cooling rates were kept constant at 300^0C/h. The obtained product was a pale grey colour powder. The X-ray diffraction data of Hf_2ON_2 sample was successfully fitted using the space group *Ia-3* (No. 206) (**Figure 5. 1**) with cell parameter a = 10.0621(4) Å in good agreement with the results by S. J. Clarke et al.[240] The nitrogen content per formula determined by chemical analyses was N = 2.05(1).

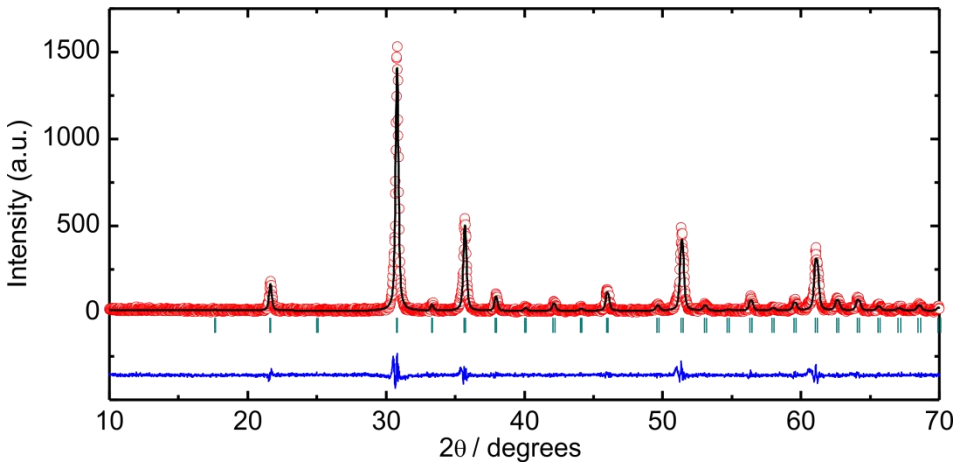

Figure 5. 1. Observed and calculated X-ray powder diffraction patterns for Hf_2ON_2.

5.3.2 Synthesis of $LaZrO_2N$

$LaZrO_2N$ was synthesised by a solid state reaction in N_2 of the stoichiometric mixture of ZrN (Alfa Aesar, 99.5 %,), ZrO_2 (Aldrich, 99.99 %), and La_2O_3. ZrO_2 was previously overnight dried under Argonne at 600^0C and ZrN was overnight dried under dynamic vacuum at 75 ^{0}C. Total oxygen present in the reactants was adjusted using the empirical ratio previously found for the synthesis of $LaMSiO_3N$: $O_{products}/O_{reactans}$= 1.055. The powders were thoroughly mixed in an agate mortar for 30 min in the glove box, pressed into a pellet, placed in a molybdenum crucible and covered with a zirconium foil. The pellet was first treated at 600 ^{0}C during 3 hours followed by treatment at 1500 ^{o}C for 25 hours using heating and cooling rates of 300 °C/h. Oxynitride zirconium perovskites with other lanthanides, such as neodymium or samarium did not form using similar synthetic conditions.

5.3.3 Chemical characterization

5.3.3.1 Determination of nitrogen content by combustion analysis

The nitrogen contents determined by combustion analyses are summarized in **Table 5. 1**.

Table 5. 1. Nitrogen content determined by combustion analysis for $LnMO_2N$ samples (M= Zr, Hf)

Sample	1st assay N (wt %)	2nd assay N (wt %)	Avg. N(wt %)	N content
$LaHfO_2N$	3.92	3.92	3.92	1.02(2)
$PrHfO_2N$	3.82	3.79	3.81	0.99(2)
$NdHfO_2N$	3.87	3.82	3.85	1.01(2)
$SmHfO_2N$	3.88	3.86	3.87	1.04(2)
$LaZrO_2N$	4.97	4.94	4.96	0.98(2)

The values of nitrogen per formula agree with the nominal value within the standard deviation.

5.3.3.2 Thermogravimetric analysis

The TGA curves in oxygen for $LnHfO_2N$ (Ln = La, Pr, Nd, Sm) are shown in **Figure 5. 2**. As expected these curves show a mass gain due to the decomposition of the oxynitride into the oxide as shown in the equation:

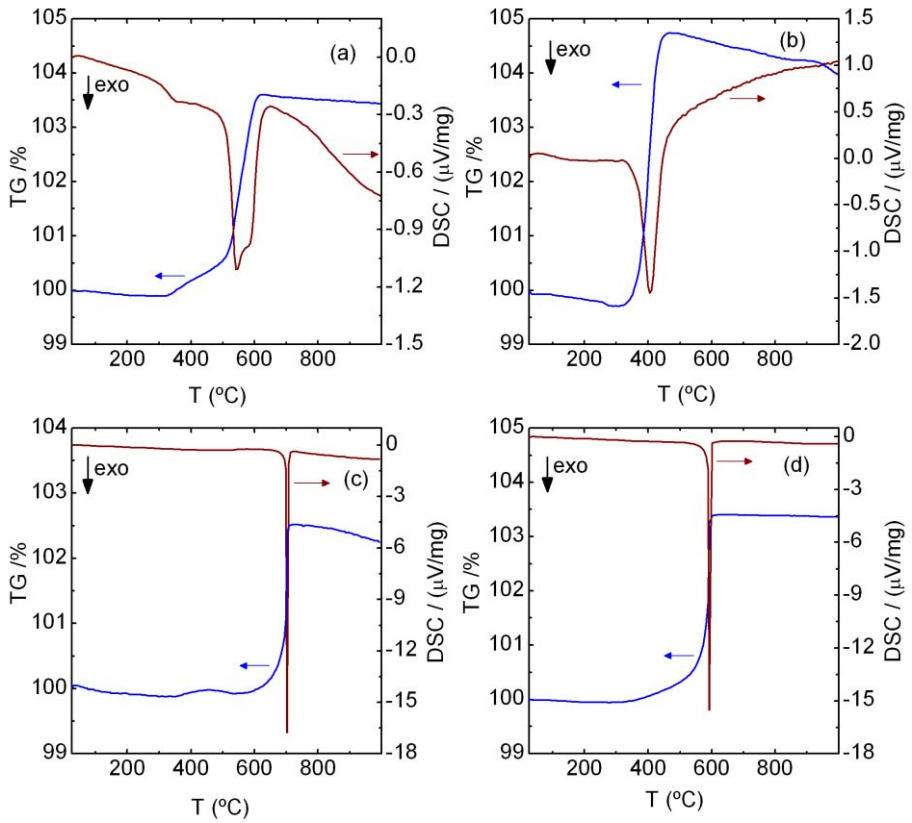

Figure 5. 2. TGA and DSC curves in O_2 for $LnHfO_2N$ with the lanthanides (a) La, (b) Pr, (c) Nd and (d) Sm.

$$LnHfO_{3-x}N_{x\,(s)} + \frac{3x}{4}O_{2\,(g)} \rightarrow \frac{1}{2}Ln_2Hf_2O_{7\,(s)} + \frac{x}{2}N_{2\,(g)}$$

This process leads to the corresponding oxides stable at the maximum temperature used in the experiments (1000 ºC) which are the pyrochlores $Ln_2Hf_2O_7$ for Ln= La, Sm and Nd. For Ln=Pr the final stoichiometry was considered to be '$PrHfO_{3.83}$' as Pr_2O_3 oxidizes to Pr_6O_{11} at high temperature.[241] The amount of evolved nitrogen can be determined from the weight gain (Δm) and can be used to quantify the nitrogen content (x):

$$x = \frac{\Delta m}{(\frac{3}{2}M(O_2) - M(N_2))} \times \frac{\frac{1}{2}M\ (Ln_2Hf_2O_7)}{m\ (Ln_2Hf_2O_7)}$$

Where $M(N_2)$ and $M(O_2)$ are the molar masses of molecular nitrogen and oxygen. $M(Ln_2Hf_2O_7)$ and $m(Ln_2Hf_2O_7)$ are the molar mass of the formed oxide and its weight, respectively.

The nitrogen contents determined by TGA are summarized in **Table 5. 2**.

Table 5. 2. Nitrogen content determined by TGA.

Sample	T_{onset}	Δm (%)	N stoichiometry
$LaHfO_2N$	325	3.65	1.31
$PrHfO_2N$	300	4.69	1.21
$NdHfO_2N$	400	2.53	0.93
$SmHfO_2N$	300	3.44	1.28

In contrast to results from chemical analysis the nitrogen contents determined from TGA for La and Sm were higher than expected. The decomposition of the samples to the oxides started at temperatures from 300 °C (for $PrHfO_2N$) to 380 °C (for $NdHfO_2N$) and involves several processes. For Ln = La, Sm and Nd an initial small increase of weight is observed followed by the main, strongly exothermic oxidation reaction. The reaction with oxygen of the Pr compound involves, in addition to the decomposition of the oxynitride, the oxidation at low temperature of Pr^{3+} into Pr^{4+}. This reaction affects the TGA profile which is different from the other derivatives.

5.3.4 Structural Characterization

5.3.4.1 X-ray diffraction

The X-ray diffraction patterns of $LnMO_2N$ (Ln = La, Pr, Nd, Sm; M = Zr, Hf) are shown in **Figure 5. 3.**

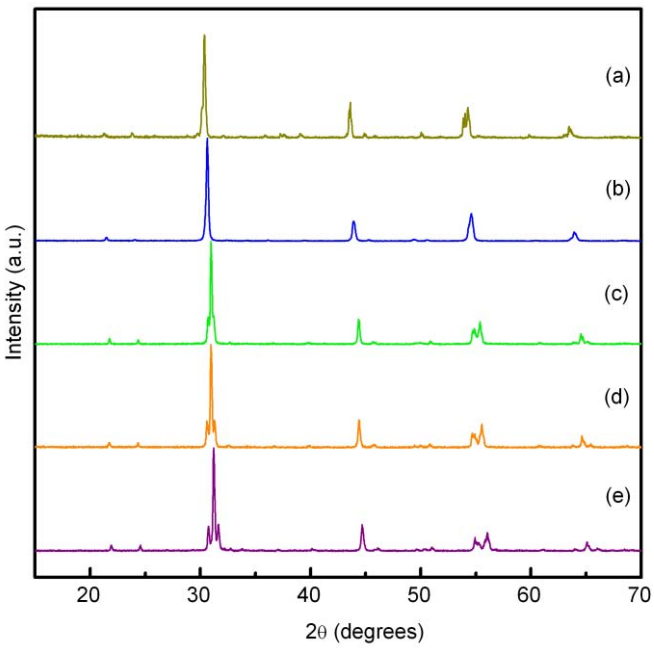

Figure 5. 3. Laboratory X-ray diffraction patterns of (a) $LaZrO_2N$, (b) $LaHfO_2N$, (c) $PrHfO_2N$, (d) $NdHfO_2N$, (e) $SmHfO_2N$.

Synchrotron data were collected from capillary (0.5 mm diameter) samples in the angular range $3.98^o \leq 2\theta \leq 51.10^o$ at the MSPD beamline of the ALBA Synchrotron (Cerdanyola del Vallès, Spain). Using a double Si (111) crystal monochromator, a short wavelength was selected and calibrated with Si NIST. The X-ray wavelengths were 0.619604 Å for $LaMO_2N$ with M = Hf, Zr, 0.6263 Å for $NdHfO_2N$ and 0.4127 Å for $LnHfO_2N$ with Ln = Pr, Sm. The

detectors used were the high resolution MAD26 (for the Pr and Sm compound) and Mythen (for the La, Nd compounds).

All compounds crystallize in the orthorhombic $GdFeO_3$-type with space group *Pnma* ($n^0 62$). The refinement results of synchrotron diffraction data are shown in **Figure 5. 4** to **5.8** and **Table 5. 3** to **Table 5. 7**. Refined cell parameters, atomic positions, selected bond lengths and agreement factors are given in **Table 5. 3** to**Table 5. 7**. Refinements were performed using Fullprof. The profile function was a Thompson-Cox-Hastings pseudo-Voigt convoluted with axial divergence asymmetry function and additional anisotropic strain broadening mode for Laue class *mmm*.[242] Background refinement was performed by linear interpolation. Initial parameters were taken from the isostructural compound $SrHfO_3$.[243] Thermal factors were isotropically refined. Cation occupancies were fixed to their nominal value. As O^{2-} and N^{3-} have similar X-ray scattering factors, the nitrogen was constrained to the combustion analysis results, and distributed in the equatorial and axial anionic sites according to the refined occupancies obtained from neutron diffraction data. A small amount (~1 %) of an unidentified impurity was present in the samarium sample, a peak around 4.5 $Å^{-1}$ that can be seen in the inset of **Figure 5. 7**. This peak was not taken into account for the refinement. The refinement against the synchrotron X-ray data of $LaZrO_2N$ includes two impurity phases: $La_2Zr_2O_7$ and ZrN with refined weight fractions of 1.34(6) % and 2.95(10) %, respectively. The secondary phase observed on the praseodymium and samarium samples in **Figure 5. 5** and **Figure 5. 7** is TiO_2 (rutile) corresponding to cryostat components.

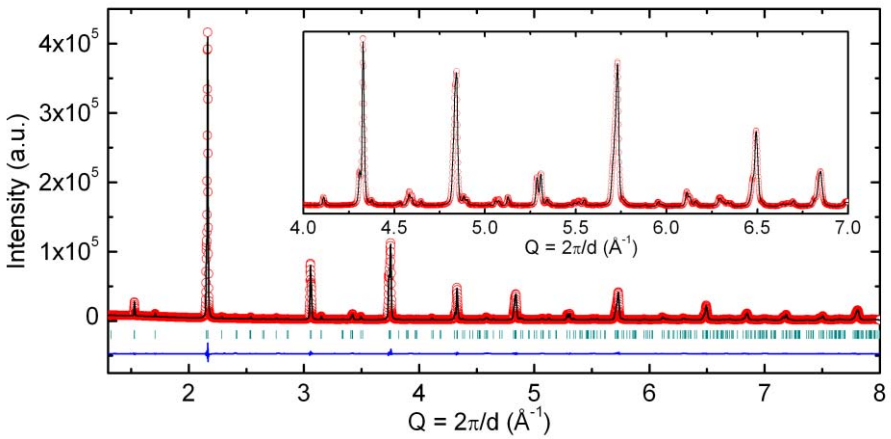

Figure 5. 4. Observed and calculated synchrotron X-ray powder diffraction patterns for $LaHfO_2N$. The inset shows a magnification of the high Q region.

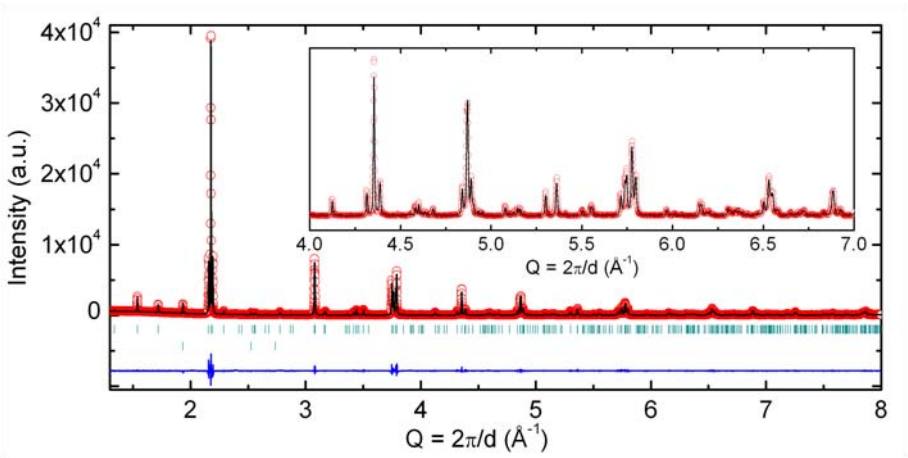

Figure 5. 5. Observed and calculated synchrotron X-ray powder diffraction patterns for $PrHfO_2N$. Tick marks indicate allowed reflections for $PrHfO_2N$ (upper set) and TiO_2 from the cryostat (lower set). The inset shows a magnification of the high Q region.

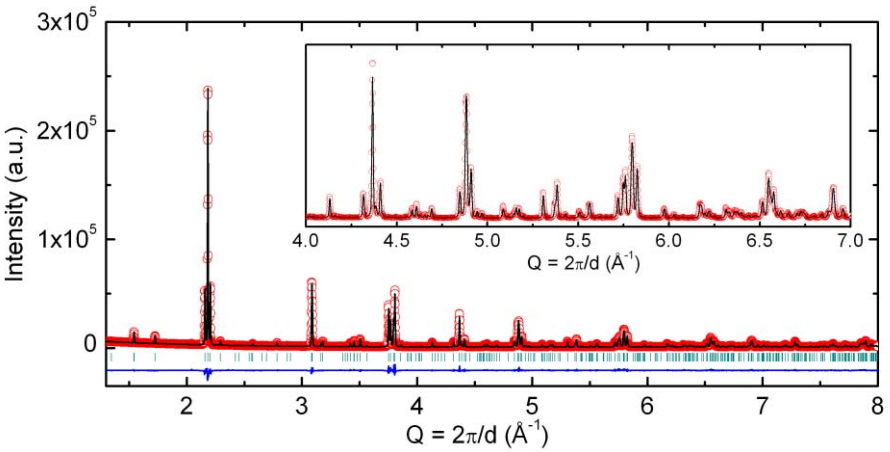

Figure 5. 6. Observed and calculated synchrotron X-ray powder diffraction patterns for $NdHfO_2N$. The inset shows a magnification of the high Q region.

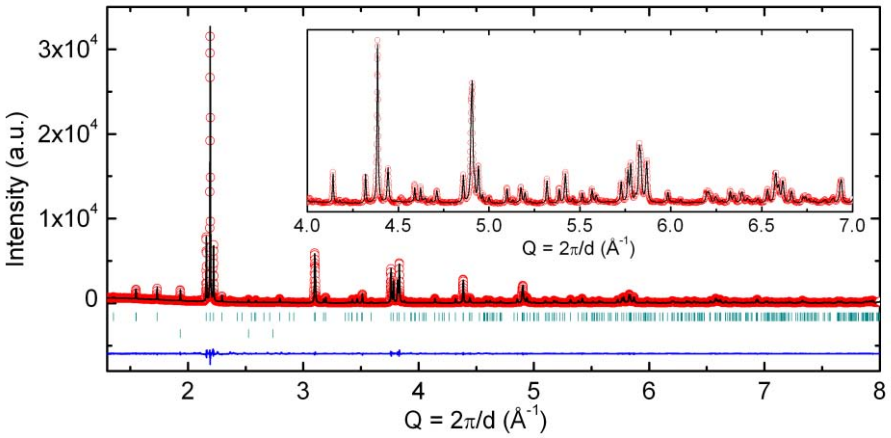

Figure 5. 7. Observed and calculated synchrotron X-ray powder diffraction patterns for $SmHfO_2N$. Tick marks indicate allowed reflections for $SmHfO_2N$ (upper set) and TiO_2 from the cryostat (lower set). The inset shows a magnification of the high Q region.

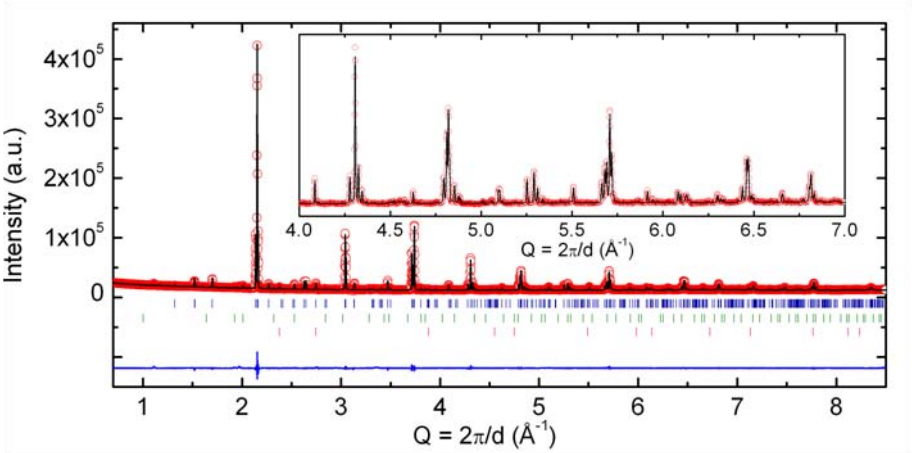

Figure 5. 8. Observed and calculated synchrotron X-ray powder diffraction patterns for $LaZrO_2N$. Tick marks indicate allowed reflections for $LaZrO_2N$ (upper set), $La_2Zr_2O_7$ impurity (middle set) and ZrN impurity (lower set). The inset shows a magnification of the high Q region.

Table 5. 3. Summary of the *Pnma* model for $LaHfO_2N$ refined against room temperature synchrotron X-ray powder diffraction data.

Cell parameters (Å)				Agreement factors	
a = 5.83312(1)				R_{Bragg} = 1.35	
b = 8.20182(2)				R_{wp} = 2.76	
c = 5.79828(2)				χ^2 = 3.70	
Atom	Site	X	y	z	B_{iso} (Å^2)
La	4c	0.02922(6)	¼	0.9926(2)	1.302(1)
Hf	4b	½	0.0	0.0	0.9324(8)
X1	4b	0.4757(9)	¼	0.0889(12)	0.52(2)
X2	8d	0.2958(8)	0.0480(7)	0.7128(11)	1.24(2)
		La-X1	La-X2	Hf-X1	Hf-X2
Bond length / Å		3.277(5)	2.792(6) ×2	2.119(2)×2	2.085(6)×2
		2.664(5)	2.453(6)×2		2.157(5)×2
		3.386(7)	3.534(6)×2		
		2.447(7)	2.940(6)×2		
$\langle La-O/N \rangle$		2.94(2)		$\langle Hf-O/N \rangle$	2.120(8)

Table 5. 4. Summary of the *Pnma* model for $PrHfO_2N$ refined against room temperature synchrotron X-ray powder diffraction data.

Cell parameters (Å)				Agreement factors	
a = 5.82447(2)				R_{Bragg} = 3.01	
b = 8.15752(1)				R_{wp} = 10.4	
c = 5.72826(2)				χ^2 = 3.65	
Atom	Site	X	y	z	B_{iso} (Å^2)
Pr	4c	0.03983(10)	¼	0.9896(2)	0.869(1)
Hf	4b	½	0.0	0.0	0.50(1)
X1	4b	0.4645(16)	¼	0.0937(16)	0.46(4)
X2	8d	0.2918(13)	0.0583(10)	0.7039(13)	0.76(3)
		Pr-X1	Pr-X2	Hf-X1	Hf-X2
Bond length / Å		3.404 (9)	2.698(8)×2	2.119(2)×2	2.139(8)×2
		2.544(9)	2.400(8)×2		2.116(8)×2
		3.370(9)	2.965(8)×2		
		2.427(9)	3.625(8)×2		
$\langle Pr-O/N \rangle$		2.93(3)		$\langle Hf-O/N \rangle$	2.125(11)

Table 5. 5. Summary of the *Pnma* model for $NdHfO_2N$ refined against room temperature synchrotron X-ray powder diffraction data.

Cell parameters (Å)				Agreement factors	
a = 5.82227(2)				R_{Bragg} = 2.24	
b = 8.13418(2)				R_{wp} = 4.80	
c = 5.69967(1)				χ^2 = 4.47	
Atom	Site	X	y	z	B_{iso} (Å^2)
Nd	4c	0.04315(8)	¼	0.98835(19)	1.048(2)
Hf	4b	½	0.0	0.0	0.747(1)
X1	4b	0.4614(14)	¼	0.0980(14)	1.13(3)
X2	8d	0.2960(10)	0.0575(8)	0.7023(11)	0.81(2)
		Nd-X1	Nd-X2	Hf-X1	Hf-X2
Bond length / Å		3.444(8)	2.698(6)×2	2.121(2)×2	2.123(6)×2
		2.514(8)	2.388(6)×2		2.126(6)×2
		3.376(8)	3.642(6)×2		
		2.405(8)	2.936(6)×2		
$\langle Nd-O/N \rangle$		2.93(2)		$\langle Hf-O/N \rangle$	2.123(9)

Table 5. 6. Summary of the *Pnma* model for $SmHfO_2N$ refined against room temperature synchrotron X-ray powder diffraction data.

Cell parameters (Å)				Agreement factors	
a = 5.81768(2)				R_{Bragg} = 2.99	
b = 8.09701(3)				R_{wp} = 10.7	
c = 5.65554(2)				χ^2 = 3.52	
Atom	Site	X	y	z	B_{iso} (Å²)
Sm	4c	0.04796(11)	¼	0.98824(25)	0.81(1)
Hf	4b	½	0.0	0.0	0.48(1)
X1	4b	0.4469(18)	¼	0.1043(19)	0.44(4)
X2	8d	0.2933(15)	0.0591(12)	0.6897(17)	1.02(4)
		Sm-X1	Sm-X2	Hf-X1	Hf-X2
Bond length / Å		3.558(11)	2.697(9)×2	2.131(3)×2	2.181(9)×2
		2.412(11)	2.365(9)×2		2.072(9)×2
		3.400(11)	3.678(9)×2		
		2.380(11)	2.901(10)×2		
$\langle Sm-O/N \rangle$		2.92(3)		$\langle Hf-O/N \rangle$	2.128(13)

Table 5. 7. Summary of the *Pnma* model for $LaZrO_2N$ refined against room temperature synchrotron X-ray powder diffraction data.

Cell parameters (Å)				Agreement factors	
a = 5.87471(1)				R_{Bragg} = 4.48	
b = 8.24302(2)				R_{wp} = 2.19	
c = 5.81034(1)				χ^2 = 2.47	
Atom	Site	X	y	z	B_{iso} (Å²)
La	4c	0.0346(1)	¼	0.9898(2)	1.213(3)
Zr	4b	½	0.0	0.0	0.317(4)
X1	4b	0.4699(14)	¼	0.0964(13)	1.65(4)
X2	8d	0.2859(11)	0.0483(7)	0.7083(11)	0.94(3)
		La-X1	La-X2	Zr-X1	Zr-X2
Bond length / Å		3.375(8)	2.761(6)×2	2.143 (2)×2	2.148(6)×2
		2.631(8)	2.495(6)×2		2.108 (6)×2
		3.427(8)	3.559(6)×2		
		2.434(8)	2.961(6)×2		
$\langle La-O/N \rangle$		2.96(2)		$\langle Zr-O/N \rangle$	2.133(9)

Figure 5. 9 shows the variation of lattice parameters and cell volume of $LnHfO_2N$ compounds against Ln^{3+} radius based on refinements of the synchrotron data. The plot reveals an increasing orthorhombic structural distortion as the radii of the rare earth decreases.

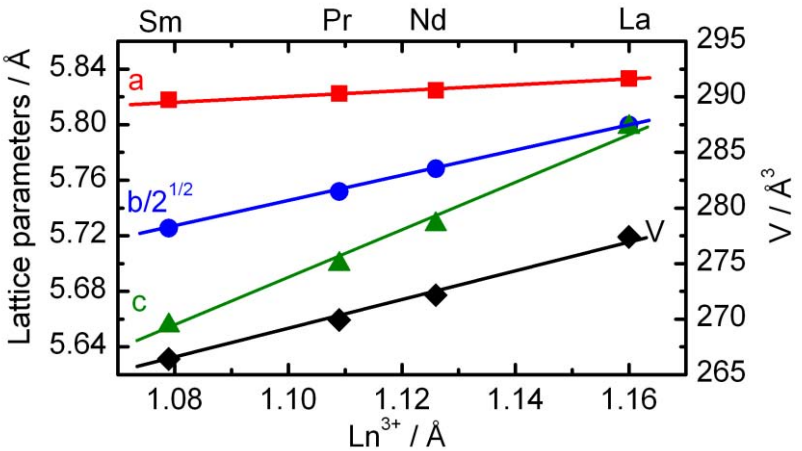

Figure 5. 9. Cell parameters and volume against the Ln^{3+} ionic radius for Ln = La, Pr, Nd, and Sm(CN=8)[11].

The crystal structures of $LnHfO_2N$ (Ln = La, Pr, Nd, Sm) compounds are shown in **Figure 5. 10**.

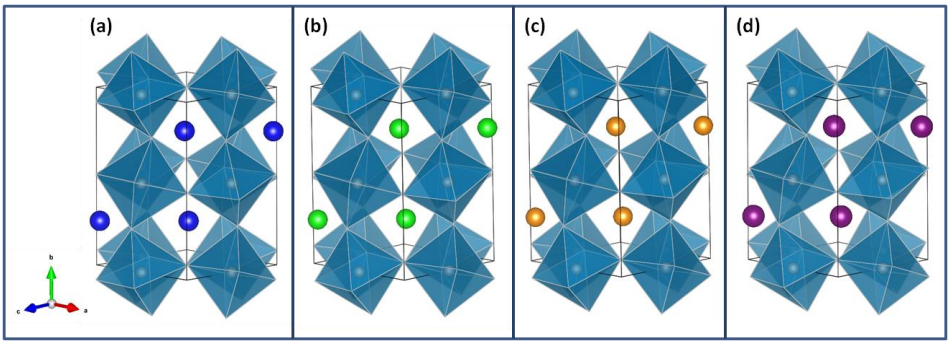

Figure 5. 10. Structural model for $LnHfO_2N$, where Ln = (a) La, (b) Pr, (c) Nd, (d) Sm. $Hf(O/N)_6$ octahedrons are represented in light blue, La^{3+} in blue, Pr^{3+} in green, Nd^{3+} in orange and Sm^{3+} in purple.

The orthorhombic $GdFeO_3$-type superstructure shown by $LnHfO_2N$ compounds is very common in perovskites. Using the Glazer notation this is described as a $a^+b^-b^-$ tilt system consisting in adjacent layers of octahedra tilting in phase around one axis and out of phase around the other two axes. The same structure is shown by the perovskite oxynitrides $NdTiO_2N$, $LaZrO_2N$, $LnVO_2N$ and $LnCrO_{3-x}N_x$ (Ln= La, Pr, Nd).[81, 130, 244] The Goldschmidt tolerance factor,[124] t_{IR} , is shown in table 5.8, calculated as:

$$t_{IR} = \frac{(R_A + R_{O,N})}{[\sqrt{2}(R_B + R_{O,N})]} \quad (2)$$

using ionic radii taken from Shannon and Prewitt (1976) (for CN=XII for La, Nd and Sm and CN=VIII for Pr)[11]. The average anion radius is calculated using $r(N^{3-})$ = 1.46 Å and $r(O^{2-})$ = 1.38 Å both for CN=IV. The tolerance factors of hafnium oxynitride perovskites are low but still in the range of stable perovskites at ambient pressure. Lanthanum titanate presents a higher tolerance factor close to the boundary of stability for the $a^+b^-b^-$ tilt system. Moreover the higher electronegativity of titanium increases the degree of M—(O,N) covalency and induces a larger second order Jahn-Teller effect, which is presumably at the origin of the unusual triclinic distortion observed in $LaTiO_2N$ perovskite.[129]

Table 5. 8. Goldschmidt tolerance factor and observed tolerance factor for selected perovskite oxynitrides.

Compound	Space group	t_{IR}
$LaTiO_2N$[129]	$I\bar{1}$	0.969
$NdTiO_2N$[129]	*Pnma*	0.938
$LaZrO_2N$	*Pnma*	0.920
$LaHfO_2N$	*Pnma*	0.924
$PrHfO_2N$*	*Pnma*	0.846
$NdHfO_2N$	*Pnma*	0.894
$SmHfO_2N$	*Pnma*	0.884
$CaHfO_3$	*Pnma*	0.918
$SrHfO_3$	*Pnma*	0.952
$BaHfO_3$	$Pm\bar{3}m$	1.009

* t_{IR} has been calculated using praseodymium ionic radii in 8 coordination.

5.3.4.2 Neutron powder diffraction

Room temperature neutron powder diffraction data of $LaHfO_2N$ and $LaZrO_2N$ were fitted in the *Pnma* space group. Neutron diffraction data were recorded on the high-resolution diffractometer HRPD at the ISIS spallation source, Rutherford Appleton Laboratory, U.K. Rietveld refinements were performed using the Fullprof program. Structural models were refined against data collected from 90° detector bank, which provide *d*-spacing ranges of 0.6 – 2.5 Å. The profile function used was a neutron time of flight convolution pseudo-Voigt with back-to-back exponential functions. The refined cell parameters obtained from X-ray diffraction data were used as initial parameters. Nitrogen and oxygen were constrained to their nominal value, starting with a statistical distribution in the equatorial and axial anionic sites and constrained to full occupation of each site. The refinement results are presented in **Figure 5. 11** and **Figure 5. 12** and **Table 5. 9** and **Table 5. 10**. Refined cell parameters, atomic positions,

anion occupancies, selected bond lengths and agreement factors are given in **Table 5. 9** and **Table 5. 10**. The $LaHfO_2N$ pattern was taken using 0.5 g of a sample free of impurities according to laboratory X-ray diffraction. Long acquisition times were needed to compensate the absorption of the sample and the low flux of HRPD beamline. Peaks corresponding to vanadium sample holder reflections were excluded from the refinement. The data acquisition of $LaZrO_2N$ pattern was performed on a 0.5 g sample containing $La_2Zr_2O_7$ and ZrN as minor impurities that were included in the refinement together with vanadium. The refinement revealed weight fractions of 6.65(4)% and 1.54(2)% for $La_2Zr_2O_7$ and ZrN, respectively. After refinement of (O/N) occupancies no significant anion order was detected in the two compounds. These results are similar to those reported by S. Clarke and J. Rosseinsky for $LaZrO_2N$.[129] Refinement of neutron diffraction data of $LaZrO_2N$ showed also a statistical distribution of the two anions in the axial and equatorial sites. The synthesis method used in the work by Clark and Rosseinsky was the ammonolysis of amorphous $La_2Zr_2O_7$ at 950 ^{0}C in contrast with the high temperature (1500 ^{0}C) solid state reaction used in this work. Our neutron diffraction results show that the anion distribution in this compound does not depend on the preparation method. The disorder observed in $LaZrO_2N$ and $LaHfO_2N$ differs from the cis-ordering of nitride determined in the perovskites $SrMO_2N$ (M=Ta, Nb),[59] $NdVO_2N$[231] and $LaNbON_2$. [245]

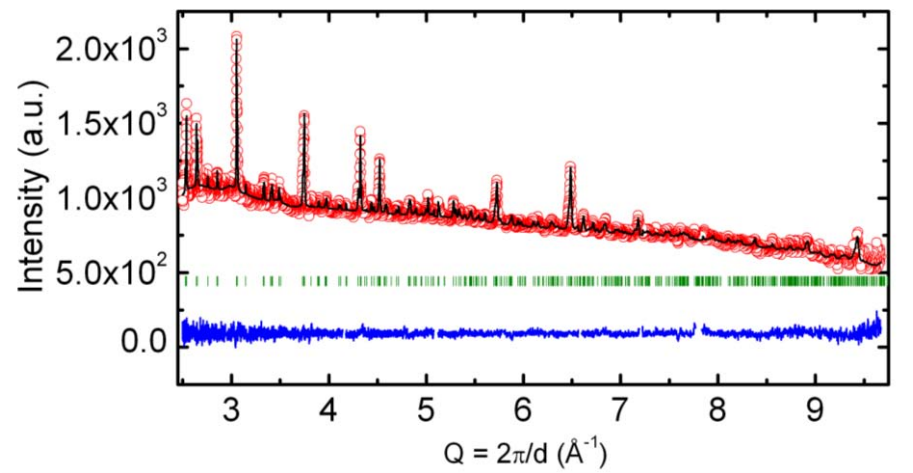

Figure 5. 11. Rietveld fit to room temperature neutron powder diffraction patterns for $LaHfO_2N$.

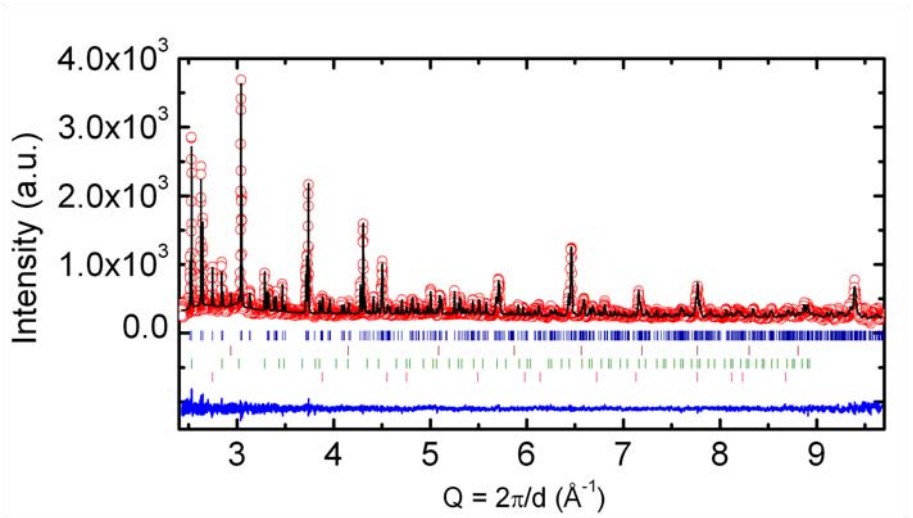

Figure 5. 12. Rietveld fit to room temperature neutron powder diffraction patterns for $LaZrO_2N$. Tick marks indicate allowed reflections for $LaZrO_2N$ (upper set), V can (middle upper set), $La_2Zr_2O_7$ (middle lower set) and ZrN (lower set).

Table 5. 9. Summary of the *Pnma* model for $LaHfO_2N$ refined against room temperature neutron powder diffraction data.

Cell parameters (Å)				Agreement factors		
a = 5.8397 (9)				R_{Bragg} = 11.4		
b = 8.2088 (12)				R_{wp} = 1.85		
c = 5.8016 (8)				χ^2 = 1.26		
Atom	Site	X	y	z	B_{iso} (Å^2)	(O/N) Occ.
La	4c	0.0295(8)	¼	0.9931(15)	0.94(2)	
Hf	4b	½	0.0	0.0	0.23(2)	
X1	4b	0.4728(12)	¼	0.0889(13)	0.9440(8)	0.35(2)/0.15
X2	8d	0.2894(8)	0.0474(5)	0.7142(8)	0.89(3)	0.65/0.35
		La-X1	La-X2	Hf-X1	Hf-X2	
Bond length / Å		3.298(9)	2.773(7)×2	2.122(2)×2	2.101(5)×2	
		2.648(9)	2.486(7)×2		2.134(5)×2	
		3.393(11)	3.509(7)×2			
		2.448(11)	2.954(6)×2			
$\langle La-O/N \rangle$		2.94(3)		$\langle Hf-O/N \rangle$	2.119(7)	

Table 5. 10. Summary of the *Pnma* model for $LaZrO_2N$ refined against room temperature neutron powder diffraction data.

Cell parameters (Å)				Agreement factors		
a = 5.8765 (8)				R_{Bragg} = 7.07		
b = 8.2465 (11)				R_{wp} = 5.96		
c = 5.8128 (8)				χ^2 = 1.62		
Atom	Site	X	y	z	B_{iso} (Å^2)	(O/N) Occ.
La	4c	0.0337(3)	¼	0.9934(6)	0.221(7)	
Hf	4b	½	0.0	0.0	0.056(8)	
X1	4b	0.4727(5)	¼	0.0916(5)	0.53(2)	0.32(1)/0.18
X2	8d	0.2918(3)	0.0505(2)	0.7085(3)	0.35(1)	0.68/0.32
		La-X1	La-X2	Zr-X1	Zr-X2	
Bond length / Å		3.346(3)	2.784(3)×2	2.1353(8)×2	2.131(2)×2	
		2.642(4)	2.471(3) ×2		2.141(2)×2	
		3.419(5)	3.578(3) ×2			
		2.439(5)	2.959(2)×2			
$\langle La-O/N \rangle$		2.955(12)		$\langle Zr-O/N \rangle$	2.136(8)	

5.3.5 Diffuse reflectance spectra

The body colour of the $LaZrO_2N$ sample is greenish-grey (**Figure 5.13**) but it may be affected by the small impurity of ZrN. For $LnHfO_2N$ with Ln = La, Pr, Nd, Sm, the body colour range from pale blue to dark blue. Diffuse reflectance spectra of $LaZrO_2N$ show a drop in reflection in the violet region of the visible spectra around 440 nm, whereas the absorption edge of for $LnHfO_2N$ is around 360 nm for lanthanum and neodymium samples and around 430 nm for the samarium compound (**Figure 5. 14**).

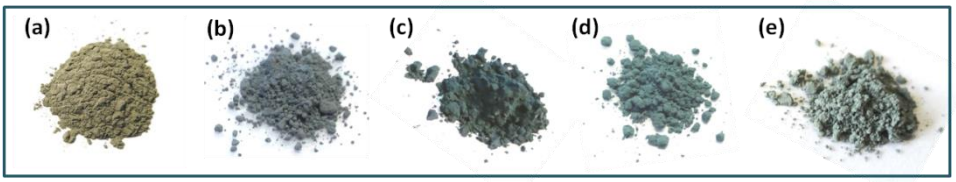

Figure 5. 13. Images of (a) $LaZrO_2N$ and $LnHfO_2N$ powders where Ln= (b) La, (c) Pr, (d) Nd, (e) Sm.

The band gaps determined using the Kubelka–Munk function are 2.80 eV for $LaZrO_2N$ and 3.35, 3.4 and 2.85 eV for the lanthanum, neodymium and samarium hafnium compounds, respectively. A quantitative comparison shows that the smallest band gap is shown by the largest distorted samarium perovskite. This correlation has been previously reported in other perovskites containing d^0 ions, such as $ATa(O,N)_3$ (A= Ca, Sr, Ba or La, Pr, Ce).[134] However the band gaps observed for the lanthanum and neodymium perovskites are identical within the experimental error. The band gap of $LaZrO_2N$ is smaller than for $LaHfO_2N$. This trend is also observed in $LaTiO_2N$ with a reported band gap of 2.41 eV. [237] The reduction in the band gap within the IV group of transition metals from the 5d to 3d row has been predicted for $Zr_3O_3N_2$ and $Ti_3O_3N_2$.[237] The alkaline earth

hafnium and zirconium perovskites AMO_3 A = Sr, Ba; M = Zr, Hf show larger band gaps than the lanthanide oxynitrides: 5.7, 4.8 and 5 eV for $SrHfO_3$, $BaHfO_3$ and $BaZrO_3$ respectively.[236] The concomitant substitution of oxygen by nitrogen and the alkaline earth by the lanthanide produces a band gap reduction of more than 2 eV. The empty *s* orbitals of alkaline earth and some lanthanide ions such as lanthanum are at higher energies and do not have a significant contribution to the band formation in perovskite compounds,[149] so the bottom of the conduction band that is mostly formed by bonding B cation d orbitals. The reduction of the band gap in the oxynitrides is to a large degree due to the rise of the top of the valence band produced by the increase of N2*p*-O2*p* overlap, which leads to a more antibonding character and narrowing of the band gap. Despite that the band gap narrowing is large, the high energy position of Hf d orbitals leads to materials with optical edges still in the UV region for lanthanum and neodymium. The three hafnium perovskite oxynitrides show a broad absorption at wavelengths longer than 550 nm, which generally indicates the presence of reduced M^{n+} species or anion defects such as O^{2-} or N^{3-} vacancies.[246] This likely suggests that a small amount of anion vacancies might be introducing localized energy levels in the band gap, close to conduction band, giving place to transitions from these localized states into the conduction band and absorption of photons with energy below the band gap. Possibly, this broad absorption band is responsible for the blue body colour observed for these compounds. In addition to the above features, the diffuse reflection spectrum of $NdHfO_2N$ exhibit several strong 4f electron transitions peaks located in the range between 400 and 800 nm. These bands are attributed to transitions between the ground-state $^4I_{9/2}$ and the excited states within the Nd^{3+} 4f shell. In particular, the most intense bands located at 530, 586 and 755 nm are ascribed to transitions

from the ground state $^4I_{9/2}$ of the neodymium ion to $^2K_{18/2}$, $^4G_{7/2}$, $^4G_{9/2}$ for the peak at 530 nm, to $^4G_{5/2}$, $^2G_{7/2}$ for the peak at 586 nm and to $^4S_{8/2}$, $^4F_{7/2}$ for the peak at 755 nm.[203, 204]

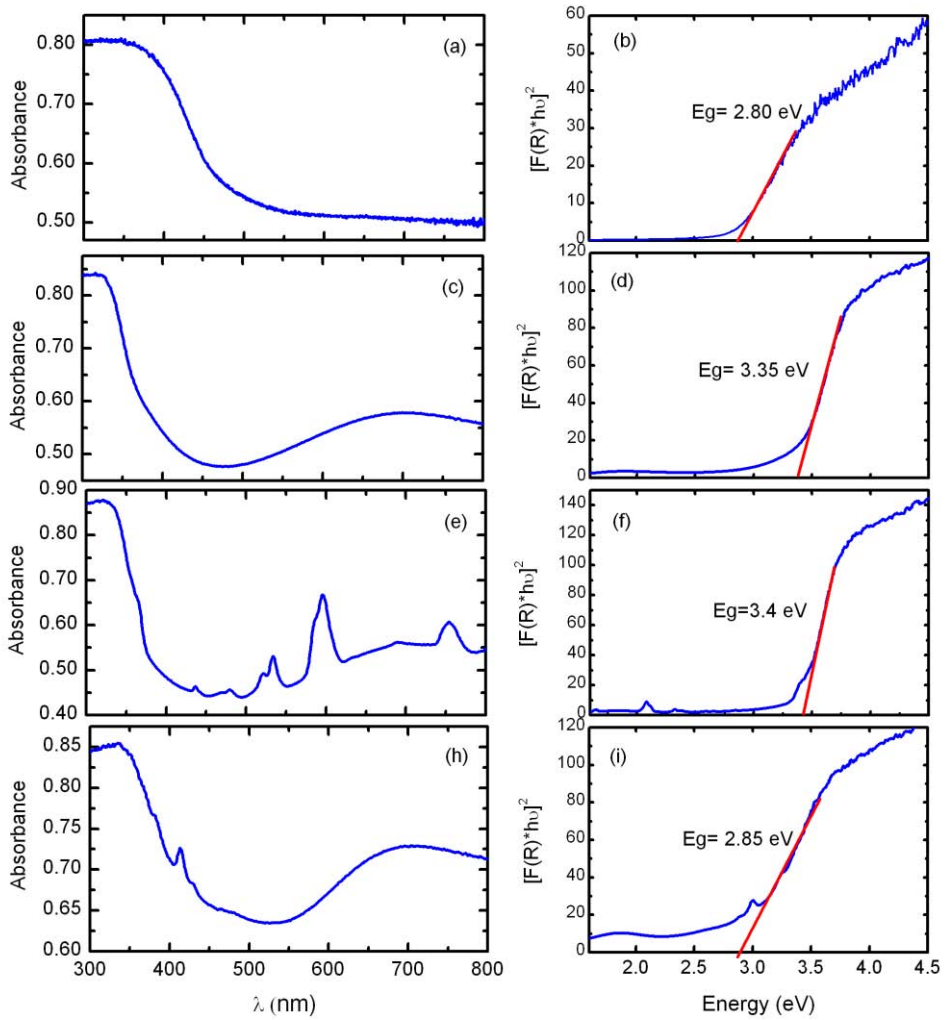

Figure 5. 14. Diffuse reflectance spectra of (a) $LaZrO_2N$, (c) $LaHfO_2N$, (e) $NdHfO_2N$, (h) $SmHfO_2N$ and Kubelka-Munk plot of (b) $LaZrO_2N$, (d) $LaHfO_2N$, (f) $NdHfO_2N$, (i) $SmHfO_2N$.

5.3.6 Photocatalytical activity

5.3.6.1 Photoelectrochemical measurements

Figure 5. 15 shows images of the photoelectrodes prepared by deposition of $LnHfO_2N$ (Ln = La, Nd, Sm) particles on fluorine-doped tin oxide (FTO) glass. The photoelectrodes were prepared by the squeezing method detailed in section 3.6. A postnecking treatment was performed to promote interparticle electron transfer on the $LnHfO_2N$ electrodes by drop wise addition of a 10 mM solution of $Cl_2HfO{\cdot}8H_2O$ in MeOH. A total of five additions of 50 µl of the hafnium dichloride oxide solution were deposited in intervals of 15 min. This was followed by heating under ammonia flow of 20 ml/min at 450 ^{0}C for 0.5 h.

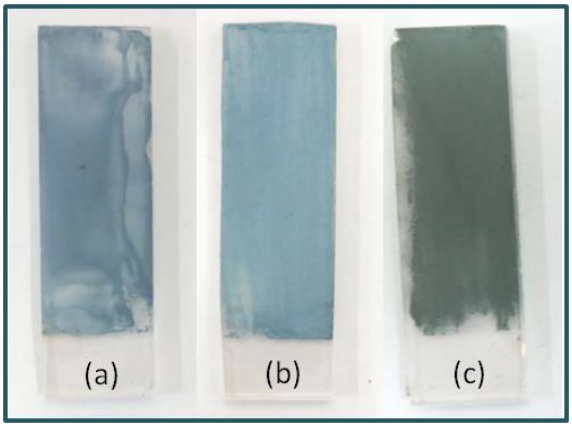

Figure 5. 15. Photoelectrodes prepared by deposition of, (a) $LaHfO_2N$, (b) $NdHfO_2N$ and (c) $SmHfO_2N$ particles on FTO glass.

Figure 5. 16 shows current-voltage curves for $LnHfO_2N$ electrodes for Ln = La, Nd and Sm under intermittent visible light irradiation ($\lambda > 420$ nm, Red line) and full lamp spectrum (blue line). The potential range examined was located between -1 and 1V (vs Ag/AgCl electrode). A 0.1 M solution of

Na_2SO_4 at pH=6 was used as buffer. The light intermittence was fixed to periods of 1s. $LnHfO_2N$ electrodes exhibited anodic photoresponse, for which positive currents are registered during the illuminated periods, indicating that $LnHfO_2N$ is an n-type semiconductor. Small photocurrents are produced under visible light conditions showing a photoelectrochemical activity of $LnHfO_2N$ electrodes (Ln = La, Nd, Sm) in the visible range of spectrum. However, the photocurrent increases significantly under full spectrum radiation. The onset potential registered for lanthanum and neodymium photoelectrodes is around 0.4 V (vs. RHE), situating the bottom of the conduction band of $LaHfO_2N$ and $NdHfO_2N$ below the reduction potential of water. However, the samarium photoelectrode showed a very stable redox behaviour in the potential range above -0.8 V (vs. Ag/AgCl) and the onset potential was found to be around -0.16 V (vs. RHE). This onset potential situates the conduction band of $SmHfO_2N$ oxynitride photoelectrode above the reduction potential of water and therefore suitable for hydrogen production.

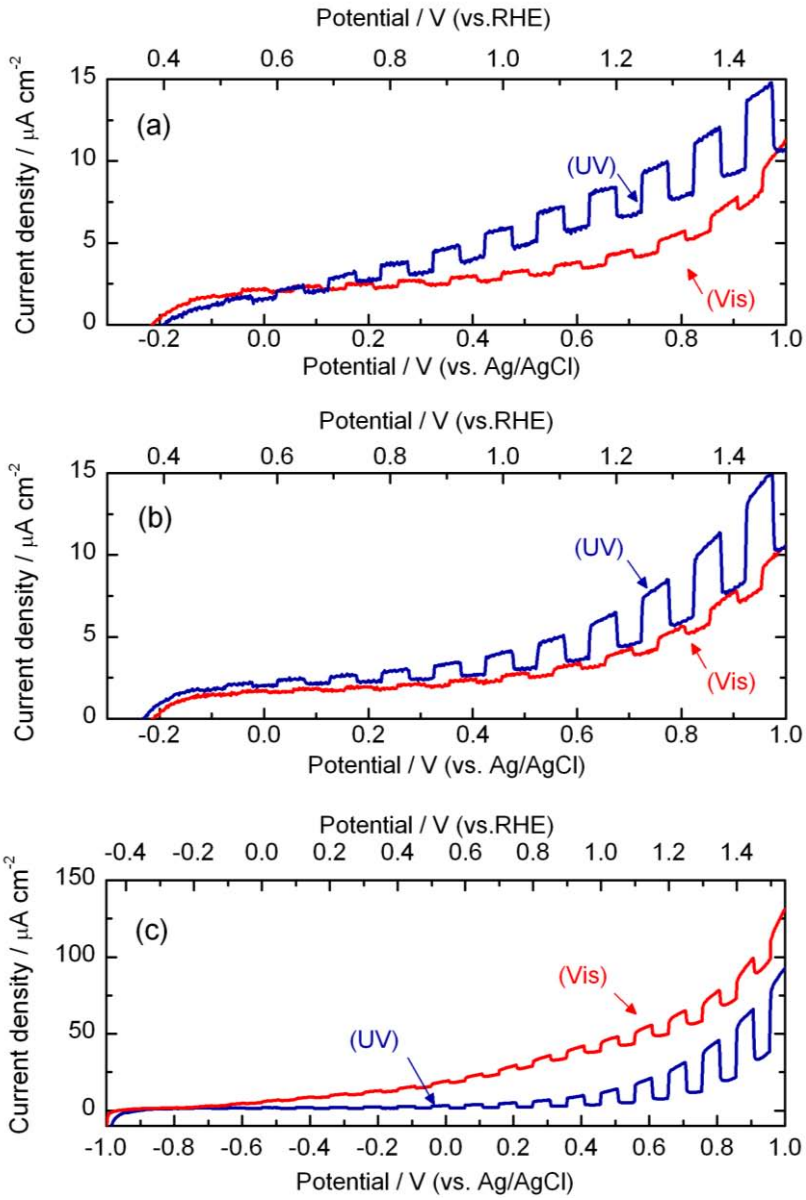

Figure 5. 16. Current-voltage curves in aqueous 0.1 M Na_2SO_4 solution (pH ≈ 6) under intermittent visible (blue line) and full range (red line) light irradiation for $LnHfO_2N$ where Ln = (a) La, (b) Nd and (c) Sm electrodes.

5.3.6.2 Hydrogen and oxygen evolution

The photocatalytic activity of $LnHfO_2N$ (Ln = La, Pr, Nd, Sm) and $LaZrO_2N$ has been evaluated by the study of the half reaction of water splitting (H_2 or O_2 evolution) from an aqueous solution containing a sacrificial reagent under UV or visible radiation. The H_2 evolution experiments were conducted in a 20 vol.% methanol solution, where the methanol acts as the sacrificial electron donor. Pt (1%wt) was loaded on all samples prior to reaction. Here platinum acts as a co-catalyst by improving charge carrier separation and inducing active sites for H_2 evolution. Pt was loaded by impregnation method from H_2PtCl_6 aqueous solution, followed by reduction in H_2 at 573 K for 0.5 h. In the photooxidation of water into O_2, the reactions were performed in an $AgNO_3$ 10 mM solution, were the Ag^+ acts as a sacrificial electron acceptor. Hafnium samples were loaded with 1 % IrO_x that acts as an O_2 co-catalyst on which the back reaction hardly proceeds. Iridium oxide was loaded by an impregnation method from Na_2IrCl_6 aqueous solution, followed by oxidation in air at 573 K for 0.5 h. For the zirconium sample cobalt oxide was used as O_2 evolution co-catalyst. CoO_x was deposited from a $Co(NO_3)_2$ aqueous solution by an impregnation method.

The photochemical reactions were carried out in a Pyrex reaction vessel connected to a gas-closed circulation system equipped with a vacuum line and a gas sampling port that is directly connected to a gas chromatographer. Prior to reaction the slurry was sonicated for 10 min to ensure the dispersion of photocatalyst particles in the suspension and vigorous stirring was kept during the reaction. The reaction vessel was immersed in a thermostatic bath and the reaction solution was evacuated

by several pump/ fill cycles to remove all air. Irradiation was performed with a 300 W Xe lamp equipped with cut-off filters. Further experimental details are included in section 2.6.

5.3.6.2.1 Photocatalytic evolution of O_2 and H_2 by $LaHfO_2N$ in aqueous solution containing a sacrificial reagent

Figure 5. 17 shows the time course of O_2 and H_2 evolution under Xenon lamp 300 W ($\lambda > 300$ nm) irradiation. The reactions were carried out in a 250 ml aqueous solution containing the sacrificial reagents Ag^+ or CH_3OH for water oxidation or reduction, respectively and 50 mg of the modified $LaHfO_2N$ powders. No reaction took place in dark condition, and the gas evolution began with the onset of irradiation. O_2 evolves with the oxidation of water molecules by photogenerated holes, whereas Ag^+ is reduced to Ag by photogenerated electrons. The reduced Ag is subsequently deposited on the surface of the photocatalyst. This mechanism was confirmed by the observation by X-ray photoelectron spectra (XPS) of reduced metallic Ag particles on the photocatalyst surface after the reaction (**Figure 5. 19c**). Further experiments performed in water slurry of IrO_x(1wt%)-SiO_2 or IrO_x(1wt%)-$LaHfO_2N$ under UV irradiation, indicated that IrO_x did not generate O_2 and confirmed that the photogenerated electrons reduced Ag^+ to Ag and holes oxidized water to O_2. The rate of O_2 production over the IrO_x(1wt%)-$LaHfO_2N$ photocatalyst was 0.9 $\mu mol \cdot h^{-1}$. O_2 production over unmodified $LaHfO_2N$ in Ag^+ aqueous solution under Xe lamp 300 W ($\lambda >$ 300 nm) irradiation took place at rate of 0.15 $\mu mol \cdot h^{-1}$, as shown in **Figure 5. 17**. This result shows that $LaHfO_2N$ has the ability to oxidize water in presence of sacrificial electron acceptor and that surface modification of $LaHfO_2N$ with IrO_2 significantly enhanced the rate of O_2 evolution. H_2

evolution occurred as a result of the reduction of H^+ to H_2 by excited electrons at the conduction band of Pt(1wt%)-$LaHfO_2N$. The rate of H_2 production over Pt(1wt%)-$LaHfO_2N$ was 0.07 $\mu mol \cdot h^{-1}$. N_2 evolution was negligible in all experiment. These results indicate that modified $LaHfO_2N$ have the adequate reduction and oxidation potentials to conduct the overall water splitting reaction and that modified $LaHfO_2N$ photocatalysts are stable against the selfoxidation process under the photoreaction conditions.

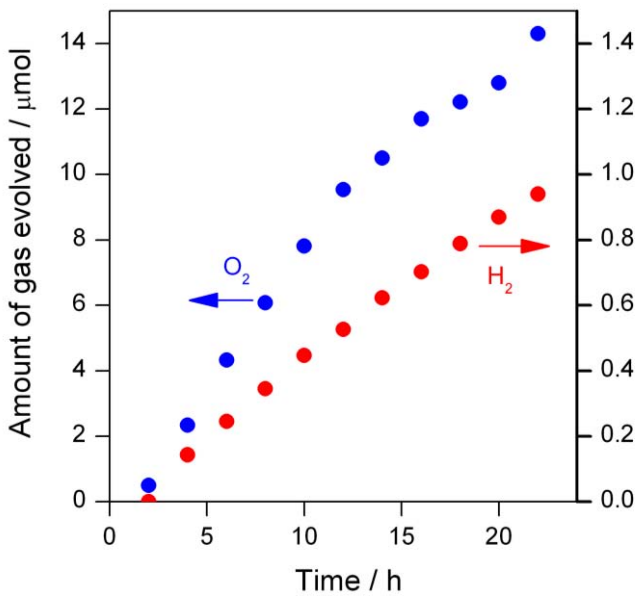

Figure 5. 17. O_2 evolution (blue spots) from 50 mg of IrO_x(1wt%)-$LaHfO_2N$ in 250 ml of a 10 mM solution of $AgNO_3$ and H_2 evolution (red spots) from 50 mg of Pt(1wt%)-$LaHfO_2N$ in 250 ml of a 20 vol.% Methanol solution under 300 W Xe lamp (λ > 300 nm).

However, gas evolution rates are still low which may be caused by several factors: first, the material is prepared at high temperature (1500 ^0C) and shows large particle size and low specific surface area. This increases the required charge carrier diffusion lengths and may affect the stability of the suspension during the reaction. Furthermore, this compound showed a

broad absorption band above 550 nm in the diffuse reflectance measurements, assignable to anion defects as O^{2-} or N^{3-} vacancies. The anion vacancies can act as recombination centers for the photogenerated electrons and holes in the photocatalyst, reducing significatively the life time of the charge carriers and the gas production rates. Finally, poor adsorption of the sacrificial agents on the particles surface could also affect the gas evolution rates.

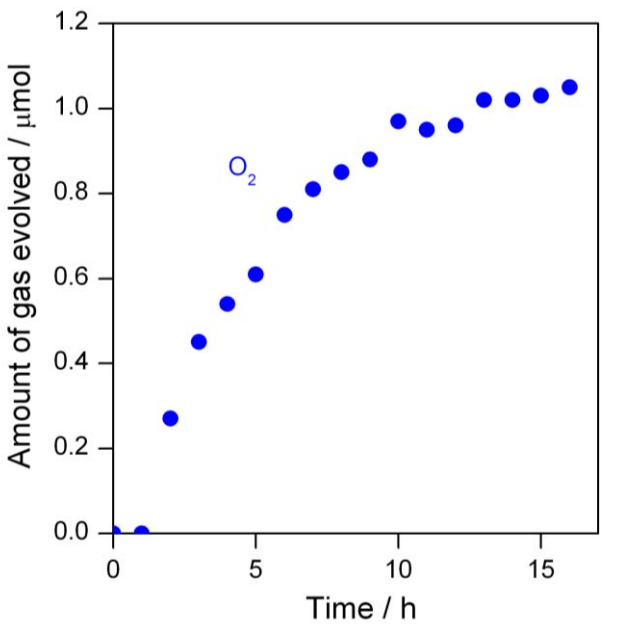

Figure 5. 18. O_2 evolution (blue spots) from 50 mg of $LaHfO_2N$ in 250 ml of a 10 mM solution of $AgNO_3$ under 300 W Xe lamp (λ > 300 nm).

Figure 5. 19a,b show the XPS spectra of the Ir and Pt regions of IrO_x-$LaHfO_2N$ and Pt-$LaHfO_2N$ photocatalysts, respectively. The Ir 4f spectra show the Ir $4f_{7/2}$ and Ir $4f_{5/2}$ spin–orbit doublet at 62.1 and 65.5 eV, respectively.

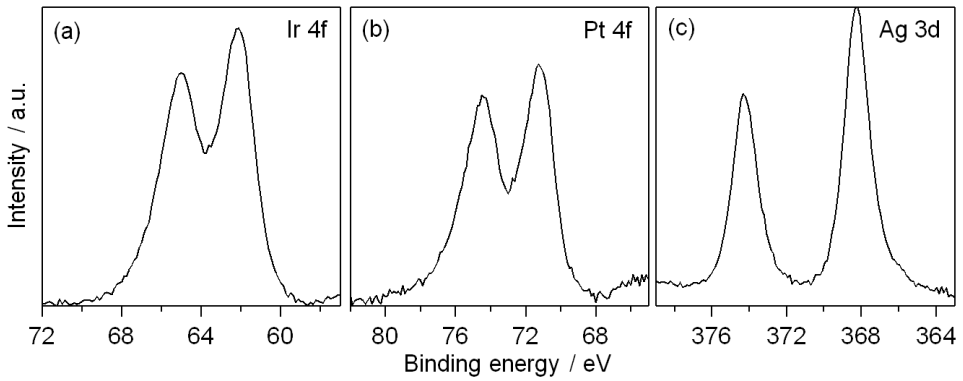

Figure 5. 19. X-ray photoelectron spectra of, (a) IrO_x-$LaHfO_2N$, (b) Pt-$LaHfO_2N$ and (c) IrO_x-$LaHfO_2N$ after O_2 evolution.

The high bonding energies of Ir 4f signals confirm that the dominant valence states of this element are IV and III.[247] In the Pt 4f spectra, the main core-level peaks of metallic Pt $4f_{7/2}$ and $4f_{5/2}$ are observed at 71.7 and 74.2 eV, respectively.[248] This confirms that Pt^0 is the dominant valence state of Pt. The Ag 3d spectrum in **Figure 5. 19c** consists of two peaks at 368.2 and 374.2 eV, attributed to Ag $3d_{5/2}$ and Ag $3d_{3/2}$ binding energies with the spin energy separation of 6 eV, respectively. This indicates that metallic Ag is present on the surface of the photocatalyst after the O_2 evolution reaction.

Figure 5. 20 shows the dependence of the O_2 generated from IrO_x(1wt%)-$LaHfO_2N$ and the H_2 generated from Pt(1wt%)-$LaHfO_2N$, respectively, on the cut-off wavelength of the incident light. In both cases, the gas evolution decreased with increasing the cut-off wavelength, reaching zero at 480 nm. These results are consistent with the diffuse reflection measurements of $LaHfO_2N$ (**Figure 5. 14c**) indicating that the water oxidation and reduction reactions occurred photocatalytically through band gap excitation, and that the broad absorption band at wavelengths longer than 500 nm, assignable to anion defects, O^{2-} or N^{3-} vacancies in the material, do not contribute to the reaction.

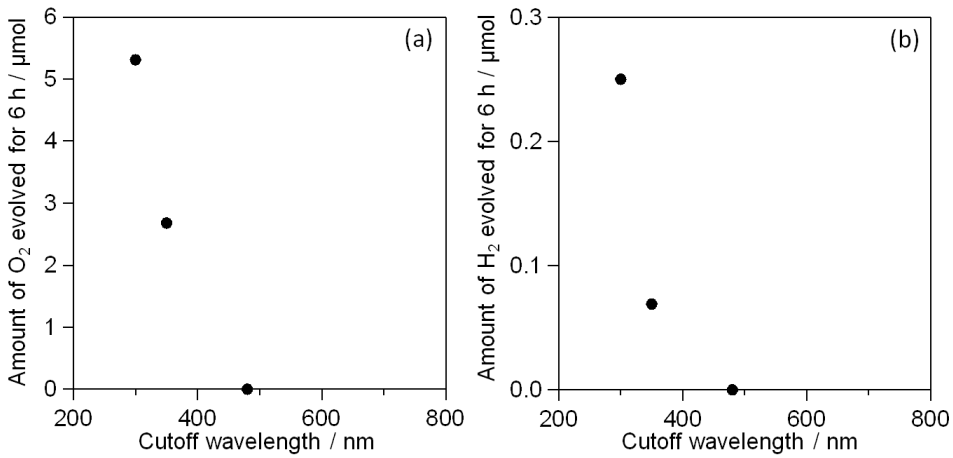

Figure 5. 20. Wavelength dependency of, (a) O_2 evolution from 50 mg of IrO_x(1wt%)-$LaHfO_2N$ in 250 ml of a 10 mM solution of $AgNO_3$, and (b) H_2 evolution from 50 mg of Pt(1wt%)-$LaHfO_2N$ in 250 ml of a 20 vol.% methanol solution under 300 W Xe lamp with different cut-off filters (λ > 300, 350, 480 nm).

5.3.6.2.2 Photocatalytic evolution of O_2 and H_2 by $NdHfO_2N$ in aqueous solution containing a sacrificial reagent

Figure 5. 21 shows the time course of O_2 and H_2 evolution under Xenon lamp 300 W (λ > 300 nm) irradiation. The reactions were carried out in a 250 ml aqueous solution containing as sacrificial reagents Ag^+ or CH_3OH and 50 mg of $NdHfO_2N$ for water oxidation, or 50 mg of Pt(0.3wt%)-$NdHfO_2N$ for water reduction. No reaction took place in dark condition. O_2 production over unmodified $LaHfO_2N$ took place at a constant rate of 0.09 $\mu molh^{-1}$ and the H_2 production rate over Pt(0.3wt%)-$NdHfO_2N$ was 0.05 $\mu molh^{-1}$. These results indicate that $NdHfO_2N$ and Pt-$NdHfO_2N$ have the adequate oxidation and reduction potential to conduct the overall water splitting reaction. N_2 evolution was negligible in these experiments,

indicating that $NdHfO_2N$ is stable in front of selfoxidation process under photoreaction conditions.

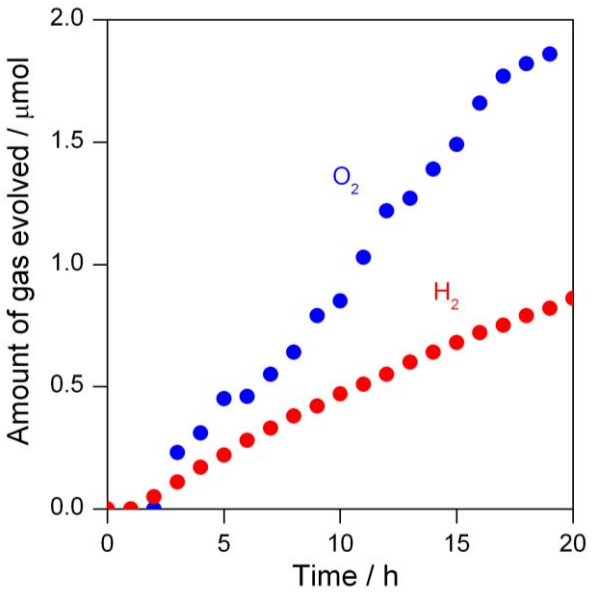

Figure 5. 21. O_2 evolution (blue spots) from 50 mg of $NdHfO_2N$ in 250 ml of a 10 mM solution of $AgNO_3$ and H_2 evolution (red spots) from 50 mg of Pt(0.3 wt%)-$NdHfO_2N$ in 250 ml of a 20 vol.% methanol solution under 300 W Xe lamp (λ > 300 nm).

5.3.6.2.3 Photocatalytic evolution of O_2 and H_2 by $LnHfO_2N$ (Ln = Pr, Nd, Sm) in aqueous solution containing a sacrificial reagent

Photocatalytic activities for water splitting of praseodymium and samarium hafnium oxynitride perovskites were evaluated following the same methodology described in precedent sections. Time course O_2 and H_2 evolution under Xenon lamp 300 W (λ > 300 nm) irradiation of a 250 ml aqueous solution containing sacrificial reagents Ag^+ or CH_3OH and 50 mg of the surface modified $LnHfO_2N$ powders, IrO_x(1wt%)-$LnHfO_2N$ and

Pt(1wt%)-$LnHfO_2N$ (Ln = Pr, Sm) for water oxidation or reduction, respectively are shown in **Figure 5. 22**. Again, without irradiation, no reaction took place and the gas evolution began with the onset of irradiation.

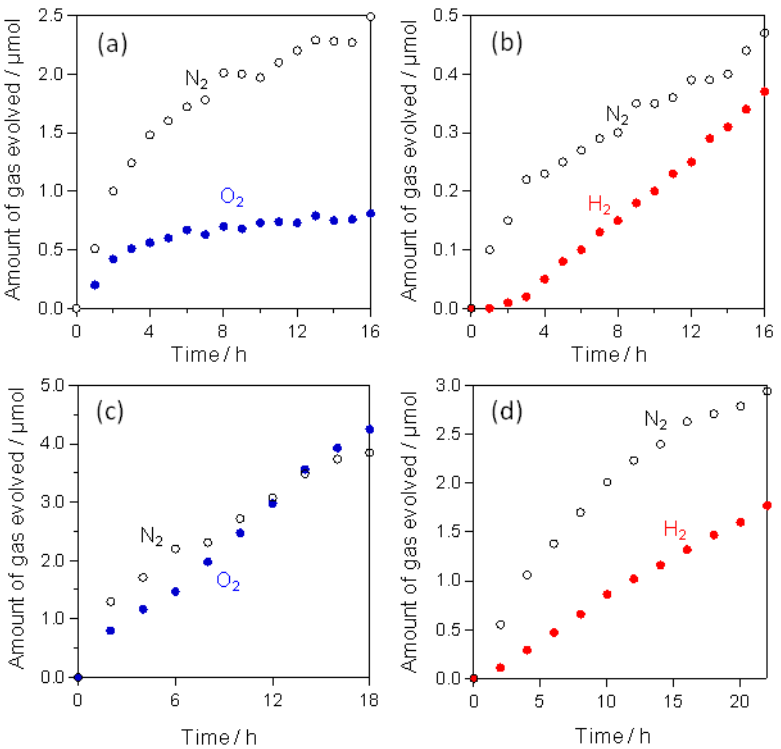

Figure 5. 22. O_2 evolution (blue spots) from 50 mg of IrO_x(1wt%)-$LnHfO_2N$ where Ln = (a) Pr, (c) Sm, in 250 ml of a 10 mM solution of $AgNO_3$. H_2 evolution (red spots) from 50 mg of Pt(1wt%)-$LnHfO_2N$ where Ln = (b) Pr, (d) Sm, in 250 ml of a 20 vol.% methanol solution and N_2 coevolution (black spots) under 300 W Xe lamp (λ > 300 nm).

O_2 evolution occurred as a result of the oxidation of water to O_2 by photogenerated holes at the valence band of the modified $LnHfO_2N$ (Ln = Pr, Sm) whereas Ag^+ is reduced to Ag by photogenerated electrons. This mechanism is confirmed by the observation of metallic Ag in the XPS

spectra of the photocatalyst after reaction shown in **Figure 5. 23c,f** for modified $PrHfO_2N$ and $SmHfO_2N$, respectively. A linear evolution of H_2 gas is observed from both praseodymium and samarium samples indicating that they show the adequate redox potentials to conduct the overall water splitting reaction. N_2 coevolution is observed for both praseodymium and samarium samples in the water oxidation and reduction experiments. N_2 coevolution has been observed in several oxynitride materials such as TaON,[61] $LaTiO_2N$,[151] $ANbO_2N$[153] and has been regarded as selfoxidative decomposition of the material, whereby nitrogen anions (N^{3-}) are oxidized to N_2 by photogenerated holes:

$$2N^{3-} + 6h^{+} \rightarrow N_2$$

However, in certain cases it has been possible to effectively suppress or minimize this reaction by controlling the pH or by selecting an electron or hole scavenger showing higher adsorptivity towards the oxynitride photocatalyst. Further modifications of the photoreaction conditions would be necessary to determine if selfoxidative decomposition of modified $PrHfO_2N$ and $SmHfO_2N$ may be suppressed by controlling the experimental conditions.

X-ray photoelectron spectra of the Ir, Pt and Ag regions of IrO_x-$LnHfO_2N$, Pt-$LnHfO_2N$ and IrO_x-$LnHfO_2N$ (Ln = Pr, Sm) after reaction are shown in **Figure 5. 23.**

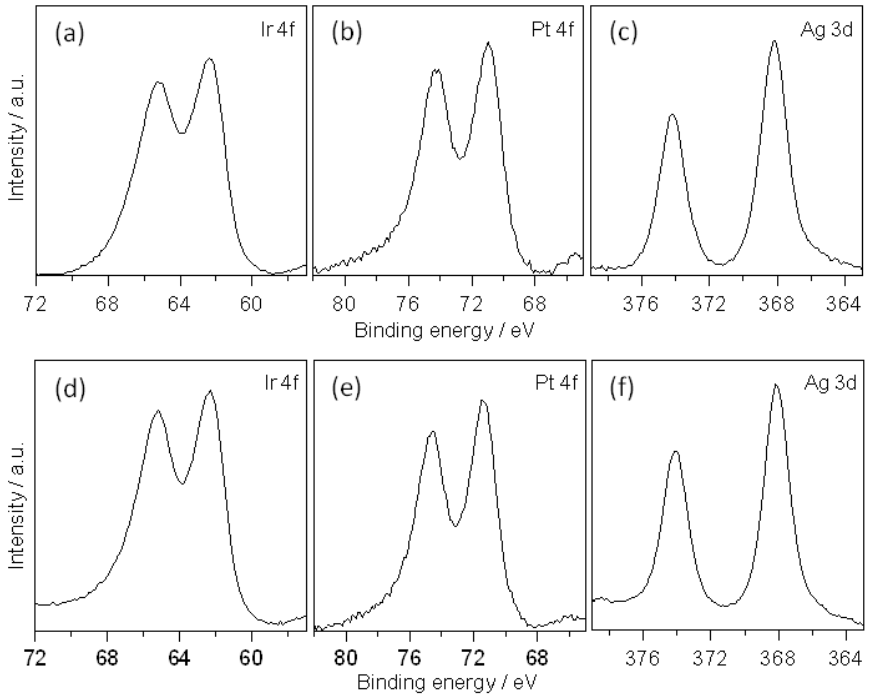

Figure 5. 23. X-ray photoelectron spectra of IrO_x-$LnHfO_2N$ where Ln = (a) Pr, (d) Sm, Pt-$LnHfO_2N$ where Ln = (b) Pr, (e) Sm and IrO_x-$LnHfO_2N$ were Ln = (c) Pr, (f) Sm after O_2 evolution.

The Ir 4f spectra (**Figure 5. 23a,d**) show the Ir $4f_{7/2}$ and Ir $4f_{5/2}$ spin–orbit doublet, appearing around 62 and 65 eV, respectively. The high binding energy Ir $4f_{7/2}$ confirms the presence of Ir^{3+} and Ir^{4+} species. The Pt 4f spectra (**Figure 5. 18b,e**) show the main core-level peaks of metallic Pt $4f_{7/2}$ and Pt $4f_{5/2}$ doublet, appearing around 72 and 75 eV, respectively, which demonstrates that Pt^0 is the dominant valence state. Finally, the Ag 3d spectrum (**Figure 5. 18b,e**) consists of two peaks at 368 and 374 eV, attributed to Ag $3d_{5/2}$ and Ag $3d_{3/2}$ binding energies, respectively. It indicates that the state of Ag is predominant Ag^0 on the surface of the IrO_x-photocatalysts after the O_2 evolution reaction.

5.3.6.2.4 Photocatalytic evolution of O_2 and H_2 by $LaZrO_2N$ in aqueous solution containing a sacrificial reagent

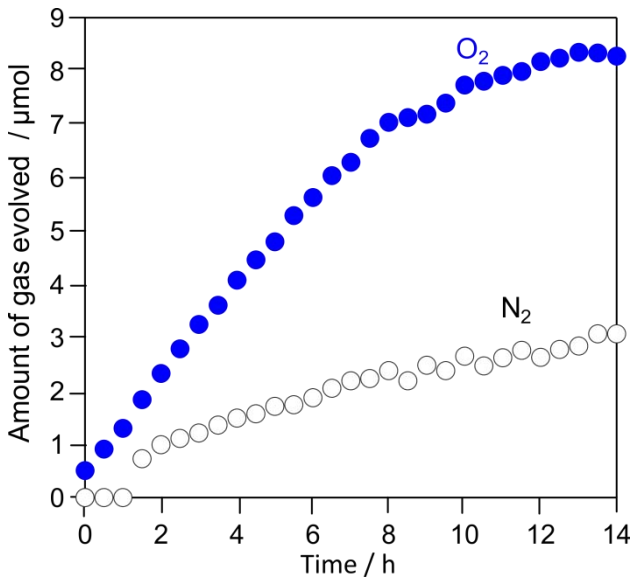

Figure 5. 24. O_2 evolution (blue spots) from 50 mg of $LaZrO_2N$ in 250 ml of a 10 mM solution of $AgNO_3$ and N_2 coevolution (black spots) under visible light 300 W Xe lamp (λ > 400 nm) irradiation.

Figure 5. 24 shows the time course of O_2 evolution under Xenon lamp 300 W equipped with cut-off filter (λ > 400 nm) irradiation. The reactions were carried out in a 250 ml aqueous solution containing Ag^+ as sacrificial reagent and 50 mg of CoO_x(0.3wt%)-$LaZrO_2N$ powder. Here cobalt oxide acts as a water oxidation co-catalyst. No reaction took place without irradiation. The rate of O_2 production over the CoO_x(0.3wt%)-$LaZrO_2N$ photocatalyst was 1 $\mu molh^{-1}$. This result shows that CoO_x(0.3wt%)-$LaZrO_2N$ has the ability to oxidize water in presence of sacrificial electron acceptor. However, N_2 coevolution is observed during the water oxidation

experiment, indicating that this oxynitride material undergoes a selfoxidation reaction in the present experimental conditions. No hydrogen was detected on the time course H_2 evolution experiment under visible light irradiation performed on aqueous solutions (20 vol.% methanol) containing 0.5 mg of M(0.3wt%)-$LaZrO_2N$ (M = Pt or Ru). This result likely suggests that the bottom of the conduction band of $LaZrO_2N$ must be situated at a lower potential than the reduction potential of water. Therefore, surface modified $LaZrO_2N$ is active only for O_2 evolution in presence of a sacrificial electron acceptor such as Ag^+.

5.3.7 Electrical properties

Electrical resistivity and dielectric permittivities of the hafnium and zirconium oxynitride perovskites have been evaluated by dc impedance analysis over the temperature range 100 -300 K and frequency range 5-1000 kHz.

5.3.7.1 Resistivity measurements

The apparent electrical resistivities of $NdHfO_2N$ and $LaZrO_2N$ ceramic pellets as function of temperature are plotted in **Figure 5. 25**. A simple two probe resistivity is measured by recording the current through sample using constant voltage source. The microstructure of the as synthesized ceramic pellets present a normal distribution of grain size, with average grain size of 0.96 μm and a random distribution of intergranular pores are

visible on SEM images presented in **Figure 5. 26**. The degree of sinterization observed in SEM images insures a sufficient intergrain electrical contact. However a certain resistive grain boundary contribution is expected. Both compounds show an insulating behaviour, with conductivities of 1.7×10^{-9} S·cm^{-1} and 2.3×10^{-8} S·cm^{-1} at room temperature for $LaZrO_2N$ and $NdHfO_2N$, respectively. The resistivities of these compounds exhibit a strong temperature dependence. The resistivity of $NdHfO_2N$ decreases by four orders of magnitude with increasing temperature from 100 K to 300 K. From the Arrhenius plot in the temperature range between 150 and 300 K the activation energies were estimated to be 0.26 eV and 0.24 eV for $LaZrO_2N$ and $NdHfO_2N$, respectively. Additionally, the resistivity vs temperature plot of $NdHfO_2N$ exhibits a small plateau around 150 K.

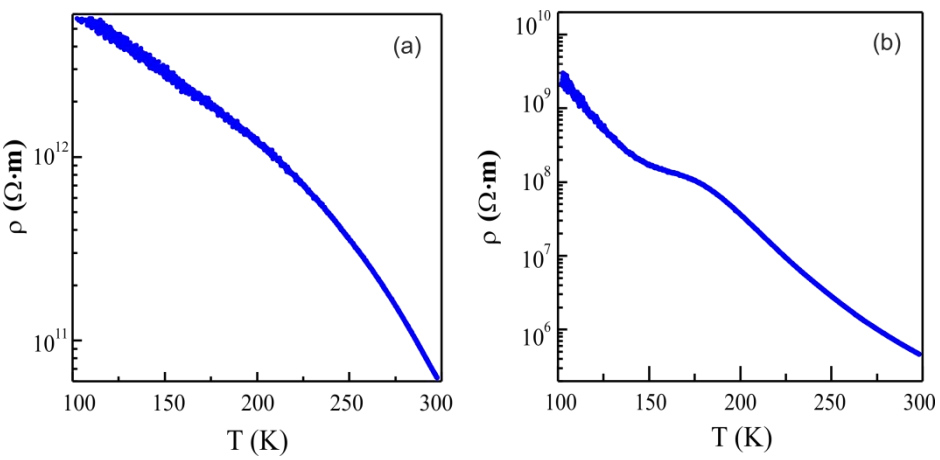

Figure 5. 25. Temperature dependence of resistivity of (a) $LaZrO_2N$ and (b) $NdHfO_2N$.

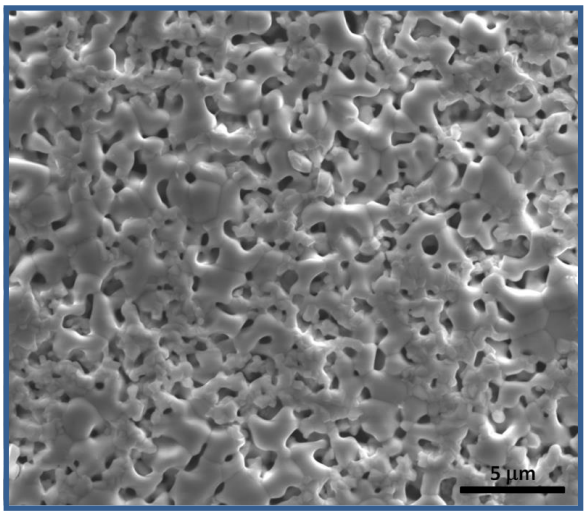

Figure 5. 26. Scanning electron microscopy image of $NdHfO_2N$ ceramic fired at 1500^0C for 3h.

5.3.7.2 Dielectric measurements

The temperature dependence of dielectric permittivities of $LaZrO_2N$ and $LnHfO_2N$ (Ln = La, Nd, Sm) measured at 100 kHz are plotted in **Figure 5. 27**. Both zirconium and hafnium oxynitride perovskites show low permittivities. The room temperature dielectric constants measured were 30 for $LaZrO_2N$ and 30, 16, 28 for $LaHfO_2N$, $NdHfO_2N$ and $SmHfO_2N$ respectively. These values are typical for insulating d^0 transition metal perovskites with centrosymmetric space groups, such as *Pnma*. A room temperature variable frequency study of dielectric permittivities in the range of 5 to 200 kHz of $LnHfO_2N$ (Ln = La, Sm) showed a very small dependence of ε_r upon frequencies (**Figure 5. 28a**), only a small increase is registered at low frequencies. At low frequency the two main contributions are small electronic and moderate ionic polarizations. Dielectric loss for

$LaZrO_2N$ and $NdHfO_2N$ measured at 5 and 1000 kHz are plotted against temperature in **Figure 5. 28b,c**. At low frequencies the dielectric loss of $LaZrO_2N$ is c.a. 0.08, indicating that a small dissipation of electric potential is produced by Joule effect. A significantly larger heat generation is observed for $NdHfO_2N$ that presents dielectric loss of about 1.6 at low frequencies. This result is indicative of heat generation at lattice defects or larger electric conduction and is consistent with the close to infrared broad absorption band observed from the diffuse reflectance spectra and with the lower resistivity observed for $NdHfO_2N$. Dielectric permittivities for $LaTiO_2N$ thin films were found in the range 290 to 1220 at 10 kHz.[144] The relatively high permittivities observed in this compound are associated to second order Jahn-Teller distortion of the TiO_6 octahedra. The dielectric constants of $LnHfO_2N$ and $LaZrO_2N$ are similar to those of analogous alkaline earth perovskites AMO_3 (A = Ca, Sr, Ba; M= Zr, Hf), which range from 36 to 30 for the zirconium compounds and from 24 to 21 for the hafnium perovskites.[234]

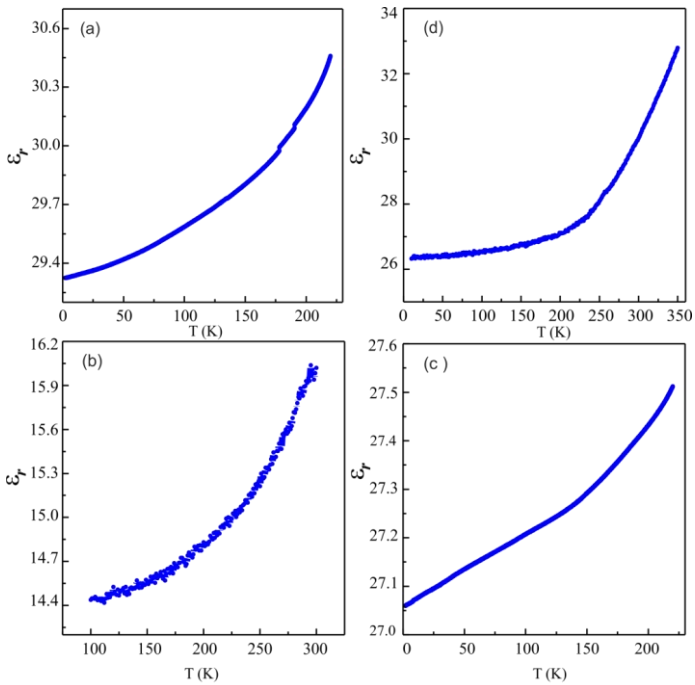

Figure 5. 27. Temperature dependence of dielectric permittivities of (a) $LaHfO_2N$, (b) $NdHfO_2N$, (c) $SmHfO_2N$ and (d) $LaZrO_2N$ measured at 100 kHz.

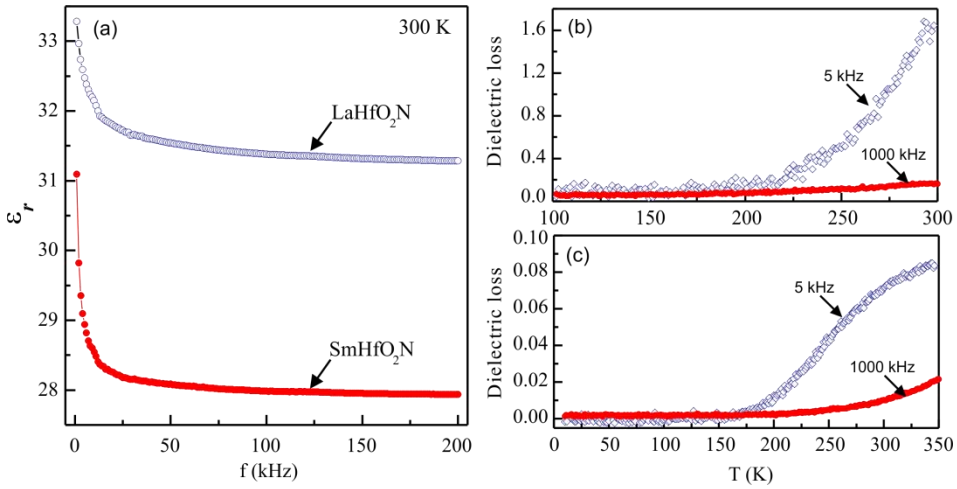

Figure 5. 28. (a) Frequency dependence of dielectric permittivities of $LaHfO_2N$ and $SmHfO_2N$; and temperature dependence of dielectric loss of (b) $NdHfO_2N$ and (c) $LaZrO_2N$ measured at 5 and 1000 kHz.

5.4 Conclusions

New lanthanide hafnium oxynitride perovskites have been prepared for the first time by solid state reaction at 1500 ^{0}C starting with a stoichiometric mixture of the rare earth metal oxide and Hf_2ON_2. The analogous Zr compound which was previously prepared by ammonolysis of amorphous $La_2Zr_2O_7$ at 950 ^{0}C,[129] has been obtained using a similar solid state reaction but with ZrN as nitride source instead of the oxynitride. The new synthetic approach is much faster than the previously reported ammonolysis method. For instance, for $LaZrO_2N$ the reaction times are 25 hours for the solid state reaction and 240 hours (10 cycles of 24 hours) for the ammonolysis of $La_2Zr_2O_7$. On the other hand it leads to highly crystalline sintered samples suitable for electrical measurements. The new compounds crystallize in the orthorhombic space group Pnma with tilt system ($a^+b^-b^-$). The tilting distortion increases as Ln^{3+} size decreases as expected from the tolerance factor. Refinement of neutron diffraction data at room temperature of $LaHfO_2N$ shows a disordered distribution of oxygen and nitrogen in the two anion sites of the Pnma structure. This is also observed in the $LaZrO_2N$ sample and it was reported for the same compound prepared by ammonolysis of $La_2Zr_2O_7$, indicating that the preparation method and the important difference in the temperatures of synthesis do not affect the anion distribution. The oxynitrides show band gaps between 2.8 and 3.4 eV which are 2 eV smaller than the analogous alkaline earth oxidic perovskites. Photoelectrodes prepared by deposition of $LnHfO_2N$ (Ln= La, Nd, Sm) particles on FTO glass exhibited an anodic photoresponse, characteristic of an n-type semiconductor. The time course of O_2 and H_2 evolution under Xenon lamp 300 W irradiation showed that

$LnHfO_2N$ (Ln= La, Pr, Nd, Sm) powders have the adequate oxidation and reduction potential to conduct the overall water splitting reaction in presence of a sacrificial agent. $LaHfO_2N$ and $NdHfO_2N$ showed better resistance towards photocorrosion. IrO_x showed to significantly enhance the O_2 evolution rate for $LaHfO_2N$ and $LaZrO_2N$ presents photocatalytic activity for O_2 evolution but not for H_2 evolution under visible light irradiation. Dielectric permittivities and resistivity measurements showed that $LnMO_2N$ (Ln= La, Nd, Sm; M= Hf, Zr) are electrical insulators with dielectric constants similar to those reported for the analogous alkaline earth perovskites.

6 Conclusions

This thesis has been directed towards the synthesis, structural characterisation and study of luminescent, magnetic and photocatalytic properties of new oxynitride materials. The main contributions can be summarized as:

We report the synthesis and characterization of two new oxynitride phosphors with potential application in warm white light LED technologies. The new compounds $LaSrSiO_3N$ and $LaBaSiO_3N$ activated with Eu^{2+} are orange-red light-emitting luminescent materials under excitation in the UV-blue range. They have been prepared by solid state reaction of mixtures of oxides and nitrides at 1500 ^oC under N_2 or N_2/H_2 gas, representing the first examples of alkaline earth oxynitridosilicates with a β-K_2SO_4 structure, and one of the few examples of oxynitride orthosilicates containing $[SiO_3N]^{5-}$ groups. Compared to isostructural Sr_2SiO_4 and Ba_2SiO_4, the two oxynitrides can be activated in addition to Eu^{2+} with Ce^{3+}, substituting to isovalent La^{3+}. The lattice parameters obtained by Rietveld refinement from X-ray powder diffraction data in the orthorhombic *Pmnb* space group (N^o 62) were a = 5.64362(14), b = 7.10719(17), c = 9.8062(2) Å for $LaSrSiO_3N$ and a = 5.733(4), b = 7.316(5), c = 9.902(7) Å for $LaBaSiO_3N$. The isostructural compound $LaEuSiO_3N$ has been obtained by the same synthetic pathway and shows the cell parameters a = 5.63246(14), b =7.11675(18), c=9.8062(2) Å which are very close to those of the Sr compound. The β-K_2SO_4 structure shows two independent crystallographic sites for the cations with coordination numbers (CN) 10 (M1) and 9 (M2) which are occupied preferentially by the alkaline earth metal or europium and the lanthanum respectively, and three anion sites X1, X2 and X3. The refined occupancies obtained by fixing the ratio of La:Ba and La:Sr to 1:1 were 0.804(8) for Ba and 0.196(8) for La at site M1 in $LaBaSiO_3N$ and 0.758(3) for Sr and 0.242(3) for La at the same site in $LaSrSiO_3N$. The

corresponding occupancies for site M(2) were 0.804(8) for La and 0.196(8) for Ba in $LaBaSiO_3N$ and 0.758(3) for La and 0.242(3) for Sr in $LaSrSiO_3N$. The refinement of cation site occupancies data in $LaEuSiO_3N$ led to similar values: 0.812(18) for Eu and 0.188(18) for La at site M1, 0.188(18) for La and 0.812(18) for Eu at site M2. Refinement of O/N occupancies from high resolution neutron powder diffraction data of $LaBaSiO_3N$ showed a partial nitrogen order with N/O occupancies of 1/0 for site X1, 0.542(14)/ 0.458 for site X2 and 0.729/0.271 for site X3. The preferential occupancy of N at site X3 agrees with Pauling's second crystal rule.

The luminescence emission spectra of Eu^{2+} doped $LaM_{1-x}Eu_xSiO_3N$ (M = Sr, Ba; x = 0.01, 0.02, 0.05) upon excitation at 405 nm consist of a broad band centered between 640 (for x = 0.01) and 675 nm (for x = 0.1), with two main components with intensities depending on the europium concentration, and wavelengths of 705 and 590 nm. Compared with the europium-doped orthosilicates with β-K_2SO_4 structure Sr_2SiO_4 and Ba_2SiO_4, the emission wavelengths of the europium doped $LaMSiO_3N$ materials are red shifted from 490–570 nm to 640–675 nm. $LaEuSiO_3N$ shows a ferromagnetic transition at T_c = 3.0 K as a result of the coupling of 7/2 spins of Eu^{2+}, with a saturated magnetization of 6.1 μ_B at 2 K.

The solid solution $Sr_{2-x}La_xSiO_{4-x}N_x$ ($0 \leq x \leq 1$), can be obtained through a similar synthesis pathway, by concomitant substitution in Sr_2SiO_4 of Sr^{2+} by La^{3+} and O^{2-} by N^{3}. The substitution of Sr and O by La and N respectively affects the cell parameters according to the differences in ionic radii, more strongly for the b and c axes. Both parameters increase with x showing that the increase of N^{3-} with larger ionic radius than O^{2-} outweighs the effect of introduction of La^{3+} which is smaller than Sr^{2+}. Synchrotron radiation X-ray powder diffraction show a transition from the monoclinic $P2_1/n$ symmetry

of the β polymorph of Sr_2SiO_4 to orthorhombic Pmnb α',β-K_2SO_4 type phase for x ≤ 0.2. By controlling the composition the emission colours can be tuned from yellow (x = 0.2) to orange-red (x = 1) for Eu^{2+} phosphors and from blue-green (x = 0.2) to orange-yellow (x = 1) in Ce^{3+} samples.

As a second important objective this thesis has been directed towards the synthesis and study of new oxynitride perovskites extending the range of this group of compounds to the transition metals Cr and Hf.

We report that chromium oxynitride perovskites $LnCrO_{3-x}N_x$ with Ln = La, Pr, Nd and Sm and nitrogen contents up to x=0.59 can be prepared by careful ammonolysis of $LnCrO_4$ precursors. All of the products were found to adopt the orthorhombic $GdFeO_3$-type perovskite superstructure in the space group *Pbnm*(N° 62). Lattice parameters obtained by Rietveld refinement of X-ray synchrotron powder diffraction data for $LnCrO_{3-x}N_x$ compounds are: a = 5.52201(4), b = 5.48192(5), c = 7.6573(7) Å ($LaCrO_{2.72}N_{0.28}$); a = 5.45535(4), b = 5.49076(3), c = 7.72751(5) Å ($PrCrO_{2.64}N_{0.19}$); a = 5.42787(3), b = 5.50102(3), c = 7.70936(4) Å ($NdCrO_{2.58}N_{0.42}$) and a = 5.38586(7), b = 5.51951(6), c = 7.6784(1) Å ($SmCrO_{2.76}N_{0.24}$). No O/N order was detected from refinement of neutron powder diffraction data, in keeping with their relatively small nitrogen contents (x < 0.42). Susceptibility measurements for $LnCrO_{3-x}N_x$ perovskites show an antiferromagnetic ordering and the transition temperature T_N is reduced as x increases. Magnetic order has been also characterised by variable temperature powder neutron diffraction of $LaCrO_{2.72}N_{0.28}$, $PrCrO_{2.64}N_{0.36}$ and$NdCrO_{2.58}N_{0.42}$ samples. G-type antiferromagnetic order, in whicheach Cr moment is antiparallel to nearest neighbours in x, y and z directions, was observed below the T_N's in all cases. Hole-doping of $LnCrO_3$ perovskites through O^{2-}/N^{3-} anion substitution

suppresses magnetic order far less drastically than Ln^{3+}/M^{2+} (M = Ca, Sr) cation substitutions do, and Nd spin-order is enhanced up to at least x = 0.4. The greater covalency of metal-nitride bonds compared to metal-oxide enhances magnetic interaction strengths, almost completely compensating for the intrinsic reduction in T_N due to hole-doping. Hence, nitride-doping may be viewed as a more benign method for doping holes into metal oxides without suppressing electronic transition temperatures than traditional cation-substitution approaches.

Finally, we report the synthesis, structure, electric and photocatalytic properties of new hafnium oxynitride perovskites $LnHfO_2N$ where Ln= La, Pr, Nd and Sm, and the previously reported analogous compound $LaZrO_2N$. These compounds have been prepared by treatment at 1500 ºC in N_2 of a stoichiometric mixture of the rare earth metal oxide and Hf_2ON_2 or a mixture of ZrN and ZrO_2. They crystallize in the orthorhombic $GdFeO_3$-type superstructure in the space group *Pnma* (Nº 62) with the following refined lattice parameters from X-ray synchrotron powder diffraction data: $LnHfO_3N$ with Ln = La, Pr, Nd, Sm; a = 5.83312(1), b = 8.20182(2), c = 5.79828(2) Å ($LaHfO_2N$); a = 5.82447(2), b = 8.15752(1), c = 5.72826(2) Å ($PrHfO_2N$); a = 5.82227(2), b = 8.13418(2), c= 5.69967(1) Å ($NdHfO_2N$); a = 5.81768(2), b = 8.09701(3), c = 5.65554(2) Å ($SmHfO_2N$), and a = 5.87471(1), b = 8.24302(2), c = 5.81034(1) Å for $LaZrO_2N$. The variation of lattice parameters reveals the expected increasing orthorhombic structural distortion as the radii of the rare earth decreases. No significant anion order was detected from refinement of (O/N) occupancies of neutron diffraction data. These oxynitrides show blue colour and present band gaps between 3.4 and 2.8 eV which involves a 2 eV reduction when compared to the analogous alkaline earth oxidic perovskites $SrHfO_3$ or $SrZrO_3$. The time course of O_2 and H_2 evolution under Xenon lamp 300 W irradiation showed

that the hafnium perovskite oxynitrides have the adequate oxidation and reduction potential to conduct the overall water splitting reaction in presence of a sacrificial agent. $LaHfO_2N$ and $NdHfO_2N$ showed better resistance towards photocorrosion. IrO_x showed to significantly enhance the O_2 evolution rate for $LaHfO_2N$, and $LaZrO_2N$ presents photocatalytic activity for O_2 evolution but not for H_2 evolution under visible light irradiation. Dielectric and resistivity measurements showed that both Hf and Zr perovskite oxynitrides are electric insulators with dielectric constants between 16 and 30 at room temperature.

7 Publications

This thesis has lead by now to the following publications:

- **Red luminescence and ferromagnetism in europium oxynitridosilicates with β-K_2SO_4 structure.**

  A.P. Black, K.A. Denault, J. Oró-Solé, A.R. Goñi, A.Fuertes

  Chem. Commun. **51**, 2166-2169 (2015).

- **Emission colour tuning through coupled N/La introduction in $Sr_2SiO_4:Eu^{2+}$.**

  A.P. Black, K.A. Denault, A.R. Goñi, C.Frontera, R. Seshadri, A. Fuertes

  J. Mater. Chem. C **3**, 11471-11477 (2015).

- **Nitride tuning of lanthanide chromites.**

  A.P. Black, H.E. Johnston, J. Oró-Solé, B. Bozzo, C. Ritter, C. Frontera,

  J.P. Attfield, A. Fuertes

  Chem. Commun. **2**, 4317-4320 (2016).

- **New hafnium oxynitride perovskites: dielectric and photocatalytic water splitting properties.**

  A. P. Black, H. Suzuki, J. Oró-Solé, C. Ritter, C. Frontera, A. Sundaresan, R. Abe, A.Fuertes

  In preparation

The following contributions have been presented at scientific meetings:

- **15th European Conference on Solid State Chemistry** – Poster

  Red luminescence and ferromagnetism in europium oxynitridosilicates with β-K_2SO_4 structure.

  A.P. Black, K.A. Denault, J. Oró-Solé, A.R. Goñi, A.Fuertes

  Vienna, Austria (23 - 26 August 2015).

- **nanoSELECT NOE meeting** - Oral presentation

  Oxynitridosilicate phosphors for white LEDs. $LaMSiO_3N$: Eu^{2+} or Ce^{3+},(M= Sr, Ba).

  A.P. Black, K.A. Denault, A.R. Goñi, C.Frontera, R. Seshadri, A. Fuertes

  Sant Feliu de Guixols, Spain (8 - 10 June 2016).

- **QIES: 17ª Reunión Científica Plenaria de Química Inorgánica y 11ª Reunión Científica Plenaria de Química del estado Sólido** - Oral presentation

  Nitride tuning of lanthanide chromites.

  A.P. Black, H.E. Johnston, J. Oró-Solé, B. Bozzo, C. Ritter, C. Frontera, J.P. Attfield, A. Fuertes

  Malaga, Spain (19 – 22 June 2016).

8 Bibliography

1. G. H. Haertling, *Journal of the American Ceramic Society*, 1999, **82**, 797-818.
2. 2,429,588, 1947.
3. S. Jin, T. H. Tiefel, M. McCormack, R. A. Fastnacht, R. Ramesh and L. H. Chen, *Science*, 1994, **264**, 413-415.
4. K. Mizushima, P. C. Jones, P. J. Wiseman and J. B. Goodenough, *Materials Research Bulletin*, 1980, **15**, 783-789.
5. A. K. Padhi, K. S. Nanjundaswamy and J. B. Goodenough, *Journal of the Electrochemical Society*, 1997, **144**, 1188-1194.
6. K. A. Muller and J. G. Bednorz, *La Recherche*, 1988, **19**, 52-60.
7. G. Blasse and A. Bril, *Applied physics letters*, 1967, **11**, 53-&.
8. P. Schlotter, R. Schmidt and J. Schneider, *Applied Physics A*, 1997, **64**, 417-418.
9. A. Fuertes, *Dalton Transactions*, 2010, **39**, 5942-5948.
10. R. G. Pearson, *Inorganic Chemistry*, 1991, **30**, 2856-2858.
11. R. Shannon, *Acta Crystallographica Section A*, 1976, **32**, 751-767.
12. M. A. Hayward, E. J. Cussen, J. B. Claridge, M. Bieringer, M. J. Rosseinsky, C. J. Kiely, S. J. Blundell, I. M. Marshall and F. L. Pratt, *Science*, 2002, **295**, 1882-1884.
13. S.-W. Kim, N. Pereira, N. A. Chernova, F. Omenya, P. Gao, M. S. Whittingham, G. G. Amatucci, D. Su and F. Wang, *ACS Nano*, 2015, **9**, 10076-10084.
14. H. Fujito, H. Kunioku, D. Kato, H. Suzuki, M. Higashi, H. Kageyama and R. Abe, *Journal of the American Chemical Society*, 2016, **138**, 2082-2085.
15. O. I. Siidra, M. Gogolin, E. A. Lukina, H. Kabbour, R. S. Bubnova, O. Mentré, A. A. Agakhanov, S. V. Krivovichev, M. Colmont and T. Gesing, *Inorganic Chemistry*, 2015, **54**, 11550-11556.
16. W. W. Ma, X. T. Dong, J. X. Wang, W. S. Yu and G. X. Liu, *J. Electron. Mater.*, 2014, **43**, 3701-3707.
17. X. Xiao, C. Liu, R. Hu, X. Zuo, J. Nan, L. Li and L. Wang, *Journal of Materials Chemistry*, 2012, **22**, 22840-22843.
18. A. Ishikawa, T. Takata, J. N. Kondo, M. Hara, H. Kobayashi and K. Domen, *Journal of the American Chemical Society*, 2002, **124**, 13547-13553.
19. L. D. Zhao, D. Berardan, Y. L. Pei, C. Byl, L. Pinsard-Gaudart and N. Dragoe, *Applied Physics Letters*, 2010, **97**, 3.
20. H. A. Seibel, II, P. Karen, T. R. Wagner and P. M. Woodward, *Journal of Materials Chemistry*, 2009, **19**, 471-477.
21. A. Fuertes, *Journal of Materials Chemistry*, 2012, **22**, 3293-3299.
22. A. Fuertes, *Materials Horizons*, 2015, **2**, 453-461.

23. S. G. Ebbinghaus, H. P. Abicht, R. Dronskowski, T. Muller, A. Reller and A. Weidenkaff, *Prog. Solid State Chem.*, 2009, **37**, 173-205.
24. V. M. Goldschmidt, *Journal of the Chemical Society (Resumed)*, 1937, DOI: 10.1039/JR9370000655, 655-673.
25. K. Keil and C. A. Andersen, *Nature*, 1965, **207**, 745-745.
26. R. Juza, in *Advances in Inorganic Chemistry and Radiochemistry*, eds. H. J. Emeléus and A. G. Sharpe, Academic Press, 1966, vol. Volume 9, pp. 81-131.
27. R. Marchand, Y. Laurent, J. Guyader, P. L'Haridon and P. Verdier, *Journal of the European Ceramic Society*, 1991, **8**, 197-213.
28. N. E. Brese and M. O'Keeffe, in *Complexes, Clusters and Crystal Chemistry*, Springer Berlin Heidelberg, Berlin, Heidelberg, 1992, DOI: 10.1007/BFb0036504, pp. 307-378.
29. W. Schnick, *Angewandte Chemie International Edition in English*, 1993, **32**, 806-818.
30. R. Niewa and H. Jacobs, *Chemical Reviews*, 1996, **96**, 2053-2062.
31. F. J. DiSalvo and S. J. Clarke, *Current Opinion in Solid State and Materials Science*, 1996, **1**, 241-249.
32. R. J. a. W. Sachsze, *Z. Anorg. Allg. Chem.*, 1945, **95**, 253.
33. D. H. Gregory, *J. Chem. Soc.-Dalton Trans.*, 1999, DOI: 10.1039/a807732k, 259-270.
34. R. Buhl, H. K. Pulker and E. Moll, *Thin Solid Films*, 1981, **80**, 265-270.
35. E. G. Gillan and R. B. Kaner, *Inorganic Chemistry*, 1994, **33**, 5693-5700.
36. A. E. Kaloyeros and E. Eisenbraun, *Annu. Rev. Mater. Sci.*, 2000, **30**, 363-385.
37. H. G. Leduc, B. Bumble, P. K. Day, B. H. Eom, J. S. Gao, S. Golwala, B. A. Mazin, S. McHugh, A. Merrill, D. C. Moore, O. Noroozian, A. D. Turner and J. Zmuidzinas, *Applied Physics Letters*, 2010, **97**, 3.
38. A. Zerr, G. Miehe and R. Riedel, *Nat Mater*, 2003, **2**, 185-189.
39. K. K. Kim, A. Hsu, X. T. Jia, S. M. Kim, Y. S. Shi, M. Hofmann, D. Nezich, J. F. Rodriguez-Nieva, M. Dresselhaus, T. Palacios and J. Kong, *Nano Lett.*, 2012, **12**, 161-166.
40. K. Cherrey, N. G. Chopra, R. J. Luyken, V. H. Crespi, M. L. Cohen, S. G. Louie and A. Zettl, *Science*, 1995, **269**, 966-967.
41. F. Calle, J. Pedros, T. Palacios and J. Grajal, in *E-Mrs 2004 Fall Meeting Symposia C and F*, ed. M. Stutzmann, Wiley-V C H Verlag Gmbh, Weinheim, 2005, vol. 2, pp. 976-983.
42. S. Nakamura, M. Senoh, S. Nagahama, N. Iwasa, T. Yamada, T. Matsushita, H. Kiyoku and Y. Sugimoto, *Jpn. J. Appl. Phys. Part 2 - Lett.*, 1996, **35**, L74-L76.

43. R. Dahal, J. Li, K. Aryal, J. Y. Lin and H. X. Jiang, *Applied Physics Letters*, 2010, **97**, 3.
44. A. Zerr, G. Miehe, G. Serghiou, M. Schwarz, E. Kroke, R. Riedel, H. Fuesz, P. Kroll and R. Boehler, *Nature*, 1999, **400**, 340-342.
45. N. Kawai, K. Tsurui, D. Shindo, Y. Motoyashiki and E. Sato, *Int. J. Impact Eng.*, 2011, **38**, 542-545.
46. R. Marchand, W. Schnick and N. Stock, *Advances in Inorganic Chemistry, Vol 50*, 2000, **50**, 193-233.
47. R. Marchand and Y. Laurent, *Eur. J. Solid State Inorg. Chem.*, 1991, **28**, 57-76.
48. J. Cabana, Z. Stoeva, J. J. Titman, D. H. Gregory and M. R. Palacin, *Chemistry of Materials*, 2008, **20**, 1676-1678.
49. A. Fuertes, M. Vlassov, D. Beltrán-Porter, P. Alemany, E. Canadell, N. Casañ-Pastor and M. R. Palacín, *Chemistry of Materials*, 1999, **11**, 203-206.
50. S. Yamanaka, H. Kawaji, K. Hotehama and M. Ohashi, *Advanced Materials*, 1996, **8**, 771-&.
51. H. Kuzel, *Journal*, 1908.
52. G. Brauer, *Journal of the Less Common Metals*, 1960, **2**, 131-137.
53. F. Pors, R. Marchand and Y. Laurent, *Journal of Solid State Chemistry*, 1993, **107**, 39-42.
54. F. Tessier and R. Marchand, *Journal of Solid State Chemistry*, **171**, 143-151.
55. P. Antoine, R. Marchand and Y. Laurent, *Rev. Int. Hautes Temp. Refract.*, 1987, **24**, 43-46.
56. J. Grins, P. O. Käll and G. Svensson, *Journal of Solid State Chemistry*, 1995, **117**, 48-54.
57. R. Marchand, P. Antoine and Y. Laurent, *Journal of Solid State Chemistry*, 1993, **107**, 34-38.
58. S. Thomas, J. Oro-Sole, B. Glorieux, V. Jubera, V. Buissette, T. Le Mercier, A. Garcia and A. Fuertes, *Journal of Materials Chemistry*, 2012, **22**, 23913-23920.
59. M. Yang, J. Oró-Solé, J. A. Rodgers, A. B. Jorge, A. Fuertes and J. P. Attfield, *Nat Chem*, 2011, **3**, 47-52.
60. G. M. Veith, M. Greenblatt, M. Croft and J. B. Goodenough, *Materials Research Bulletin*, 2001, **36**, 1521-1530.
61. R. Abe, *Journal of Photochemistry and Photobiology C: Photochemistry Reviews*, 2010, **11**, 179-209.
62. K. Maeda, K. Teramura and K. Domen, *Journal of Catalysis*, 2008, **254**, 198-204.
63. M. Jansen and H. P. Letschert, *Nature*, 2000, **404**, 980-982.

64. Y.-I. Kim, P. M. Woodward, K. Z. Baba-Kishi and C. W. Tai, *Chemistry of Materials*, 2004, **16**, 1267-1276.
65. Y. Hinuma, H. Moriwake, Y.-R. Zhang, T. Motohashi, S. Kikkawa and I. Tanaka, *Chemistry of Materials*, 2012, **24**, 4343-4349.
66. R. L. Withers, Y. Liu, P. Woodward and Y.-I. Kim, *Applied Physics Letters*, 2008, **92**, 102907.
67. D. Oka, Y. Hirose, H. Kamisaka, T. Fukumura, K. Sasa, S. Ishii, H. Matsuzaki, Y. Sato, Y. Ikuhara and T. Hasegawa, *Scientific Reports*, 2014, **4**, 4987.
68. I. KOUTSAROFF, S. Higai and A. Ando, *Journal*, 2013.
69. D. Logvinovich, R. Aguiar, R. Robert, M. Trottmann, S. G. Ebbinghaus, A. Reller and A. Weidenkaff, *Journal of Solid State Chemistry*, 2007, **180**, 2649-2654.
70. A. B. Jorge, J. Oró-Solé, A. M. Bea, N. Mufti, T. T. M. Palstra, J. A. Rodgers, J. P. Attfield and A. Fuertes, *Journal of the American Chemical Society*, 2008, **130**, 12572-12573.
71. M. Yang, J. Oró-Solé, A. Kusmartseva, A. Fuertes and J. P. Attfield, *Journal of the American Chemical Society*, 2010, **132**, 4822-4829.
72. K. H. Jack and W. I. Wilson, *Nature-Physical Science*, 1972, **238**, 28-&.
73. O. Yoichi, *Japanese Journal of Applied Physics*, 1972, **11**, 1572.
74. E. Strassburger, M. Hunzinger, P. Patel and J. W. McCauley, *J. Appl. Mech.-Trans. ASME*, 2013, **80**, 11.
75. H. Lutz, S. Joosten, J. Hoffmann, P. Lehmeier, A. Seilmeier, H. A. Hoppe and W. Schnick, *Journal of Physics and Chemistry of Solids*, 2004, **65**, 1285-1290.
76. J. W. H. van Krevel, H. T. Hintzen, R. Metselaar and A. Meijerink, *Journal of Alloys and Compounds*, 1998, **268**, 272-277.
77. H. A. Höppe, H. Lutz, P. Morys, W. Schnick and A. Seilmeier, *Journal of Physics and Chemistry of Solids*, 2000, **61**, 2001-2006.
78. Y. Q. Li, A. C. A. Delsing, G. de With and H. T. Hintzen, *Chemistry of Materials*, 2005, **17**, 3242-3248.
79. A. P. Black, K. A. Denault, J. Oro-Sole, A. R. Goni and A. Fuertes, *Chemical Communications*, 2015, **51**, 2166-2169.
80. A. P. Black, K. A. Denault, C. Frontera, R. Seshadri, A. R. Goni and A. Fuertes, *Journal of Materials Chemistry C*, 2015, **3**, 11471-11477.
81. A. P. Black, H. E. Johnston, J. Oro-Sole, B. Bozzo, C. Ritter, C. Frontera, J. P. Attfield and A. Fuertes, *Chemical Communications*, 2016, **52**, 4317-4320.
82. S. Nakamura, T. Mukai and M. Senoh, *Applied Physics Letters*, 1994, **64**, 1687-1689.

83. U. D. Energy, *Build. Technol. Off. Energy Effic. Renew. Energy U.S. Dep. of Energy*, 2016, **DOE/EE-1418**.
84. I. E. Agency, 2006, 558.
85. I. L. Azevedo, M. G. Morgan and F. Morgan, *Proceedings of the IEEE*, 2009, **97**, 481-510.
86. N. George, K. Denault and R. Seshadri, *Annual review of materials research*, 2013, **43**, 481-501.
87. P. Schlotter, J. Baur, C. Hielscher, M. Kunzer, H. Obloh, R. Schmidt and J. Schneider, *Materials Science and Engineering: B*, 1999, **59**, 390-394.
88. C. Jørgensen, *Molecular physics*, 1962, **5**, 271-277.
89. M. D. Chambers and D. R. Clarke, *Annual Review of Materials Research*, 2009, **39**, 325-359.
90. T. Justel, H. Nikol and C. Ronda, *Angewandte Chemie-International Edition*, 1998, **37**, 3085-3103.
91. M. Lax, *The Journal of chemical physics*, 1952, **20**, 1752-1760.
92. G. Blasse and A. Bril, *Philips Technical Review*, 1970, **31**, 303-&.
93. P. Rack and P. Holloway, *Materials science & engineering. R, Reports*, 1998, **21**, 171-219.
94. P. Dorenbos, *Journal of Luminescence*, 2003, **104**, 239-260.
95. K. A. Denault, J. Brgoch, S. D. Kloß, M. W. Gaultois, J. Siewenie, K. Page and R. Seshadri, *ACS Applied Materials & Interfaces*, 2015, **7**, 7264-7272.
96. G. Blasse, *Physics letters. A*, 1968, **A 28**, 444-445.
97. P. Dorenbos, *Journal of Physics: Condensed Matter*, 2005, **17**, 8103.
98. R. J. Xie, N. Hirosaki, M. Mitomo, K. Uheda, T. Suehiro, X. Xu, Y. Yamamoto and T. Sekiguchi, *The Journal of Physical Chemistry B*, 2005, **109**, 9490-9494.
99. R.-J. Xie, N. Hirosaki, M. Mitomo, Y. Yamamoto, T. Suehiro and N. Ohashi, *Journal of the American Ceramic Society*, 2004, **87**, 1368-1370.
100. R.-J. Xie, M. Mitomo, K. Uheda, F.-F. Xu and Y. Akimune, *Journal of the American Ceramic Society*, 2002, **85**, 1229-1234.
101. B. Dierre, R.-J. Xie, N. Hirosaki and T. Sekiguchi, *Journal of Materials Research*, 2007, **22**, 1933-1941.
102. V. Bachmann, C. Ronda, O. Oeckler, W. Schnick and A. Meijerink, *Chemistry of materials*, 2009, **21**, 316-325.
103. Y. Q. Li, J. E. J. van Steen, J. W. H. van Krevel, G. Botty, A. C. A. Delsing, F. J. DiSalvo, G. de With and H. T. Hintzen, *Journal of Alloys and Compounds*, 2006, **417**, 273-279.

104. K. Uheda, N. Hirosaki, Y. Yamamoto, A. Naito, T. Nakajima and H. Yamamoto, *Electrochemical and solid-state letters*, 2006, **9**, H22-H25.
105. P. Pust, V. Weiler, C. Hecht, A. Tücks, A. S. Wochnik, A.-K. Henß, D. Wiechert, C. Scheu, P. J. Schmidt and W. Schnick, *Nat Mater*, 2014, **13**, 891-896.
106. S. Schmiechen, H. Schneider, P. Wagatha, C. Hecht, P. J. Schmidt and W. Schnick, *Chemistry of Materials*, 2014, **26**, 2712-2719.
107. P. Pust, F. Hintze, C. Hecht, V. Weiler, A. Locher, D. Zitnanska, S. Harm, D. Wiechert, P. J. Schmidt and W. Schnick, *Chemistry of Materials*, 2014, **26**, 6113-6119.
108. X.-J. Wang, L. Wang, T. Takeda, S. Funahashi, T. Suehiro, N. Hirosaki and R.-J. Xie, *Chemistry of Materials*, 2015, **27**, 7689-7697.
109. N. Hirosaki, T. Takeda, S. Funahashi and R.-J. Xie, *Chemistry of Materials*, 2014, **26**, 4280-4288.
110. D. Durach, L. Neudert, P. J. Schmidt, O. Oeckler and W. Schnick, *Chemistry of Materials*, 2015, **27**, 4832-4838.
111. R.-J. X. a. K. S. N. Hirosaki, *Bull. Ceram. Soc. Jpn.*, 2006, **41** 602.
112. D. Geng, H. Lian, M. Shang, Y. Zhang and J. Lin, *Inorganic Chemistry*, 2014, **53**, 2230-2239.
113. J. W. H. van Krevel, H. T. Hintzen and R. Metselaar, *Materials Research Bulletin*, 2000, **35**, 747-754.
114. N. Hirosaki, R.-J. Xie, K. Kimoto, T. Sekiguchi, Y. Yamamoto, T. Suehiro and M. Mitomo, *Applied Physics Letters*, 2005, **86**, 211905.
115. Y. Q. Li, C. M. Fang, G. de With and H. T. Hintzen, *Journal of Solid State Chemistry*, 2004, **177**, 4687-4694.
116. R. Le Toquin and A. K. Cheetham, *Chemical Physics Letters*, 2006, **423**, 352-356.
117. T. Takeda, N. Hirosaki, S. Funahshi and R.-J. Xie, *Chemistry of Materials*, 2015, **27**, 5892-5898.
118. H. F. Kay and P. C. Bailey, *Acta Crystallographica*, 1957, **10**, 219-226.
119. T. Kimura, S. Kawamoto, I. Yamada, M. Azuma, M. Takano and Y. Tokura, *Physical review. B, Condensed matter*, 2003, **67**.
120. J. Wang, J. B. Neaton, H. Zheng, V. Nagarajan, S. B. Ogale, B. Liu, D. Viehland, V. Vaithyanathan, D. G. Schlom, U. V. Waghmare, N. A. Spaldin, K. M. Rabe, M. Wuttig and R. Ramesh, *Science*, 2003, **299**, 1719-1722.
121. Y. Moritomo, A. Asamitsu, H. Kuwahara and Y. Tokura, *Nature*, 1996, **380**, 141-144.
122. K. L. Kobayashi, T. Kimura, H. Sawada, K. Terakura and Y. Tokura, *Nature*, 1998, **395**, 677-680.

123. A. Kojima, K. Teshima, Y. Shirai and T. Miyasaka, *Journal of the American Chemical Society*, 2009, **131**, 6050-6051.
124. V. M. Goldschmidt, *Naturwissenschaften*, 1926, **14**, 477-485.
125. A. M. Glazer, *Acta Crystallographica Section B-Structural Science*, 1972, **B 28**, 3384-&.
126. N. E. Brese and F. J. DiSalvo, *Journal of Solid State Chemistry*, 1995, **120**, 378-380.
127. D. Logvinovich, S. C. Ebbinghaus, A. Reller, I. Marozau, D. Ferri and A. Weidenkaff, *Zeitschrift Fur Anorganische Und Allgemeine Chemie*, 2010, **636**, 905-912.
128. R. Pastrana Fabregas, J. Isasi Marin, C. Cascales, R. Saez Puche, R. Pastrana Fábregas, J. Isasi Marín and R. Sáez Puche, *Journal of Solid State Chemistry*, 2007, **180**, 92-97.
129. S. J. Clarke, B. P. Guinot, C. W. Michie, M. J. C. Calmont and M. J. Rosseinsky, *Chemistry of Materials*, 2002, **14**, 288-294.
130. J. Oro-Sole, L. Clark, N. Kumar, W. Bonin, A. Sundaresan, J. P. Attfield, C. N. R. Rao and A. Fuertes, *Journal of Materials Chemistry C*, 2014, **2**, 2212-2220.
131. G. Tobias, D. Beltran-Porter, O. I. Lebedev, G. Van Tendeloo, J. Rodriguez-Carvajal and A. Fuertes, *Inorganic Chemistry*, 2004, **43**, 8010-8017.
132. S. J. Clarke, K. A. Hardstone, C. W. Michie and M. J. Rosseinsky, *Chemistry of Materials*, 2002, **14**, 2664-2669.
133. R. Marchand, *Comptes Rendus Hebdomadaires Des Seances De L Academie Des Sciences Serie C*, 1976, **282**, 329-331.
134. S. H. Porter, Z. Huang and P. M. Woodward, *Crystal Growth & Design*, 2014, **14**, 117-125.
135. A. Fuertes, *Inorganic Chemistry*, 2006, **45**, 9640-9642.
136. L. Pauling, *Journal of the American Chemical Society*, 1929, **51**, 1010-1026.
137. L. Clark, J. Oró-Solé, K. S. Knight, A. Fuertes and J. P. Attfield, *Chemistry of Materials*, 2013, **25**, 5004-5011.
138. M. E. Lines and A. M. Glass, *Principles and Applications of Ferroelectrics and Related Materials*, Oxford University Press, Oxford, 2001.
139. Y. Saito, H. Takao, T. Tani, T. Nonoyama, K. Takatori, T. Homma, T. Nagaya and M. Nakamura, *Nature*, 2004, **432**, 84-87.
140. M. S. Senn, J. P. Wright and J. P. Attfield, *Nature*, 2012, **481**, 173-176.
141. S.-W. Cheong and M. Mostovoy, *Nature Materials*, 2007, **6**, 13-20.
142. C. M. Fang, G. A. de Wijs, E. Orhan, G. de With, R. A. de Groot, H. T. Hintzen and R. Marchand, *Journal of Physics and Chemistry of Solids*, 2003, **64**, 281-286.

143. W. Zhu, H. Kamisaka, D. Oka, Y. Hirose, A. Leto, T. Hasegawa and G. Pezzotti, *Journal of Applied Physics*, 2014, **116**, 053505.
144. A. Ziani, C. Le Paven-Thivet, L. Le Gendre, D. Fasquelle, J. C. Carru, F. Tessier and J. Pinel, *Thin Solid Films*, 2008, **517**, 544-549.
145. C. Tassel, Y. Kuno, Y. Goto, T. Yamamoto, C. M. Brown, J. Hester, K. Fujita, M. Higashi, R. Abe, K. Tanaka, Y. Kobayashi and H. Kageyama, *Angewandte Chemie International Edition*, 2015, **54**, 516-521.
146. D. Logvinovich, J. Hejtmánek, K. Knížek, M. Maryško, N. Homazava, P. Tomeš, R. Aguiar, S. G. Ebbinghaus, A. Reller and A. Weidenkaff, *Journal of Applied Physics*, 2009, **105**, 023522.
147. N. S. Lewis and D. G. Nocera, *Proceedings of the National Academy of Sciences*, 2006, **103**, 15729-15735.
148. F. E. Osterloh, *Chemistry of Materials*, 2008, **20**, 35-54.
149. A. Kudo and Y. Miseki, *Chemical Society Reviews*, 2009, **38**, 253-278.
150. C. Pan, T. Takata, M. Nakabayashi, T. Matsumoto, N. Shibata, Y. Ikuhara and K. Domen, *Angewandte Chemie International Edition*, 2015, **54**, 2955-2959.
151. A. Kasahara, K. Nukumizu, G. Hitoki, T. Takata, J. N. Kondo, M. Hara, H. Kobayashi and K. Domen, *The Journal of Physical Chemistry A*, 2002, **106**, 6750-6753.
152. G. Hitoki, T. Takata, J. N. Kondo, M. Hara and H. Kobayashi, *電気化学および工業物理化学*, 2002, **70**, 463-465.
153. B. Siritanaratkul, K. Maeda, T. Hisatomi and K. Domen, *ChemSusChem*, 2011, **4**, 74-78.
154. T. Hisatomi, C. Katayama, K. Teramura, T. Takata, Y. Moriya, T. Minegishi, M. Katayama, H. Nishiyama, T. Yamada and K. Domen, *ChemSusChem*, 2014, **7**, 2016-2021.
155. K. Sayama, K. Mukasa, R. Abe, Y. Abe and H. Arakawa, *Journal of photochemistry and photobiology. A, Chemistry*, 2002, **148**, 71-77.
156. R. Abe, K. Sayama, K. Domen and H. Arakawa, *Chemical Physics Letters*, 2001, **344**, 339-344.
157. M. Higashi, R. Abe, K. Teramura, T. Takata, B. Ohtani and K. Domen, *Chemical Physics Letters*, 2008, **452**, 120-123.
158. A. H. White and W. Melville, *Journal of the American Chemical Society*, 1905, **27**, 373-386.
159. A. Hellwig and A. Hendry, *Journal of Materials Science*, 1994, **29**, 4686-4693.
160. N. N. Greenwood and A. Earnshaw, *Chemistry of the Elements* Pergamon Press, Oxford, 1997.
161. *United States Pat.*, 1967.
162. K. Jiang, J. T. Anderson, K. Hoshino, D. Li, J. F. Wager and D. A. Keszler, *Chemistry of Materials*, 2011, **23**, 945-952.

163. L. A. Chick, L. R. Pederson, G. D. Maupin, J. L. Bates, L. E. Thomas and G. J. Exarhos, *Materials Letters*, 1990, **10**, 6-12.
164. P. Kubelka, Munk, F, *Zeit. Für Tekn. Physik*, 1931, **12**, 593.
165. J. Tauc, *Materials research bulletin*, 1968, **3**, 37-46.
166. V. Bachmann, C. Ronda, O. Oeckler, W. Schnick and A. Meijerink, *Chemistry of Materials*, 2009, **21**, 316-325.
167. J. E. J. van Steen, J. W. H. van Krevel, G. Botty, A. C. A. Delsing, Y. Q. Li, G. de With, H. T. Hintzen, F. J. DiSalvo, G. de With and H. T. Hintzen, *Journal of alloys and compounds*, 2006, **417**, 273-279.
168. Y. Sato, H. Kato, M. Kobayashi, T. Masaki, D.-H. Yoon and M. Kakihana, *Angewandte Chemie International Edition*, 2014, **53**, 7756-7759.
169. R. Le Toquin and A. K. Cheetham, *Chemical Physics Letters*, 2006, **423**, 352-356.
170. G. F. Shuji Nakamura, *The Blue Laser Diode*, Springer-Verlag Berlin Heidelberg 1997.
171. I. Azevedo, M. G. Morgan and F. Morgan, *Proceedings of the IEEE*, 2009, **97**, 481-510.
172. J. A. Kechele, O. Oeckler, F. Stadler and W. Schnick, *Solid State Sciences*, 2009, **11**, 537-543.
173. O. Oeckler, F. Stadler, T. Rosenthal and W. Schnick, *Solid State Sciences*, 2007, **9**, 205-212.
174. H. A. Hoppe, F. Stadler, O. Oeckler and W. Schnick, *Angewandte Chemie-International Edition*, 2004, **43**, 5540-5542.
175. K. Uheda, N. Hirosaki, Y. Yamamoto, A. Naito, T. Nakajima and H. Yamamoto, *Electrochemical and Solid State Letters*, 2006, **9**, H22-H25.
176. J. Lang and J. P. Charlot, *Revue De Chimie Minerale*, 1970, **7**, 121-&.
177. S. Titeux, R. Dauce, P. Verdier and Y. Laurent, *Annales De Chimie-Science Des Materiaux*, 2001, **26**, 25-34.
178. E. Kendrick, D. Headspith, A. Orera, D. C. Apperley, R. I. Smith, M. G. Francesconi and P. R. Slater, *Journal of Materials Chemistry*, 2009, **19**, 749-754.
179. M. Zeuner, S. Pagano and W. Schnick, *Angewandte Chemie International Edition*, 2011, **50**, 7754-7775.
180. H. A. Höppe, G. Kotzyba, R. Pöttgen and W. Schnick, *Journal of Solid State Chemistry*, 2002, **167**, 393-401.
181. R. Marchand, *Comptes Rendus des Seances de l'Academie des Sciences, Serie C: Sciences Chimiques*, 1976, **283**, 281-183.
182. S. H. M. Poort, W. Janssen and G. Blasse, *Journal of Alloys and Compounds*, 1997, **260**, 93-97.

183. J. S. Kim, Y. H. Park, S. M. Kim, J. C. Choi and H. L. Park, *Solid State Communications*, 2005, **133**, 445-448.
184. J. K. Han, M. E. Hannah, A. Piquette, G. A. Hirata, J. B. Talbot, K. C. Mishra and J. McKittrick, *Journal of Luminescence*, 2012, **132**, 106-109.
185. K. A. Denault, J. Brgoch, M. W. Gaultois, A. Mikhailovsky, R. Petry, H. Winkler, S. P. DenBaars and R. Seshadri, *Chemistry of Materials*, 2014, **26**, 2275-2282.
186. T. L. Barry, *Journal of The Electrochemical Society*, 1968, **115**, 1181-1184.
187. J. K. Park, M. A. Lim, C. H. Kim, H. D. Park, J. T. Park and S. Y. Choi, *Applied Physics Letters*, 2003, **82**, 683-685.
188. S. Miao, Z. Xia, M. S. Molokeev, M. Chen, J. Zhang and Q. Liu, *Journal of Materials Chemistry C*, 2015, **3**, 4616-4622.
189. M. Catti, G. Gazzoni and G. Ivaldi, *Acta crystallographica. Section C, Crystal structure communications*, 1983, **39**, 29-34.
190. M. Catti, G. Gazzoni, G. Ivaldi and G. Zanini, *Acta Crystallographica Section B*, 1983, **39**, 674-679.
191. J. Zhou, Z. Xia, M. Chen, M. S. Molokeev and Q. Liu, *Scientific Reports*, 2015, **5**, 12149.
192. A. K. Cheetham and A. J. Skarnulis, *Analytical Chemistry*, 1981, **53**, 1060-1064.
193. J. Rodríguez-Carvajal, *Physica B: Condensed Matter*, 1993, **192**, 55-69.
194. R. Marchand, P. L'Haridon and Y. Laurent, *Journal of Solid State Chemistry*, 1978, **24**, 71-76.
195. L. Stenberg, J. R. Sellar and B. G. Hyde, *Nature*, 1986, **320**, 428-429.
196. R. L. Withers, J. G. Thompson and B. G. Hyde, *Crystallography Reviews*, 1989, **2**, 27-61.
197. J. Felsche, *Naturwissenschaften*, 1971, **58**, 218-219.
198. R.-J. Xie and H. T. Hintzen, *Journal of the American Ceramic Society*, 2013, **96**, 665-687.
199. P. Dorenbos, *Journal of Physics: Condensed Matter*, 2003, **15**, 4797.
200. M. Zhang, J. Wang, Q. Zhang, W. Ding and Q. Su, *Materials Research Bulletin*, 2007, **42**, 33-39.
201. J. Brgoch, C. K. H. Borg, K. A. Denault, A. Mikhailovsky, S. P. DenBaars and R. Seshadri, *Inorganic Chemistry*, 2013, **52**, 8010-8016.
202. T. Suehiro, N. Hirosaki and R.-J. Xie, *ACS Applied Materials & Interfaces*, 2011, **3**, 811-816.
203. W. T. Carnall, P. R. Fields and K. Rajnak, *The Journal of Chemical Physics*, 1968, **49**, 4412-4423.

204. B. R. Judd, *Physical Review*, 1962, **127**, 750-761.
205. L. O. Pålsson and A. P. Monkman, *Advanced Materials*, 2002, **14**, 757-758.
206. J. Hou, X. Yin, Y. Fang, F. Huang and W. Jiang, *Optical Materials*, 2012, **34**, 1394-1397.
207. G. Blasse and N. Sabbatini, *Materials Chemistry and Physics*, 1987, **16**, 237-252.
208. D. Van Der Voort and G. Blasse, *Journal of Solid State Chemistry*, 1990, **87**, 350-359.
209. D. Van der Voort and G. Blasse, *Chemistry of Materials*, 1991, **3**, 1041-1045.
210. E. Kaldis, P. Streit and P. Wachter, *Journal of Physics and Chemistry of Solids*, 1971, **32**, 159-165.
211. F. Stadler, O. Oeckler, H. A. Höppe, M. H. Möller, R. Pöttgen, B. D. Mosel, P. Schmidt, V. Duppel, A. Simon and W. Schnick, *Chemistry – A European Journal*, 2006, **12**, 6984-6990.
212. S. Tao and J. T. S. Irvine, *Nat Mater*, 2003, **2**, 320-323.
213. J. Sfeir, P. A. Buffat, P. Möckli, N. Xanthopoulos, R. Vasquez, H. Joerg Mathieu, J. Van herle and K. Ravindranathan Thampi, *Journal of Catalysis*, 2001, **202**, 229-244.
214. R. M. Hornreich, *Journal of Magnetism and Magnetic Materials*, 1978, **7**, 280-285.
215. J. S. Zhou, J. A. Alonso, V. Pomjakushin, J. B. Goodenough, Y. Ren, Y. Ren and J. Q. Yan, *Physical Review B Condensed matter and materials physics*, 2010, **81**.
216. K. Tezuka, Y. Hinatsu, A. Nakamura, T. Inami, Y. Shimojo and Y. Morii, *Journal of Solid State Chemistry*, 1998, **141**, 404-410.
217. K. H. L. Zhang, Y. Du, P. V. Sushko, M. E. Bowden, V. Shutthanandan, S. Sallis, L. F. J. Piper and S. A. Chambers, *Physical Review B*, 2015, **91**, 155129.
218. X. L. G. Gouin, L.; Marchand, R.; Laurent, Y., *Annales De Chimie-Science Des Materiaux*, 1995, **20**, 293-299.
219. J. Cabana, C. D. Ling, J. Oró-Solé, D. Gautier, G. Tobías, S. Adams, E. Canadell and M. R. Palacín, *Inorganic Chemistry*, 2004, **43**, 7050-7060.
220. A. H. Gudat, Sabine; Kniep, Ruediger; Rabenau, Albrecht, *Zeitschrift fuer Naturforschung, B: Chemical Sciences*, 1990, **45**, 111-120.
221. M. H. Maunaye, Christian; L'Haridon, Paul; Laurent, Yves, *Bulletin de la Societe Francaise de Mineralogie et de Cristallographie* 1976, **99**, 203-205.
222. P. S. Devi and M. S. Rao, *Thermochimica Acta*, 1989, **153**, 181-191.

223. J. D. Gordon, R. M. Hornreich, S. Shtrikman and B. M. Wanklyn, *Physical Review B*, 1976, **13**, 3012-3017.
224. F. Bartolomé, J. Bartolomé, M. Castro and J. J. Melero, *Physical Review B*, 2000, **62**, 1058-1066.
225. N. Shamir, H. Shaked and S. Shtrikman, *Physical Review B*, 1981, **24**, 6642-6651.
226. K. R. Chakraborty, S. Mukherjee, S. D. Kaushik, S. Rayaprol, C. L. Prajapat, M. R. Singh, V. Siruguri, A. K. Tyagi and S. M. Yusuf, *Journal of Magnetism and Magnetic Materials*, 2014, **361**, 81-87.
227. J. J. Neumeier and H. Terashita, *Physical Review B*, 2004, **70**, 214435.
228. J. P. Attfield, *International Journal of Inorganic Materials*, 2001, **3**, 1147-1152.
229. J. P. Attfield, *Crystal Engineering*, 2002, **5**, 427-438.
230. H. Wolff and R. Dronskowski, *Journal of Computational Chemistry*, 2008, **29**, 2260-2267.
231. J. Oro-Sole, L. Clark, W. Bonin, J. P. Attfield and A. Fuertes, *Chemical Communications*, 2013, **49**, 2430-2432.
232. M. Yang, J. A. Rodgers, L. C. Middler, J. Oró-Solé, A. B. Jorge, A. Fuertes and J. P. Attfield, *Inorganic Chemistry*, 2009, **48**, 11498-11500.
233. J. C. Wang, D. C. Shie, T. F. Lei and C. L. Lee, *Journal of Applied Physics*, 2005, **98**, 024503.
234. A. Feteira, D. C. Sinclair, K. Z. Rajab and M. T. Lanagan, *Journal of the American Ceramic Society*, 2008, **91**, 893-901.
235. B. Kennedy, C. Howard and B. Chakoumakos, *Physical review. B, Condensed matter*, 1999, **60**, 2972-2975.
236. O. Fursenko, J. Bauer, G. Lupina, P. Dudek, M. Lukosius, C. Wenger and P. Zaumseil, *Thin Solid Films*, 2012, **520**, 4532-4535.
237. Y. Wu, P. Lazic, G. Hautier, K. Persson and G. Ceder, *Energy & environmental science*, 2013, **6**, 157-168.
238. S. K. Sun, T. Motohashi, Y. Masubuchi and S. Kikkawa, *Journal of the European Ceramic Society*, 2014, **34**, 4451-4455.
239. Y. S. Malghe and U. C. Yadav, *Journal of Thermal Analysis and Calorimetry*, 2015, **122**, 589-594.
240. S. J. Clarke, C. W. Michie and M. J. Rosseinsky, *Journal of Solid State Chemistry*, 1999, **146**, 399-405.
241. R. L. N. Sastry, C. N. R. Rao and P. N. Mehrotra, *Transactions of the Faraday Society*, 1966, **62**, 1632-&.
242. P. Stephens, *Journal of applied crystallography*, 1999, **32**, 281-289.
243. J. A. Guevara, S. L. Cuffini, Y. P. Mascarenhas, R. E. Carbonio and J. A. Alonso, *The structure of orthorhombic hafniates by neutron powder*

diffraction and perturbed-angular-correlation spectroscopy (PAC), 1998.
244. S. J. Clarke, B. P. Guinot, C. W. Michie, M. J. C. Calmont and M. J. Rosseinsky, *Chemistry of Materials*, 2002, **14**, 288-294.
245. P. Camp, A. Fuertes and J. P. Attfield, *Journal of the American Chemical Society*, 2012, **134**, 6762-6766.
246. M. Higashi, K. Domen and R. Abe, *Journal of the American Chemical Society*, 2013, **135**, 10238-10241.
247. H.-S. Oh, H. Nong, T. Reier, A. Bergmann, M. Gliech, E. Willinger, R. Schlögl, D. Teschner and P. Strasser, *Journal of the American Chemical Society*, 2016, **138**, 12552-12563.
248. K. Duckers, K. Dückers and H. P. Bonzel, *Surface science*, 1989, **213**, 25-48.